Light coupling and light trapping in alkaline etched multicrystalline silicon wafers for solar cells

Jessica Davina Hylton

To my children

Light coupling and light trapping in alkaline etched multicrystalline silicon wafers for solar cells

Lichtinkoppeling en lichtopsluiting in alkalisch geëtste multikristallijn-siliciumwafers voor zonnecellen

(met een samenvatting in het Nederlands)

Proefschrift

Ter verkrijging van de graad van doctor aan de Universiteit Utrecht,
op gezag van de Rector Magnificus, Prof. Dr. W.H. Gispen,
ingevolge het besluit van het College voor Promoties in het openbaar te verdedigen
op woensdag 12 april 2006 des middags te 12:45 uur

door

Jessica Davina Hylton

geboren op 30 april 1971 te Paddington, Londen (Groot-Brittannië).

Promotor: **prof. dr. W.C. Sinke**
Verbonden aan de Departementen Natuur- en Sterrenkunde en Scheikunde van de Faculteit Bètawetenschappen van de Universiteit Utrecht (www.uu.nl).

Universiteit Utrecht

ISBN-10: 90-810463-1-4
ISBN-13: 978-90-810463-1-2

(www.ecn.nl)

(www.nwo.nl)

The research described in this thesis was made possible by financial support from the Energy research Centre of the Netherlands (ECN) and the Nederlandse Organisatie voor Wetenschappelijk Onderzoek (NWO) within the program 'Solar cells for the 21st century'.

Contents

1: Introduction

1.1 Photovoltaics

The sun is an abundant and virtually inexhaustible source of energy. It irradiates the earth with 1.5 x 10^{18} kWh of energy per year, amounting to more than 10,000 times the annual world consumption. An elegant way of harnessing this energy is by means of photovoltaics (PV), the effect whereby solar energy is converted directly into electricity.

Silicon is the most important of the available photovoltaic energy conversion materials. Crystalline silicon cells currently comprise more than 90% of all solar cells produced worldwide, with multi- and mono- crystalline constituting approximately two-thirds and one-third of this total respectively. The solar cell industry currently obtains its silicon base material from the by-products of hyperpure poly-Si production and from remelt from Czochralski (Cz) and Float-Zone (FZ) material originating from the microelectronics industry. This off-spec material is forecast to increase in price from US$ 32/kg in the first half of 2004 to as high as US$ 50/kg this year [1,2], prices being driven upwards by the short supply of feedstock in the light of the growth of the PV industry and demand due to an upturn in the semiconductor industry [1]. The silicon is melted and recrystallised in ingots to form multicrystalline silicon material (defined in [3] as material with crystal grain sizes varying from approximately 1 mm-10 cm). Silicon wafers are typically 300 μm thick as-cut, with approximately 200 μm thick saw kerf (sawing dust due to cutting the wafer from the ingot). Sawing techniques can be improved to reduce kerf losses, but significant cost and energy reduction can also be achieved if thinner silicon wafers are used. For this reason, the general trend is towards the use of still thinner silicon wafers.

An important consequence of reducing the cell thickness arises due to the low absorption coefficient of crystalline silicon. An increasing proportion of light of longer wavelengths will not be fully absorbed on its first passage through the cell thickness, so that very effective light trapping schemes have to be built in. High efficiency silicon solar cells often employ geometrical texturisation schemes, notably inverted pyramid textures formed by anisotropic etching in alkaline solutions. These textures serve a dual purpose; they possess anti-reflection properties through multiple bounce incidence of light at the front surface, and also provide light trapping through the oblique passage of light through the cell, which increases the pathlength for absorption and promotes total internal reflection at the back surface. However,

such light trapping schemes are limited in their application to laboratory cells, using expensive processing techniques such as photolithography on small area monocrystalline wafers. This thesis concentrates on the optical characterisation of geometrical textures formed by wet chemical etching, as may be employed in a standard industrial solar cell processing line on multicrystalline silicon wafers.

1.2 Solar cell operation

A standard silicon solar cell consists of a sandwich of p-type and n-type material separated by a junction. When p- and n- type silicon are brought into contact, free electrons from the n-type side and free holes from the p-type side naturally diffuse to the opposite side of the junction. The departing electrons and holes leave behind ionised donors and acceptors respectively. This sets up an electric field at the junction between the p and n material which opposes the flow of diffusing carriers. When the cell is illuminated, excess electron-hole pairs are generated throughout the material. The excess minority carriers (electrons in the p-type material, holes in the n-type material) diffuse to the junction where they are swept across to the other side by the built-in electric field. The generated electrons and holes are thus separated from each other spatially, which in open circuit conditions leads to the build up of an open-circuit voltage V_{oc}, and in short-circuit conditions results in the short-circuit current density J_{sc}. The separated carriers can thus be collected at the contacts and electrical power extracted from the cell when the voltage V lies between zero and V_{oc}, preferably at the maximum power point of the cell (see Figure 1.1). The proportion of generated carriers that is finally collected is limited by the number of electrons and holes which recombine before reaching the junction. Carrier diffusion lengths in the p-type bulk must thus be greater than the cell thickness to obtain high collection efficiency.

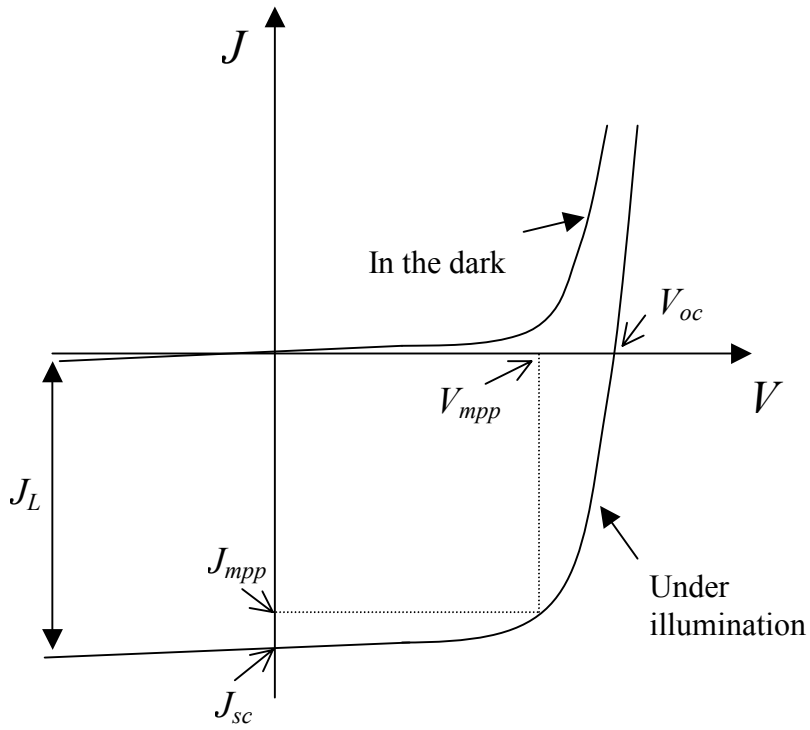

Figure 1.1 *JV characteristics of a silicon solar cell.*

The current generating characteristics of an ideal silicon solar cell [4] can be described by the equation

$$J = J_0(\exp(qV/kT) - 1) - J_L \qquad (1.1)$$

This is basically the ideal diode equation, shifted down by an amount J_L, the light-generated current density, as is plotted in Figure 1.1. This equation relates the current density J (A/m^2) to the voltage V across the device, where k is Boltzmann's constant, q is the elementary charge and T is the absolute temperature. J_0 is the reverse thermal current or dark saturation current density, dependent on the recombination parameters within the bulk and at the surfaces of the cell. A cell with larger recombination will have a larger J_0.

The efficiency η of a solar cell is defined by:

$$\eta \equiv \frac{P_{out,\max}}{P_{in}} = \frac{FF.V_{oc}.J_{sc}}{P_{in}} \qquad (1.2)$$

where P_{in} is the total light intensity incident upon the cell, $P_{out,\max}$ is the actual power per unit area extracted from the cell at the maximum power point of the cell, and FF is the fill factor of the cell, defined as $P_{out,\max}$ divided by the product of V_{oc} and J_{sc}. The ideal FF can be accurately approximated using the expression (see [4])

$$FF = \frac{v_{oc} - \ln(v_{oc} + 0.72)}{v_{oc} + 1} \qquad (1.3)$$

where v_{oc} is the normalised V_{oc}, equal to $V_{oc}/(kT/q)$.

1.3 Electrical characteristics of real cells

To describe the J-V curve of a solar cell more precisely, it is necessary to add a current density $J_{02}(\exp(qV/m_{DR}kT)-1)$ to equation (1.1) to account for the recombination in the depletion region (DR). Setting $V_T = kT/q$:

$$J(V) = J_{01}(\exp(V/V_T) - 1) + J_{02}(\exp(V/m_{DR}V_T) - 1) - J_L \qquad (1.4)$$

The difference with the J_{01} diode term is that the diode factor m_{DR} is included in the exponent. In the most simple case, m_{DR} is fixed at 2, independent of V. Although this is not so precise, it is still widely used when fitting J-V curves. More detailed information about the value of m_{DR} as a function of V and the junction properties can be found in [5].

The other widely used equation for $J(V)$ is related to the more empirical one diode model. The one diode equation is similar to (1.1), the most important difference being the introduction of the diode factor m in the exponent:

$$J(V) = J_T - J_L = J_{0T}(\exp(V/mV_T) - 1) - J_L \qquad (1.5)$$

where J_T is the total recombination current density and J_{0T} the saturation current density of J_T. There is no direct physical interpretation for m, it is used as a fit parameter that determines the

roundness of the diode curve. One would expect that $1<m<2$, because J_{NR} (NR = neutral region) and J_{DR} that are replaced by J_T have diode factors of 1 and <2, respectively. A low m is preferable, because that results in a more rectangular J-V curve.

When all resistance losses are neglected, a cell would have an intrinsic fill factor FF_i which only depends on V_{oc} and m and is given to a good approximation by the empirical relation [4]:

$$FF_i = \frac{\frac{V_{oc}}{mV_T} - \ln\left(\frac{V_{oc}}{mV_T} + 0.72\right)}{\frac{V_{oc}}{mV_T} + 1} \qquad (1.6)$$

In practice, FF_i will never be reached because series and shunt resistances will always result in a FF decrease (which can be very large).

The series and shunt resistance in a cell are usually described by the specific series resistance ρ_{se} and the specific shunt resistance ρ_{sh}. 'Specific' refers to the area independence of the terms, which are obtained by multiplication of the resistance values for the cell with the total cell area. An increase of ρ_{se} or a decrease of ρ_{sh} both lead to a decrease of the FF; J_{sc} and V_{oc} are almost not affected unless the resistance problems are really severe. The different components of the series resistance in a solar cell are the sheet resistance ρ_s of the emitter (n-type region), the bulk resistance of the base (p-type region), the contact resistance between metallisation and silicon at the front side and at the back side and the resistance of the metallisation itself. The shunt resistance can be lowered by local defects in material or problems in the processing. By inserting ρ_{se} and ρ_{sh} in equation (1.5) and setting $V' = V - J\rho_{se}$, the $J(V)$ relation for the one diode model including resistances is obtained:

$$J(V) = J_{0T}(\exp(V'/mV_T) - 1) + (V'/\rho_{sh}) - J_L \qquad (1.7)$$

For the two diode model, a similar equation holds. It is standard practice to fit a measured J-V curve to the equation above or its two diode equivalent. To find accurate values for all parameters is generally difficult because of their strong interdependence in the fit procedure: it is possible to exchange between parameters with only very little influence on the fit residue.

It is important to note that one should be very careful when interpreting results obtained by fitting J-V curves to the models given above. They have been developed for one dimension (or small lateral differences), but in the real world large two-dimensional differences can make the fitting results very difficult to interpret. For example, it was shown recently that one of the most disturbing 2D effects is a non-uniformly high contact resistance [6]. This leads to an increase of diode factor or second diode current, although the origin of the problem is not related to space charge region recombination.

1.4 Optical properties of silicon

1.4.1 Absorption coefficient of crystalline silicon

The light absorbing characteristics of silicon are characterized by the wavelength-dependent absorption coefficient, as plotted in Figure 1.2. The light transmitted into the silicon is attenuated on its passage through the semiconductor, according to the equation

$$I(x) = I_0 e^{-\alpha x} \qquad (1.8)$$

where I_0 is the initial light intensity transmitted into the silicon, $I(x)$ is the intensity of the light after attenuation due to its passage over a distance x in the silicon, and α is the absorption coefficient.

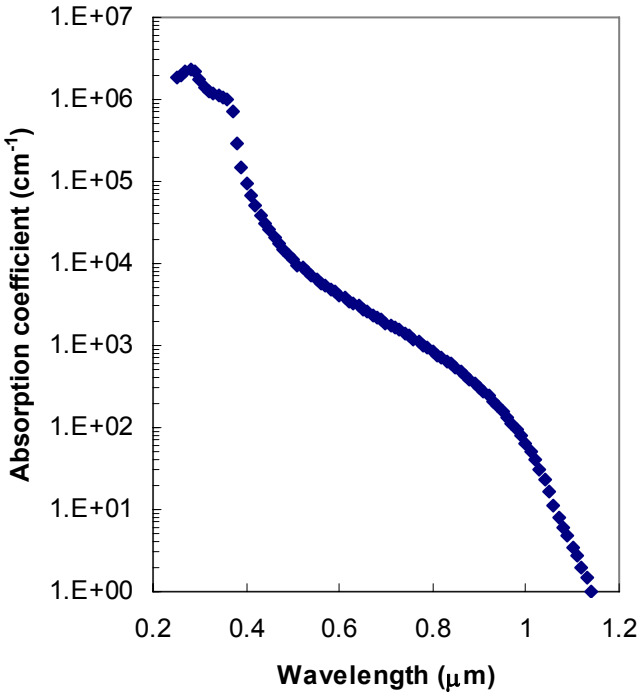

Figure 1.2 *Absorption coefficient of pure silicon at a temperature of 300 K.*

At short wavelengths the absorption coefficient is extremely high, so that light is absorbed within the first 10 nm of its passage through the silicon. The energy of these photons is far greater than the indirect silicon bandgap of 1.12 eV, and even direct bandgap absorption is possible for photon energies above 3.4 eV. The excess energy is released as heat, as only one electron-hole pair is created by a single photon on absorption. As the wavelength increases, the photon energy becomes too small to allow direct excitation of electrons from the valence to the conduction band. The absorption process must therefore be assisted by one or more phonons which accommodate the change in crystal momentum between the initial and final states. For wavelengths above 1.1 μm where the absorption coefficient tends to zero, photon energies are below that of the silicon bandgap so that electron-hole pairs are no longer generated. The silicon is thus effectively transparent for long wavelengths.

1.4.2 Reflectance characteristics

The absorption characteristics can be clearly observed in the reflectance curves for polished silicon. The silicon has a complex refractive index $n_c = n - ik$, where k is the extinction coefficient. k is related to α by the equation

$$\alpha = \frac{4\pi f k}{c} \tag{1.9}$$

where f is the frequency of a light wave propagating through a material, and c is the speed of light in vacuum. The reflectance of normally incident light at an interface between two materials having different refractive indices is described by the equation

$$R = \left(\frac{n_{ct} - n_{ci}}{n_{ct} + n_{ci}} \right)^2 \tag{1.10}$$

where i and t are subscripts pertaining respectively to the incident medium and the medium into which the light is transmitted. For the case where air and silicon are the incident and transmitting medium respectively, this equation reduces to

$$R = \frac{(n_{Si} - 1)^2 + k_{Si}^2}{(n_{Si} + 1)^2 + k_{Si}^2} \tag{1.11}$$

since $n = 1$ and $k = 0$ for air, to a very good approximation.

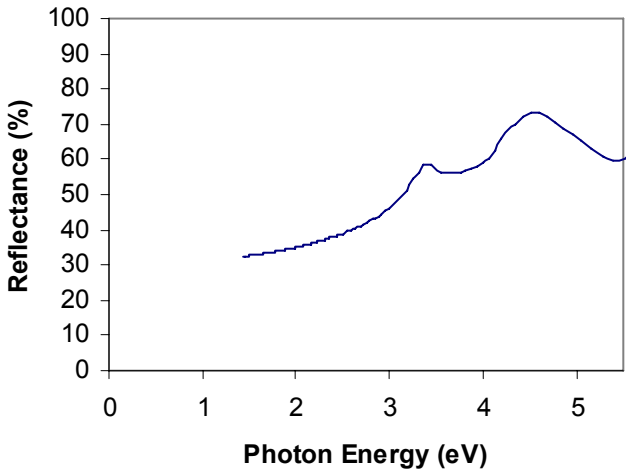

Figure 1.3 *Reflectance at a silicon surface in air as a function of photon energy.*

Figure 1.3 shows the variation of reflectance at the silicon-air interface with photon energy. Reflectance is seen to increase gently initially from a value of around 31 % at low photon energies, rising up to a peak at a photon energy of approximately 3.4 eV. Reflectance continues to peak and undulate for photon energies above 3.4 eV, with reflectivity values varying between 50 and 70%. For photon energies lower than the direct bandgap energy of 3.4 eV, indirect electron transitions occur across the bandgap, with electrons near the valence

band maximum crossing to the conduction band minimum. A phonon is required for momentum conservation in this transition. This is by far the most important process for silicon illuminated by sunlight. The peaks in reflectance at higher energies of 3.4 and 4.5 eV (λ = 0.36 and 0.28 μm respectively) correspond to "critical points" in momentum space. Here the gradients of the conduction and valence band edges are equal [7], with the first peak at 3.4 eV corresponding to the direct bandgap.

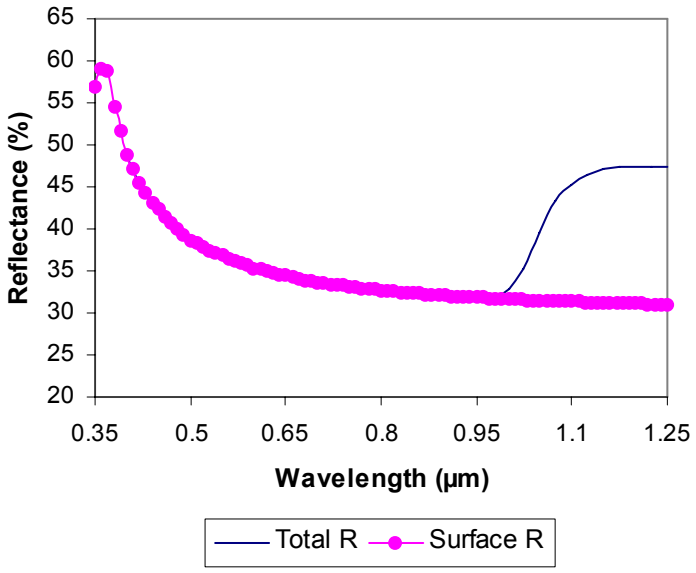

Figure 1.4 *Calculated total and surface reflectance for a 200 μm thick double polished wafer in air, showing the emergence of the back surface reflectance in the total reflectance curve.*

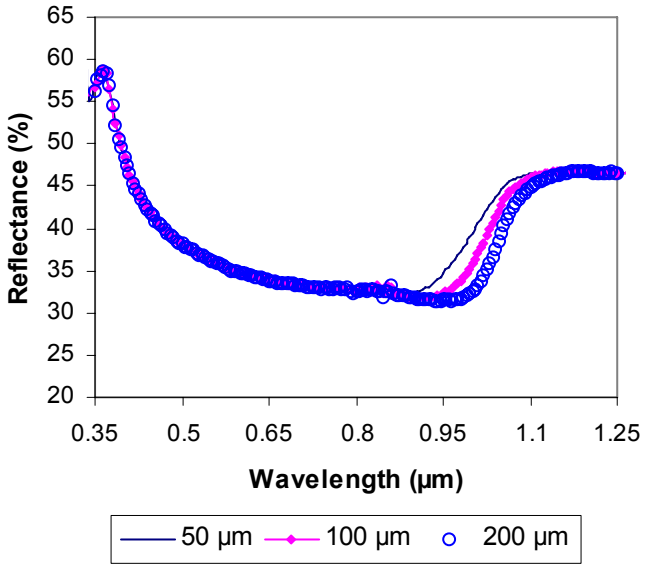

Figure 1.5 *Measured total reflectances for different thicknesses of polished silicon in air. Reflectance from the back surface becomes visible at still shorter wavelengths as the wafer thickness decreases.*

Figure 1.4 shows the measured total (diffuse + specular) reflectance curve for a 100 μm polished silicon wafer in air as a function of wavelength. This was measured at 8º incidence with respect to the normal using a spectroradiometer/integrating sphere set-up (see Chapter 2). As expected, a reflectance peak is observed at a wavelength of approximately 0.36 μm corresponding to strong direct absorption, with reflectances tailing off with increasing wavelength to values around 31%. However, at a wavelength value of approximately 0.9 μm, the measured reflectance begins to rise again up to a maximum of approximately 47 %. The reason for the measured rise in reflectance at longer wavelengths is a direct result of the decreasing absorbing capabilities of the silicon for photon energies approaching that of the indirect band gap.

As the absorption coefficient decreases with wavelength (Figure 1.2), the pathlength which must be traversed by the photon to ensure its absorption in the silicon increases, until it becomes greater than the thickness of the wafer itself. On reaching the back surface of the silicon, the light will be partially transmitted into the air, and the rest is re-reflected towards the front surface. Once pathlengths are long enough to reach the front surface, light transmitted at the front into the air begins to add to the total reflectance values measured. As the absorption coefficient continues to decrease, photons experience multiple passes within the silicon and the total reflectance thus increases accordingly. At wavelengths above 1.1 μm, corresponding to the indirect bandgap energy of 1.12 eV, electron-hole pairs are no longer generated within the silicon. The photons ricochet between the front and back surfaces with absorption tending to zero and the total reflectance plateauing off to a maximum. As the wafer thickness decreases, the back surface reflectance becomes visible at still shorter wavelengths leading to a shift in the reflectance curve as shown in Figure 1.5.

1.5 Reducing optical losses

1.5.1 Introduction

Optical losses are generally seen in a reduction of the short-circuit current density in the cell. This is because fewer electron-hole pairs are generated than would be possible if all the energy contained in the incident light were to be usefully absorbed in the silicon cell. Typical optical losses are due to reflection of light at metallic front contacts, reflection at the surface of the silicon and/or the front encapsulation, and transmission of the weakly absorbed wavelengths of light out of the silicon prior to its absorption. These losses are introduced and discussed below.

Reflection losses at the metallic contacts can be reduced by minimising the top contact coverage of the cell (although this may result in increased series resistance), so light falls upon a greater surface area of silicon in the cell. The algorithms introduced in [8] have been specifically developed for the optimisation of metallic contact design for both maximum efficiency at a particular irradiation condition and maximum yearly yield. Reflection losses from the exposed silicon front surface can be reduced by applying anti-reflection coatings on the front surface of the cell, and/or the use of geometrical surface texturing.

Overall absorption of light coupled into the cell is limited by the strong wavelength dependence of the silicon absorption coefficient. Increasing cell thickness would increase optical absorption (although any light which is absorbed more than a diffusion length away from the junction will not typically contribute to short-circuit current since the carriers

recombine), but would also increase material costs in the manufacturing of the cell. The current trend towards thinner silicon cells means that the issue of optical absorption becomes increasingly important. The silicon cell thickness must be reduced whilst still maximising the amount of light absorbed within the silicon, particularly at the partially transmitting wavelengths at the infra-red end of the spectrum. This can be achieved by increasing the optical path length of light traversing the silicon solar cell using a combination of surface texturing and light trapping.

1.5.2 Reflection reduction

1.5.2.1 Anti-reflection coatings

Reflectance properties can be improved by employing an anti-reflection coating (ARC) on the silicon front surface. So-called "quarter wavelength", predominantly single layered ARC's are generally employed industrially, applied directly upon the silicon, which for a coating thickness d_1 and refractive index n_1 satisfy the relationship:

$$d_1 = \frac{\lambda_0}{4n_1} \tag{1.12}$$

Light of incident wavelength λ_0 which is reflected away at the silicon-ARC interface initially, will destructively interfere with light reflected directly away from the ARC-encapsulant (e.g. air or glass) interface with which it will be 180° out of phase, thereby ideally cancelling out reflection (see e.g. [9]). ARC's for silicon solar cells are usually optimised for a maximum current output in the terrestrial solar spectrum (AM1.5G). This is achieved for coatings with a reflectance minimum at wavelengths of around 600 nm, these ARC's giving the finished cells their characteristic blue colour.

The AR layer gives interference effects so that reflectance can be reduced to a minimum value at a specific wavelength, as given by the equation

$$R_{\min} = \left(\frac{n_1^2 - n_0 n_2}{n_1^2 + n_0 n_2} \right)^2 \tag{1.13}$$

where n_0, n_1 and n_2 are the refractive indices of the encapsulant, anti-reflection coating and the silicon respectively. A reflectance minimum of zero can be achieved for λ_0 if the refractive index of the ARC corresponds to the geometric mean of the refractive indices of the adjacent media, whereby:

$$n_1 = \sqrt{n_0 n_2} \tag{1.14}$$

Taking refractive index values of $n_{\text{air}} = 1.0$, $n_{\text{glass}} = 1.5$ and $n_{\text{Si}} = 3.8$, then optimal refractive index values for the ARC will be 1.9 and 2.3 respectively for the silicon cell in air and under encapsulation. Such coatings reduce the average amount of sunlight lost by reflectance on polished silicon in air from 30% to only 10% as weighted over the useful solar wavelengths, and from approximately 20% to 5% under glass [4].

Typical coatings consist of dielectric materials such as TiO_x, with $n \sim 2.3$ [10] and SiN_x:H (whose refractive index can be varied between 1.9 and 2.3 typically [11]); for laboratory cells these are sometimes applied in double layers with two complementary dielectric materials so as to broaden the band of reflectance reduction. SiN_x:H coatings additionally provide front surface and also bulk passivation, in part by virtue of hydrogen contained in the coating which passivates recombination centres. Unfortunately, the application of a SiN_x:H anti-reflective layer necessitates the implementation of a vacuum deposition step within the solar cell production line.

1.5.2.2 Surface texturisation

Another way of reducing reflectance is by applying a geometrical surface texture to the front surface of the silicon. This can be done mechanically, for example using specially developed dicing saws (e.g. [12]), or (electro-) chemically, by etching the silicon in an alkaline or acidic solution (e.g. [13],[14]). The anti-reflection properties pertaining to the geometry of the texture are demonstrated for a simple two-dimensional structure in Figure 1.6. Light incident normally to the silicon wafer falls upon the grooves at a point *a*. About 70% of this light is transmitted into the silicon and the rest is reflected. However, the reflected light is now angled downwards towards a neighbouring groove, instead of away from the silicon surface as would be the case for a planar cell. Thus the light falls re-incident at the silicon surface for a second chance of transmission into the silicon at point *b*. In this way, light is more efficiently coupled into the silicon, leading to reflection reduction without the use of an anti-reflection coating. The number of "bounces" upon the front surface for such a periodic symmetrical texture depends upon the facet angle α of the texture with respect to the wafer surface. Minimal facet angles of 30º and 54º are required for double and triple bounce reflectance respectively. For the double bounce case shown in Figure 1.6, the light reflected away from the silicon at b is lost. However, if the silicon is encapsulated under glass, it is possible to totally internally reflect light arriving at the glass-air interface at above the critical angle of 42º, whereby it will be re-directed towards the silicon yet again for possible re-incidence.

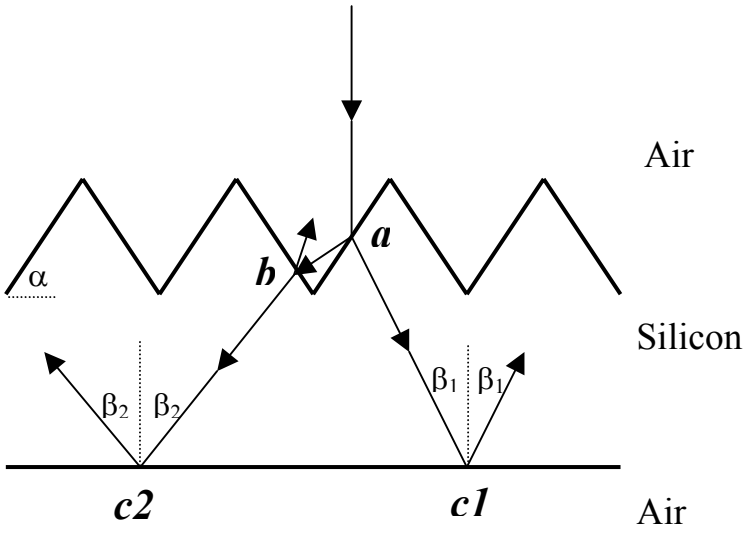

Figure 1.6 *Reflection reduction and light trapping in geometrically textured silicon.*

1.5.3 Light trapping

1.5.3.1 Introduction

An obvious way of reducing the costs of silicon solar cell production is to reduce the quantity of the expensive silicon base material used. Improved wafering techniques allow the production of thinner silicon slices from ingots, from typical thicknesses currently of 300 μm down to thicknesses of under 150 μm. The reduction in the silicon volume also has a physical advantage, in that bulk recombination is correspondingly reduced. This yields higher V_{oc} values for the cell, provided that surfaces are well passivated to ensure minimum recombination.

However, the poor absorption of useful photon energies at wavelengths approaching the band gap is a serious problem for thin cells, counteracting the efficiency improvements gained through the reduction of bulk SRH recombination resulting from a reduced bulk volume. At each traversal of the light across the cell, light may be partially transmitted out of the silicon at the front and rear surfaces (unless a highly reflective back surface reflector BSR is employed), as the required pathlength for absorption will significantly exceed the wafer or film thickness. Therefore schemes must be incorporated which trap the light into the cell, so that light which is not absorbed during the first passage through the cell will have additional opportunities for absorption.

1.5.3.2 Basic Principles

The most obvious method of extending the pathlength of the light in the silicon is to make the rear surface highly reflective, so that no light can escape at the rear on its first passage through the silicon. The deposition of a single 100 nm layer of silver metal for example will reflect approximately 95 % of the light incident at the back surface at normal incidence. This is substantially higher than the 30 % reflectance of the uncoated rear silicon in air and adds a component to the long wavelength reflectance above 1 μm (see Figure 1.7). Rear reflectances can be further improved by the incorporation of a dielectric layer between the silicon and the metallic layer. For example, reflectances of up to 98% are achievable experimentally at a wavelength of 1.15 μm, for a silicon oxide layer of 110 nm thickness interposed between silicon and an aluminium rear reflector [15]. However, much light will still escape at the front surface at each second passage through the silicon.

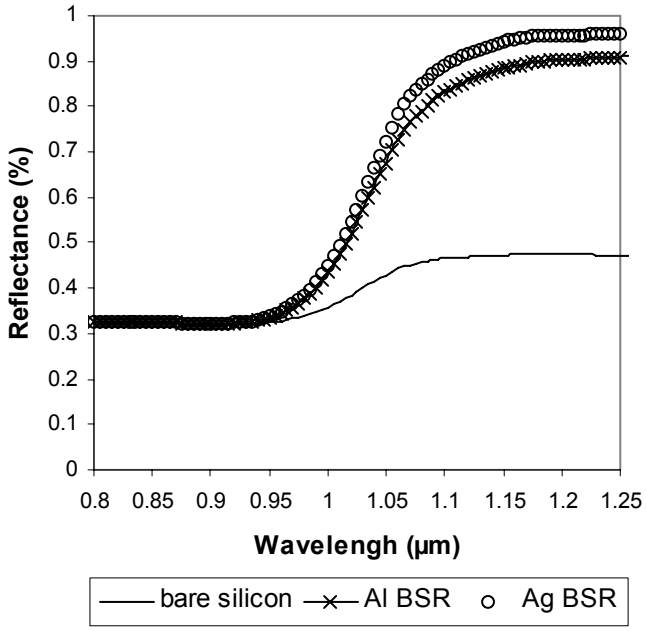

Figure 1.7 *Effect of aluminium and silver back surface reflectors on the total reflectance curve at near infrared wavelengths for 100 µm polished silicon.*

A very effective means of light trapping within the silicon is presented by the geometrical or random texturisation of one or both of the silicon surfaces. These schemes take advantage of total internal reflection within the silicon at the interface between the optically denser silicon (refractive index n = 3.5) and its less dense surroundings (e.g. glass encapsulation with n = 1.5). The texturisation of the silicon surface can allow the weakly absorbed light to be scattered obliquely into the silicon on initial incidence at the front surface, or internally from a textured back surface, in directions that are totally internally reflected. The critical angles for total internal reflectance are 16-17º for the silicon-air interface, compared with ~42º at a silicon-glass interface, with light falling outside of these angles being trapped within the silicon. Light trapping by means of geometrical surface texturisation can also be demonstrated using Figure 1.6. Weakly absorbed light which has been coupled in at points *a* and *b* will travel for distances far greater than the cell thickness before absorption and thus will approach the rear surface at points *c1* and *c2* as shown. The oblique coupling of this light into the silicon at *a* and *b* enhances the pathlength of the light above the thickness of the cell during its first pass to the silicon rear. If the light falls incident at the rear Si-air interface at angles β_1 and β_2 greater than 16-17º, total internal reflection occurs. Thus all the light is trapped within the silicon with light re-reflected obliquely towards the front surface, where further trapping may occur depending upon the incident angle of the light and the particular texture used.

This method of light trapping can considerably increase the pathlengths of light within the silicon. For example, if the silicon is provided with a 100% reflecting and fully randomising (Lambertian) rear (which scatters light with uniform intensity in all directions, irrespective of its incident angle) the average maximum pathlength of rays may be increased to approximately 50 times the cell thickness at non-absorbed longer wavelengths [16]. This is because only the small fraction of light falling within the 16-17º escape cone will be partially transmitted out of the front of the silicon at each second pass, the rest being totally internally

reflected within the silicon. This maximises the probability of absorption for useful wavelengths as the cell thickness decreases.

1.5.4 Practical formation of geometrical surface textures using alkaline etchants

The use of alkaline anisotropic etchants for the texturisation of (100)-oriented monocrystalline silicon wafers is an established technique in solar cell processing. Alkaline etchants such as sodium hydroxide (NaOH) or potassium hydroxide (KOH) at low concentrations (<5%) and temperatures typically of 80-90 °C expose {111} oriented facets resulting in square-based pyramids randomly distributed over the cell surface. The 54.7º facet angles of these textures allow double bounce reflectance of all light and triple bounce reflectance at the base of the pyramids, with the three dimensional structure (as opposed to two-dimensional grooves) allowing for more possible ray paths for multiple reflection and transmission into the silicon. These textures are thus ideal for providing reflection reduction and light trapping on monocrystalline (100) wafers. Moreover, the etching stage required is easily incorporated into industrial processing lines, where at least one etch step (for the removal of wafer sawing damage) is already required.

However, in the case of multicrystalline silicon, only a small proportion of the crystals are oriented close to (100) for the formation of pyramidal textures, with many orientations etching flat thus having reflectances equivalent to polished silicon. The level of reflection reduction and light trapping achieved for multicrystalline silicon is inherently bound with the geometry of the texture formed per orientation, and thus with the anisotropy of the chemical etch used and the distribution of crystal orientations in the wafer. In order to understand the optical characteristics observed for chemically textured multicrystalline surfaces, it is essential that the texture is quantified geometrically so that the passage of light can be fully described.

1.6 This thesis

The aim of this thesis is to relate the measured optical characteristics of multicrystalline silicon to the surface geometries formed by (potentially) industrial wet chemical etch processes. Hereby statements can be made as to the quality of reflection reduction and light trapping at both a localised level per orientation and for complete multicrystalline cells.

In order to explain the optical characteristics observed for the multicrystalline etch textures, it is essential that the geometries of these textures can be fully quantified so that the passage of the incident light can be followed by ray-tracing. Several experimental techniques were employed and specially developed for the analysis of both optical and surface morphological properties of the textures investigated, these methods being introduced in Chapter 2 of this thesis. In Chapter 3, an overview is given of chemical texturisation methods. The surface morphology is analysed for varying etch parameters for alkaline chemical etchants. The textures provided by isotropic etchants are analysed for comparison, both with acidic etchants and with reactive ion etching. Chapter 4 concentrates upon the quantification of the texture geometries formed by two particular alkaline etching solutions for multicrystalline wafers. Comparisons are made between the two solutions on a per orientation basis, using neighbouring multicrystalline wafers as well as monocrystalline wafers of seven principal orientations. The surface morphologies are quantified in terms of the azimuthal and facet tilt angles of the textures exposed, as well as through the determination of the crystallographic

etch facet orientations exposed by the two etches as described by their Miller indices. The performance of the textured wafers under encapsulation is investigated in detail. Using the weighted average of quantitative reflectance data for the seven orientations, alkaline surface texturisation is assessed for multicrystalline silicon in air and under encapsulation. In Chapter 5, the light trapping properties of these textures are investigated in detail. A novel ray-tracing program [17] is employed, whereby atomic force microscope (AFM) height scans of the complex etch surfaces, up to 50 x 50 μm in size, are used as input for the description of the actual etch surface in each case. Work focuses on thin silicon wafers (~ 200 μm), with ray-tracing data being compared directly with experimentally measured data through measured and modelled reflectance curves. The light trapping properties of multicrystalline wafer textures were examined on the basis of results for the seven monocrystalline wafer orientations, for bare and encapsulated silicon, with or without a silver back surface reflector. In Chapter 6, the results of the preceding chapters are summarised.

References

[1] M. Schmela, "Solar report sees undamped PV market growth", PHOTON International: The Photovoltaic Magazine, September 2004

[2] W.P. Hirshman, "The good spin on PV's market angst", PHOTON International: The Photovoltaic Magazine, August 2005

[3] P.A. Basore, "Defining Terms for Crystalline Silicon Solar Cells", Prog. Photovolt: Res. Appl. **2** (1994) 177-179

[4] M.A. Green, "Solar Cells, Operating Principles, Technology and System Applications", Prentice Hall Inc. (1982) ISBN 0-13-82270

[5] K.R. McIntosh, P.P. Altermatt, G. Heiser, "Depletion-region recombination in silicon solar cells: when does $m_{DR} = 2$?", in Proc. 16th EPVSEC, Glasgow (2000) 251-254

[6] A.S.H. van der Heide, A. Schönecker, J.H. Bultman, W.C. Sinke, "Explanation of high solar cell diode factors by non-uniform contact resistance", Prog. Photovolt: Res. Appl. **13** (2005) 3-16

[7] M.A. Green, "Silicon Solar Cells, Advanced Principles and Practice", Bridge Printery Pty. Ltd (1995) ISBN 0 7334 0994 6

[8] A.R. Burgers, "How to Design Optimal Metallization Patterns for Solar Cells", Prog. Photovolt: Res. Appl. **7** (1999) 457-461

[9] E. Hecht, "Optics", Addison-Wesley Publishing Company Inc. 2nd Edition (1987)

[10] F. Duerinckx, A. Noppe, P. Choulat, J. Szlufcik, J. Nijs, B. Habraken, "Advanced industrial processes for large area screen printed multicrystalline silicon solar cells", in Proc. 16th EPVSEC, Glasgow (2000) 1301-1304

[11] F. Duerinckx, J.Szlufcik, "Defect passivation of industrial multicrystalline solar cells based on PECVD silicon nitride", Solar Energy Materials & Solar Cells **72** (2002) 231-246

[12] M. Spiegel, C. Gerhards, F. Huster, W. Joos, P. Fath, E. Bucher, "Industrially attractive front contact formation methods for mechanically V-textured multicrystalline silicon solar cells", Solar Energy Materials & Solar Cells **74** (2002) 175-182

[13] M.A. Green, "Two New Efficient Crystalline Silicon Light-trapping Textures", Prog. Photovolt: Res. Appl. **7** (1999) 317-320

[14] S. de Wolf, P. Choulat, E. Vazsonyi, R. Einhaus, E. v. Kerschaver, K. de Clercq and J. Szlufcik, "Towards industrial application of isotropic texturing for multi-crystalline silicon solar cells", in Proc. 16th EPVSEC, Glasgow (2000) 1521-1523

[15] M.A. Green, "High efficiency silicon solar cells", Trans Tech Publications (1987) ISBN 0-87849-537-1

[16] E. Yablonovitch, G.D. Cody, "Intensity Enhancement in Textured Optical Sheets for Solar Cells", IEEE Trans. Elec. Dev. ED-**29** no. 2 (1982) 300-305

[17] D. Thorp, S.R. Wenham, "Ray-tracing of arbitrary surface textures for light-trapping in thin silicon solar cells", Solar Energy Materials and Solar Cells **48** (1997) 295-301

2: Experimental techniques

In order to fully understand the optical properties of textured solar cells, it must be possible to follow the path of light and the level of its absorption throughout its passage through the (encapsulated) cell structure. The texturisation of the silicon surface serves to divert the passage of the light both on reflection and refraction at the different material interfaces, for example between the silicon and air, as was described in chapter 1. The effects of these interactions can be observed quantitatively in the measured reflectances of the textured wafer, through lower reflectances in the visible to near infrared for example indicating a texture beneficial to light coupling, or a high near infrared reflectance indicating a highly reflective rear. However, the observed optical properties can only be explained fully if the surface morphology of the different interfaces is quantified. In this way it is possible to predict the likely paths of incident light and thus to explain the measured optical characteristics. This chapter introduces the experimental methods used. Particular attention is paid to techniques developed specifically for the analysis of the textured etch surface morphology.

2.1 Total hemispherical reflectance and transmittance measurements

2.1.1 Apparatus and measurement procedures

Reflectance and transmittance measurements form one of the most important experimental methods used in this thesis for determining the optical properties of the textured silicon samples. Measurements were performed using an integrating sphere and spectroradiometer set-up, as shown in Figure 2.1. The integrating sphere from Labsphere (RT-060-SF) has a sputtered internal coating of white "Spectraflect" material (based on $BaSO_4$). This coating has a total reflectance of 95% on average in the wavelength range from 300 to 1400 nm, and has a very high diffusivity for incident light approaching the Lambertian ideal (see chapter 1.5.3.2). The sphere has a 15.2 cm (6 inch) external diameter, with six ports in total, 5 ports around the equator with 22 mm internal diameter (25.4 mm = 1 inch external diameter), and a (fibre) port at the top (12.7 mm = 0.50 inch diameter). Portplugs are also coated internally with Spectraflect. The spectroradiometer from Instrument Systems GmbH (SP320) has a maximum specified wavelength detecting range from 250 nm to 2500 nm. This wide range is made possible through the use of a monochromator containing two gratings with 1200 and 610 lines per mm, the first grating operating in the range 250 – 860 nm, and the second for the longer wavelengths. Secondly, two detectors are employed, the first being a silicon

photodetector for the lower wavelength range, and the second an InGaAs detector for the longer wavelengths. Measurements in this thesis were performed from 0.33 μm up to 1.4 μm. This range was used both due to the very low intensity of the light source used beyond these wavelengths, and considering the spectral response of silicon, which becomes fully transparent for wavelengths above 1.25 μm.

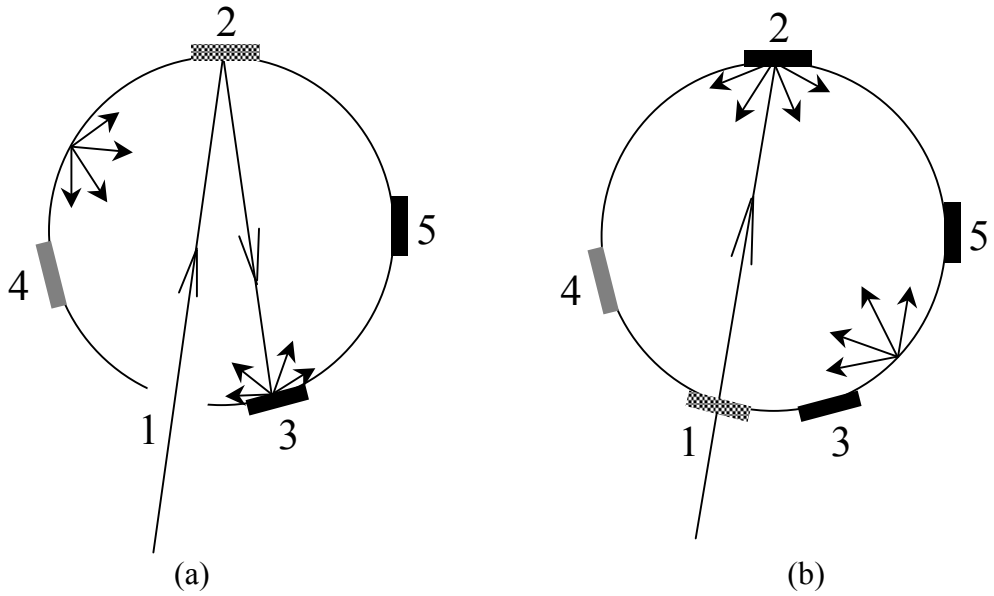

Figure 2.1 *Positions of sample and reference during total hemispherical a) reflectance (R) & b) transmittance (T) measurements. The sample is at positions 2 and 1 for R & T measurements respectively, the reference at position 4 in both cases, port 5 (the detector port) is open and the remaining ports are closed with Spectraflect coated port plugs. The sample and reference positions are substituted for the reference measurement. Specularly reflected/transmitted light paths are shown.*

A halogen white light source (KI-125 Koehler illuminator from Labsphere) is used for measurements. This source uses internal lenses and iris diaphragms for focusing, spot size variation and intensity control. Light is focused upon the sample at an incident angle of 8°. The sample is positioned on the sphere wall at either the sample or entrance port for reflectance or transmittance measurements respectively, as shown in Figure 2.1. The reflected or transmitted light is randomised on successively hitting the coated sphere walls, so that the intensity finally detected is independent of directionality of reflectance/transmittance for the (textured) sample. In this way the total reflectance or transmittance is measured. (For measurement of the diffuse reflectance of a sample without the specular component, an optical light trap is placed in the specular port 3 in Figure 2.1; the light trap is placed at port 2 for diffuse transmittance measurements.).

2.1.2 Effect of internal scattering within the sample

In order to measure the total reflectance or transmittance of the sample, all the reflected or transmitted light respectively must enter the integrating sphere, without escaping out of the field of view of the sphere, beyond the bounds of the sample porthole. However, for diffusely reflecting or transmitting materials, light can easily be scattered internally within the sample, so that it may exit the sample outside the sphere, as is shown in Figure 2.2.

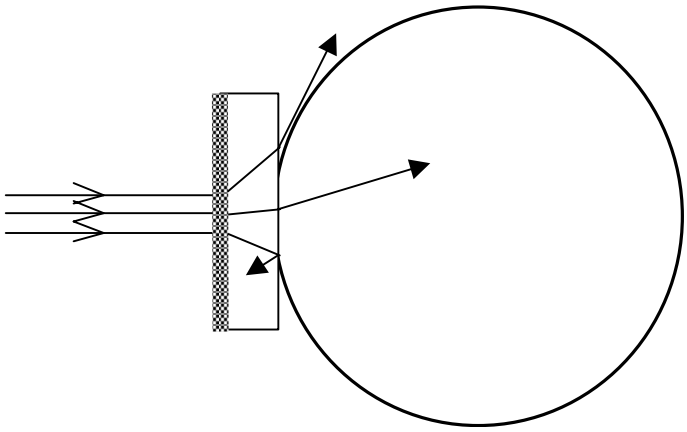

Figure 2.2 *Possible light paths through a sample with a randomising front surface texture, showing how light can be scattered outside of the view of the integrating sphere. This leads to an artificially low transmittance measurement in this case.*

Considering the case of bare textured silicon, this effect is negligible for reflectance measurements for the absorbing wavelengths, as long as the light does not traverse the silicon more than twice. In that case, the light transmitted into the sample is either completely absorbed or else transmitted at the rear. The reflectance measured is then correct, in the limits of sphere reflectance, light loss through portholes, sample curvature etc. However, for wavelengths above the bandgap, light travelling obliquely through the silicon may exit the front surface outside the sphere, instead of contributing to the total reflectance measured. This effect is potentially greater still for transmittance, where light can be scattered outside the field of view of the sphere after only its first pass from front to rear of the silicon. This leads to the underestimation of the reflectance or transmittance for highly diffusing samples and will become increasingly large with thickness of the sample, as less of the obliquely scattered light is returned within the boundaries of the port. Glass encapsulation increases this effect, causing errors even at visible wavelengths for light reflected/transmitted at an angle from the front textured silicon surface. Although this effect generally occurs at less important non-absorbing wavelengths for silicon, the measurement error is important for the correct modeling and interpretation of reflectances (and consequently the correct quantification of light trapping) by ray-tracing, as will be described in chapter 5.

Two methods have been suggested whereby this error can be minimised [1, 2]. The first method for transmission measurements is a single beam technique, using illumination of the sample with a large area parallel beam for uniform irradiation of the whole sample surface. The sample in this case is greater than the port diameter and has a large area relative to its thickness. Here, incident light which is scattered out of the field of view of the sphere on transmission, is compensated by light scattered inwardly from the sample perimeter, which otherwise would fall externally to the sphere in the absence of the sample. In the second method, a small light spot is used, with a diameter smaller than port size (reference [3] and later the ASTM standard E903-82 [4] state a minimum distance between the beam edge and the edge of the porthole of ten times the sample thickness). The small spot size should ensure that light is collected even for wide angled scatter. This latter method, suitable for reflectance and transmittance measurements, is used in experimentation for this thesis. For 300 μm and 500 μm thick wafers, maximum spot diameters of *(22-6 =)* 16 mm and 12 mm can be used respectively according to [3,4]. For encapsulated samples however, with glass thicknesses of 1-3 mm, measurements according to this standard are not possible for the sphere used, since

the minimum distance between spot and porthole edges would be 20-60 mm for the glass alone. In this case, as small a spot as possible is used. The effect of spot size is shown for an encapsulated sample in Figure 2.3, showing the reduction in measured reflectance with increased spot size at partially transmitting wavelengths above 1 µm. Decreasing the spot size however cannot be continued indefinitely, as the reduction in intensity leads to increased proportions of noise. This can be seen for the 5 mm spot in the visible and at the detector transition at 850 nm. For this reason, a spot size of ~10 mm was generally held as a minimum for measurements on encapsulated samples.

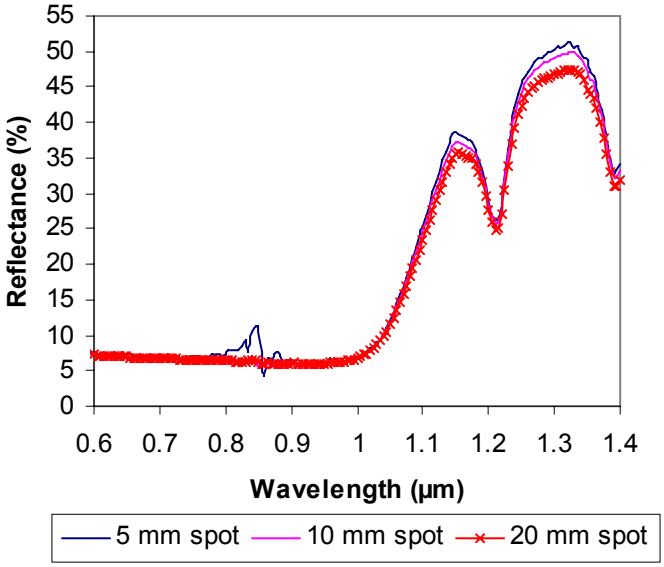

Figure 2.3 *The effect of spot size on measured reflectance for a pyramidally textured (100) silicon wafer under 1mm glass + 0.3 mm EVA (ethyl vinyl acetate) encapsulation. A 20 mm spot diameter gives a lower reflectance reading at the transmitting wavelengths due to scattering out of the sphere view. A 5 mm spot gives a better long wavelength reading, but the low reflecting intensity leads to a noisy signal at the (for silicon more important) lower wavelengths.*

2.2 Laue recordings and localised laser scatter measurements

2.2.1 Laue photography

Laue photography (see e.g. [5]) was performed at the University of Amsterdam. In this method, a parallel beam of X-rays with a continuous wavelength distribution is directed onto a crystal surface at normal incidence, whereby each light wavelength is scattered elastically from specifically oriented crystal planes according to Bragg's law. This leads to a diffraction pattern on a flat projection screen of X-ray film positioned either in front of the crystal (back-reflection method) or behind it (detecting transmitted diffraction beams).

Individual crystallites in the textured multicrystalline wafers were examined using Laue photography in the back-reflection set-up (see Figure 2.4). The specified orientations of monocrystalline wafers used were also validated using this technique. The wafer is positioned parallel to and facing the photographic film, using a film-to-wafer distance of 4 cm and an X-ray beam diameter of 1 mm.

The orientation of the crystal is determined according to the positions and intensities of the Laue spots on the X-ray film (the intensities being represented by larger spot sizes as additional orders of reflection superpose), using the available computer program "Orient Express". This is calculated [5] by comparing the spatial co-ordinate systems for the wafer/crystal surface and the principal crystal axes *X'Y'Z'* for silicon. The former orthogonal Cartesian system *uvw*, contains the wafer surface normal and crystal plane normal for a particular reflectance spot, whilst the principal silicon crystal axes *X'Y'Z'* are described by Miller indices *h'k'l'* and lattice parameters *a b c*. A third co-ordinate system is also used specifically for non-cubic crystal structures, where a plane and its normal are not generally described by the same indices as given by its principal crystal axes. Here, an *h'k'l'* plane is described in a Cartesian system $\xi\eta\zeta$ as an *(hkl)* plane, so that the [*hkl*] direction is normal to the (hkl) plane. For the cubic silicon (diamond type structure), *hkl* and *h'k'l'* are equivalent. Computer simulations of the Laue photograph can thus be made, detailing the Miller indices of the crystal planes corresponding to selected Laue spots.

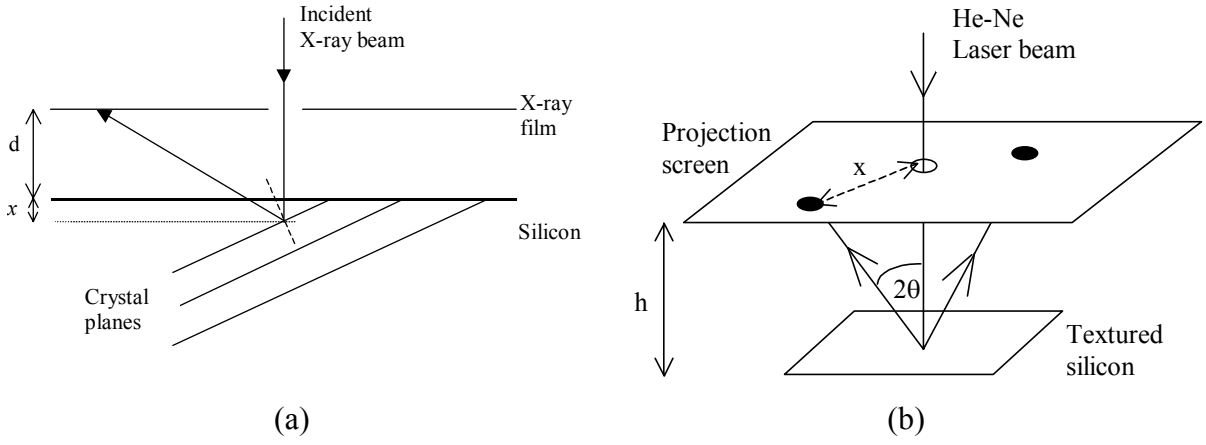

Figure 2.4: *Illustrations of a) Laue X-ray diffraction in the back-reflecting mode, for X-rays reflected from a crystal plane at depth x in the silicon, and b) localised laser scatter recordings.*

2.2.2 Localised laser scatter measurements

The localised reflectance patterns from He-Ne laser light incident on textured silicon samples give important information about the directionality of scatter resulting from the etch surface morphology [6,7,8]. He-Ne laser light of 0.5 mm diameter, with a wavelength of 632.8 nm, is directed at normal incidence to a particular mono-wafer or crystal in multicrystalline silicon, via a hole in a semi-transparent projection screen (see Figure 2.4). Light is reflected back from the crystal in preferential directions according to the surface texture resulting from the particular etch used and the crystal/wafer orientation examined. The reflected light impinges upon and is diffused by the projection screen giving a pattern characteristic of the surface morphology. The screen, made of glass with one side sandblasted facing the sample, is scribed with a centimeter grid for quantitative location of the reflection spot. Light transmitted through the screen is recorded with a CCD camera.

This method can be used quantitatively to determine the tilt angles of facets for textured surfaces, provided the reflection spot corresponds to a single direct reflectance from the facet. In this case, the facet tilt angle can be calculated from the equation $\tan 2\theta = x/h$, where θ is the

facet tilt angle, x is the distance of the reflectance spot from the point of normal incidence of the laser through the screen centre, and h is the height of the projection screen above the sample. However, for higher facet angles where double reflectances may occur, scatter patterns only give indicative information about the paths of light at the surface. In addition, multiple bounce reflectances lead to a large reduction of intensity for the light arriving at the projection screen, making for poor detection visually with a CCD camera. Wide angled single reflectances are also difficult to detect within the finite limits of the projection screen and CCD field of view.

For these reasons, photogoniometry was additionally used for recording localised laser scatter patterns in these limiting cases. The photogoniometer used was designed and located at TNO-Bouw in Delft, for the measurement of angularly dependent light transmission through architectural glazings. Despite the large dimensions of the instrument (with measurement arms over a metre in length), very good measurements could be made of the localised laser scatter from textured silicon samples; the method is described in detail in [9]. A silicon photodiode of 2 mm diameter was used for detection of the laser light. A convex lens placed in front of the detector served to increase the light intensity at the photodiode, and the detected signal was (pre-) amplified as necessary via a feedback circuit and further via a lock-in amplifier. The detector is positioned on a two armed rotational support, these arms allowing independent movement of the detector in the x and y directions respectively. In this way it was possible to make a hemispherical scan of the light scattered from the textured wafer.

2.2.3 A method for the determination of facet orientations

There are parallels between the Laue and scatter pattern measurements. For the Laue technique, the reflection of X-rays from crystal planes is recorded giving crystallographic information, whilst for the scatter technique, light reflected from the surface gives information about the surface morphology. These methods can be combined to give the crystallographic orientation of the etch facets [8].

The wafer-to-projection screen distances (h) are set to be equal at 4 cm for both Laue and scatter measurements and it is ensured that the position of the wafer with respect to the incident light and the projection screen is the same in both cases. Then the (mirror image of the) scatter reflection patterns corresponding to exposed etch facets should, when superimposed on the Laue photograph/simulations, correspond with the Laue reflection spot for the crystal plane with the same surface normal. Thus the orientation of the etch facet should be directly determinable, expressed in terms of its crystallographic Miller indices. Similarly, where photogoniometer measurements are used, the mercator projection of the scatter pattern (projection of a sphere on a flat surface) can be superimposed upon the Laue pattern for determination of the etch facet orientations. The results of this technique are detailed for alkaline etched wafers in Chapter 4 of this thesis.

2.3 Optical and scanning electron microscopy

Microscopic investigation of the surface textures was essential for qualitative analysis and limited quantification of the etch morphology. Scanning electron microscopy (SEM), using JEOL JSM-T300 and JEOL JSM-6330F microscopes, was the most important technique for visual inspection. SEM microscopy uses acceleration voltages up to 20 kV. Optical

microscopy (Leica Leitz Aristomet up to x1000 magnification) was also used, although it is poorly applicable to rough textures (with height differences above 4-5 μm) which cannot be properly focussed.

Photographs were generally taken from directly above the sample (i.e. 0° tilt) or in cross-section. In the latter case, samples were broken by hand rather than using polishing/embedding techniques in order to preserve the texture profile with the minimum of damage or disturbances.

2.4 Atomic Force Microscopy

A Nanoscope® III atomic force microscope (AFM) from Digital Instruments was specially adapted for the accurate scanning of textures with heights in the micron (as opposed nanometer to sub-micron) range. The AFM provides high resolution, three dimensional scanning of sample surfaces, providing both visual and, most importantly for this thesis, quantitative data for the surfaces measured. The height data files obtained from the AFM scan consist of a total of 256 x 256 measured data points, and the typical scan area used for samples in this work was 50 x 50 μm².

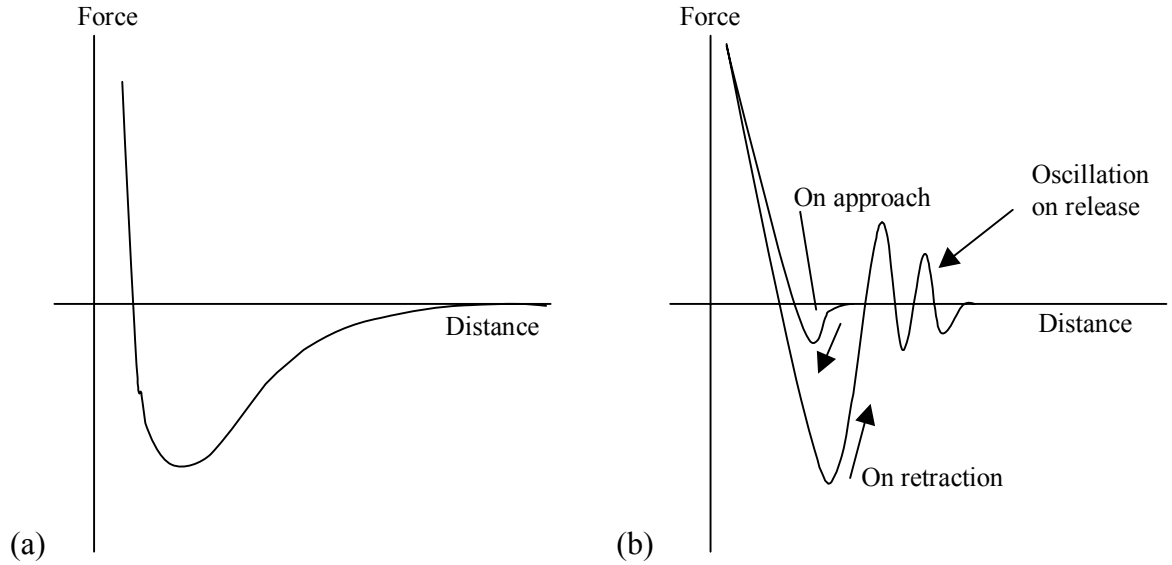

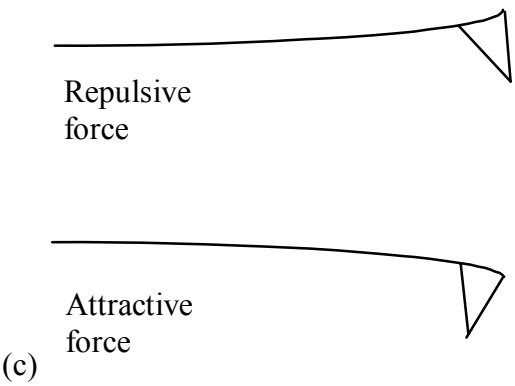

Figure 2.5 *a) The force-distance relationship shown graphically between the probe and the sample in a) the ideal case, b) the actual situation whereby forces on approach and retraction of the probe vary for example due to oscillation on retraction, external forces due to capillary action of contaminant layers, etc. The deflection of the cantilever in repulsive and attractive force regions is shown in c). Scans are performed in the repulsive region for contact AFM measurements.*

The height of the surface textures and the steepness of the features are the two major limiting factors for accurate mapping of the surface. The provided scanner (type J) with a maximum height range of 4 μm (125 x 125 μm scan area), was replaced by a scanner with an 8 μm height range (200 x 200 μm scan area), in order to accommodate for the roughness of the surface texture found in experimentation. Similarly, the standard AFM needle has a symmetrical pyramidal shape with a large tip angle of ~75°, whereby steep slopes cannot be traced correctly and texture cannot scanned in narrow troughs in the surface, even at higher resolution. An asymmetric needle was therefore used with lower tip angle of ~34°, whereby maximum slope angles of 70-80° could be measured in the trace direction and troughs were better accessible to the needle.

2.4.1 Principles of atomic force microscopy

The AFM operates through the measurement of the forces between the probe and sample. These forces are strongly dependent upon the distance between the two. On approaching the sample, the probe experiences attractive forces initially, for example from long range Van der Waals forces. However, when in close proximity to the sample, the electron orbitals of surface atoms on the probe and sample begin to interact and repel, until at even smaller distances repulsive forces neutralise and finally dominate attractive forces between the sample and probe. The force-distance relationship is described ideally by the curve in Figure 2.5a, with attractive forces dominant in the curve area under the line of zero force, and repulsive forces represented above this line. Probe geometry and the presence of surface contamination also influence the forces measured.

The scanning probe of the AFM consists of a very sharp tip supported on the underside of a flexible cantilever. The sample is supported upon the piezoelectric scanner situated below the probe, which provides the actual rastering movement of the sample during the scan. Laser light falling upon the topside of the cantilever reflects onto a split photodiode sensor. The reflected light is used to detect changes in the deflection of the cantilever as it scans the textured sample surface. Height variations on the surface cause the laser light to be deflected onto varying positions on the detector. The cantilever deflection or surface height is determined from the differential voltage from the photodiode elements. Changes in the photodiode output are used to adjust the z-piezoelectric ceramic and the measured height data in the z direction.

The deflection of the cantilever as a function of the applied force F is described theoretically by Hooke's law $F = -kx$, where k is the spring constant of the cantilever, and x is its displacement. For contact mode scanning, the cantilever used is weak with a very low spring constant and a low resonant frequency, so that the probe is able to follow the surface smoothly without jolting from the surface at texture peaks, for example. The actual force-distance relationship obtained during AFM operation differs from the theoretical ideal, as shown in Figure 2.5b, with different curves obtained on approach and withdrawal of the probe to/from the surface influenced by the cantilever properties, interaction of the needle with contaminating layers, etc. The AFM is operated in the repulsive region of the force curves for scanning in the contact mode, whereby the cantilever is pushed away from the sample due to the repulsive forces (Figure 2.5c).

2.4.2 Measurement accuracy

2.4.2.1 Calibration of the scanner

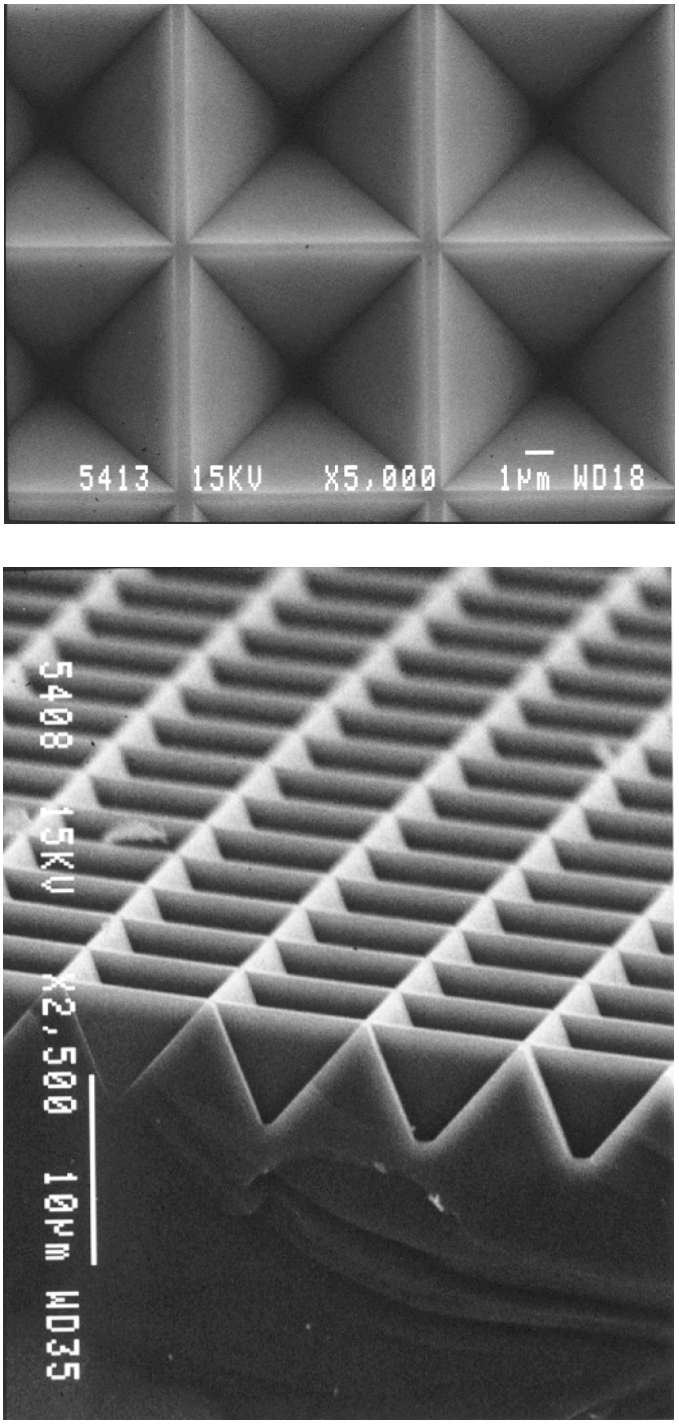

(a)

(b)

Figure 2.6 *SEM photographs taken a) above and b) tilted to show the cross-section of the inverted pyramid texture used for height calibration.*

The scan width calibration is performed using a calibration grid as supplied with the original scanner. This grid contains an array of 5 μm square pits, with a period of 10 μm (not illustrated). The pit depth of 180 nm is however far too small to allow for sensible *height*

calibration within the range of the textured silicon surfaces. In order to provide a more suitable height calibrating tool, a (100) oriented monocrystalline silicon wafer with a periodic inverted pyramid texture was used (see Figure 2.6) as formed by photolithographic etching. The facets of the four-sided pyramids are composed of intersecting {111} oriented planes at 54.7° to the base orientation.

The dimensions of the texture are checked using scanning electron microscopy from directly above the substrate for lateral dimensions and at cross-section for control of facet angles and depth of inverted pyramid peaks. SEM micrographs also provide the basis for controlling the quality of the AFM scan, since SEM and AFM scans of the surface should be identical for the same viewing angle. This calibration sample allows control on three aspects of dimension; laterally, through the periodicity of the pyramidal grid, vertically, through the depth of the inverted peaks, and angularly, since the tilt and azimuthal angles of four facet directions must be determined. These details can be most easily represented through plotting the height data from the scan in terms of a facet transform (see Figure 2.12), as will be discussed in section 2.4.4. If the tilt angles of the {111} facets are too high or low, the Z sensitivity of the piezoelectric (the change in height registered in nanometers for a given applied voltage) is corrected to give the correct height and thus angular height data for the repeat scan of the surface. The soft piezoelectric in the 8 µm scanner used is particularly subject to deformation beyond its calibrated values. For this reason, the system was calibrated for every series of measurements (at least once per day of measurement), with a final scan of the calibration sample at the end of each measurement session to check for eventual variations in the measurement accuracy during the session.

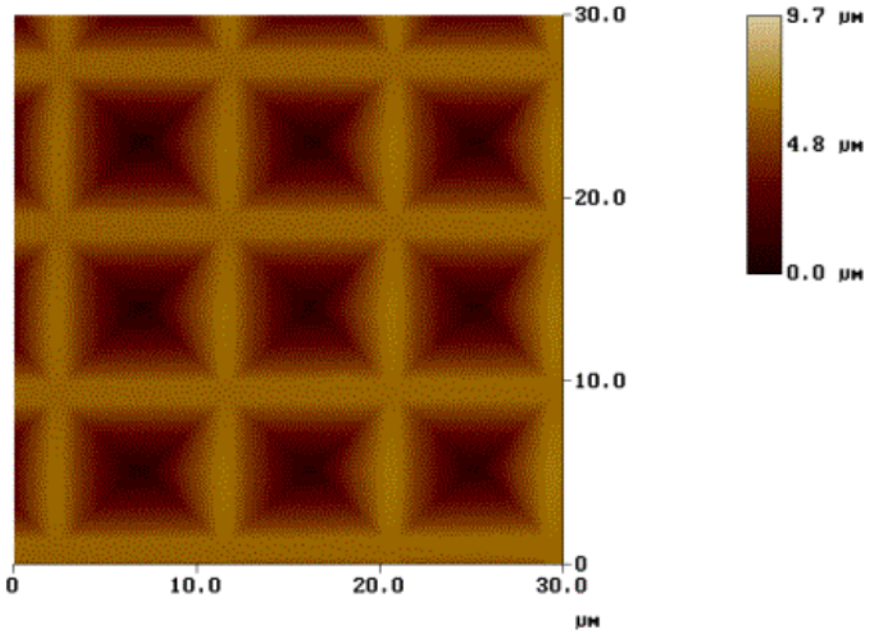

Figure 2.7 *AFM scan corresponding to the inverted pyramid structure shown in Figure 2.6 previously.*

2.4.2.2 Shape of the scanning needle tip

The shape of the scanning needle tip is particularly important to the quality of the AFM scan. The image/height data results from a convolution of both the sample surface morphology and the shape of the probe itself. The probes used are made of etched silicon, and provide a high aspect ratio and sharpness for the tip. The intended probe shape is shown in Figure 2.8, as taken from [10]. The asymmetric tip has a kite-shape when viewed from below. Considering the probe as drawn in Figure 2.8a, the trace direction is towards the right, with retrace direction to the left. The probe is asymmetric from front-to-back along the length of the lever (i.e. in the trace direction). The right hand side (back) of the tip has a very steep 10° half angle; the left hand side (front) has a 25° half angle. Combined with the 10° mounting angle of the cantilever, this means that the back edge is vertical. For the front side of the tip, this gives a maximum scanning angle of 55°. In the lateral directions (see Figure 2.8b) the probe is symmetric, with tip half angles of 17° each giving maximum lateral scanning angles of 73°.

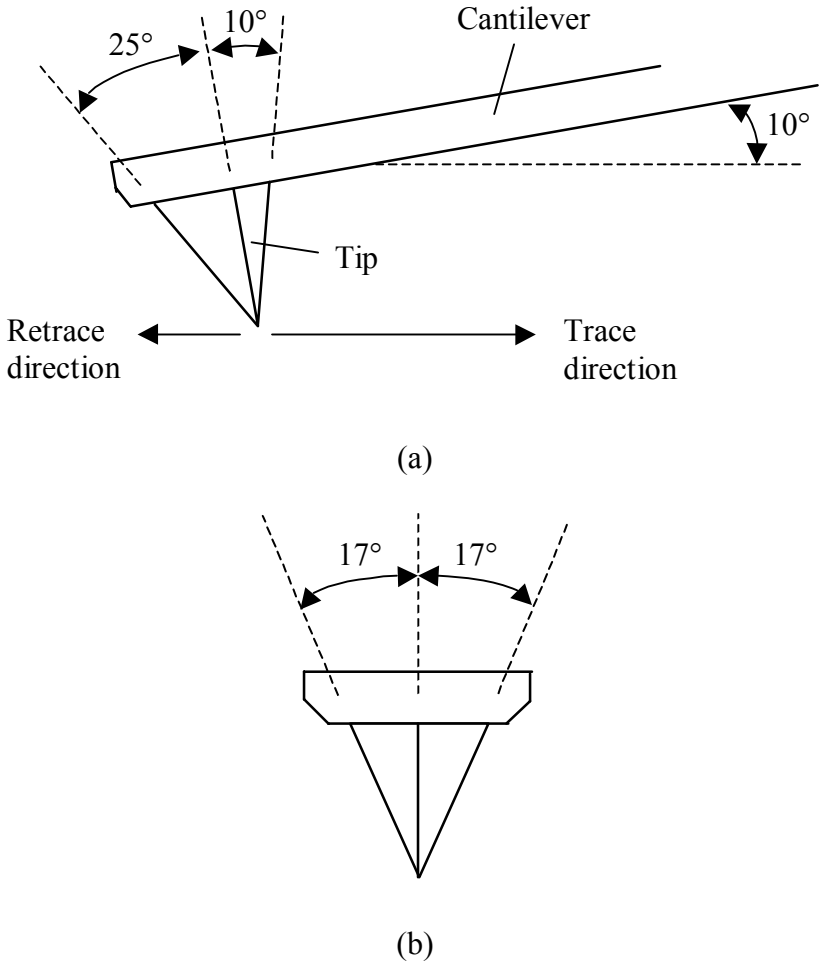

Figure 2.8 *Intended shape of the AFM tip and cantilever. a) Side view showing the 10° mounting angle of the cantilever with respect to the sample during scanning. b) Lateral view of the tip.*

However in practice, the etching process used to form the tip can give artefacts in the tip shape. There is often (in practice, it has been observed for all tips used) a short angled ridge near the highest point of the tip on the right hand (steeper) side. This ridge varies in length

but is rarely longer than 0.5 μm in total. It has a half angle of 20-30° as opposed to the theoretical 10° and can give apparently shallower slopes as a measurement artefact; this leads to a maximum measuring angle of 70-80° with the back edge of the tip. In addition, prolonged use of the needle for many scans on particularly rough surfaces leads to the rubbing down of the tip, leading to loss of the angular definition through chipping and abrasion. Breakage of the tip can also occur more readily for the rough textures scanned, particularly where a high scan speed/low resolution is chosen for larger scan areas. A typical needle is shown in Figure 2.9.

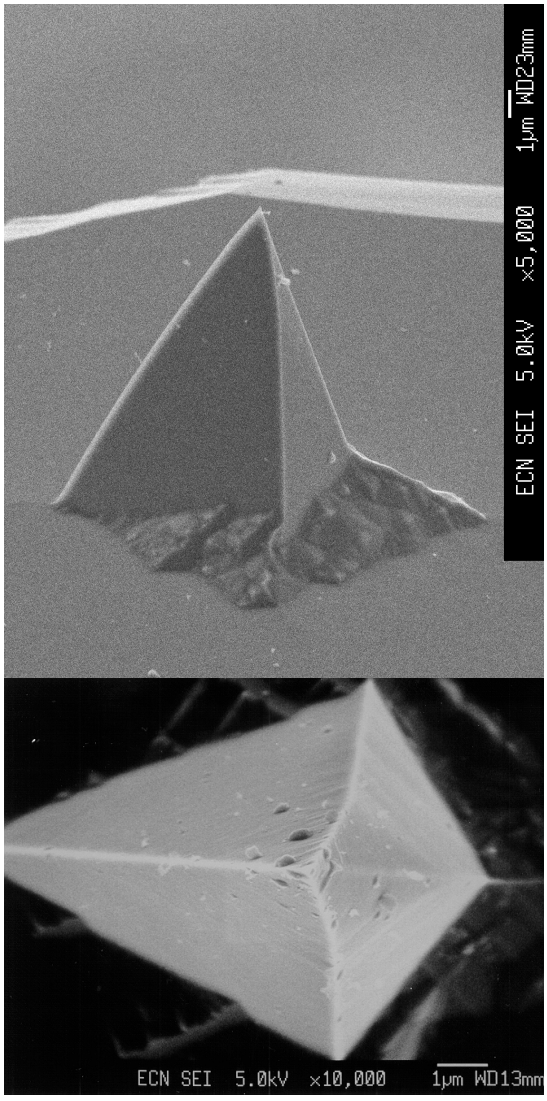

Figure 2.9 *SEM photographs of a typical AFM needle used in measurements from a) the asymmetrical side and b) directly below the tip showing its kite shape. The artefactual ridge is visible in the latter photograph, seen as a small dark diamond shape centred to the right of the peak between the steeper rear side slopes.*

To ensure that the tips used have minimal artefacts in terms of shape, all the scan tips are examined prior to use using scanning electron microscopy. Apart from the presence of an artefactual ridge, it was found that many of the tips exhibited lumpy residues resulting presumably from poor etching or cleaning, which rendered them unusable for accurate scanning. It was also found that the base of several probes was poorly etched (see Figure

2.9a), so that the facets were no longer defined giving a rough, circular base instead of the expected "kite" shape, whose width was appreciably larger than the sharp tip of the needle. Lateral symmetry was also poor in some cases. The tips having a minimum number of artifacts were used for scanning, and regularly renewed prior to abrasion. Abrasion was also minimised by using slow scan speeds in all cases.

2.4.2.3 Optimisation of AFM scan quality

The image obtained for the AFM provides the most direct means of determining whether the scan has been properly performed. The samples are first examined (*without* the deposition of Ag or Pt conducting layer) using SEM microscopy at the same position, sample orientation and with approximately the same magnification as for the AFM scan, viewed with 0° tilt (i.e. directly above the sample). The AFM image must correspond to that viewed by the SEM in order to be sure of the quality of the scan. For well defined structures such as the inverted pyramid structures discussed in Chapter 2.4.2.1, a more quantitative control of accuracy is by comparison of the measured and expected angular data. However this is not possible for the (as yet) undefined random multicrystalline textures obtained by alkaline etching.

Several factors influence the quality of the measured scan (image). An obvious factor is the resolution used for the scan, which should be chosen appropriately for the texture dimensions being measured. The scan speed is particularly important; if it is too fast the needle will not follow the surface accurately, leading to poor scanning at peaks and troughs as the needle springs between points at speed.

Another factor influencing the scan is surface contamination [11]. This is present to an extent on all samples in ambient conditions in the form of a thin layer composed of water, ambient contaminants and contaminants resulting from fabricating the sample. As the probe approaches the sample surface, it is strongly drawn towards the contaminant layer by capillary attraction, so that attractive forces are much greater than when this layer is absent. Similarly, on retraction of the wafer from the surface, capillary attraction will tend to hold the tip firmly. Thus, the forces experienced by the tip at a given distance from the sample will be less on moving the probe towards the sample, and more on moving it away, leading to a distortion of the height and image data obtained. Also, the thickness of the capillary layer can vary between 25 to 500 Å [11], depending for example upon humidity; it was found in this experimentation that it was impossible to obtain sensible measurements on particularly humid days. The smaller the radius of the tip, the sharper it is and the higher its aspect ratio, the lower the capillary attraction it will experience. In order to minimise the presence of contamination due to preparation of the silicon sample, the sample is given an extra cleaning step after laser cutting. This consists of a 2 minute dip in vol. 5% HF solution, followed by 2 x 1 minute rinsing in de-ionised water baths and a three minute ultrasonic clean in de-ionised water for the removal of any remaining loose particles from the laser step. The sample is dried using nitrogen gas.

2.4.2.4 Measurement restrictions for steep angled textures

Despite the use of a sharper probe tip and a scanner with larger z-range, there are still possible measurement difficulties for very rough textures, particularly on the scanning of very steep slopes. Considering the scanning of the calibration sample with inverted pyramids, a cross-section of the trace and retrace scans along the scanning direction should show a profile of V-grooves with constant gradient, separated at the tops by flat regions of approximately 1 μm.

However, the alternating slopes of the V-grooves are found to be slightly curved for both trace and retrace scans, being convex for the inclining slopes where the needle is climbing the texture, and concave where the needle is descending the texture (see Figure 2.10). Also, in the retrace case, the flat ridge between the pyramids is actually shown as a concave dip in the top surface.

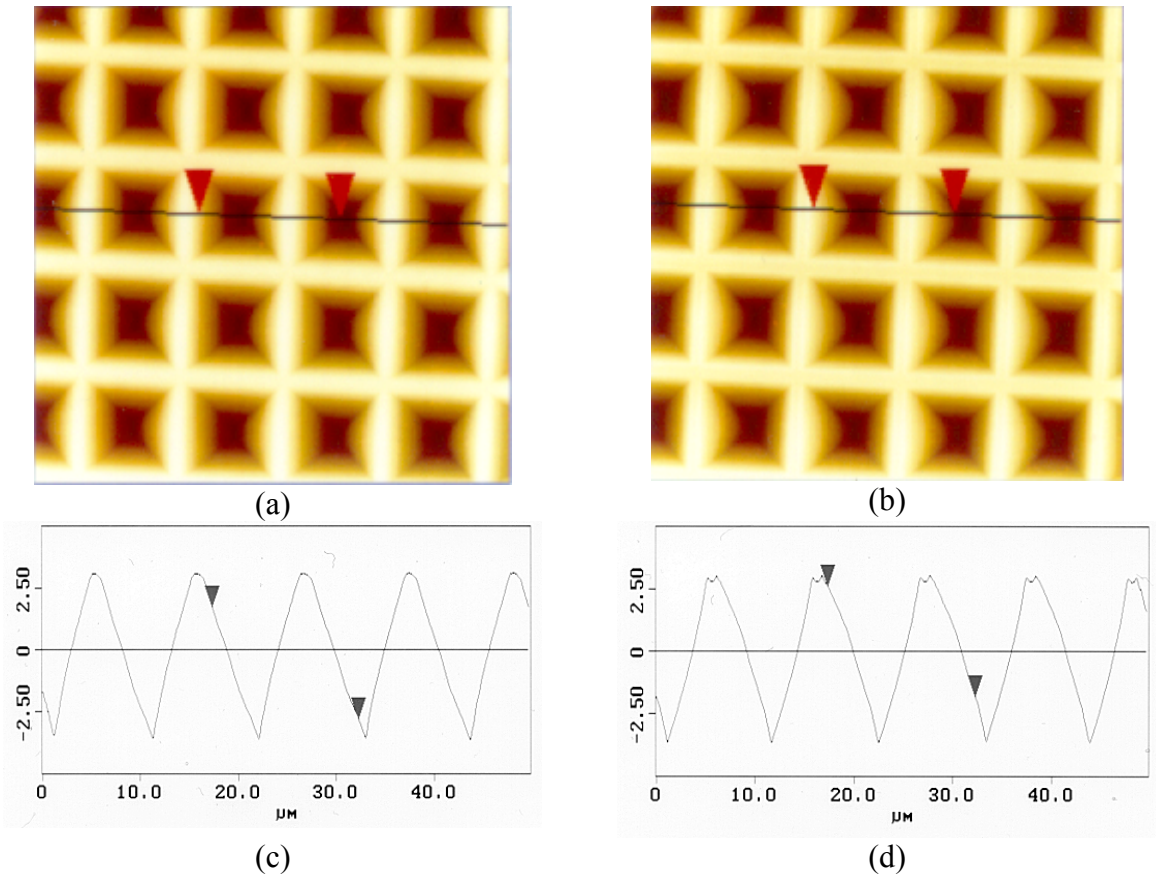

Figure 2.10 *a) Trace and b) retrace scans of the inverted pyramid texture produced simultaneously due to the rastering motion of the tip back and forth across the scan surface. The lines with pointers across the scan surfaces show the position of the scan cross-sections represented in c) and d) for trace and retrace scans respectively. The scan area is 50 x 50 µm and both the x and y axes in c) and d) correspond with µm scales.*

This is because the force on the probe resulting from the scanning motion in the *x* direction competes with that resulting from displacement in the *z* direction for the steep slopes, causing the cantilever to bend against the scanning direction and give an artificially high or low reading (Figure 2.11). This effect becomes larger as the scan speed increases. Similarly, the artefactual dips shown on scanning the flat ridges in the retrace direction, result from the probe tip first springing off the top of the ascending slope, but then remaining in contact through attractive forces pulling the tip back to the surface for further scanning. These effects are also seen in the trace direction (i.e. scanning from left to right), but to a lesser extent as the direction of scanning no longer opposes the deflecting forces.

Additionally, the inverted pyramid structure, with its facets angled at 54.7° to the wafer surface, lies at the outermost limit of the scanning angles for the left hand half of the asymmetric probe, which has a theoretical scanning maximum angle of 55°. The use of the

probe in contact repulsive mode slightly reduces the likelihood of the probe edge and the surface being in total contact on scanning the pyramid facet, in particular in the trace direction, pushing the cantilever and tip away from the surface at a (very small) angle.

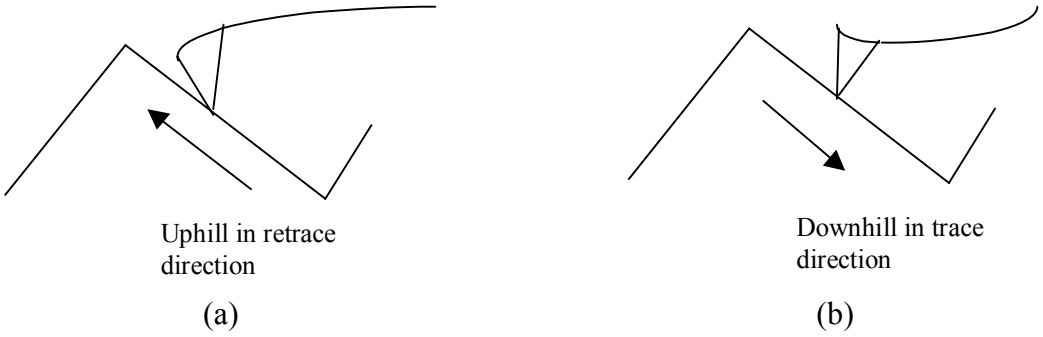

Figure 2.11 *Illustration of the difference in cantilever deflection for the same slope on (a) scanning uphill in the retrace direction as opposed to (b) downhill in the trace direction. This leads to artificially high and low readings giving convex and concave slopes on measurement. It can also be seen that the angle between the tip and the surface texture is far smaller in a), leading more readily to intimate contact of the full needle edge as opposed to the sharp peak of the tip alone.*

However, intimate contact of the probe edge (rather than just its tip) with the surface is probable for inclining slopes in the retrace direction. This effect is accentuated if the sample does not lie completely flat upon scanner surface, or if the cantilever is supported at too high an angle with respect to the sample surface. As a result of this, the angle of the inverted pyramid facets to the left along the scanning axis is less accurately determined than for the three remaining facets, in particular when scanned by the needle on inclination in the retrace direction.

2.4.3 Measurement protocol

In the light of the above observations for the scanning of steep walled textures with large height differences over the scanning area, it was particularly important that a form of scanning protocol be adhered to. In this way the most accurate measurement data must be obtained and the interpretation of the scan results should be clear.

For all the textured samples measured, the following measurement procedures are followed:

1) Calibration/control with the inverted pyramid sample is performed at the beginning and end of every measurement session, this procedure being performed at least once per day of measurement.
2) The (calibration) sample surface must be clean (see procedure as section 2.4.2.3) and dry, and the room humidity should be as low as possible to reduce the thickness of the surface contamination layer.
3) Probe tips were controlled using SEM microscopy prior to use for artefacts. Control/replacement of the probe during measurement sessions is performed if considered necessary, where measurement quality is seen to deteriorate due to possible needle abrasion/breakage.

4) A SEM micrograph of the sample surface is made, preferably with the same magnification and orientation as for the sample itself so that the scan quality can be controlled visually.
5) The "trace" scan is preferably used for analysis.
6) For samples with high angled slopes, the sample must be oriented on the scanner with respect to the cantilever so that the steepest facets are on the LEFT side of the scanner plateau. In this way the steepest facets will be scanned most accurately with the sharpest half of the probe in the trace direction.
7) The scan area for the calibration sample is 50 x 50 μm²; similarly scans of up to 50 x 50 μm² are used for measurements, this area having been found to encompass several texture features in most cases investigated in this thesis. Occasionally larger scans (up to 100 x 100 μm²) were made for very flat samples with large feature dimensions, such as texture etched (111) oriented wafers (see chapter 4).
8) The maximum measurement speed used was 2 Hz; faster than this leads to noise lines for 50 x 50 μm² scans due to the probe springing over texture peaks as well as oscillation of the cantilever for very rough textures. This lead to a scan duration of approximately 5-10 minutes. Lower speeds than this give very slow scans (up to 45 minutes) with a negligible improvement in measurement accuracy.
9) For the scanning of very rough textures (roughness can be estimated initially using an optical microscope, with very rough surfaces being unfocusable), 50 x 50 μm may be too large for accurate scanning without reaching the limits of the z range of the scanner. For this reason, scanning is started with as small a scan area/resolution as possible and increased gradually up to 50 x 50 μm or until the z limit is exceeded (in this case, a slightly smaller scan size is used where possible). This reduces unnecessary abrasion and breakage of the probe tip.

2.4.4 AFM Facet Transforms

The AFM facet transform analysis method was developed by Burgers [7]; an equivalent procedure, the "radial-histogram transform" was reported later in [12]. This technique enables the three dimensional height maps to be converted into angular data, describing the tilt and azimuthal angles θ and ϕ of facets on the textured surface as scanned.

The AFM gives heights z_{ij} on a square grid consisting of 256 x 256 data points, as was described above in section 2.4.3. The AFM facet transform procedure uses a specially developed computer program for the computation of the density of facet normals from the height maps. The AFM scan is approximated locally at every point with a plane $z = a + b(x-x_c) + c(y-y_c)$ on a subgrid of 3 x 3 or 5 x 5 data points, where x_c and y_c are the coordinates of the centrepoint of the subgrid. The coefficients a, b and c are calculated by least squares and the residual sum of squares is calculated. The normal vector $(b, c, -1)$ from the fitted plane is expressed in terms of the angular components θ and ϕ in a spherical coordinate system, where.

$$\phi = \begin{cases} \arctan(c/b) & (c > 0) \\ \arctan(c/b) + \pi & (c < 0) \end{cases}$$

$$\theta = \arctan(1/(b^2 + c^2)^{1/2})$$

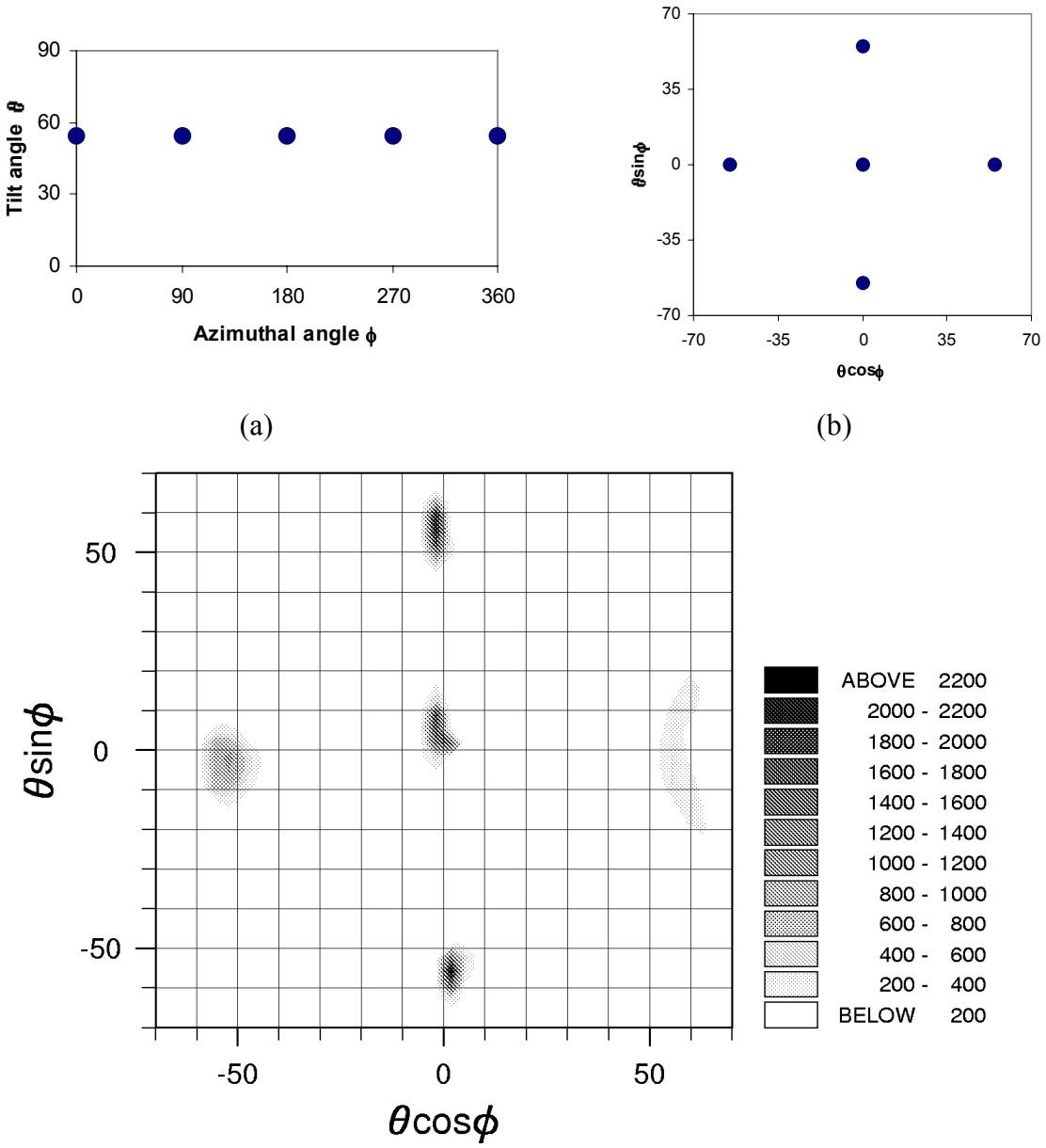

Figure 2.12 *The AFM facet transform for the inverted pyramid calibration sample, with facets at tilt angles of 54.7° separated azimuthally by 90°. (a) and (b) show the facet transforms for the ideal scan, represented in (a) terms of the angles of tilt and azimuth θ and ϕ and in (b) as a polar representation in terms of θsinϕ and θcosϕ. (c) shows the actual facet transform from a typical 50 x 50 μm AFM scan in the trace direction.*

Of the large number of normal vectors calculated, the 10% having worst residual sum of squares are rejected. The density function of the normal vectors is then calculated in terms of θ and ϕ. This is the number of normal vectors per unit solid angle $d\Omega = \sin(\theta)d\theta d\phi$.

Considering the inverted pyramid calibration sample, the ideal θ and ϕ coordinates to be determined by the facet transform method are represented graphically as shown in Figure 2.12a. The pyramid facet tilt angles θ are shown at 54.7°, with azimuth angles positioned at

every 90°. The flat ridges between textures have 0° tilt and are represented by the *x*-axis. Representing the graph axes in terms of the functions θcosϕ and θsinϕ makes the link between the scanning image of the surface and angles calculated somewhat more apparent (see Figure 2.12b); this method of representation of the AFM facet transform is used throughout this thesis. Figure 2.12c shows a typical facet transform obtained from the actual scanning of the calibration sample in the trace direction; this clearly shows the poor determination of the left hand facet due to its interaction with the ridge of the probe.

2.5 Conclusions

The experimental techniques to be used for optical and surface morphological analysis of textured silicon have been described. Existing techniques such as total hemispherical reflectance and transmittance measurements, and optical and SEM microscopy, form basic elements for quantitative analysis. However, a number of auxiliary techniques have been developed or adapted to give more complete information. Localised laser scattering patterns make visible the directionality of reflected light from the textured surfaces, for scatter spots resulting from the direct (single) reflection of the incident light. When used in combination with Laue photography, using the superimposition of localised laser scatter spots upon Laue back-reflectance patterns, not only angular details but also the crystallographic orientations of the exposed etch facets can be determined, expressed in terms of their Miller indices.

Adaptations to an atomic force microscope allow for high z range scanning (specified 8 μm maximum) and accurate profiling of steep angled textures making it a valuable tool for three dimensional quantification of the etch surface. With the help of the AFM facet transform technique, it is possible to use the height data from the scan to give the tilt and azimuthal angles for etch facets up to 70-80° in angle.

References

[1] D.I. Milburn, K.G.T. Hollands, "Solar transmittance measurements using an integrating sphere with broad area irradiation", Solar Energy **522** no. 6 (1994) 497-507

[2] J. Ferber, W. Platzer, "Correct optical measurement of scattering samples", in Proc.SPIE **2255,** Freiburg (1994) 708-717

[3] E. Krochmann, J. Krochmann, "On the measurement of photometric characteristics of diffusing materials", Proceedings of CIE 20th Session on Physical Measurement of Light and Radiation, Amsterdam (1983) D203/1 – D203/4

[4] ASTM E903-82, Standard Test Method for "Solar Absorptance, Reflectance, and Transmittance of Materials Using Integrating Spheres", (1992)

[5] E. Preuß, B. Krahl-Urban, R. Butz, "Laue Atlas", Halsted Press (1973)

[6] B.L. Sopori, "Reflection characteristics of textured polycrystalline silicon substrates for solar cells", Solar Cells **25** (1988) 15-26

[7] A.R. Burgers, R. Kinderman, J.D. Hylton and W.C. Sinke, "Comparison of alkaline etches on multi-crystalline wafers", in Proc. 13th EPVSEC, Nice (1995) 129-132

[8] J.D. Hylton, A.R. Burgers, R. Kinderman, W.C. Sinke, "Determination of facet orientations on alkaline etched multicrystalline wafers", in Proc. 25th IEEE PVSC, Washington (1996) 729-732

[9] E. Schoonderwaldt, "Hoekafhankelijke reflectiemetingen aan getextureerde silicium zonnecellen", Netherlands Energy Research Foundation ECN (1998) ECN-DE Memo-98-010

[10] From "Dimension™ 5000 Instruction Manual", obtained via THiScientific B.V., Sliedrecht, The Netherlands

[11] "AFM Imaging Modes", Technical Report from Topometrix B.V, The Netherlands

[12] D. Schleef, D.M. Schaefer, R.P. Andres, R. Reifenberger, "Radial-histogram transform of scanning-probe-microscope images", Physical Review B **55** no. 4 (1997) 2535-2542

3: Overview of chemical texturisation methods

Wet chemical etching is routinely used in the solar cell industry for the texturisation of silicon. The geometry of the resulting texture is strongly dependent upon the nature of the chemical etchant, in particular upon the isotropy or anisotropy of the etch. Alkaline etchants, such as NaOH and KOH, are anisotropic etchants for silicon, whereby particular crystallographic orientations are etched preferentially to others. Acidic etchants such as those on the basis of HF, HNO_3 etc. are classed as isotropic etchants, with similar etch rates/characteristics on all orientations. However, the measure of (an)isotropy of an etchant is intrinsically bound with the composition and temperature of the solution employed. This in turn will influence the surface morphology of the etched silicon, and thus the effectiveness of reflection reduction and light trapping in the (multi)crystalline wafer, as was introduced in Chapter 1. This chapter presents an overview of chemical texturisation methods, illustrated by experiments showing the effect of etching conditions on the silicon surface morphology.

3.1 Chemical etching for silicon solar cells

3.1.1. Saw-damage removal from as-cut wafers

Wet chemical etching is routinely used in (multi) crystalline silicon cell processing, both for the removal of sawing damage for the wafers cut from the ingot, as well as for the formation of crystallographic surface textures for reflection reduction.

Sawing damage leads to an electrically inactive layer several microns deep on both sides of the wafer and also to waviness and thickness variations across the wafer. In the micro-electronics industry, saw-damage on monocrystalline Czochralski (Cz) grown silicon is generally removed by a series of processes, namely a) lapping, b) etching and cleaning, c) grinding/polishing of the wafer edges and d) polishing. In the lapping process, saw-marks and surface defects are removed, the wafer thinned and planarised and much of the surface stress resulting from sawing is relieved, usually on both sides of the wafer. The wafers are set in a carrier between two rotating “lapping” plates, between which an abrasive slurry (e.g. aluminium oxide) is fed. Etching and cleaning processes using sodium hydroxide NaOH or acetic and nitric acids are for removal of microscopic cracks and surface damage caused by

lapping. Polishing (usually single-sided) is performed in about 2-3 stages using a progressively finer slurry or polishing compound with polishing pads. This leads to lapped/polished silicon wafers.

In the solar cell industry, as-cut wafers generally form the starting material for the solar cell production line. Rather than using complicated polishing and/or lapping processes, saw-damage is removed by etching away the electrically inactive or "dead" layer in a (wet) chemical etching station. The most commonly used etchants for saw-damage removal are alkaline etches based on sodium or potassium hydroxide, at high concentrations and temperatures, but acidic etchants based on hydrofluoric acid HF and nitric acid HNO_3 are progressively being used for simultaneous saw-damage removal and surface texturisation for reflection reduction [e.g. 1]. The composition of these so-called "saw-damage etches" is generally chosen with the aim of removing the required wafer thickness in a minimum of time in order to reduce processing times.

3.1.2 Reflection reduction by alkaline texture etching

Although saw-damage etching leads to the effective removal of the "dead" layer, the reflectance characteristics of wafers etched in this way are equivalent to polished wafers, indicating that flat etch surfaces are formed. Although reflection losses from the exposed silicon front surface can be reduced by applying anti-reflection coatings on the top surface of the cell, it would be more attractive to incorporate both saw-damage removal and geometrical surface texturing (as described in Chapter 1) in a single etching step. This can be achieved using alkaline etchants at low-concentration and temperature.

The first "black" cells employing anisotropically etched pyramidal textures, appeared in the mid-1970's [2,3], although the idea of mechanically texturising silicon for reflection reduction in solar cells was suggested as early as 1961 by Rudenberg et al [4]. These cells had the advantage of giving very low reflectances without the use of an anti-reflection coating, with the pyramids giving the wafer a dark grey/black colour. The inspiration for the use of alkaline etchants for pyramid formation originated from research in the microelectronics industry, where microscopically smooth etch/growth textures are required on silicon. It had been observed that undesirable tetrahedral defects would form during the epitaxial growth of silicon. Such defects had square or triangular bases respectively on (100) and (111) oriented material [5], and sometimes occurred as thermal etch pits. These etch pits appeared to form readily in the presence of SiC deposits resulting from the chemical attack of grease and oil vapours in the vacuum [6]. Pyramidal "hillock" defects were also observed on the bottom of device structures etched in (100) silicon using the organic alkali hydrazine (N_2H_4) and water with iso-2-propyl alcohol (C_3H_7OH, also known as IPA)[7].

Initial experiments for the deliberate formation of pyramidal textures for solar cells employed alkali hydroxides, namely KOH & NaOH (e.g. [8]). An alcohol such as ethyl glycol [2] or IPA [3] was frequently employed, following the assumption that its carbon content would "sensitise" the etch thus ensuring etching uniformity. Several other organic and inorganic aqueous alkaline solutions have also been investigated for anisotropic pyramidal texturisation, for example the (toxic) organic mixture EDP (ethylenediamine ($NH_2(CH_2)_2NH_2$), pyrocatechol ($C_6H_4(OH)_2$) which acts as the sensitiser and water), and etchants such as ammonium hydroxide NH_4OH. The pyramids formed in these cases are however poorly defined having rounded tops and have a greater tendency to give incomplete coverage of the wafer, giving poorer reflectance reduction than for KOH or NaOH [9].

3.1.3 This chapter

Despite the standard use of alkaline etching in particular for pyramidal texturisation of (100) oriented monocrystalline silicon cells, the etch compositions and conditions used and the resulting surface morphologies do not necessarily constitute the only suitable conditions for attaining adequate reflection reduction and/or saw-damage removal.

The exposure of pyramids on (100) for example results from the anisotropy of the alkaline etchant used. This property causes etching to occur more readily in a particular crystallographic direction in the silicon than in another so that the etch surface becomes composed of slow etching planes. In the case of (100) silicon, this apparently leads to the exposure of intersecting slow etching {111} facets yielding the pyramidal textures described previously. However, using a high concentration of alkali as for saw-damage etchants, the etch anisotropy appears to be different and apparently flat textures occur.

Similarly, isotropic etchants (which etch at approximately the same rate in all crystallographic directions) based upon HF:HNO_3 may also yield concave "tub" shaped surface textures which are beneficial to reflection reduction, and dry plasma based etching has also been used for producing reflection reducing textures. However, when used at other etch compositions, isotropic etchants can also be used for the polishing of silicon.

This chapter presents an overview of the action of a number of chemical etchants, namely alkaline, acidic and reactive ion etching (RIE), upon the silicon surface morphology. In each case an overview is given of the different etching mechanisms which have been suggested in literature to (partially) explain the action of the etches upon silicon. The surface morphologies and resulting reflectances are examined for alkaline and acidic solutions in which etching concentration, temperature, the use of additives are varied to develop an insight into the effect of etching conditions upon the (an)isotropy of the etch and the resulting surface texturisation.

3.2 Alkaline etching

3.2.1 Etch reaction

The etching and growth of silicon and other crystals is anisotropic in nature. The source of this anisotropy lies in the crystallographic properties of the silicon. Etch anisotropy can be most simply observed by comparing the etch rates of different wafer/crystal orientations for a particular etch composition. Reported etch ratios for the principal crystal orientations vary substantially in the literature, for example from 35:1 for the {100}/{111} planes for a KOH solution of 10-15 weight percent [10], compared to even higher ratios (e.g. 300:600:1 for (100):(110):(111), [11]) for more concentrated solutions. Anisotropic etchants thus tend to form etch structures bounded by the slowest etching crystallographic planes.

Although several etch reaction schemes have been proposed for the alkaline etching of silicon, a universally accepted mechanism, in particular for the observed etch anisotropy, remains absent.

It is generally accepted that the surface of the silicon is hydrogen terminated during the alkaline etching (see [12, 13]). This has been observed by several groups after treatment in HF solutions for example (e.g. [14], [15], [16]). There is some disagreement as to the active etching species. In [17, 18], OH^- is cited as the active etching species (see equations 3.2 – 3.4 below). This was highlighted in [17] by Raman spectroscopy investigations where the intensity of the OH^- line substantially decreases during etching. However, others cite water as the active species [e.g. 12,13] as summarised in equation 3.1 below, with OH^- acting to catalyse the etching reaction. It is agreed that the active species hydrolyses the (hydrogen terminated) surface silicon atom to become a hydroxyl-terminated silicon atom [e.g. 13] or (ionised) complex [18]: this is generally assumed to be the rate-determining step [13].

Thereafter the water or OH^- attacks the back-bonds of the silicon atom to form a silicate which can leave the surface, whereby it is generally accepted that the reaction products include a silicon hydroxide complex, e.g. $Si(OH)_4$ or $Si(OH)_2O_2^{--}$, with hydrogen gas released during the etch process [17,19,20]. Investigations in [13] using nuclear magnetic resonance showed that the lower the concentration of alkaline solution (KOH), the higher the level of polymerisation of this complex.

In summary, the proposed overall reaction where water is assumed to be the active species [e.g. 12] is:

$$Si + 4H_20 \rightarrow Si(OH)_4 \text{ (or other complex)} + 2H_2 \qquad (3.1)$$

A suggested (electrochemical) reaction with OH^- as the active species [18] is:

$$Si + 4OH^- \rightarrow Si(OH)_4 \qquad (3.2)$$

$$Si(OH)_4 + 2OH^- \rightarrow SiO_2(OH)_2^{--} + 2H_20 \qquad (3.3)$$

$$4H_20 + 4e^- \rightarrow 4OH^- + 2H_2 \qquad (3.4)$$

3.2.2 Etch anisotropy

In Seidel's work [18], the differences in etch rate between e.g. the {100} and {111} orientations are attributed to the number of dangling bonds (or hydrogen terminated Si-H bonds) for the surface silicon atoms per unit cell. The {100} orientation, with two dangling bonds will thus etch faster than the {111} with only 1 dangling bond. In this latter case, three Si-Si backbonds have to be broken and three hydroxide ions bonded (rather than two for {100}) before the formation of the soluble silicon hydroxide complex. This is purported to cause the far lower {111} etch rate. However, this reasoning would suggest that the {110} orientations, also with two dangling bonds, should etch at the same rate as {100}, in contradiction with reported values as shown previously.

Allongue [21] investigates alkaline etch mechanisms and anisotropy experimentally on {100} and particularly {111} oriented silicon, using in situ scanning tunnelling microscopy (STM). Etching on the {111} orientation was seen to take place at kink sites (atoms with as many bonds to the crystal as to the liquid) at the edges of atomically smooth terraces covering the surface. The necessary presence of kink sites for etching leads to the lower etch rate of {111} in comparison to the {100}, which is essentially covered in kink sites. Rappich [22] also emphasizes the importance of kink sites in the etching of {111} orientations, indicating the

increase of SiH and SiH_2 seen in STM imaging as evidence of terrace and kink site creation during electrochemical etching.

3.2.3 Pyramidal textures

The stability of pyramidal textures on the (100) orientation is also poorly understood. For etching processes, one would expect etch pits to form, whereas in this case, upright pyramids form on top of the etching surface. Such structures are more in keeping with observations of crystal growth, and have lead to the proposal of reversible regrowth mechanisms for the formation of pyramids, such as that proposed by Tan [23]; thermodynamic data however shows such growth to be impossible [12]. Elwenspoek [24] has suggested that screw dislocations in the surface may also provide points for pyramid nucleation. (Nijdam [13] has also shown the significance of defects to the formation of etch pits in silicon, showing with Yang etching that bulk stacking faults and dislocations in the crystal lattice lie at the centre of etch pits on (111) and (110) oriented wafers respectively. These dislocations are proposed to lead to localised stress fields about which etching occurs somewhat faster than the surrounding stress-free areas, thus generating steps and pits.) Bressers [25] uses an atomic model of a pyramid defined by four triangular {111} facets on a square base with sides parallel to the <110> direction, to suggest that the pyramid stability lies with the stability of the {111} oriented pyramid sidewalls. These sidewalls consist of silicon monohydrides with three backbonds into the pyramid, as opposed to the intersecting edges, where the backbonds are more exposed to the etchant, and to the peak with two back bonds and a dihydride. Silicon atoms are more easily removed from the edges or from the peak atom, this removal probably giving rise to a step (kink). These steps propagate over the {111} facets, so the pyramid is "peeled" during etching. The pyramid remains stable whilst the etch rate of the (100) substrate is higher than the peeling rate of the {111} facets. A pyramid can nucleate with as few as seven silicon atoms according to this model, and these initiating pyramids may act as self-propagating masks for further propagation of the pyramid structure. Nijdam [13] observes experimentally and by simulation that semi-permeable particles, possibly silicate colloid particles resulting from the etch reaction, act to mask and thereby stabilize the top and ridges of a developing hillock down to a size as low as four silicon atoms.

Pyramid formation on alkaline etched wafers has been shown to be suppressed by adding an oxidizing agent such as potassium or ammonium peroxodisulphate [26] ($(NH_4)_2S_2O_8$) or ferricyanide [25] ($Fe(CN)_6^{3-}$) to the etchant, provided that the concentration of oxidising agent does not exceed a critical value beyond which the Si passivates and etching ceases. Conversely, it was observed by Bressers et al. that pyramid formation is promoted by lowering the oxygen concentration in the solution, argon being bubbled through the etchant to exclude dissolved oxygen. This leads to a higher density of pyramids, distributed evenly over the whole wafer surface. On the basis of these observations, Bressers [25] proposes a model for etching and passivation: in the etching process, water chemically attacks the hydrogenated silicon surface atoms, which go into solution (as $Si(OH)_4$ or an equivalent species), leaving the surface hydrogen-terminated. When dissolved oxygen or other oxidising agents are present in the solution, oxidation reactions produce Si-OH bonds which can result in bridged oxygen structures, thus forming an oxide on the Si.

3.2.4 Experimental

In order to observe the effect of changing alkaline etch conditions upon etch anisotropy and the resulting texture geometries on the silicon, experiments were performed whereby the

surface morphology is analysed for varying etching parameters for alkaline etchants. Experimental investigations focused on three issues; the variation of surface morphology with etching parameters of concentration and temperature, the influence of IPA, and the requirements for uniform pyramid formation on monocrystalline (100) wafers.

Monocrystalline, p-type wafers of 1-10 Ωcm with (100), (110) & (111) orientations are etched in alkaline solutions of NaOH or KOH. Temperatures of 70 or 90°C and concentrations between 0.2 and 10 M were used. For investigations into the influence of IPA, 0-10 vol % IPA was added to solutions containing 2-4 wt% NaOH. The wafers, which are initially polished/lapped, are first sandblasted with Al_2O_3 powder, to give a starting surface equivalent in roughness to an as-cut wafer (i.e. the typical starting surface for wafers to be etched in industrial cell processing). This "gritting" step removes approximately 8-10 μm of the total silicon thickness. Following gritting, loose particles are removed from the samples by vibration in water using an ultrasonic bath, followed by rinsing/stirring in fresh de-ionised water. Prior to etching, wafers receive a one minute dip in 5% HF in order to remove the native oxide, followed by rinsing in water.

3.2.5 Results

3.2.5.1 Surface morphology

The surface morphology resulting from etching is as expected strongly dependent upon the concentration of the solution and the wafer orientation investigated. No appreciable differences were found in surface morphology where KOH is used instead of NaOH at the same concentrations and temperatures.

Taking the (100) orientation (Figure 3.2), a 15 minute etch in 0.2 M NaOH leads to the formation of pyramids with base lengths varying between <1 and 10 μm (pyramids formed at KOH solutions of the same molarity were somewhat larger). The density of pyramids tends to vary widely over the wafer surface. Dark patches are visible where pyramid density is high, covering approximately 80-90% of the silicon surface and light patches with polished appearance where pyramid density is low. The reproducibility of such textures is very poor with pyramid densities and thus reflectances varying widely between etch runs; pyramid uniformity and reproducibility can be improved on the addition of 2-propanol and/or by the exclusion of oxygen from the solution, as will be seen in the following section.

On increasing the concentration to 1.5 M, the (100) etch surface exhibits large square plateaus (tens of microns in dimension), which are essentially smooth, with the exception of pyramidal "nucleation" points of typically < 1 μm. Increasing the concentration further sees a complete disappearance of these points, leading to a surface dominated by smooth square plateaus.

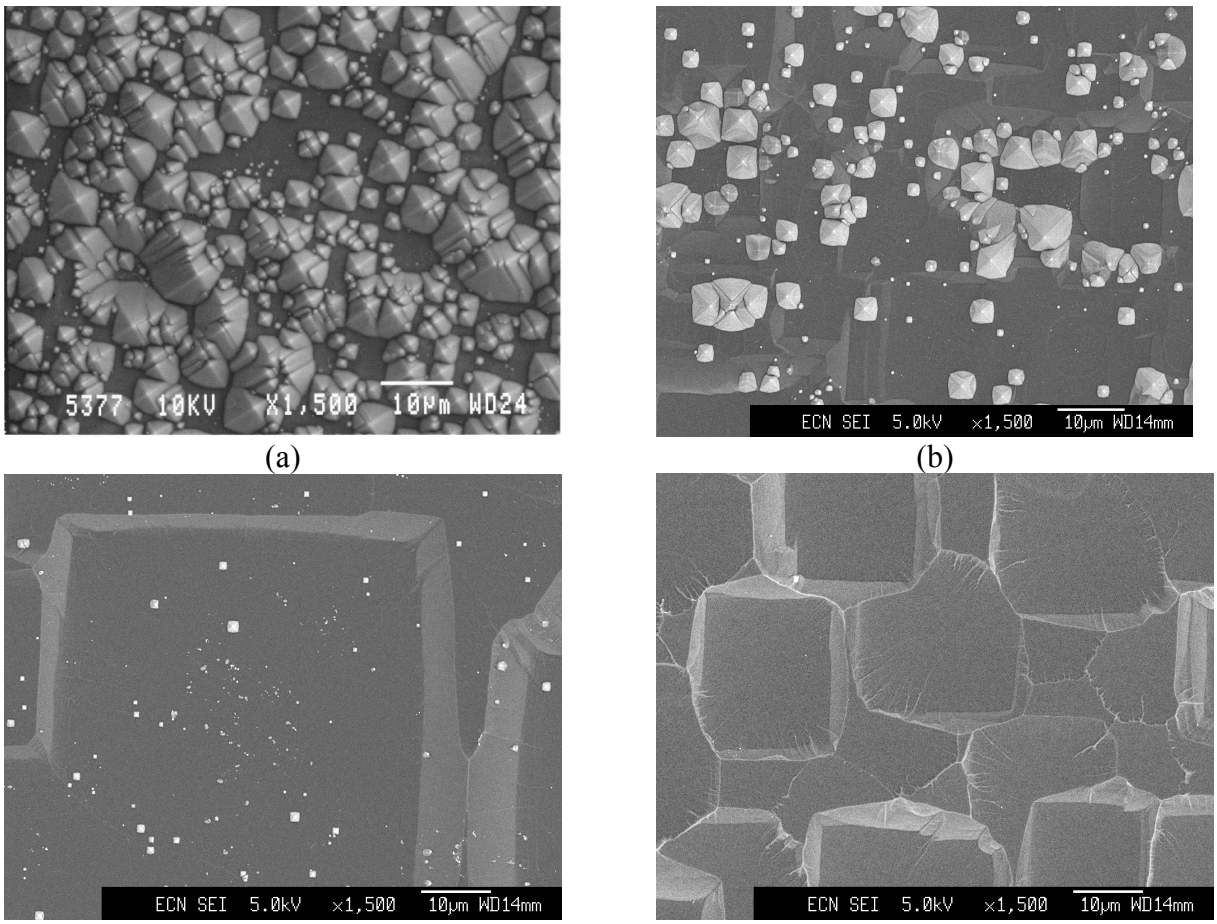

Figure 3.2 *SEM photographs of the (100) oriented surface for a 15 minute etch at 70 °C for a) 0.2 M with high pyramid density, b) 0.2 M with low pyramid density, c) 1.5 M and d) 10 M concentrations.*

Etching at a higher temperature shows the same morphologies for these concentrations, although the dimensions of the texture vary; the pyramids at 90°C are larger than at 70ºC, with bases up to 10 µm, whilst the height differences between the plateaus is minimal at higher concentrations. The variation in (100) texture shown in Figure 3.2 below, from rough pyramids to smooth plateaus on increasing the concentration, leads to the increase in reflection shown later in Figure 3.5.

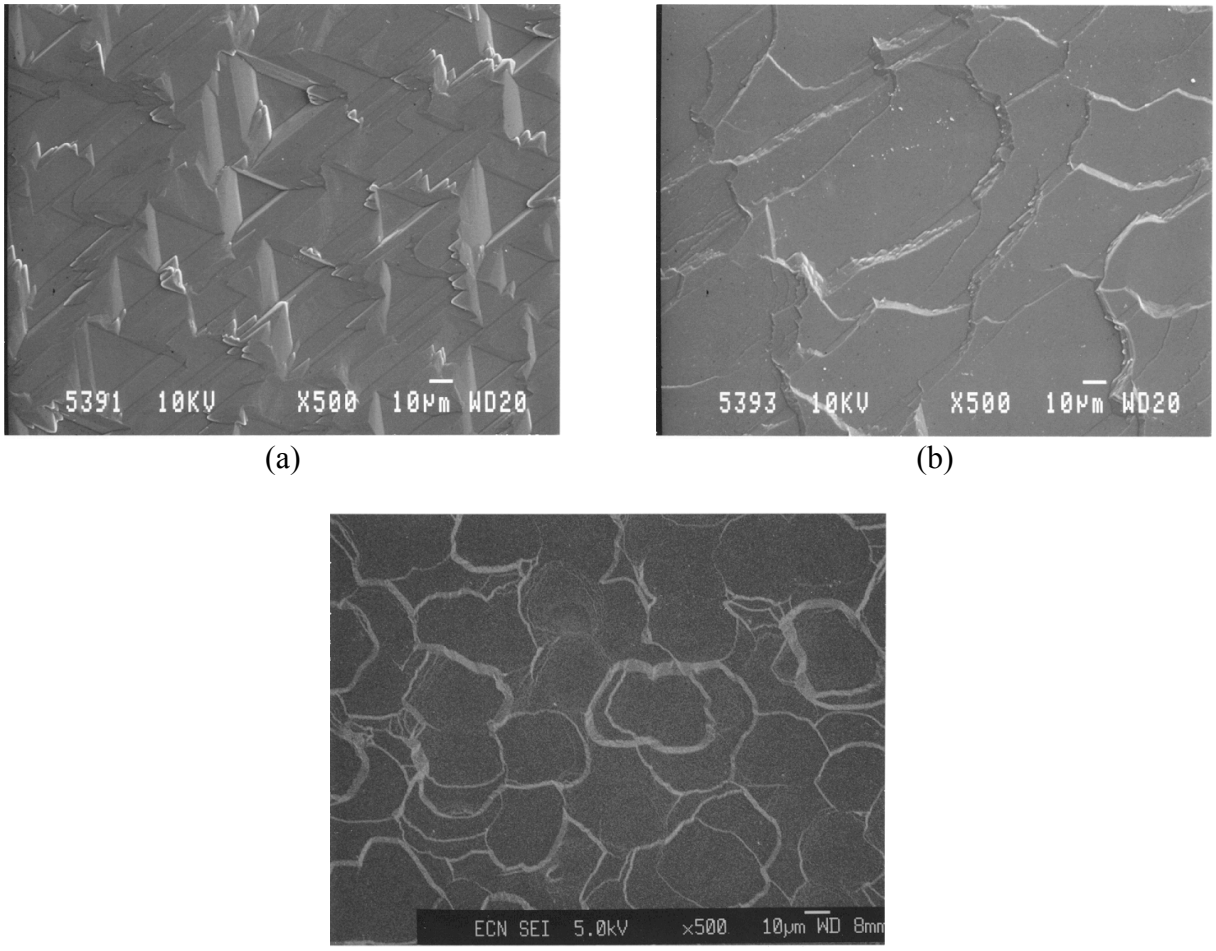

Figure 3.3 *SEM photographs of the (111) oriented surface for a 15 minute etch at 70 °C for a) 0.2 M, b) 1.5 M and c) 10 M concentrations.*

For the (111) orientation (Figure 3.3), etching at low concentration at 70 ºC leads to shallow, triangular etch pits. At a higher temperature the pits barely remain visible, with the surface acquiring a lightly grooved appearance. Increasing the concentration sees the formation of semicircular terraces which at 10 M form closed circular (polygonal) etch pits.

These observations are in keeping with those of Allongue [21] during STM imaging of n-type {111} etch surfaces in 1-2 M NaOH; in this case, increasing the anodic bias during electrochemical etching was seen to increase the roughening of steps and the generation of triangular etch pits on atomic terraces.

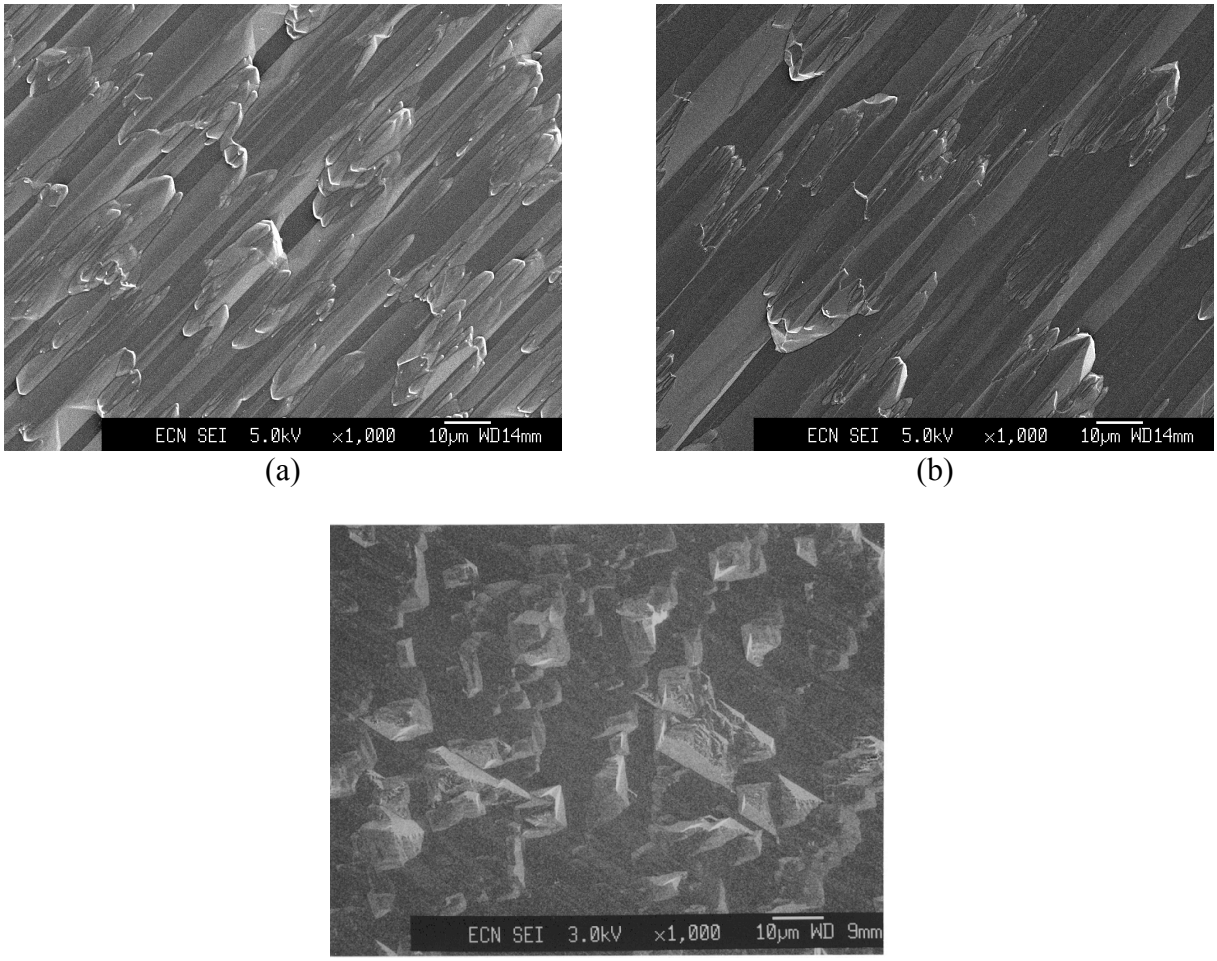

(a) (b)

(c)

Figure 3.4 *SEM photographs of the (110) oriented surface for a 15 minute etch at 70 °C for a) 0.2 M, b) 1.5 M and c) 10 M concentrations.*

In the case of the (110) orientation (Figure 3.4), low concentrations lead to a grooved surface morphology. Higher concentrations give increasingly rough surfaces, which at 10 M barely resemble a crystallographic texture, with rock-like structures jutting out randomly from the wafer surface.

The reflectance for both the (111) and (110) orientations remains equivalent to that of polished silicon irrespective of the concentration; investigation using AFM facet transforms (see Chapter 2) shows that all of these textures have facet normals between 0 and 18 ° maximum with respect to the wafer normal, so that no double reflectances will occur for normally incident light in these cases.

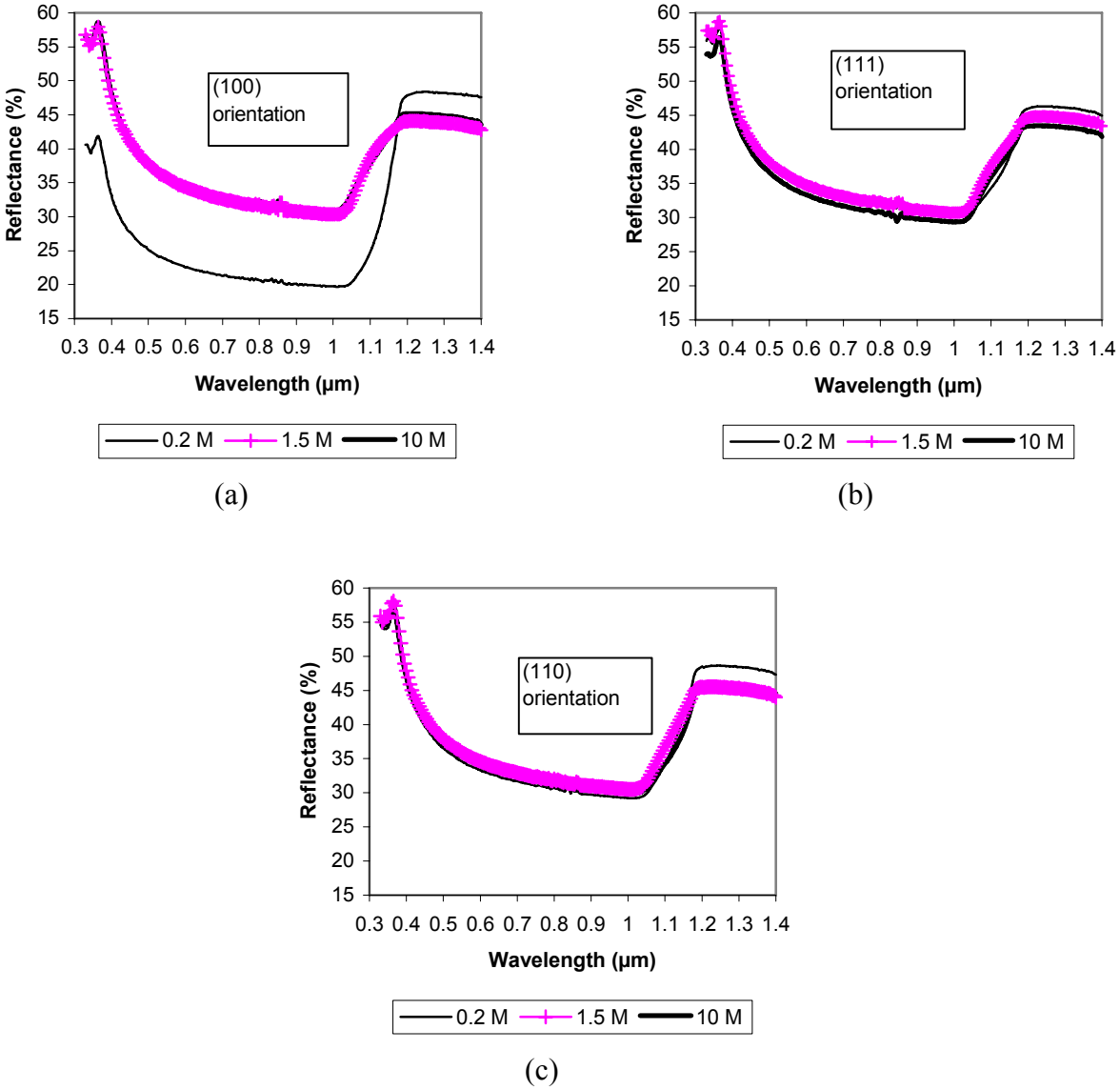

Figure 3.5 *Measured reflectances as a function of concentration for a 15 minute etch at 70 °C for a) (100) b) (111) and c) (110) orientations.*

3.2.5.2 Etch rates

The etching rates were determined from the total mass of silicon removed during etching for the 30 x 30 mm samples. In general, increasing the etch concentration increases the rate of the etch (see Figure 3.1) for all orientations, as does increasing the temperature of the solution.

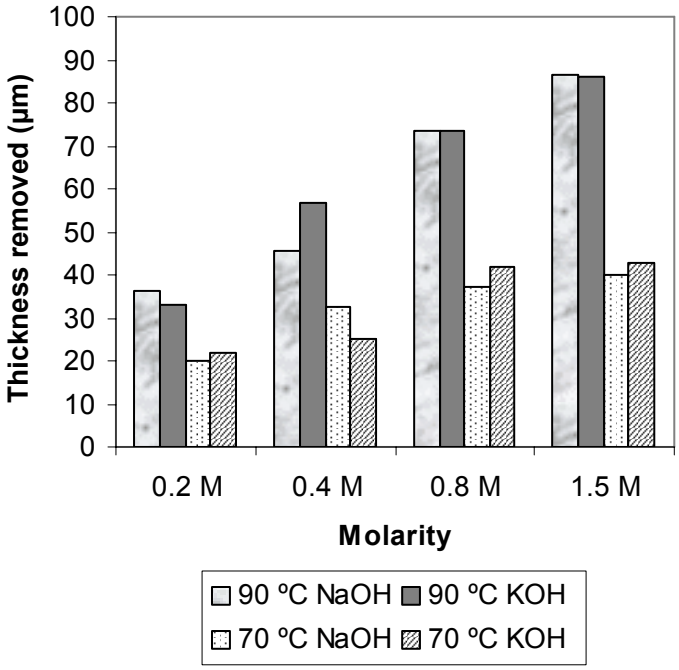

Figure 3.1 *Etch rates for the (100) orientation for a 15 minute etch at 70 and 90°C showing the increase in etch rate with temperature and concentration and the similarity in etch rate for NaOH and KOH solutions.*

Table 3.1 shows the results for the three orientations individually. Increasing the etch concentration from 0.2 M to 10 M leads to a four to six fold increase in etch rate for all three orientations for a particular etch temperature. In most cases the (110) orientation was the fastest etching orientation, in agreement with the findings of Price [10] but for the 0.2 M and 1.5 M solution at 90 ºC, the (100) etched at an equivalent or even higher etch rate. This would suggest that the effect of temperature may be to influence the (100)/(110) etch rate ratio. Although this cannot be seen for the 10 M concentration at the temperatures used, it was found that for a 12 M solution at 120 ºC, the (100) indeed etches very slightly faster than the (110), at 27 and 24 µm/min respectively.

NaOH Concentration	Etch Temperature °C	Etch rates (µm/min)		
		(110) orientation	(100) orientation	(111) orientation
0.2 M	70	0.8	0.4	0.2
0.2 M	90	1.1	1.1	0.4
0.4 M	90	1.6	2.8	1.0
1.5 M	70	1.6	1.4	0.9
1.5 M	90	2.5	3.8	1.5
10 M	70	2.1	1.6	0.6
10 M	90	6.5	4.7	1.0

Table 3.1 *Total etch rates for the (110), (100) and (111) orientations in NaOH of various concentrations as determined from the mass removed.*

The (111) was the slowest etching orientation in all cases. However the etch rate of (111) in 10 M solutions is disputable; in the first 15 minutes of the etch, 15-20 µm was removed by weight for the 70 and 90 ºC NaOH solutions. Despite this, further etching up to 45 and 60

minutes for the 90 and 70 ºC baths respectively lead to the removal of only 1-5 μm more, so that the etching was minimal, indeed closer to nanometres per minute (Figure 3.6). This would suggest that the (111) etch rate, after removal of the saw-damage in this case, reduces with etch concentration, in contradiction with the (100) and (111) orientations. Looking at the surface morphology at prolonged etching at 90 ºC, the surface as observed by SEM microscopy was completely smooth, devoid of any pitting or terracing. It is possible that etching in this regime is equivalent to that of Allongue [21], with etching occurring at terraces at an atomic level. The etch rates obtained for the (111) e.g. by weight as shown are sometimes considered to be "pseudo"-etch rates for this orientation since the ledges etch faster laterally than the {111} surface etches downward [11, 20]. The etch rates obtained for etching in KOH are equivalent to that of NaOH, with KOH generally etching very slightly faster at lower temperatures.

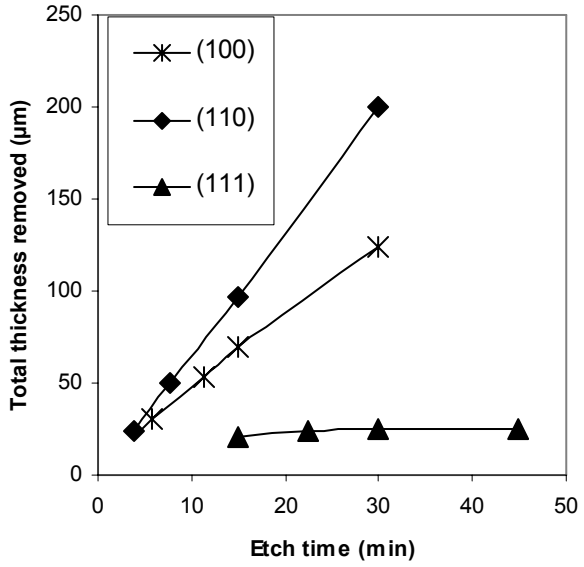

Figure 3.6 *Etch rates for the (110), (100) and (111) orientations for 10 M NaOH at 90°C fitted linearly.*

3.2.5.3 Etching to equivalent etch depths

Comparing the surface geometries for particular orientations with the same etch depth (25 and 50 μm) but different etch compositions, it is clear that the observed etch anisotropy is not simply a consequence of the etching depth. Etching to the same depths for different concentrations gives the same trends in surface morphology as for etching with equal etch times. Pyramids on (100) at 0.2 M tend to flattened plateaus at 10 M, and grooves on (110) tend to "boulders" on a grooved background. The shallow triangular pits on the (111) orientation at 0.2 M are hardly visible after a 25 μm etch with the surface polishing so that only the outlines of the corners remain; the surface is fully polished after 40 μm has been removed. The terraces on (111) at 1.5 M tend to mirror polished surfaces at 10 M with sporadical circular outlines of ~100 μm diameter at 70 ºC. The 50 μm etch depth was not attained for the (111) at the 10 M concentration despite prolonged etching for the reasons described in the previous section; this is in contrast to etching at lower concentrations, where 50 μm by weight was readily achieved. The observed variations in etch anisotropy are thus not simply a result of differing etch rates due to higher concentrations.

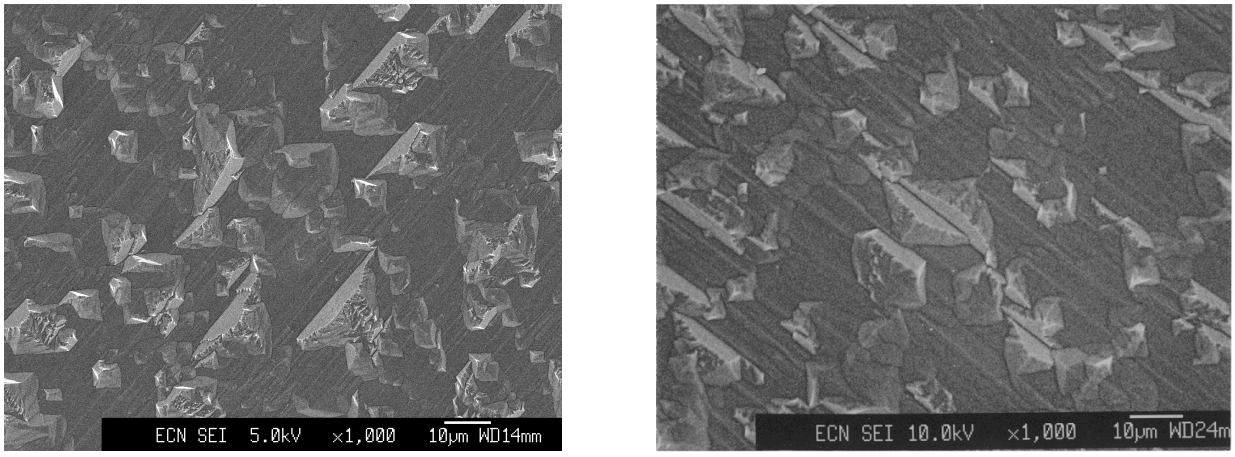

(a) (b)

Figure 3.7 *SEM photographs of the (110) oriented surface for a 25 µm etch depth in 10 M NaOH at a) 70°C and b) 90 °C indicating the minimal effect of temperature on surface morphology.*

In contrast, the effect of etching temperature for a particular composition is fairly subtle. The etch shapes are similar at both 70 and 90 ºC. Taking the example of the (110) orientation at a 10M concentration (Figure 3.7), etching at 70 ºC and 90 ºC to approximately equal etch depths gives almost identical textures, despite a factor three difference in etch rates measured for the two temperatures. This suggests that etching temperature influences etch rate without significantly affecting the etch geometry.

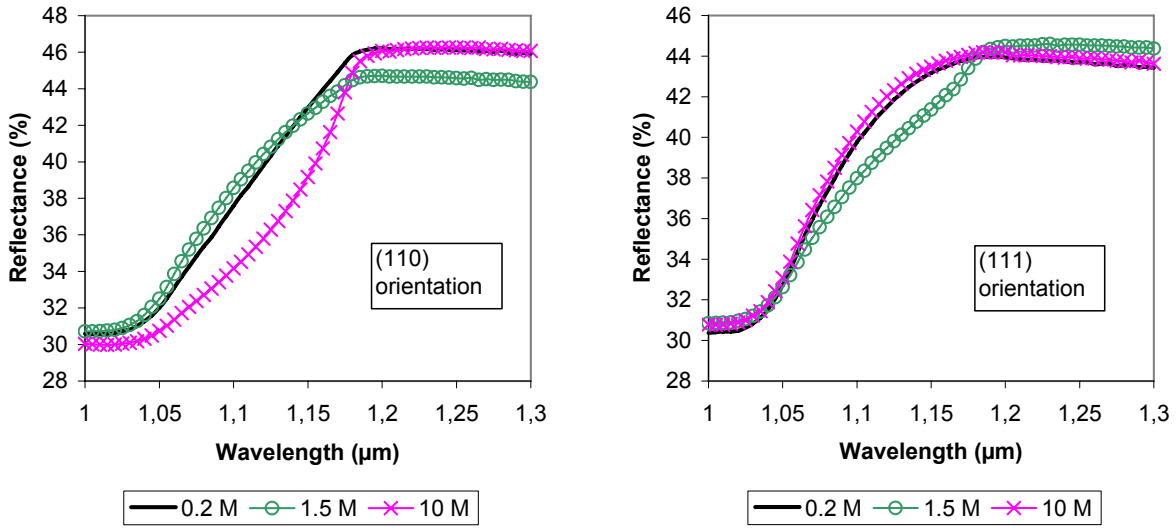

(a) (b)

Figure 3.8 *Long wavelength reflectance for (110) and (111) orientations etched to the same 25 µm etch depth for different etch concentrations (90 °C) shows the effect of changing surface morphology on light scattering. Despite having facet angles too low to achieve front surface reflectance reduction, the surface roughness is sufficient for good light trapping.*

It is also interesting to note that although for the (111) and (110) orientations, the low facet angles lead to reflectances equivalent to polished silicon in the visible, the change in roughness with etch composition can lead to significant differences at near infrared wavelengths. This is particularly evident for the reflectance curves with etching to the same etch depth (Figure 3.8). This indicates that these low facet angles may be sufficient to cause enough internal scattering of the less absorbing wavelengths to improve light trapping (see Chapter 1) for thinner wafers. This subject will be investigated in the following chapters.

3.2.5.4 Effect of IPA (iso-propyl-alcohol)

The addition of IPA to KOH solutions has been shown to reverse the etch ratio between (100) and (110) in much the same way as is indicated for higher etch temperatures, with (100) etching faster than (110) with solutions containing IPA, but slower than (110) in KOH without additives [10]. IPA addition leads to the reduction in etch rate for a particular concentration, but also to an increase in the density of texture features and to a smaller texture size, as shown in Figure 3.9. However, a problem with etches containing IPA is its low boiling point of 80 ºC, which is a typical temperature for which texture etching is performed. This leads to evaporation of the alcohol during the etch giving an unstable etching system and reducing the reproducibility of the etch. It may be possible to control the etching conditions by using a closed etching system, such as that proposed in [27].

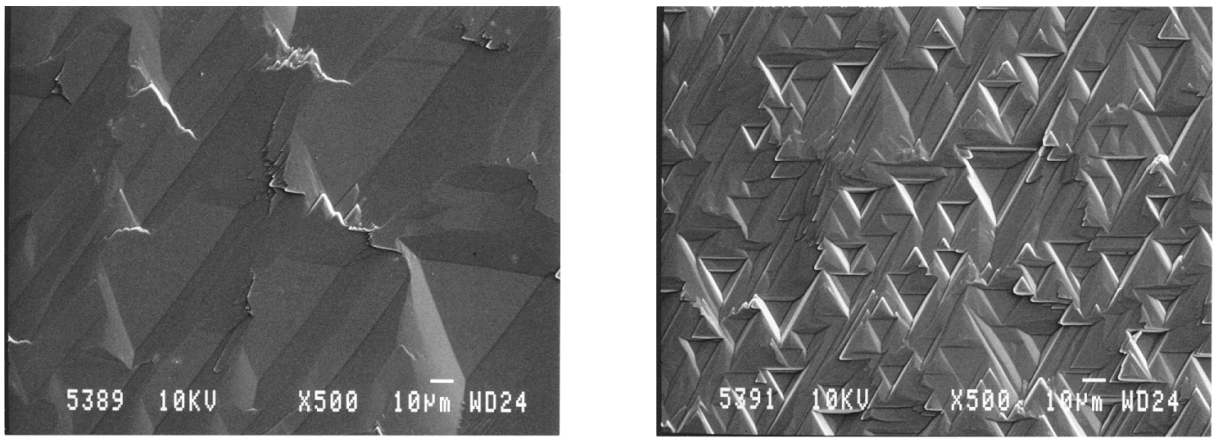

(a) (b)

Figure 3.9 *SEM photographs of the (111) orientation in solutions containing a) 0% and b) 10% IPA, showing the smaller size and higher density of texture features for a 15 minute etch.*

3.2.5.5 Effect of oxygen on the population density of pyramids

From the previous sections it has been seen that alkaline solutions at low concentrations give pyramidal textures most readily, with a higher percentage of pyramidal coverage being obtained on the addition of IPA. As shown in Figure 3.10, the texturisation process begins with the sporadic "nucleation" of pyramids on the wafer surface, which increase in number and size so that the surface gradually becomes covered with the pyramidal texture. In the case of as-cut wafers, this nucleation occurs more readily than in the polished case, since the roughness of the starting surface provides many points for initiation. This incomplete

pyramidal texturisation of the wafers is problematic, with non-textured polished areas between pyramids yielding high values of reflectance.

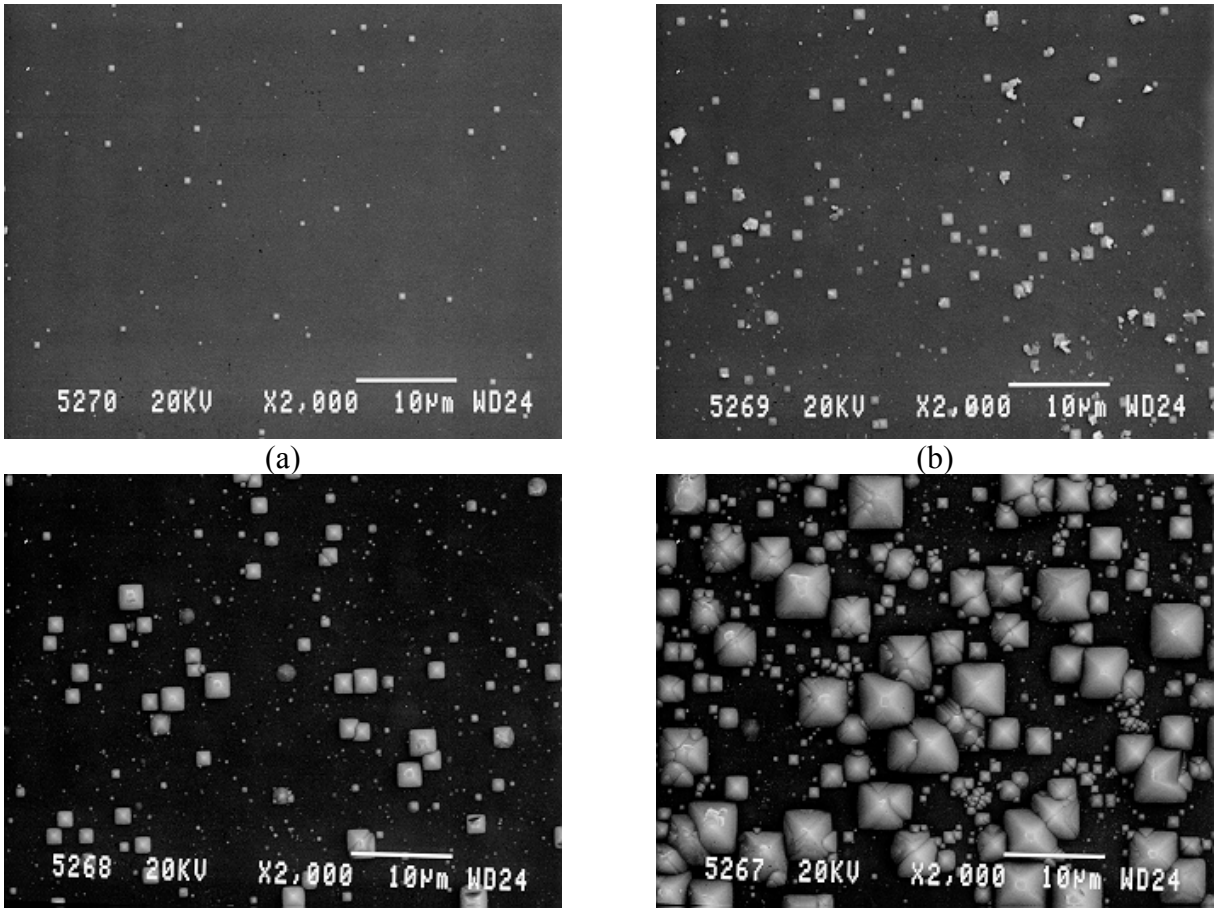

Figure 3.10 *Development of pyramidal texturisation with etch time: surface texture after a) 1 min, b) 2 min, c) 5 min and d) 10 min etching.*

According to Bressers [25] (see section 3.2.3), the presence of (dissolved) oxygen in the solution should have a detrimental effect upon the pyramidal coverage resulting from etching. A procedure was therefore tested on the basis of this theory whereby etching was performed in an oxygen free environment. (100)-oriented, 1-2 Ωcm p-type wafers with polished/lapped front/back surfaces respectively, were etched using a typical texture etch recipe [9] comprising 90 vol% water + 10 vol% iso-propyl-alcohol (IPA) + 2 wt% NaOH at 80 °C for 15 min. Prior to and following etching, the wafers received 5 vol% HF dips for the removal of oxide. Nitrogen gas was bubbled through the solution (in a glass beaker) throughout the etch at a flow rate of approximately 25 litres/min to expel oxygen. The water and IPA were pre-heated prior to making up the solution, in order to expel dissolved oxygen present in the solution and also to counteract the temperature decrease which results on passing the nitrogen through the solution, the temperature being maintained at roughly 80ºC during the etch.

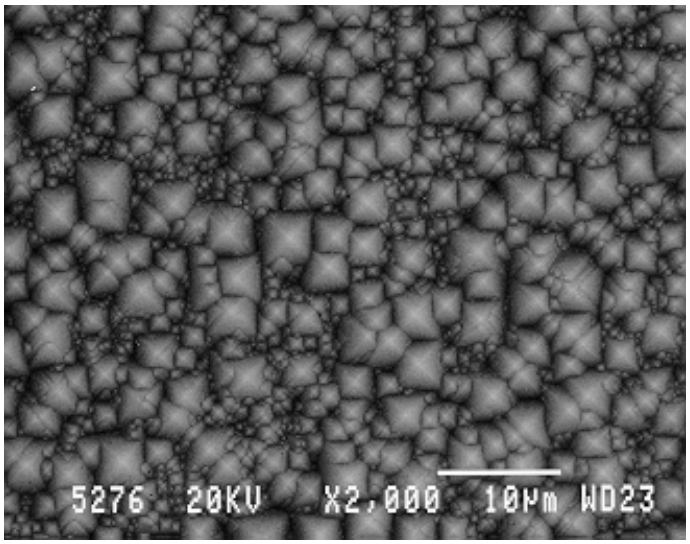

Figure 3.11 *Pyramids on polished Si etched in an oxygen-free environment.*

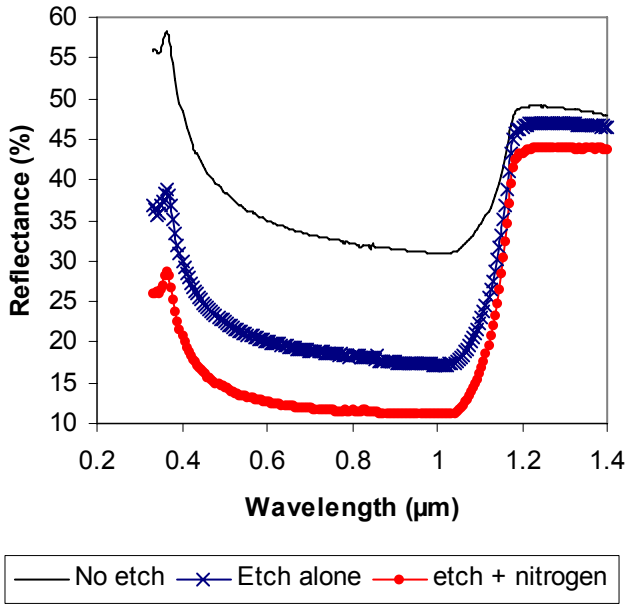

Figure 3.12 *Comparison of reflectance curves for polished sides of texture-etched monocrystalline (100) silicon wafers.*

Wafers textured in the etch alone exhibit non-textured mirror-polished regions on the wafer surface where pyramids of widely varying sizes (<1 µm up to 10-15 µm) were found to be sparsely distributed or in clusters, although reflectance was reduced compared to a polished wafer without etching (Figure 3.12). In contrast, the bubbling of nitrogen through the etch solution gave rise to a uniform texture, as shown in Figure 3.11 where the wafer surface was completely covered in pyramids, with bases up to 4 µm in length (3 µm in height), in support of Bressers' theory and observations using argon for the exclusion of oxygen [25]. Between these larger pyramids, there are very small pyramids to be found with base < 1 µm in length. The average total wafer thickness removed by the etch was 8.5 µm. The reflectances obtained for (100) are 6% lower on average than when etched without the exclusion of oxygen.

These results were also reproduced for n- and p-type Cz(100) wafers of various doping concentrations, suggesting that this method is insensitive to the wafer type or doping

concentration. On larger samples the etch quality was more difficult to reproduce, although the same quality of texturisation has been obtained for a larger 50 x 50 mm² sample. This is attributed to the simplicity of the set-up used, whereby oxygen from the surroundings can easily (re)-enter the solution from above; a closed system would ensure the exclusion of external oxygen from the system.

3.2.6 Discussion

3.2.6.1 Effect of etch concentration

From the above experimentation, it can be seen that the concentration of alkali has a significant influence upon both the etch rate and the surface morphology for all orientations. In principle this would support a reaction mechanism whereby OH^- acts as the active species, such as the reaction proposed by Seidel [18]: the more $(OH)^-$ ions available to form surface Si-OH bonds and induce the formation of the soluble hydroxide complex, the faster the reaction would be expected to progress, assuming unhindered removal of the complex into the solution. From the above measurements of etch rate by weight for the three orientations, the (100) and (110) orientation, each with two dangling bonds, were found to etch at equivalent rates in some cases, also in agreement with this model. However, whilst Seidel's reaction may explain the difference in the etch rate with concentration, it does not explain the change in shape of the textures so formed.

3.2.6.2 Surface morphology on (111) wafers

Allongue [21] addresses the issue of changing surface morphology during electrolytic etching of n-type (111) silicon. The variation of texture from terracing to triangular pits on applied anodic bias (comparable with the variation from terraces to triangular pits on varying from higher to lower concentrations as above) is attributed to an increasingly electrochemical reaction. At anodic bias, the etch reaction is proposed to be electrochemical. OH^- ions attack both at di-hydride kink sites on the terrace edges and at ≡Si-H monohydrides on the terrace plateaus, allowing the initiation of etch pits. At cathodic bias, etching is proposed to progress chemically, with lateral etching by water at kink sites at the stepped terrace edges.

Translating this to our above observations on (111), triangular etch pits would be expected to form more readily at high $[OH^-]$ concentrations, rather than at the low concentrations (0.2-0.4M) at which they in fact were observed. Indeed, whilst OH^- ions play a specific role in the proposed electrochemical etching route, Allongue cites the small influence of OH^- concentration for $[OH^-] < 2M$ compared to the major role of water molecules. There is also no distinction made between circular and triangular etch pits, as observed above at high (10 M) and low NaOH (0.2 M) concentrations respectively. A direct comparison of these two etching systems is thus not possible, although the necessity of kink sites for etching of terraces appears to be a likely mechanism in both electrolytic and electroless etching.

3.2.6.3 Pyramid formation on (100) oriented wafers

The increased pyramidal coverage observed on etching (100) in oxygen free solutions suggests that the presence of oxygen indeed plays an important role in the initial nucleation of pyramids on the silicon. This appears to support the theory and observations found in [25,26], as discussed in section 3.2.3.

It was also observed that the four individual pyramid sidewalls occasionally appear to consist of two facets. The mechanism proposed by Bressers [25], whereby pyramids may be etched by the "peeling" of {111} facets may possibly explain this observation. Assuming layer by layer peeling, it may be possible that depending on the peeling rate, this lateral etching "wave" begins from two edges and eventually summates at the centre of the sidewall, giving the appearance of a double facetted sidewall. As in the work of Allongue [21], this mechanism depends upon the presence of kink sites, here at the intersecting edges of the {111} oriented pyramid sidewalls. Some groups have determined crystallographic orientations for these facets; Reed suggests that pyramids consist of 8 planes having {567} orientations, rather than four {111} faces. However, in our observations, double faceting was generally only found for a few free-standing pyramids; the level of double faceting is extremely varied, from very slight faceting up to pyramids which have acquired an octagonal shape, in particular in the early stages of pyramid development. It would thus appear incorrect to attempt to assign a particular orientation to such "split" facets, since their shapes may vary during the course of the etch. The observed pyramidal development is more in line with what may be expected from a progressing "peeling" mechanism.

3.3 Acidic Etching

3.3.1 Introduction

Acidic etchants based on the HF:HNO_3 system are isotropic in nature. The essential mechanism for etching is an oxidation-reduction reaction, whereby the Si is oxidised by the HNO_3 (nitric acid), whilst the HF serves to remove the oxide so formed. In HF rich regions, the rate-limiting factor is the oxidation step by HNO_3, whilst in HNO_3 rich regions the metathesis reaction whereby the oxide is removed by the HF is rate-limiting.

The resulting surface morphology is, as for alkaline etching, strongly dependent upon the etch composition (in particular the HF:HNO_3 ratio, and the amount and choice of diluent). However, in contrast with the anisotropic alkaline etchants, the surface morphology and etch rates are to a large extent orientation independent. Etch textures vary with etch composition between rough, concave shaped "tub" structures and smooth surfaces. The rough textures have generated interest in the solar-cell industry, as a means of reflection reduction for multicrystalline silicon [28-33], particularly under encapsulation. Since the acidic etch acts isotropically over the wafer, reflectance reduction is achievable on all orientations, as opposed to exclusively near-(100) orientations in the case of alkaline texture etches. Initial problems for the industrial implementation of such etches, notably the formation of hazardous NO_x gases and the strongly exothermic nature of the reaction, have largely been overcome through the development of industrial in-line cell processing systems for example [34]. Wafers are transported individually by conveyor belt between various enclosed processing stations, whereby isotropic etching is performed in a controlled environment with adequate cooling and replenishment of the etching constituents. Indeed, even in batch processes where etch conditions are well controlled, it has been shown [35] that several hundreds of 10 x 10 or 12.5 x 12.5 cm^2 wafers can be etched equivalently in a single bath. Thus acidic etching has proven to be a promising alternative to alkaline etchants for the industrial texturisation of multicrystalline silicon. The following sections describe the acidic etching mechanisms and the effect of the etch upon the multicrystalline surface morphology.

3.3.2 Etch reactions

The HF:HNO_3 system, using either water or acetic acid CH_3COOH as a diluent, has been studied extensively by Robbins and Schwartz [36-39]. As an oxidation-reduction reaction, depending on electron transfer processes, the etch rate differs for n & p-type material. The active oxidising species is in fact HNO_2:

$$2\ HNO_2 + R \rightarrow RO + H_2O + 2\ NO \qquad (3.5)$$

where R is the material to be etched e.g. Si or Ge. The HNO_2 forms by an autocatalytic, two step process. HNO_2 reduces the undissociated HNO_3 in the first step, which is slow and rate determining. The resulting reaction products generate more HNO_2 in the fast second step:

$$HNO_2 + HNO_3 \leftrightarrow N_2O_4 + H_2O \qquad (3.6)$$

$$N_2O_4 + 2NO + 2H_2O \leftrightarrow 4HNO_2 \qquad (3.7)$$

Alternatively, HNO_2 can be generated by the reaction of the molecular HNO_3 with NO;

$$HONO_2 + NO \leftrightarrow NOOH + NO_2 \qquad (3.8)$$

The overall oxidation reaction can be summarised as

$$HNO_3 + R \rightarrow RO + HNO_2 \qquad (3.9)$$

In HNO_3 rich regions, where silicon oxidation occurs readily, the reaction is predominantly controlled by the diffusion of the HF to the silicon surface for the removal of the oxide. In HF rich regions, where the surface is essentially stripped of oxide, initiation of the etch process appears to rely upon the presence of a small amount of HNO_2 and NO, as well as sufficiently high formation rates of these substances in order for the process to remain self-sustaining. The oxidation reaction thereby becomes rate limiting. It is presumed that the process proceeds with an induction phase whereby the undissociated HNO_3 attacks the Si directly to give the required reaction products. Crystal imperfections and defects can also trigger the process, whereby catalyst can be generated for further propagation of the reaction. A steady state condition is attained when the concentration of HNO_2 at the surface is in excess of a threshold, either through the natural autocatalysis of the reaction up to a sufficient rate or by addition of a trace of $NaNO_2$ (which decomposes in acid solutions to give nitrogen oxides) as a catalyst [36]. A boundary layer exists in the vicinity of the silicon surface consisting of a maximum concentration of HNO_2, NO (the final reduction product of HNO_3) and HNO_3 which diffuses in from the bulk solution. The HNO_2 which diffuses into the bulk solution will either decompose via reversal of equations 3.7 & 3.6 at low concentrations of HNO_3 to give NO and HNO_3, or else react at high concentrations according to the forward reaction to give N_2O_4, emitted in the form of NO_2. The final reaction product is thus influenced not by surface reactions but by secondary reactions within the boundary and bulk. The reaction of the HNO_3 within the boundary layer as opposed to on the silicon surface, leads to etch rates in the high HF region which may be higher than those expected purely from the simple diffusion of HF to silicon as calculated by Fick's law [38].

3.3.3 Effect of diluent

In the HF rich and HNO_3 rich regions with low dilutions ("low" depending upon the diluent and the strength of stock acids used), the diluent has minimal effect upon etch rate. The etch rate in these regions is influenced only by the rate of diffusion of the kinetically important species to the specimen surface. This is true on the addition of diluent up to a critical value, whereby the oxidising power of the solution is so reduced that etch rates start to decrease and catalysts (e.g. $NaNO_2$ or saw-damage) begin to play a kinetic role. At intermediate HF:HNO_3 ratios however, the addition of diluent does appear to moderate the reaction and slow the rate, although the mechanisms in this region are less well understood [39].

The two most commonly used diluents for the HF:HNO_3 system are acetic acid CH_3COOH and water, although H_3PO_4 is also used [28,29,31]. The differences observed in the reaction rates and the action of the etch can be ascribed to the differences in the basicity and dielectric constants of the diluents. Comparing acetic acid and water, the higher basicity of water with respect to acetic acid will more readily lead to the dissociation of HNO_3 in the solution, thus hindering the propagation of the oxidation-reduction reaction more than in the acetic acid case. This can be observed for the etch rates in the two systems, which are much lower in the water diluted case. However the kinetics of both water and acetic acid diluted systems are the same, so that reaction rates are determined by the diffusion rates of the kinetically important species to the specimen surface and autocatalytic factors have the same role in both systems. Schwartz and Robbins [36-39] conclude that etching behaviour in the acetic acid system can thus be duplicated by that of the water diluted system and vice-versa.

3.3.4 Surface morphology

Schwartz [36-39] investigates the surface morphology of silicon etched in the HF:HNO_3 system for both water and acetic acid diluents. Using triangular co-ordinate systems a qualitative description of the observed surface texture is given for the entire range of possible etch compositions. However, since these descriptions are aimed at work in the semiconductor industry, where etching is desired to yield smooth polished surfaces, descriptions such as "somewhat rough" could be equivalent in roughness to saw-damage etch textures in the solar cell industry. In addition, the effects of etching on multicrystalline material are absent, and acceptable etch rates for solar cell processing may be largely different to those of the semiconductor industry. In the following experimentation, etching is performed on both multi- and monocrystalline silicon materials over a wide range of etch compositions and the surface morphologies and resulting optical properties examined in detail.

3.3.5 Experimental

Multicrystalline Bayer and monocrystalline (100), (110) & (111) wafers of ~ 30 x 30 mm^2 were etched in $HF:HNO_3:CH_3COOH$ solutions with a wide range of compositions, for etch times varying between 15s and 5 minutes. The initially polished/lapped mono- (110) & (111) wafers were gritted to give a starting surface comparable to the as-cut Bayer and (100) material. The wafers were p-type and 1-2 Ωcm, except for the (111) material with 1-10 Ωcm. Etching was performed at room temperature with 2-4 samples in 250 ml of solution in a Teflon beaker without stirring or a temperature control mechanism. CH_3COOH is used as diluent due to its reported tolerance for undissociated HNO_3. The chosen etch compositions correspond to those investigated in [31] where the etch geometries are described qualitatively, with particular attention to the areas described as yielding "rough" textures. Using SEM photography in combination with reflectance measurements, the surface morphology is related to the optical properties of the wafers from the perspective of reflectance reduction in bare and encapsulated solar cells.

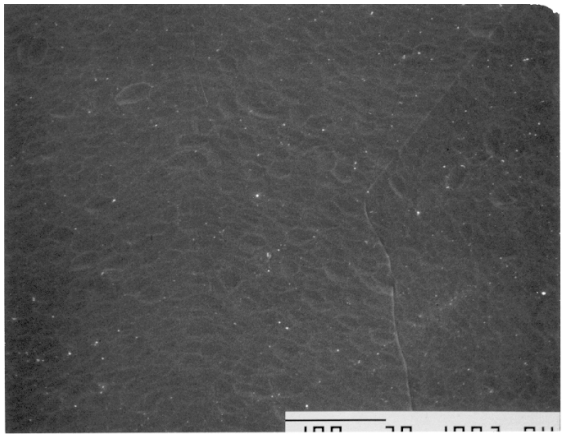

(a)

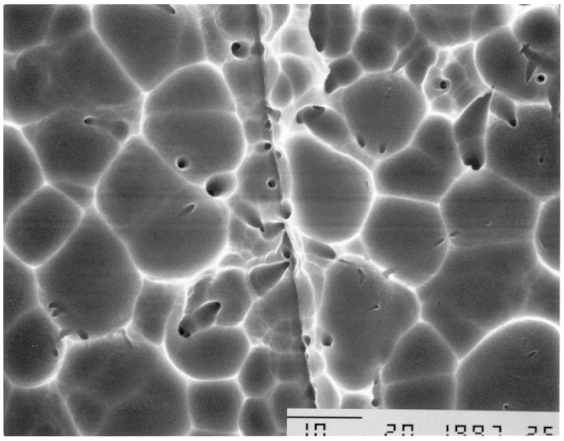

(b)

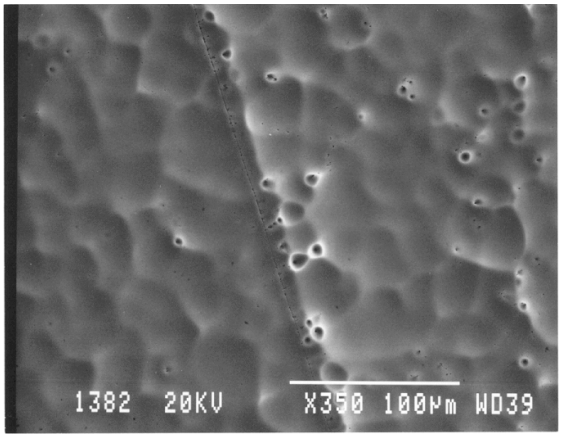

(c)

Figure 3.13 *SEM photographs of multicrystalline silicon for $HF:HNO_3$ volume ratios of a) 20:80, b) 80:20 and c) 90:10, using standard 49% HF and 70% HNO_3 concentrated acids. (The scale lines for a), b) and c) represent lengths of 100, 10 and 100 µm respectively.)*

3.3.6 Results and Discussion

3.3.6.1 Variation of surface morphologies as a function of $HF:HNO_3$ ratios

Figures 3.13 and 3.14 show the surface morphologies and etch rates for silicon etched in the simplest case of the undiluted $HF:HNO_3$ system (i.e. with no additional water or diluent except for that contained within the concentrated 49% HF and 70% HNO_3 acids used).

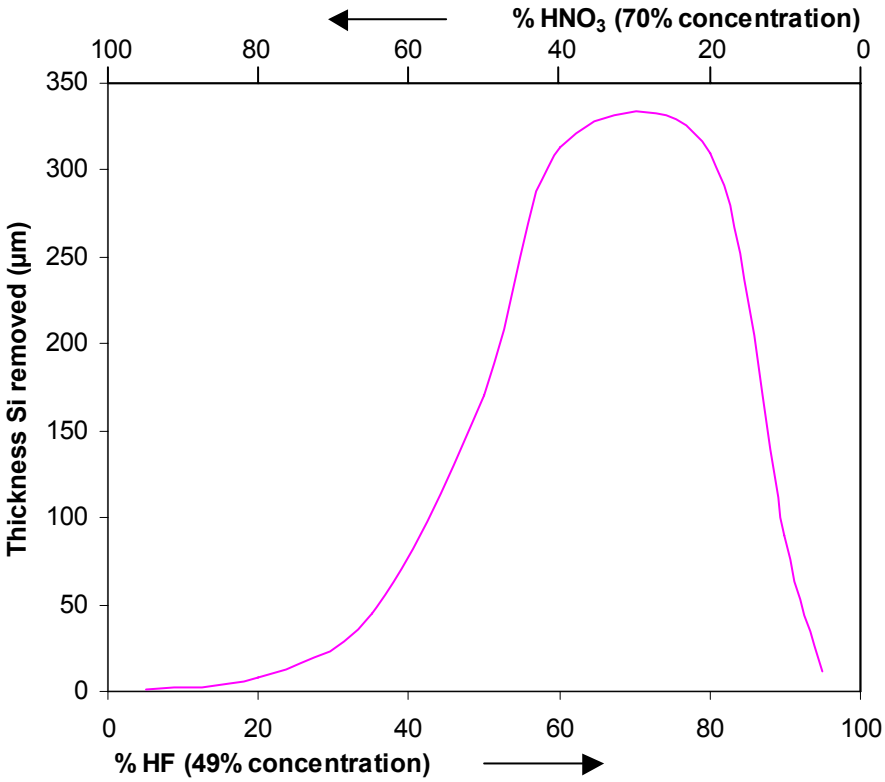

Figure 3.14: *Etch rates for (100) oriented monocrystalline silicon wafers etched for 15s as a function of the $HF:HNO_3$ ratio without added diluent.*

At high ratios of HNO_3 to HF, the etch rate is limited by the rate of diffusion of HF to the silicon surface for the removal of the formed oxide. Etching is slow, in the order of 5-15 microns per minute. The multicrystalline wafer is polished by the etch, since all orientations etch microscopically flat at the same rate and defect/grain boundaries are barely attacked by the etch (e.g. Figure 3.13a). This regime would appear suited for saw-damage removal. Etch rates are equivalent to high concentration alkaline saw-damage etches, but without height differences between differently oriented grains which may be less desirable in further processing (e.g. application of metallisation).

As the proportion of HF in the solution is increased past an HF:HNO_3 ratio of 30:70, the etch rate increases dramatically, up to a maximum for HF:HNO_3 ratios of ~65:35 where tens of microns are removed per second (Figure 3.14). The reaction is extremely exothermic. Autocatalysis (which occurs to some extent for all HF:HNO_3 ratios), fuelled by increasing amounts of reaction products, causes reaction rates and etch temperatures to spiral, with dark brown fumes of NO_x gases being emitted. Paradoxically, although this regime is the most unstable for etching, it also yields the concave etch pit or "tub" morphologies discussed in section 3.3.1 which are desirable for reflectance reduction (see Figures 3.13b and 3.17). The etch pits, which form on all crystal orientations, suggest a 'physical' attack of the etch upon the silicon, as if the surface has been bombarded with individual circular "wavefronts". With the use of controlled conditions such as provided by in-line processing systems (section 3.3.1), this region of the HF:HNO_3 system is potentially the most promising for an eventual alternative to alkaline texture etching for monocrystalline wafers under encapsulation. However, defects/grain boundaries are severely attacked by the etch, causing a potential problem for multicrystalline wafers. A solution to this problem may be found in reducing the etch depth used, as will be discussed in section 3.3.6.2 below.

Increasing the proportion of HF further beyond the etch rate peak sees the smoothening of the texture (Figure 3.13c). In contrast with the high HNO_3 region however, defects are now attacked by the etch, these providing the aforementioned "sparks" required to trigger the reaction. The surface is seen to be composed of extremely shallow concave pits. However the flatness of this texture is such that reflectances of wafers in this region are approximately equal to that of polished silicon. (This is incidentally a region described as yielding "rough" surfaces by Schwartz & Robbins [39], highlighting the differences in terminology in the solar cell and semiconductor technologies/disciplines.) In general, the HF rich regime seems to have no particular advantage compared to other regions of the HF:HNO_3 system in terms of the etch surface morphologies formed.

Figure 3.15 illustrates the effect of the addition of acetic acid as diluent upon etch rate in the HF:HNO_3 system. The triangular co-ordinate system shown has axes as described in [36], representing the volume percentage of the stock acid used relative to the other acids in the solution (see also Figure 3.14). In agreement with the observations in [36-39], the addition of diluent in the high HF and high HNO_3 regions of the system did not appreciably affect the etch rates (dilutions of up to 40% were investigated). In the intermediate region around the etch rate maximum, dilution leads to a dramatic decrease in etch rate. For example, at an HF:HNO_3 ratio of 60:40, the etch rate on multicrystalline silicon decreases from 1040 μm/min when undiluted to 70 μm/min when 40% acetic acid is added. In summary, dilution of the system yields a lowering and a broadening of the peak etch rates.

Figure 3.16 shows the corresponding surface geometries on dilution. Initially, surface textures follow the same trends as observed for the undiluted system described above. However, the concave pit region found at intermediate HF:HNO_3 ratios in the undiluted system diminishes with increasing diluent ratios, and was absent at a dilution of 40%. Etching at the same HF:HNO_3 ratios at this dilution yields surfaces more akin to those in the high HNO_3 region, with very flat, specular surfaces.

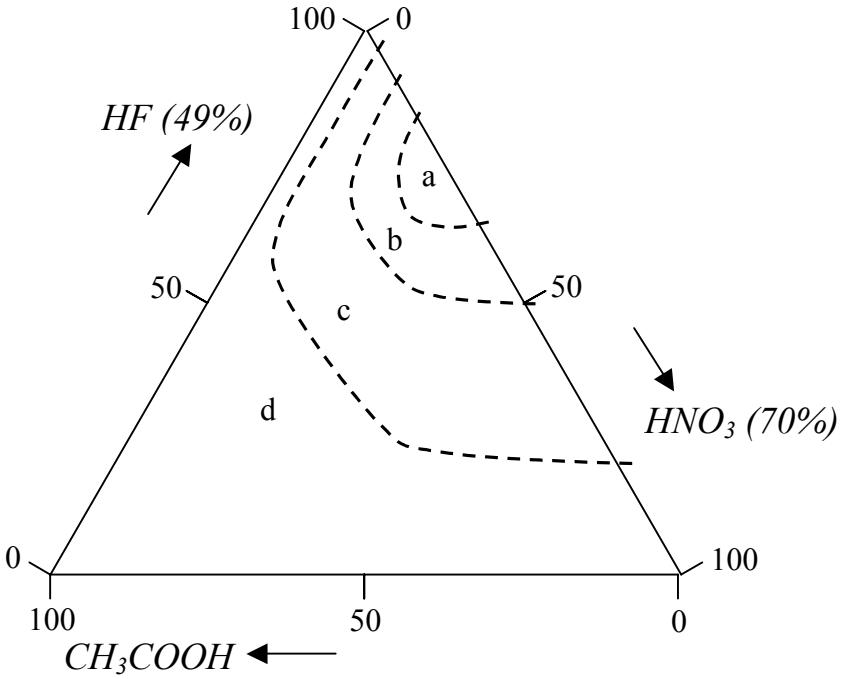

Figure 3.15: *Sketch of the etch rates as a function of etch composition in the 49% HF, 70% HNO_3, 100% CH_3COOH system, using the triangular co-ordinate system described in [36]. (a) > 1000 µm/min, (b) > 500 µm/min, (c) > 50 µm/min, (d) 0 - 50 µm/min.*

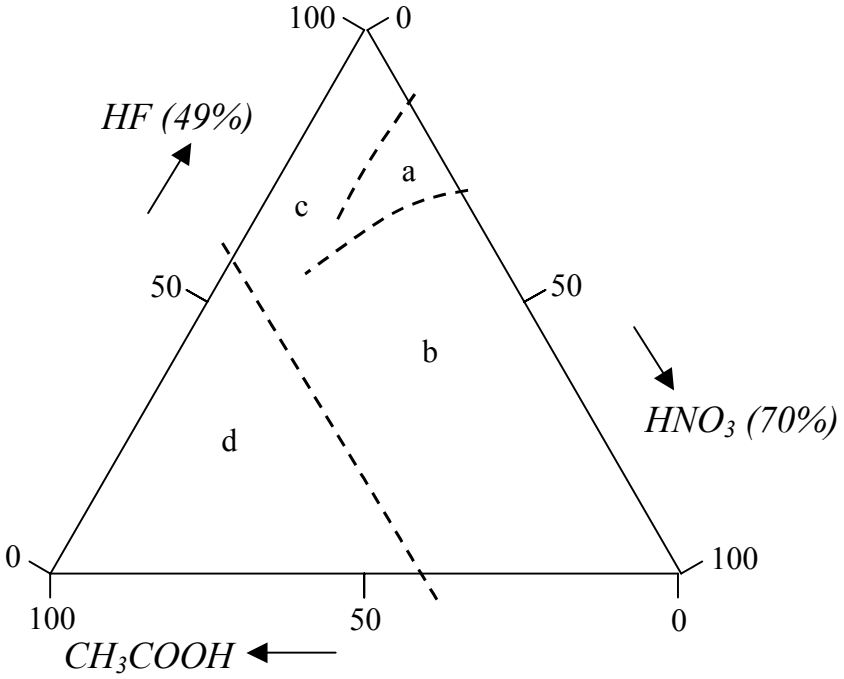

Figure 3.16: *Sketch showing the effect of etch composition on surface morphology. (a) Concave pit structures; reflectance R in air at (an arbitrary visible) wavelength λ=630 nm typically ±20%, (b) etches flat, tends to mirror polished on prolonged etching, minimal attack on defects, R ~ 30%, (c) etches flat, attack on defects, R ~ 30%. Region (d) (high concentration of added diluent) was not investigated.*

3.3.6.2 Influence of etch depth on the surface morphology of "pitted" structures

A simple way of minimising grain boundary and defect etching in multicrystalline silicon wafers for HF:HNO_3 compositions yielding "pitted" structures, is to reduce the etch depth used. Assuming that potential etch solutions will be employed for the simultaneous removal of saw-damage and application of texture, the minimum etch depth used will be determined by the thickness of the saw-damage layer. However for optimisation it is important to investigate the effect of etch depth upon the resulting surface morphologies and reflectances.

The multicrystalline etch surfaces shown in Figure 3.17 are typical of those in the pitted etch region, showing the surface morphology at different stages of etching. The etch initially progresses from as-cut by the formation of narrow elongated worm-shaped pits (Figure 3.17a), markedly similar to those presented in reference [40] in earlier attempts to texture multicrystalline silicon in acidic solutions. On further etching, these elongated pits become larger and more rounded yielding concave etch pit structures as shown in Figure 3.17b. Although grain boundaries are visible by eye at this stage, their depth is not large enough in comparison to the pit structures to be able distinguish them with SEM photography. With prolonged etching (tens of microns) the etch pits become flatter and broader in diameter and grain boundaries and defects are severely attacked (Figure 3.17c).

Figures 3.18 and 3.19 show the measured reflectance curves for bare and encapsulated multicrystalline silicon wafers etched to different depths. Reflectances increase with etch depth in correspondence with the increased flatness of the texture. Encapsulated reflectances lie around 10% lower than for a polished wafer for the shallowest etches with correspondingly the highest etch pit curvature, as a result of TIR at the glass-air interface. This implies that, provided saw-damage is sufficiently removed, as low an etch depth as possible should be used for acidic texturisation, to maximise eth pit curvature and thereby yielding lower reflectances, with the advantage of minimal attack of the etch upon defects and grain boundaries.

3.3.6.3 Effect of etch agitation upon curvature of pitted structures

Since the diffusion of reactants and products to and from the crystal surface during etching plays an important role in the reaction process, agitation of the etch solution (e.g. by stirring) can have a considerable effect on both reaction rate and etch pit curvature. When isotropic etching is performed using photolithographic masks for example [24], it is found that without stirring the hole formed becomes flat on etching, whilst with stirring the hole approaches a hemispherical shape. This is interesting for HF:HNO_3 ratios further away from the etch rate peak with flatter etch pit structures but lower more controllable silicon etch rates; stirring of the solution could potentially increase the etch pit curvature resulting in lower reflectances.

In the "pitted" etch regime, the volatility of the reaction can itself provide a situation tantamount to stirring. This was observed for the specific case of the (100) orientation for the etch solution HF:HNO_3:CH_3COOH:H_2O = 6:3:1:1. On removal of 120 μm total thickness of Si, dark patches could be clearly observed visually on the silicon, seemingly encroaching inwards from the lower corners and edges of the silicon wafer where the availability of the reagent is greater than at the centre of the specimen. On further etching, this dark patch covers almost the entire wafer. Inspection with SEM photography (Figure 3.20) showed that whereas the light patches corresponded to areas of flattened pits with high reflectance (approximately 30%), the dark patches corresponded to pits of exceptionally high curvature with reflectances of below 20%.

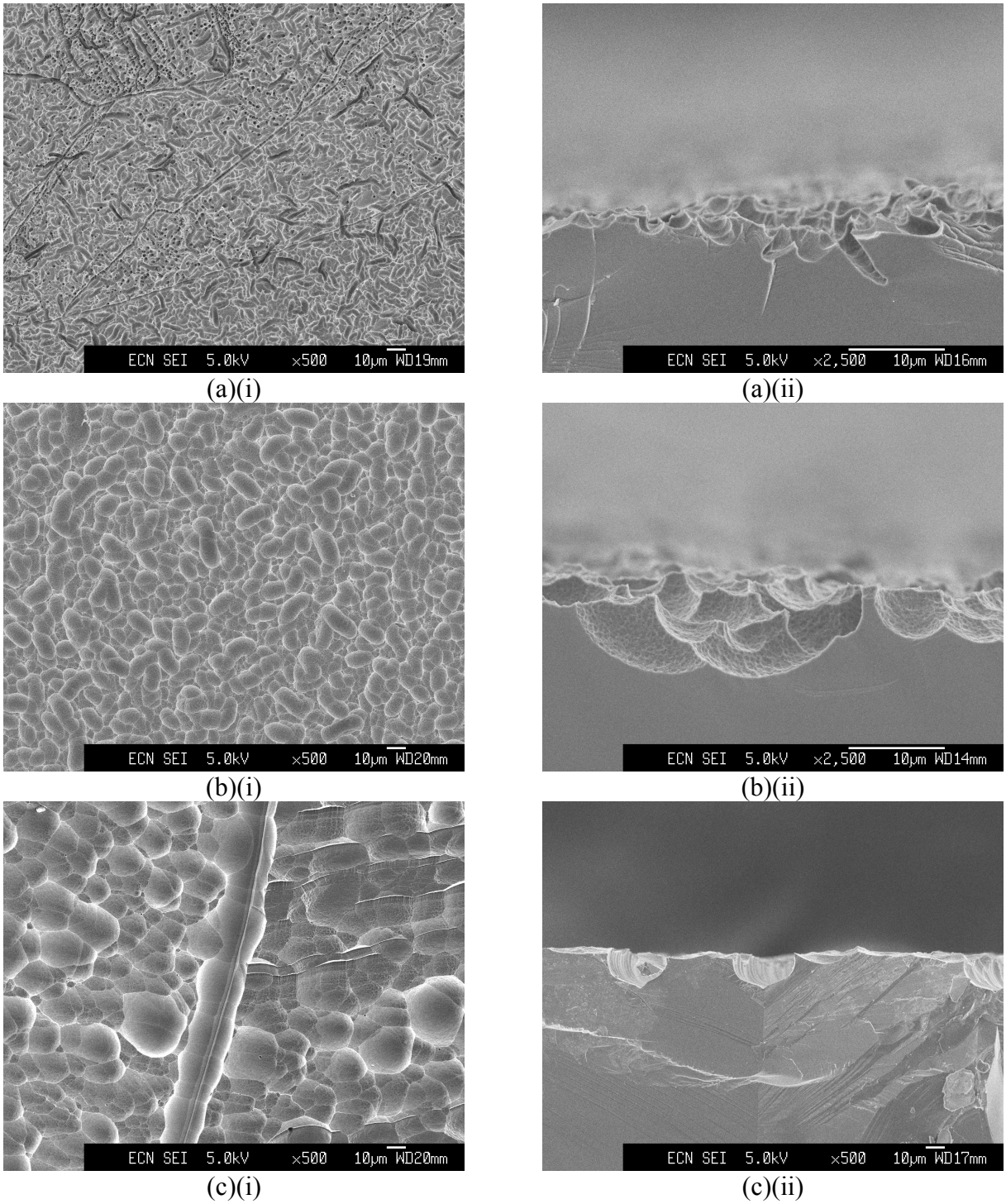

Figure 3.17 *SEM photographs of multicrystalline silicon showing the change in surface morphology from above (i) and at cross-section (ii) on the etching of "pitted" structures for reflectance reduction at etch depths of a) 3.7, b) 7.8 and c) 45 μm per side of the wafer. The attack of the etch on grain boundaries and defects with prolonged etching is clearly seen in c), with grain boundaries being etched tens of microns deeper than the rest of the wafer surface.*

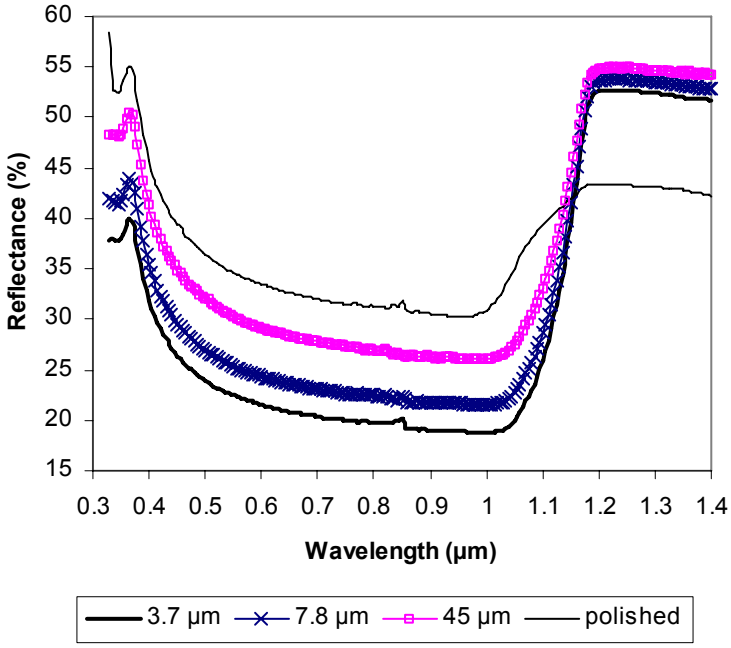

Figure 3.18 *Reflectances of the multicrystalline wafers shown in Figure 3.15 with pitted textures on increasing etch depths of 3.7, 7.8 and 45 µm per wafer side. A wafer polished to a depth of 31 µm per wafer side is shown for reference.*

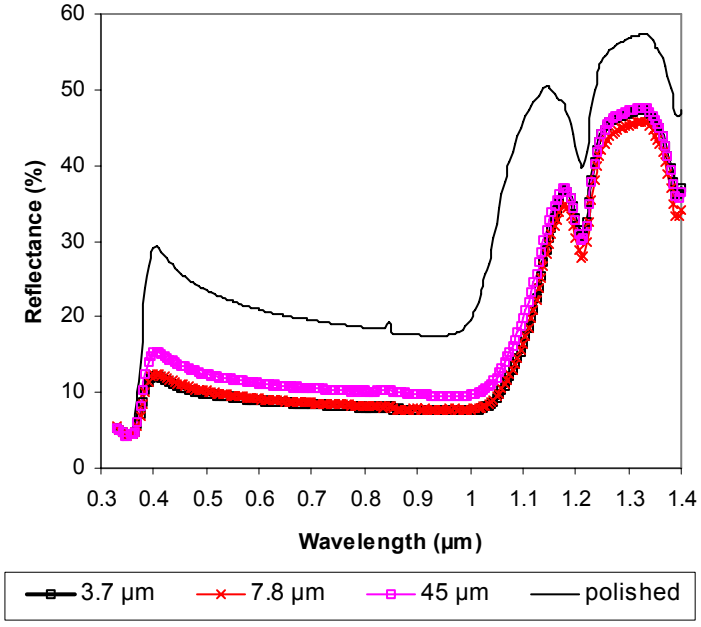

Figure 3.19 *Reflectances of the encapsulated multicrystalline wafers shown in Figures 3.15 and 3.17 with pitted textures on increasing etch depths of 3.7, 7.8 and 45 µm per wafer side, with a polished wafer shown for reference.*

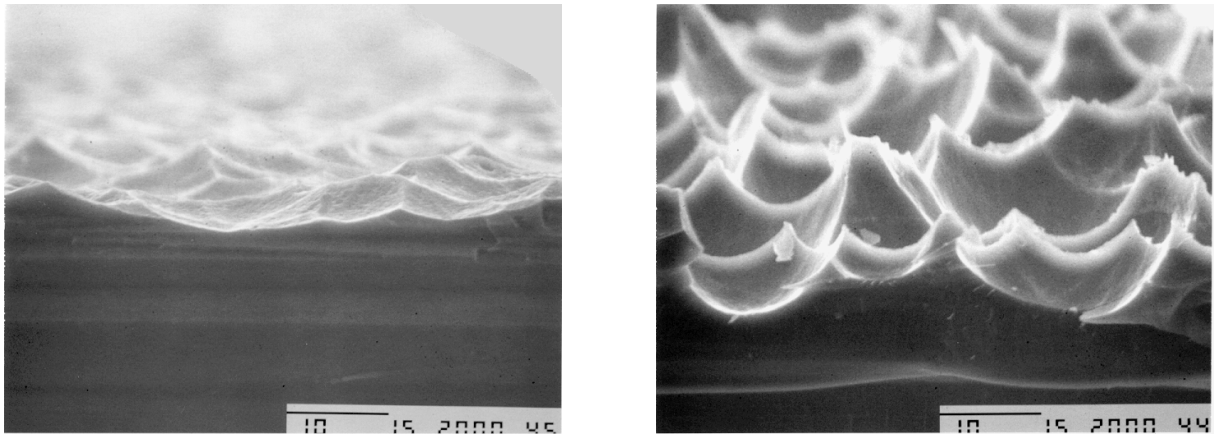

(a) (b)

Figure 3.20 *SEM photographs at a) the centre and b) a corner of a single (100) oriented wafer showing the effects of diffusion upon the surface morphology within a single wafer (HF:HNO_3:CH_3COOH:H_2O = 6:3:1:1, scale line = 10 μm).*

3.4 Reactive ion etching

Another etching method whereby all crystal orientations receive equivalent texturisation is reactive ion etching (see e.g. [41]). Reflection reduction is achieved due to the formation of needle-like structures, whose diameters and separations are small compared to the useful solar wavelengths and whose heights are comparable with or larger than these wavelengths [42]. In experimentation in collaboration with the MESA institute (at the University of Twente, The Netherlands), it was attempted to form a pillar structure with very low reflectance and a high mechanical resistance which can withstand further processing.

3.4.1 Etching mechanism

The etch consists of a chemical etchant for etching the substrate, a passivator for blocking the etching of sidewalls and an ion source for local removal of passivator at the bottom of the etch trenches [43]. The plasma used consisted of SF_6, O_2 and CHF_3. SF_6 provides $F^{\bullet}$ radicals for etching the silicon, leading to volatile SiF_6 as a reaction product, O_2 gives $O^{\bullet}$ radicals which passivate the silicon with SiO_xF_y, and CHF_3 gives CF_x^+ ions which remove the passivating SiO_xF_y to give CO_xF_y. Low energy ions (20-90eV) are used for a high etch selectivity and for low damage to the substrate and passivating layers. The control of these ions depends on the DC self-bias (the potential developed between the plasma and the powered electrode). Increasing the flow of O_2 (and also the CHF_3) gives very high bias voltages, since the rate of formation of the passivating layer competes with the slow etch rate of this layer, leading to an increase in ion energy. SF_6 gives low voltages, and the bias also decreases when power decreases or pressure increases.

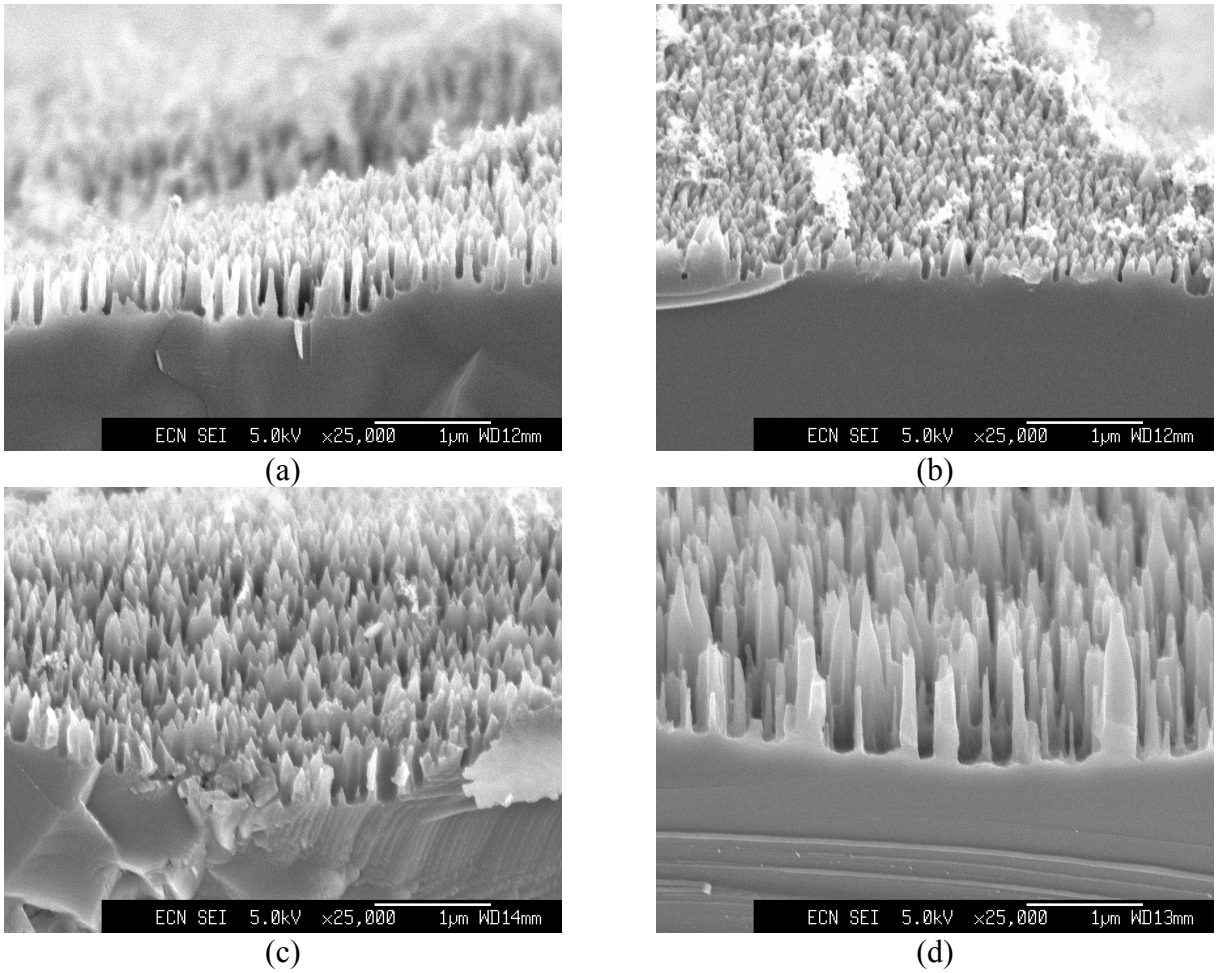

Figure 3.21 *Multicrystalline Si texture after reactive ion etching at different SF_6/O_2 ratios.*

3.4.2 Surface morphology

The etch texture can be varied by varying the gas proportions and/or the power and pressure [43]. Increasing the SF_6 content reduces the formation of the passivating layer and leads to a more isotropic etch. Increasing the O_2 content gives a more physical etch and positively tapered profiles, whilst increasing CHF_3 increases the removal of the blocking layer and leads to more negatively tapered profiles. A higher pressure or lower power leads to a positively tapered profile due to the lower ion energy, with off-normal ions more likely to reflect from sidewalls without etching. The height of the texture was seen to be determined by the etch time and the shape determined by the SF_6/O_2 ratio.

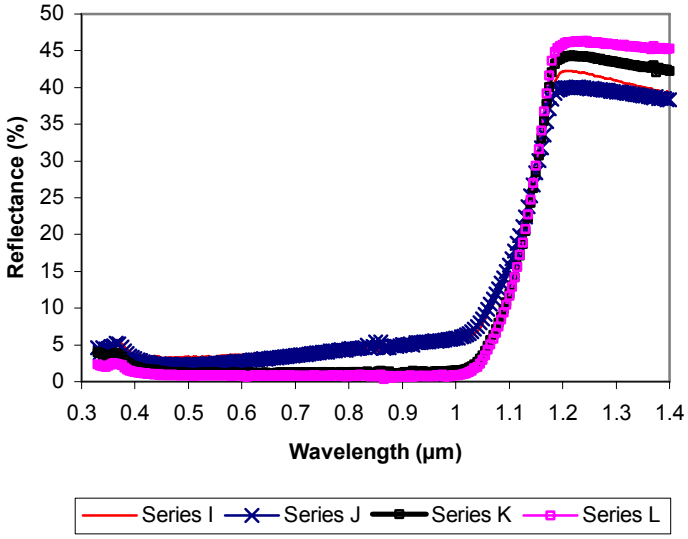

(a)

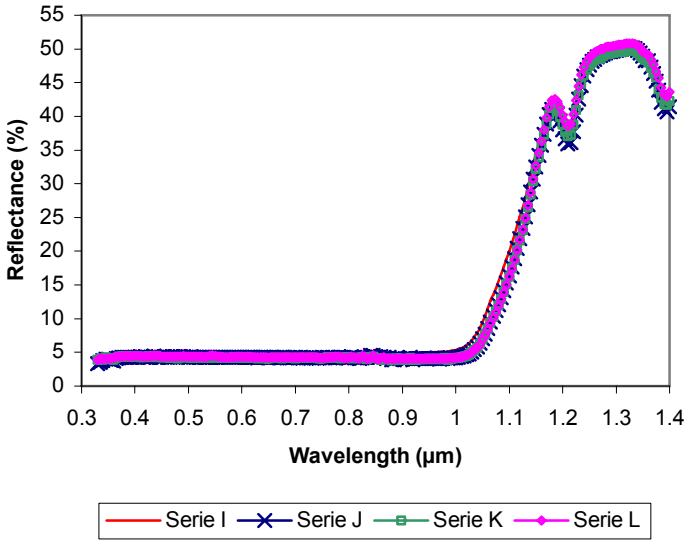

(b)

Figure 3.20 *Reflectances of a) bare and b) encapsulated neighbouring multicrystalline wafers with RIE texturisation. Series I, J, K and L have textures corresponding to a), b), c) and d) in the previous Figure 3.19.*

Variation of these etch parameters lead to mechanically stable needles with dimensions of between 0.2-1 µm in height and a diameter of 0.1-0.2 µm (Fig 3.19). The spacing between needles was 0.1-0.2 µm. Although there was a slight difference in reflectance for these cases, with lower R for longer needles (see Fig 3.20a), front surface reflectances of 5% or less were obtained for bare multicrystalline wafers, the etch being orientation independent. The reflectance barely changes on encapsulation under EVA (ethyl vinyl acetate) + glass as in a module (Fig 3.20b), with the front surface reflectance assuming that of the encapsulating materials. However, the internal quantum efficiencies (IQE) of cells textured in this manner is much lower for wavelengths below 800 nm when compared to a standard cell, due to the absorption of light in the needles instead of the bulk. Carriers so generated have a high

probability of recombination at the needle surfaces and will not reach the p-n junction. A higher IQE can be obtained by performing an alkaline NaOH etch after plasma etching; however, the needle structure is lost in this step, becoming shorter and more rounded, with encapsulated reflectances lying a few percent higher at around 7.5% [44].

3.5 Conclusions

This chapter presents an overview of chemical texturisation methods, through an investigation of the texture geometries formed on crystalline silicon of different orientations. Chemical etching has been investigated for alkaline, acidic and reactive ion etching systems. The surface morphology is related to the temperature and etch concentration for the (100), (110) and (111) orientations. In the case of alkaline etchants based on NaOH, etch rates are seen to increase with etch concentration, with the (111) being the slowest etching orientation in all cases. The (110) etch rate was higher than for the (100) at 70°C. For lower molarities at 90°C, etch rates were equivalent or slightly higher for the (100) than the (110). Whilst temperature is seen to influence etch rate without significantly affecting the surface geometry (70°C and 90°C were investigated), changing the etch concentration leads to large variations in the structures formed. Due to parallels with experimental investigations of others [21], it is thought that kink sites are essential for the etching of the silicon on the (111) orientation in particular. This explains the formation of terraces on the (111) orientation, and supports the theory proposed by Bressers [25] for the stability of pyramidal textures whereby the pyramid develops by the propagation of steps starting at the intersecting edges of the {111} facets. It remains difficult however to fully explain the variation in surface morphology which arises on the variation of the etch concentration. A method is introduced for the pyramidal texturisation of (100) polished silicon, whereby nitrogen gas is used to expel (dissolved) oxygen in the alkaline solution which otherwise leads to mirror polished surfaces.

Acidic etching was performed with solutions based on 49% HF, 70% HNO_3 and glacial acetic acid. For the undiluted HF:HNO_3, etch rates were found to peak at HF:HNO_3 ratios of approximately 65:35. On increasing dilution, the peak broadens and etch rates generally decrease. In the region of the etch rate peak at low dilutions, concave etch pits are formed upon silicon whose curvatures lead to reduced reflection in air and particularly under encapsulation, in the latter case down to as low as ~10%. However, defects and grain boundaries are preferentially attacked by the etch at these ratios, which is a problem when texturing multicrystalline wafers. Defect etching can be minimised whilst retaining the favourable etch pit geometries by keeping etch depths to a minimum, since etch pits become flatter and reflectance higher as the etch depth is increased.

Reactive ion etching is investigated as an isotropic etching method for the texturisation of multicrystalline silicon. The texture formed consists of columnar structures, whose heights and shapes are determined by the etch time and plasma composition respectively. Needles up to approximately a micron in height were found to be mechanically stable, and gave bare reflectances of under 5% for multicrystalline wafers, this value barely changing under encapsulation where the front surface reflectance assumes that of the glass. However, absorption in the needles leads to a higher recombination before reaching the p-n junction whereby the IQE for these textures is low; an alkaline etch improves the IQE values but stumps the needle textures so that their reflection reducing properties are somewhat impaired.

References

[1] A.W. Weeber, A.R. Burgers, M.J.A.A. Goris, M. Koppes, E.J. Kossen, H.C. Rieffe, W.J.Soppe, C.J.J. Tool, J.H. Bultman, "16% mc-Si Cell Efficiencies using industrial in-line processing", in Proc. 19th EPVSEC, Paris (2004) 532-555

[2] F. Restrepo, C.E. Backus, "On Black Solar Cells or the Tetrahedral Texturing of a Silicon Surface", IEEE Trans. Elec. Dev. ED-**23** no.10 (1976) 1193-1195

[3] S.R. Chitre, "A high volume cost efficient production macrostructuring process", in Proc. 13th IEEE PVSC, New York/ Washington (1978) 152-154

[4] Rudenberg H.G. & Dale B., "Radiant Energy Transducer", US Patent 3, 150,999, filed Feb. 17 1961

[5] Miller D.P., Watelski S.B. & Moore C.R., "Structure Defects in Pyrolytic Silicon Epitaxial Films", J. App. Phys. **34** no.9 (1963) 2813-2821

[6] R.C. Newman, J. Wakefield, "The formation of Etch Pits and of Silicon Carbide on Silicon Surfaces at High Temperatures", in Proc. of an international conference held in Brussels, Vol. 1, Semiconductors Part 1 (1958)

[7] D.B. Lee, "Anisotropic Etching of Silicon", J. Appl. Phys. **40** no.11 (1969) 4569-4574

[8] D.L. King, M.E. Buck, "Experimental optimization of an anisotropic etching process for random texturization of silicon solar cells", in Proc. 22nd IEEE PVSC (1991) 303-308

[9] E. Demesmaeker, "Theoretical and experimental study of advanced concepts for high efficiency crystalline silicon solar cells", PhD thesis, Catholic University of Leuven, Belgium, (1993)

[10] J.B. Price, "Anisotropic Etching of Silicon with KOH-H_20-Isopropyl Alcohol", in "Semiconductor Silicon", editors Burgess R.R. & Huff H.R., The Electrochemical Society Softbound Proceedings Series, Princeton, NJ (1973) 339

[11] D.L. Kendall, "Vertical Etching of Silicon at very high aspect ratios", Annual Review of Materials Science **9** (1979) 373

[12] P.M.M.C. Bressers, "Silicon Etching, An Electrochemical Study", PhD thesis, University of Utrecht, The Netherlands (1995)

[13] A.J. Nijdam, "Anisotropic wet-chemical etching of silicon", PhD thesis, University of Twente, The Netherlands (2001)

[14] V.A. Burrows, Y.J. Chabal, G.S. Higashi, K. Raghavachari, "Infrared spectroscopy of Si (111) surfaces after HF treatment: hydrogen termination and surface morphology", Appl. Phys. Lett. **53** (1988) 998-1000

[15] G.S. Higashi, Y.J. Chabal, G.W. Trucks, K. Raghavachari, "Ideal hydrogen termination of the Si (111) surface", Appl. Phys. Lett. **56** (1990) 656-658

[16] N. Hirashita, M. Kinoshita, I. Aikawa, T. Ajioka, "Effects of surface hydrogen on the air oxidation at room temperature of HF-treated Si (100) surfaces", Appl. Phys. Lett. **56** (1990) 451-453

[17] E.D. Palik, H.F. Gray & P.B. Klein, "A Raman Study of Etching Silicon in Aqueous KOH", J. Electrochem. Soc **130** (1983) 956-959

[18] H. Seidel, L. Cespregi, A. Heuberger, H. Baumgartel, "Anisotropic Etching of Crystalline Silicon in Alkaline Solutions: I. Orientation Dependence and Behaviour of Passivation Layers", J. Electrochem. Soc. **137** no.11 (1990) 3612-3626

[19] R.M. Finne & D.L. Klein, "A Water-Amine-Complexing Agent System for "Etching Silicon", J. Electrochem. Soc **114** no.9 (1967) 965-970

[20] E.D. Palik, V.M. Bermudez, O.J. Glembocki, "Ellipsometric Study of Orientation-Dependent Etching of Silicon in Aqueous KOH", J. Electrochemical Society (Solid-State Science & Technology) **132** (1998) 871-884

[21] P. Allongue, V. Costa-Kieling, H. Gerischer, "Etching of Silicon in NaOH Solutions, II. Electrochemical Studies of n-Si(111) and (100) and Mechanism of the Dissolution", J. Electrochem. Soc. **140** no.4 (1993) 1018-1026

[22] J. Rappich, H. Jungblut, M. Aggour, H.J. Lewerenz, "Electrochemical Smoothing of Silicon (111)", J. Electrochem. Soc **141** no.8 (1994) L99-L102

[23] S. Tan, M.L. Reed, R. Boudreau, "Mechanisms of Etch Hillock Formation", J. Microelectromechanical Systems **5** no.1 (1996) 66-72

[24] M. Elwenspoek, "Etching Technology", Lecture notes for UETP-MEMS course "Etching Technology", Vienna, Austria (1995)

[25] P. M. M. Bressers, J. J. Kelly, J.G.E. Gardeniers, M. Elwenspoek, "Surface morphology of p-type (100) silicon etched in aqueous alkaline solution", J. Electrochemical Society **143** no.5 (1996) 1744-1750

[26] L. Albrecht, R. Pfeiffer, A. Wigand, "Ätzmittel zum anisotropen naβchemischen German Ätzen von Silizium", Patent DD 300 622 A7, filed 26 June 1990

[27] S. Büttgenbach, "Mikromechanik", B. G. Teubner 1st Edition (1994)

[28] M.J. Stocks, A.J. Carr, A.W. Blakers, "Texturing of polycrystalline silicon", in Proc. 1st WCPEC, Hawaii (1994) 1551-1554

[29] M.J. Stocks, A.J. Carr, A.W. Blakers, "Texturing of polycrystalline silicon", Solar Energy Materials and Solar Cells **40** (1996) 33-42

[30] R. Einhaus, E. Vazsonyi, J. Szulfcik, J.Nijs, R. Mertens, "Isotropic texturing of multicrystalline silicon wafers with acidic texturing solutions", in Proc. 26th IEEE PVSC, Anaheim (1997) 167-170

[31] J. Zhao, A. Wang, M.A. Green, "19.8% efficient "honeycomb" textured multicrystalline and 24.4% monocrystalline silicon solar cells", Appl. Phys. Lett. **73** no.14 (1998) 1991-1993

[32] M.A. Green, J. Zhao, A. Wang, "23% module and other silicon solar cell advances", in Proc. 2nd WCPEC, Vienna (1998) 1187-1192

[33] Y. Nishimoto, T. Ishihara, K. Namba, "Investigation of Acidic Texturization for Multicrystalline Silicon Solar Cells", J. Electrochem. Soc. **146** no.2 (1999) 457-461

[34] http://www.rena.de

[35] S. de Wolf, P. Choulat, E. Vazsonyi, E. van Kerschaver, K. de Clercq, J. Szlufcik, "Towards industrial application of isotropic texturing for multi-crystalline silicon solar cells", in Proc. 16th EPVSEC, Glasgow (2000) 1521-1523

[36] H. Robbins, B. Schwartz, "Chemical Etching of Silicon", J.Electrochem. Soc. **106** no.6 (1959) 505-508

[37] H. Robbins, B. Schwartz, "Chemical Etching of Silicon", J.Electrochem. Soc. **107** no.2 (1960) 108-111

[38] H. Robbins, B. Schwartz, "Chemical Etching of Silicon", J.Electrochem. Soc. **108** no.6 (1961) 365-372

[39] B. Schwartz, H. Robbins, "Chemical Etching of Silicon", J.Electrochem. Soc. **106** no.6 (1976) 1903-1909

[40] D. Sarti, Q.N. Lê, S. Bastide, G. Goaer, D. Ferry, "Thin Industrial multicrystalline Solar cells and improved Optical Absorption", in Proc. 13th EPVSEC, Nice (1995)

[41] W.A. Nositschka, C. Beneking, O. Voigt, H. Kurz, "Texturisation of multicyrstalline silicon wafers for solar cells by reactive ion etching through colloidal masks", Solar Energy Materials & Solar Cells **76** (2003) 155-166

[42] G. Willeke, P. Fath, "Texturisation methods for multicrystalline silicon solar cells", in Proc. 13th EPVSEC, Nice (1995) 399-402

[43] H. Jansen, M.de Boer, R. Legtenberg, M. Elwenspoek, "The black silicon method: a universal method for determining the parameter setting of a fluorine-based reactive ion etcher in deep silicon trench etching with profile control", J. Micromech. Micoreng. **5** (1995) 115-120

[44] A.R. Burgers, C.J.J. Tool, J.D. Hylton, A.W. Weeber, A.G.B.J. Verholen, J.G.E. Gardeniers, M.J. de Boer, M.C. Elwenspoek, "Silicon solar cells structured by reactive ion etching and processed with screen printing", in Proc. 2nd WCPEC, Vienna (1998) 1531-1534

4: Alkaline etching for reflectance reduction in multicrystalline silicon wafers

The reflection reducing properties of alkaline etched multicrystalline wafers are investigated experimentally. A high concentration saw-damage etch and a low concentration texture etch are assessed. Etch surface geometries are quantified in terms of the tilt and azimuth angles of the texture features on a per orientation basis. In the case of saw-damage etching, the {100}, {111}, {110}, {311} & {211} sets of crystallographic planes are stable to the etch. The resulting textures are too flat for multiple bounce reflectance in air, with only 1.6% of the multicrystalline wafer surface calculated to have facet tilt angles above 45° whereby double bounce reflectance is guaranteed. For texture etching, it is found that contrary to the accepted principles of texture etching, not only {111} planes are stable to etching but the whole range of {XXY} crystallographic planes between these and {110} orientations, challenging the validity of the accepted theory. The orientations in the vicinity of the (100) yield (tilted) pyramid structures with etch facets angled up to 54.7°, whereby 13% of the multicrystalline etch surface has tilt angles above 45°, and reflectances are 3% lower than for saw-damage etched wafers in air. However, under encapsulation, both saw-damage and texture etched multicrystalline wafers couple light more effectively into the silicon. Encapsulated reflectances compare only 7 and 5.5% higher respectively than upright pyramid textures on monocrystalline (100) silicon, compared to 18 and 15% higher in air. This is because a far larger proportion of the multicrystalline wafer is facetted at tilt angles greater than the 20.9° satisfying the condition for total internal reflection of escaping light at the glass-air interface.

4.1 Introduction

4.1.1 Alkaline etchants for solar cell processing

Alkaline etchants are employed standardly in solar cell processing. “High” temperatures (above 100°C) and concentrations (around 10 M or more) of alkali are used for the removal of sawing damage for as-cut silicon wafers. These etching conditions are chosen in order to remove the required depth of saw-damaged silicon as quickly as possible. In contrast, “low” temperatures (below 100°C) and concentrations (< 0.5 M) of alkali are used in the processing of (100) oriented monocrystalline wafers. In this case, the anisotropic action of the alkaline etchant is exploited, whereby slow etching planes, apparently of {111} orientation, are exposed and intersect to form upright four-sided pyramids with square bases up to 10 x 10 μm^2. These pyramidal textures have geometries which allow sunlight to be more easily

coupled into the silicon (see Chapter 1), and thus to allow as much light as possible to be absorbed and converted to electrical current in the solar cell.

4.1.2 Reflectance reduction through geometrical texturisation

Figure 4.1 uses two dimensional groove textures to demonstrate how geometrical texturisation can reduce the amount of light lost by front surface reflectance, without the use of an anti-reflection coating, for silicon in air. Light which is reflected away from a groove facet at its first point of incidence (e.g. at (i) in Figure 4.1) may be re-directed towards the silicon via a neighbouring texture facet, for a second chance of transmission into the silicon (e.g. at (ii) in Figure 4.1), thereby lowering reflectance at the front surface. The probability with which light will receive such "double bounce incidence" or still higher orders of multiple incidence depends upon the facet tilt angles of the geometrical textures with respect to the surface of the wafer, as represented by α in the figure. For normally incident light falling upon periodic textures, angles of $\alpha > 45°$ ensure double bounce reflectances will occur; angles of $\alpha > 60°$ yield triple bounce reflectances at least. As facet tilt angles decrease below $\alpha < 45°$, less and less light will receive double bounce incidence, closer to the base of the grooves, until at angles below 30°, no light will receive multiple bounce incidence in air, and reflectance levels are equivalent to that of polished silicon. For the upright pyramids formed on (100) oriented wafers, the {111} facets are angled at 54.7° to the base so that double bounce reflectances are predominant. As a result, texturing of the (100) silicon leads to an absolute reflection reduction of approximately 20% compared to a flat polished wafer in air.

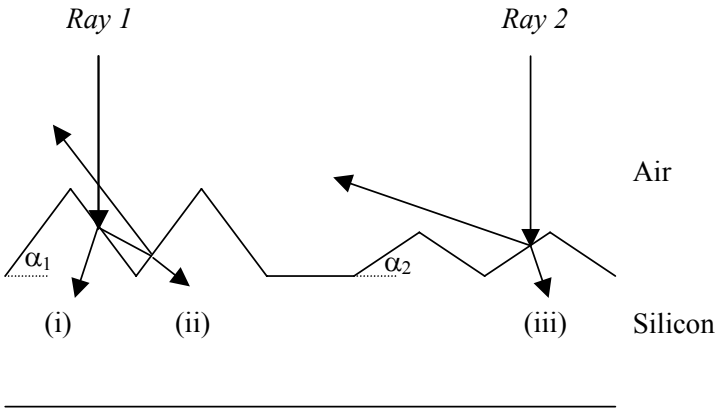

Figure 4.1 *Possible paths for light incident upon geometrically textured silicon in air. Ray 1 experiences "double bounce incidence" at a facet tilted at angle $\alpha_1 > 30°$. Light which is not coupled into the silicon for absorption at (i) falls re-incident for a 2nd chance of transmission into the silicon at (ii), thereby reducing front surface reflection. Ray 2 falls incident on texture whose facet tilt angle $\alpha_2 < 30°$ and is reflected directly away without a second chance of incidence. However, if $\alpha_2 > 20.9°$, then ray 2 will experience multiple incidence from this facet under encapsulation, as shown in Figure 4.2 below.*

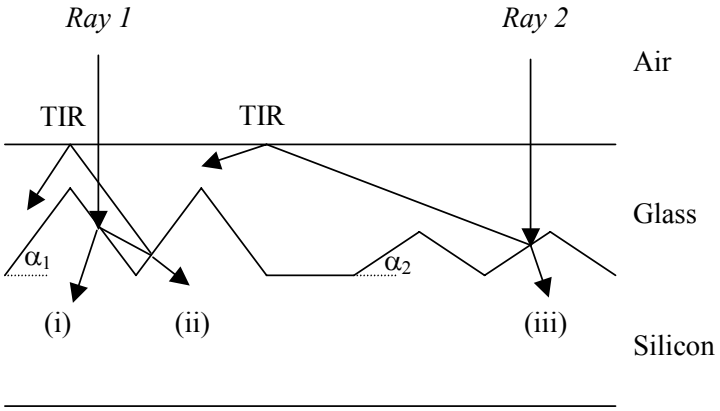

Figure 4.2 *Possible paths for light incident upon the geometrically textured silicon surface shown in Figure 4.1 for the silicon under encapsulation. Light reflected away at 1st or 2nd incidence at (ii) and (iii) (where facet tilt angles α_1 and α_2 > 20.9°) is trapped at the glass-air interface by total internal reflectance (TIR), so that light is re-directed towards the silicon for a 2nd or 3rd chance of absorption.*

Also important in the assessment of textures is their optical performance under encapsulation, as is the situation for the finished silicon solar cells in a module. Figure 4.2 shows how light escaping on initial incidence at the silicon front surface may be confined at the glass-air interface and re-directed towards the silicon for a second chance of incidence, thus reducing front surface reflectance losses. From Snell's laws of refraction (see e.g. [1]), light approaching the glass-air interface at angles greater than the critical angle α_c will receive total internal reflectance (TIR), where $\alpha_c = \arcsin(n_{air}/n_{glass})$, n being the refractive index. Setting $n_{air} = 1$ and $n_{glass} = 1.5$, then α_c for the glass-air interface is 41.8°. Thus whilst facet tilt angles of 30° or more are required for double bounce incidence of light on bare silicon, texture angles of only 20.9° are sufficient for glass encapsulated wafers to confine light reflected away from the silicon at the glass-air boundary (e.g. at (iii) in Figure 4.2). This light will fall re-incident upon the surface for a second chance of incidence whereby reflection reduction is also achieved.

4.1.3 Geometrical surface morphologies for multicrystalline wafers

The surface reflection of periodic geometrical structures is relatively easily explained using basic ray-tracing, as demonstrated in Figures 4.1 & 4.2. The accuracy of ray-tracing depends on how completely the etch surface geometry is quantified. However for unmasked alkaline etched wafers, quantification of the etch surface morphology is more complex. Etch structures are non-periodic, their dimensions are non-uniform, and the homogeneity of the structures varies over the wafer.

For a multicrystalline wafer, i.e. with crystal grains of between 1 mm² and 10 cm² [2], the situation is further complicated. Anisotropic etching will lead to a surface morphology which will vary over the wafer according to the orientation of the crystals present. The shape of the surface texture and correspondingly the reflecting properties per crystal, are dependent upon the angular proximity of the slow etching crystallographic planes with respect to the wafer surface. However, many different crystal orientations are present; indeed the distribution of crystal orientations in multicrystalline Solsix (formerly Baysix) wafers for example has been found to be essentially random, with no preferential orientation being present (see earlier

related work [3] and e.g. [4], [5], [6]). Thus a number of different surface geometries will determine the interaction of incident light with the surface and will contribute to the overall reflectance of the multicrystalline wafer.

4.1.4 Effect of etch composition upon surface texture geometries

Furthermore, the action of the alkaline etch depends strongly upon the composition of the etch used, thereby affecting the effectiveness of texturisation and consequently the level of front surface reflection, as shown for two etch compositions on neighbouring wafers in Figure 4.3.

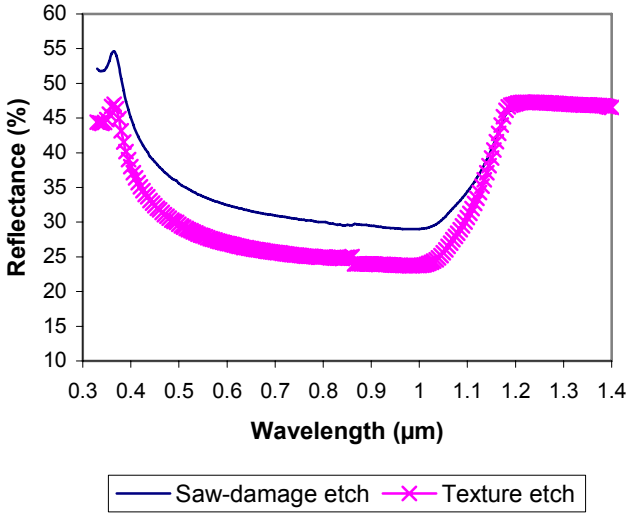

Figure 4.3 *Measured reflectances of saw-damage and texture etched multi-wafers in air.*

Figure 4.3 shows the measured total reflectances of two bare neighbouring multicrystalline wafers (i.e. sawn adjacently from the ingot so that they are essentially identical as-cut), which have received either a saw-damage or a texture etch. The differences between the two measured reflectances suggest a difference in surface morphology between the neighbouring wafers. The two etch compositions apparently attack the silicon surface differently, suggesting that lower facet angles are exposed after the saw-damage etch (due to its relatively high reflectance) than for the texture etch.

In order to explain such differences, the surface geometries must be fully quantified on a per orientation basis for the etch compositions used, and related to the measured reflectances for the multicrystalline wafers. However, perhaps as a consequence of the aforementioned complexities, relatively little attention has been paid to the quantification and optimisation of alkaline etching for multicrystalline wafers. High concentration "saw-damage" etches are employed industrially purely for their high and relatively well controllable etch rates (typically a few tens of micron per minute), and without knowledge or understanding of the resulting optical properties. The high measured reflectance of saw-damage etched wafers in air would initially suggest that such surface textures will not contribute to reflectance reduction, and these surface geometries are generally poorly investigated. Indeed, there has so far been no attempt made in literature (except by these authors, see [3],[7]) to describe these surfaces geometrically for either mono- or multicrystalline wafers.

Low concentration "texture" etches, being optimised for their action on {100} orientations, i.e. pyramidal textures, are rarely investigated for their effect on other crystal orientations. It

is assumed that {111} facets will be exposed exclusively by etching, regardless of the base crystal orientation. This would imply that for "good" texture etching (i.e. under conditions whereby a mono- (100) oriented wafer is completely covered by pyramids), the shape of the etch structures for any crystal will be defined by the positions of the {111} planes closest to the surface orientation [8]. According to this theory, (tilted) pyramid structures will form on (near) (100) orientated crystals. For the extremes of the (111) and (110) crystal orientations, the exposure of {111} etch facets would lead to three sided pyramids and two-dimensional V-shaped grooves (with respective facet tilt angles 70.5 and 35.3° to the surface) respectively. However for the (111), shallower triangular structures or even polished structures may possibly be expected since the surface orientation itself is of course a stable (111) plane. Thus potentially, texture etching would lead to extremes in reflectance over the bare multicrystalline wafer, on varying from pyramidal textures to essentially polished silicon.

However, the validity of this theory has not been tested experimentally for multicrystalline textures. Indeed, the exposure of {111} facets has even been questioned for monocrystalline (100) wafers, with suggestions that the pyramid facets may not be {111} planes but in fact be split into two facets of near {111} orientation [9].

4.1.5 Reflection reduction in air versus light confinement under encapsulation

Until now, the reflection reducing properties of alkaline etched multicrystalline wafers, have usually been quantified by somewhat disappointing values of short circuit current density J_{sc} or efficiency η (for example compared to mono- wafers) of the fully processed solar cells [10,11,12]. As a result, isotropic texturisation methods, such as mechanical grooving or acidic etching, have received more attention in recent years. However, the measured electrical output parameters of the complete cell can only give an indication of the optical properties of the resulting from texturisation, since other processing parameters (such as emitter quality etc.) and material qualities will also contribute to these values. Also, where unencapsulated wafers are used for assessment of reflection reduction (e.g. [10]) results do not indicate the possible benefits attainable through light confinement at the glass-air interface on encapsulation as in the module. The number of surface textures yielding multiple reflectance could be greatly increased under encapsulation. In the light of the random distribution of wafer orientations in the silicon, a potentially far larger proportion of crystals will have etch facets allowing reflectance reduction through light confinement on encapsulation, than will give multiple incidence of light in air.

4.1.6 Reflectance reduction in alkaline etched multicrystalline silicon

In this chapter, it is aimed to establish experimentally whether alkaline etching methods can provide levels of reflection reduction approaching those of pyramidally textured monocrystalline (100) silicon. Investigations concentrate purely upon the reflection reduction achieved due to the physical geometry of the etch surface, without the aid of an anti-reflection coating, and in particular by exploiting the benefits of light confinement under encapsulation. To determine this, the etch surface morphology for multicrystalline wafers are quantified using existing and specially developed techniques and related to the measured reflectances. A secondary aim is to investigate and test the validity of the accepted texture etch theory.

4.2 Experimental

4.2.1 Wafers used in experimentation

Monocrystalline wafers of 7 different orientations (see Figure 4.4d) as well as neighbouring multicrystalline Bayer wafers are used in experimentation. The orientations of the monocrystalline wafers are distributed evenly over the triangle joining the (normals to the) principal (100), (110) and (111) crystallographic planes. Figure 4.4 below shows the wafer orientations represented spatially in a spherical polar co-ordinate system by the tilt (Θ) and azimuth (Φ) angles of their surface normals. Angles in this co-ordinate system are described with respect to the surface normal to the (100) plane, with co-ordinates $(\Theta,\Phi) = (0,0)$.

The orientations contained within the principal triangle can be used to represent all the different possible crystal orientations present within a multicrystalline wafer. This includes all related planes (for example, the (110) orientation also represents (011), (101), (-110) etc. from the {110} set of planes), since their crystallography and resulting etch surface textures are analogous.

4.2.2 Sample preparation

The mono-wafers were initially polished/lapped; the surfaces were therefore sandblasted with Al_2O_3 powder followed by thorough rinsing and cleaning step to give a starting surface equivalent to the as-cut multicrystalline wafers.

Wafers were cut to 30 x 30 mm² and were given either a low concentration texture etch, or a high concentration saw-damage etch in NaOH. Mono- and multicrystalline wafers were etched together, so that both had received precisely the same etch treatments for comparison. The etch times used were chosen to correspond with a total etch depth of 25 μm by weight on the as-cut multicrystalline silicon, for both the saw-damage and the texture etch. For the effects of encapsulation upon the reflecting properties, wafers were encapsulated in the order of glass-EVA-silicon-EVA-white backing foil. The glass at the front surface is 1 mm thick window glass, and the white backing foil is from ICOSOLAR, no. 2116.

4.2.3 Experimental techniques

In all cases the resulting etch surface morphologies were observed by optical or scanning electron (SEM) microscopy, and total hemispherical reflectance measurements were performed using an integrating sphere and spectroradiometer set-up. In addition, for the quantification of the etch surface geometries, the specially developed experimental methods using Atomic Force Microscopy (AFM facet transforms), localised laser reflectance patterns and Laue photography as described in Chapter 2 were employed.

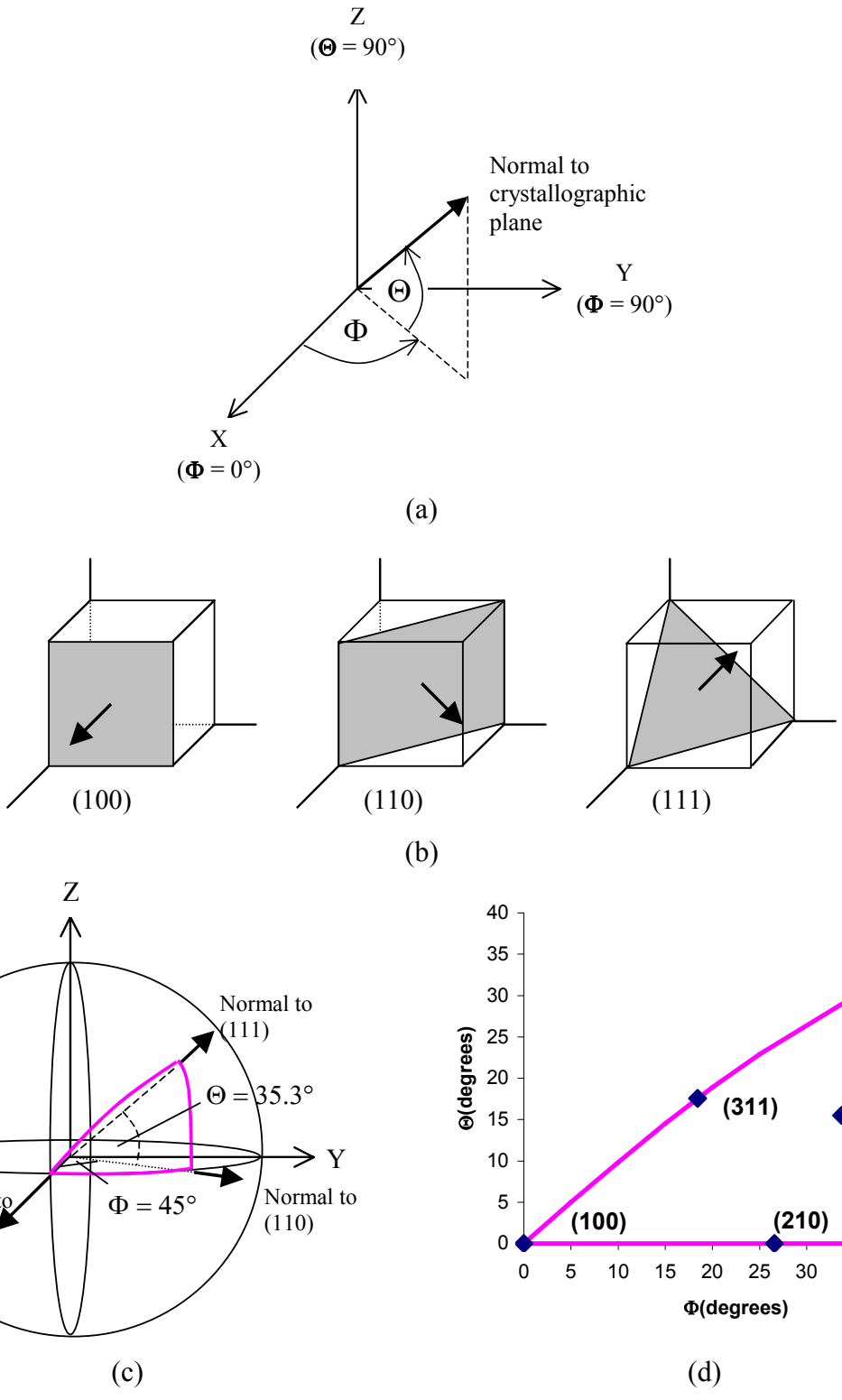

Figure 4.4 *(a) The polar co-ordinate system defining wafer and crystal orientations. (b) The positions of the principal (100), (110) & (111) crystallographic planes with respect to the co-ordinate system, with arrow representing surface normals. (c) The position of the triangle of principal orientations. This is represented by joining between the points of intersection of the surface normals to the (100), (110) & (111) with a sphere centred at the origin of the polar co-ordinate system. (d) 2D representation of the principal triangle of orientations in (c) showing the positions of the 7 monocrystalline orientations used in experimentation.*

4.2.4 Co-ordinate system used for the quantification of the etch surface morphology

The surface morphology of the alkaline etched wafers is quantified using a spherical polar co-ordinate system, as was the case for describing the relationship between different wafer or crystal orientations. However in this case, the tilt (θ) and azimuth (ϕ) angles refer to the positions of the normals to a particular facet of the textured surface exposed by the etch. These angles are measured relative to a particular crystal or wafer orientation, whose surface is parallel to the XY plane in the co-ordinate system and whose surface normal is parallel to the Z axis (see Figure 4.5). The positions of the etch facets formed on a particular crystal or wafer orientation are thus described in terms of their angles θ and ϕ with respect to the base orientation.

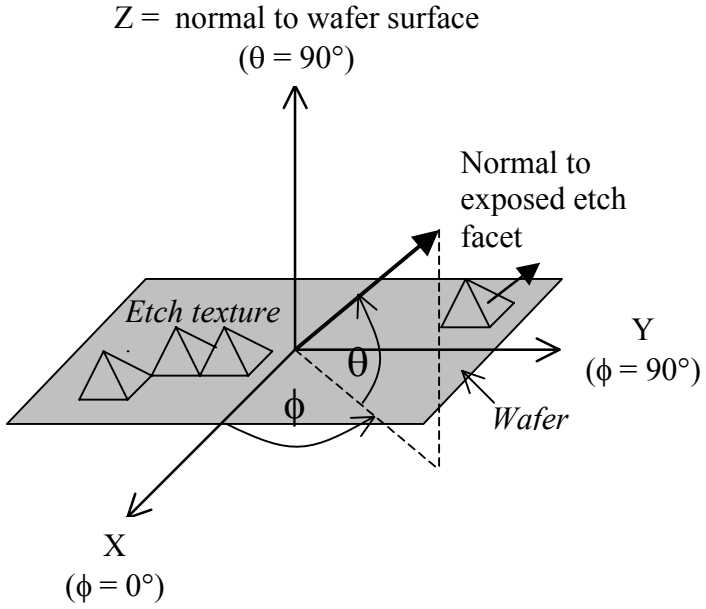

Figure 4.5 *The polar co-ordinate system defining the positions of exposed etch facets in geometrical alkaline etch structures, with respect to the base wafer or crystal orientation.*

4.2.5 Modelling of texture etched surfaces using ray-tracing program "Sunrays"

Theoretical surface morphologies and reflectances, whereby the etch surface is composed exclusively of {111} facets, could be modelled on a per orientation basis using the ray-tracing program "Sunrays" [13,14]. This program calculates the optical properties of geometrically textured silicon cell structures, these textures being described in terms of a geometrically defined unit cell structure. Theoretical texture etch geometries are described geometrically for a particular base wafer orientation using the matrix transformation described in [15]. Modelling with "Sunrays" leads to an idealized view of the texture etched surface, since only texture features of identical size can be modelled, with no flat areas between these features.

4.3 Results

4.3.1 Saw-damage etching

4.3.1.1 Surface morphology

Figures 4.6 and 4.7 show the saw-damage etched surfaces for the seven representative orientations from SEM and AFM microscopy. The surface morphologies of the saw-damage etched wafers are generally relatively flat, in terms of their optical reflective properties in air. The majority of exposed etch facets have surface normals with tilt angles of less than 30°. i.e. lower than is required for even minimal double bounce incidence of light (see Table 4.1). This flatness arises due to the large number of crystallographic planes which are stable to the etch, these being predominantly the {100}, {111}, {110}, {311} & {211} sets of planes, as found in investigations with Laue photography/scatter patterns. With so many planes being stable to the etch, the angle of intersection of a stable plane to any miscellaneous base orientation is relatively low, resulting in generally flat but nevertheless often complex geometrical structures.

The {100} and {111} planes are particularly stable to the etch. This is exhibited on etching the (100) and (111) wafer orientations, since they etch down towards the base orientations giving particularly flat etch surface morphologies. Correspondingly, their AFM facet transforms show that facets are angled normally to the wafer surface, and laser light is reflected back upon itself yielding a distinct reflectance spot centred around the wafer surface normal. {111} planes are exposed as polygonal stepped crater-like etch pits of several tens of microns in dimension, with steps expanding out from the pit centres. In contrast, the square shaped plateaus of {100} planes are smooth, with no steps visible. Both {100} and/or {111} planes are found exposed on all the wafer orientations to a greater or lesser extent.

Crystals oriented away from the {100} and {111} yield more complex etch surfaces, with structures composed from several of the stable etch facets, as is summarised in Table 4.1. The exposed facets are not always distinct, with some facets merging into others (in particular, neighbouring {211} and {311} facets which are separated spatially by a tilt angle of only 10°) or being somewhat rounded or even broken up whereby facet normals are spread up to several degrees around the central exposed facet normal.

The most complex etch structures are found on the (110) wafer orientation, which has etch facets exposed in no less than 7 directions. The majority of facet normals are oriented within a very diffuse spot (±20°) centred around the normal to the wafer surface. However, the remaining facets have tilt angles around 30° or more. Limited double bounce reflectance is possible between azimuthally opposite (100) and (010) exposed etch facet pairs, which have tilt angles of 45°. This leads to the slightly lower reflectance of the bare (110) wafer with respect to the other saw-damage etched wafer orientations.

Figure 4.6 *SEM micrographs of surface morphologies for saw-damage etched wafers as viewed (a) from above and (b) in cross-section.*

(100) orientation

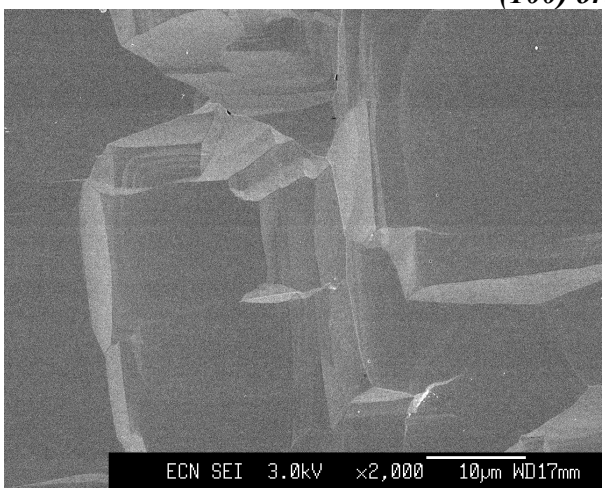

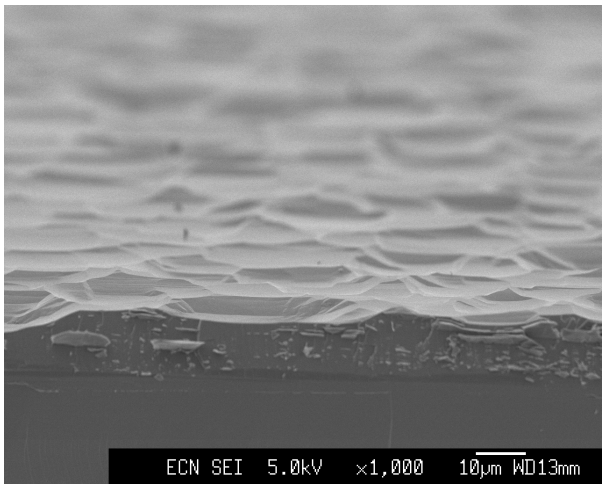

(311) orientation

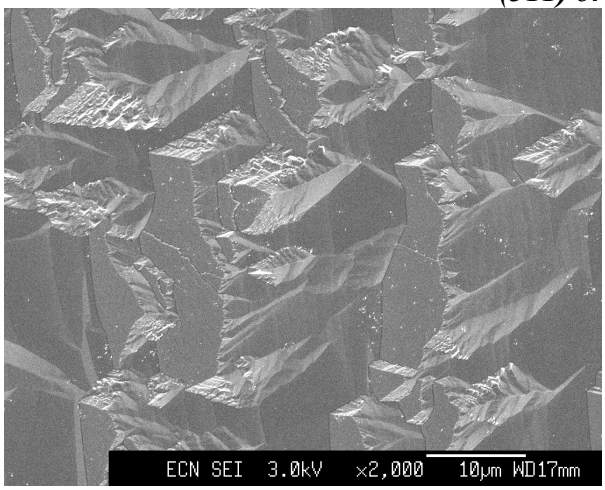

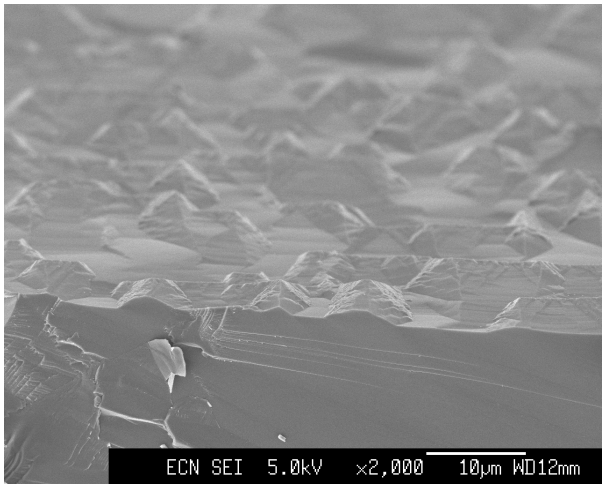

(210) orientation

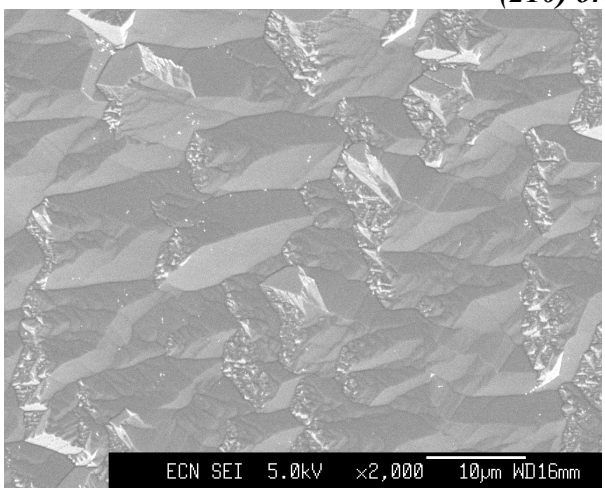

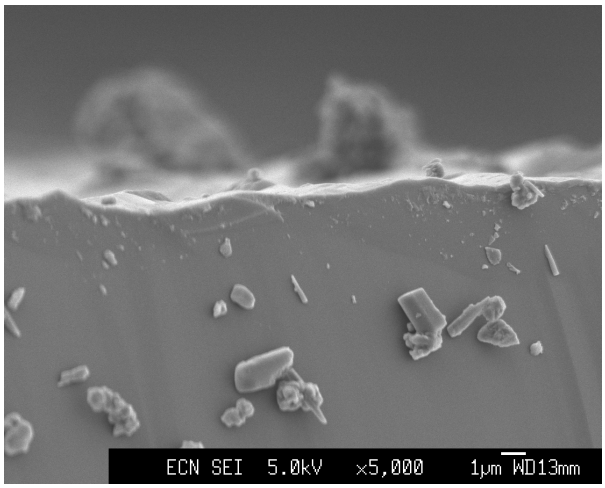

(a) ***(b)***

Figure 4.6 (cont.) *SEM micrographs of surface morphologies for saw-damage etched wafers as viewed (a) from above and (b) in cross-section.*

(321) orientation

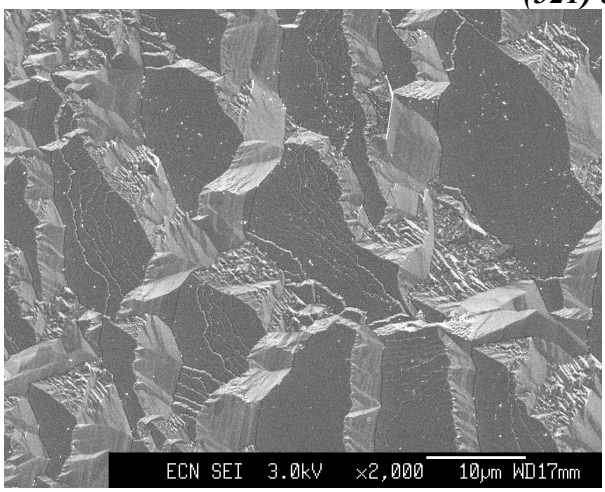

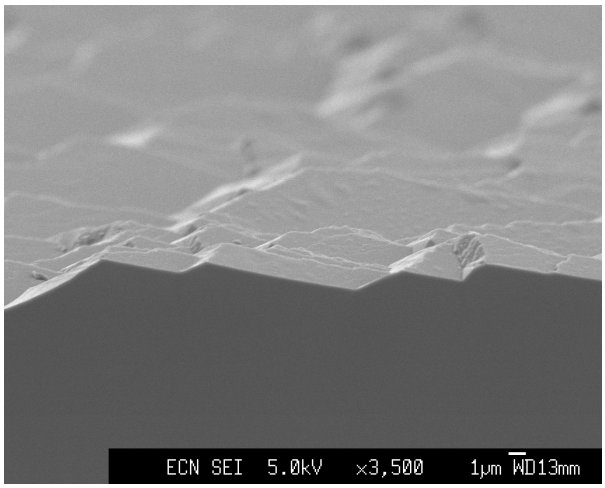

(110) orientation

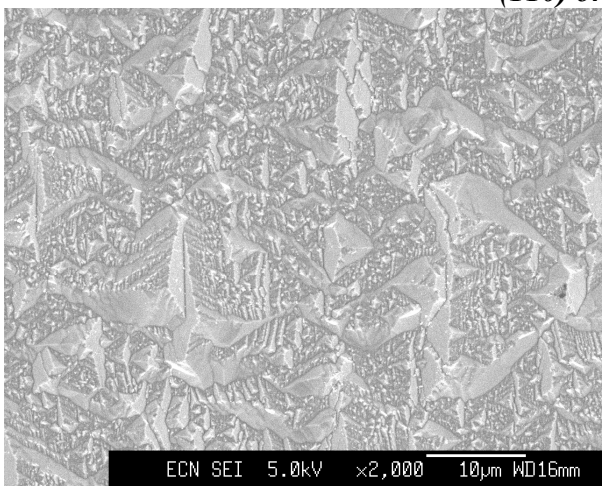

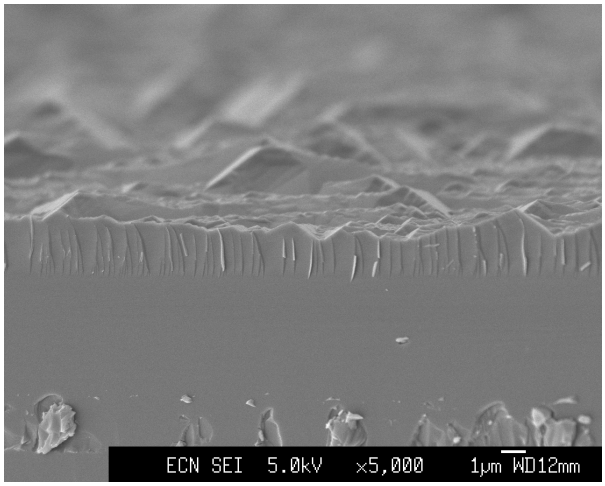

(221) orientation

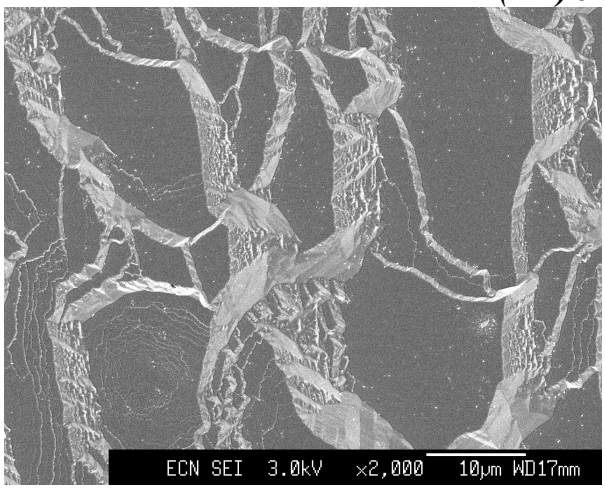

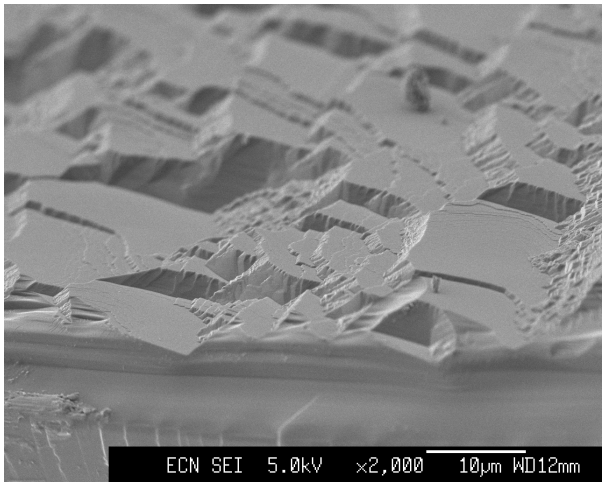

(a) ***(b)***

Figure 4.6 (cont.) *SEM micrographs of surface morphologies for saw-damage etched wafers as viewed (a) from above and (b) in cross-section.*

(111) orientation

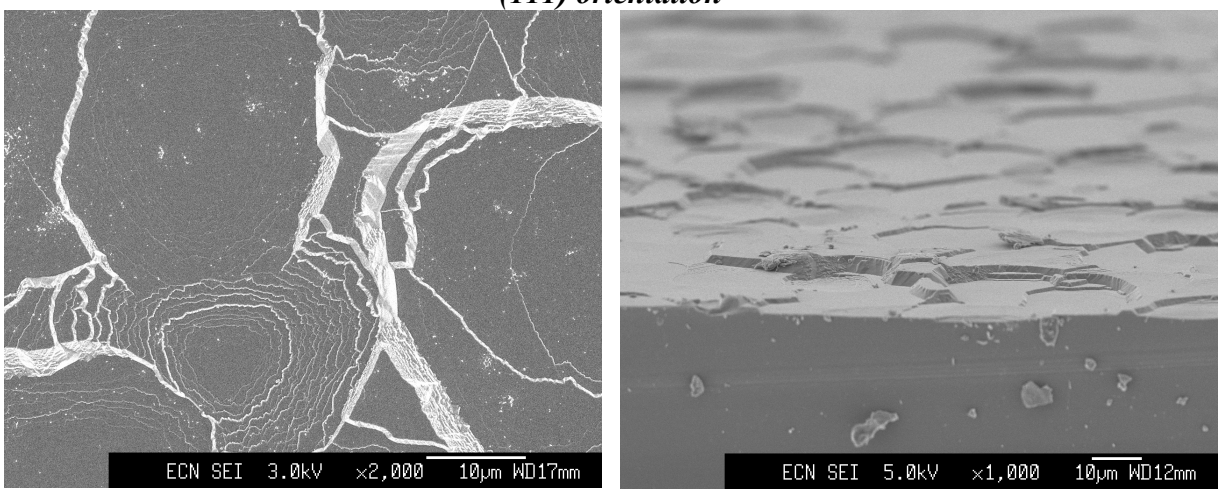

(a) ***(b)***

Figure 4.7 *(a) AFM height mappings of saw-damage etch surface morphologies as viewed from above. The adjacent height scale applies for all the AFM scans shown. (b) Resulting AFM facet transforms of saw-damage etched wafers. ● = position of etch facet as calculated from theory[1].*

(100) orientation

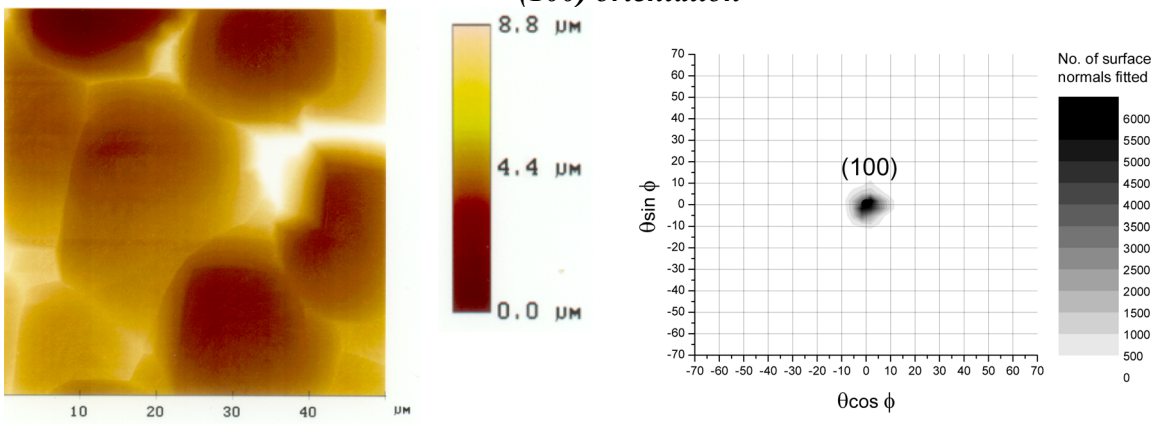

(a) ***(b)***

[1] *Facet angles are calculated from the x,y co-ordinates of the axes of the facet transforms by solving the simultaneous equations* $x = \theta \cos\phi$, $y = \theta \sin\phi$.

Figure 4.7 (cont.) *(a) AFM height mappings of saw-damage etch surface morphologies as viewed from above and (b) resulting AFM facet transforms of saw-damage etched wafers. ● = position of etch facet as calculated from theory*[1].

(311) orientation

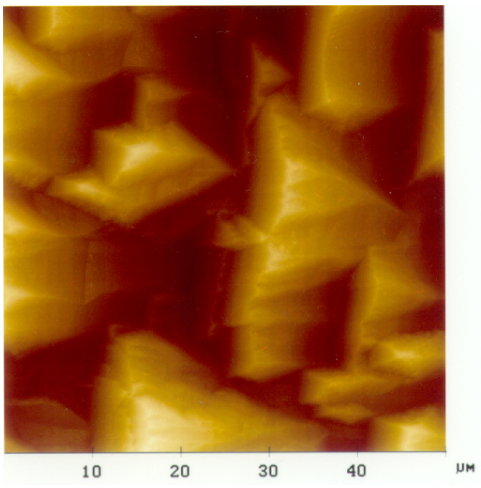

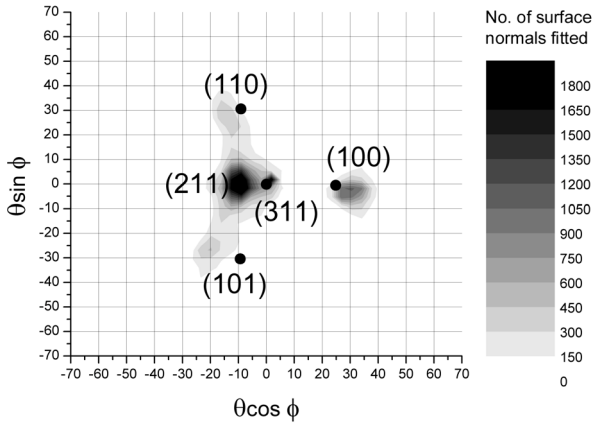

(210) orientation

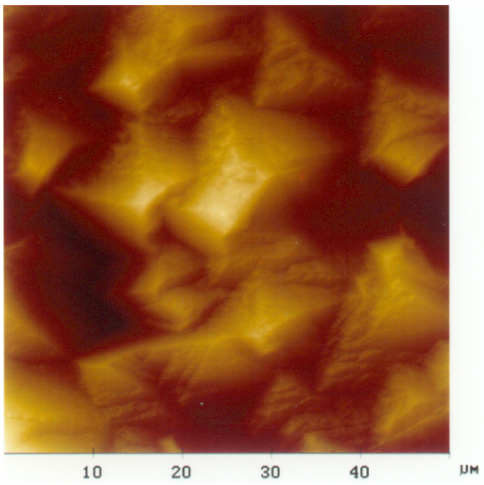

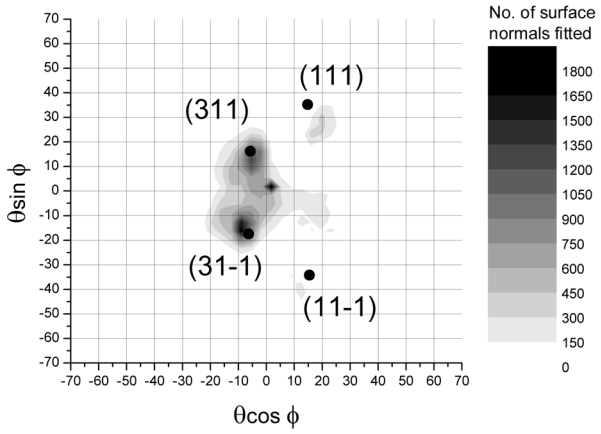

(321) orientation

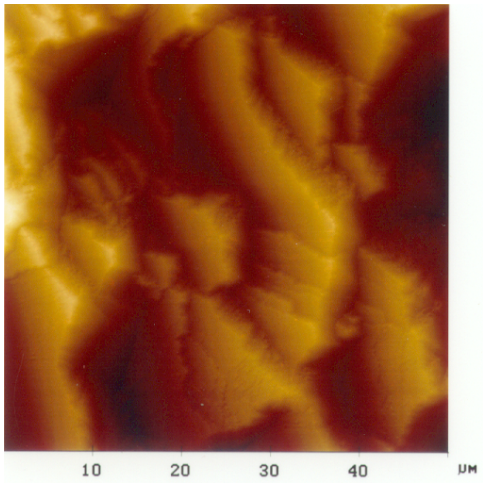

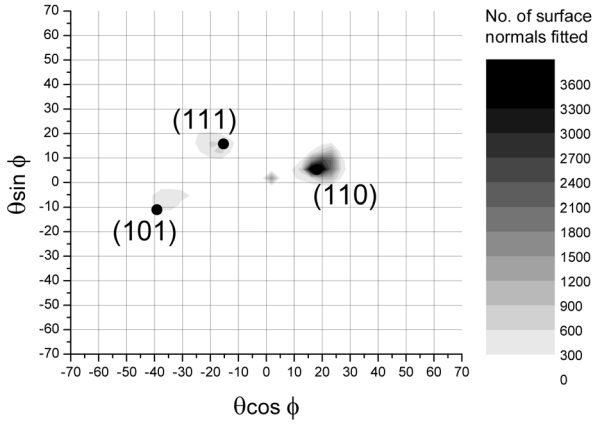

(a) ***(b)***

[1] *Facet angles are calculated from the x,y co-ordinates of the axes of the facet transforms by solving the simultaneous equations* $x = \theta\cos\phi$, $y = \theta\sin\phi$.

Figure 4.7 (cont) *(a) AFM height mappings of saw-damage etch surface morphologies as viewed from above and (b) resulting AFM facet transforms of saw-damage etched wafers. ● = position of etch facet as calculated from theory*[1].

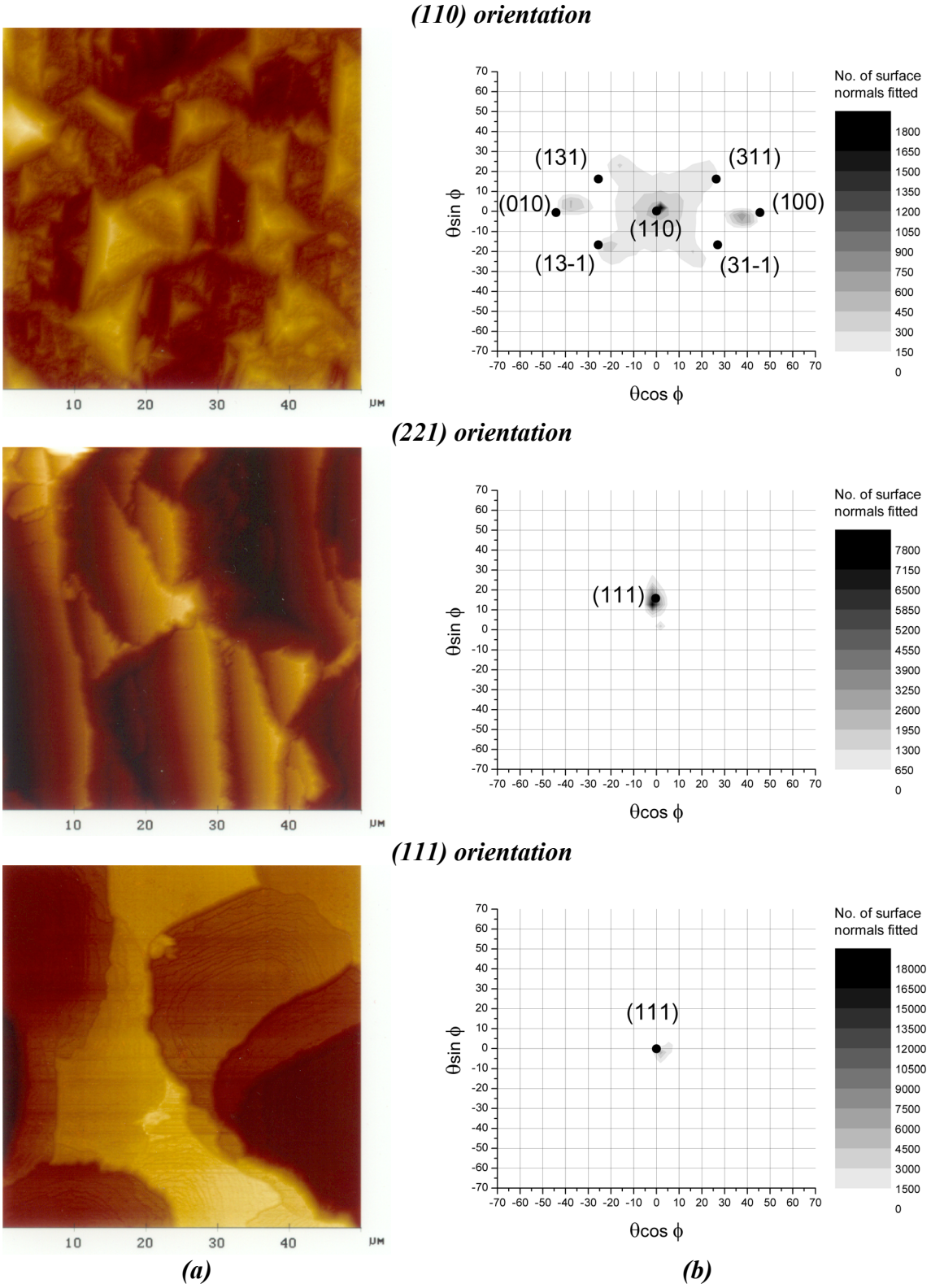

[1] *Facet angles are calculated from the x,y co-ordinates of the axes of the facet transforms by solving the simultaneous equations* $x = \theta\cos\phi$, $y = \theta\sin\phi$.

Orientations in terms of Miller indices		Facet angles (°) as measured *(calculated)*		Multiple incidence (Y/N/P) due to facet tilt angle θ as measured *(calculated)*	
Wafer	Etch facet	Tilt θ	Azimuth ϕ	In air	Encapsulated
(100)	(100)	1.5 *(0.0)*	0.0 *(0.0)*	N *(N)*	N *(N)*
(311)	(211)	10.0 *(10.0)*	180.0 *(180.0)*	N *(N)*	N *(N)*
	(100)	30.1 *(25.2)*	-3.8 *(-0.0)*	P *(N)*	Y *(Y)*
	(311)	0.0 *(0.0)*	0.0 *(0.0)*	N *(N)*	N *(N)*
	(110)	31.8 *(31.5)*	118.2 *(106.8)*	P *(P)*	Y *(Y)*
	(101)	26.9 *(31.5)*	-116.9 *(-106.8)*	N *(P)*	Y *(Y)*
(210)	(311)	14.1 *(19.3)*	112.9 *(114.1)*	N *(N)*	N *(N)*
	(31-1)	18.4 *(19.3)*	-119.4 *(-114.1)*	N *(N)*	N *(N)*
	(111)	31.6 *(39.2)*	53.0 *(65.9)*	P *(P)*	Y *(Y)*
	(11-1)	42.4 *(39.2)*	-72.9 *(-65.9)*	P *(P)*	Y *(Y)*
(321)	(110)	19.0 *(19.1)*	15.0 *(15.0)*	N *(N)*	N *(N)*
	(111)	23.4 *(22.2)*	129.8 *(133.1)*	N *(N)*	Y *(Y)*
	(101)	36.5 *(40.9)*	-170.5 *(-165.0)*	P *(P)*	Y *(Y)*
(110)	(110)	0.0 *(0.0)*	0.0 *(0.0)*	N *(N)*	N *(N)*
	(100)	37.8 *(45.0)*	-4.6 *(-0.0)*	P *(Y)*	Y *(Y)*
	(010)	38.2 *(45.0)*	174.0 *(180.0)*	P *(Y)*	Y *(Y)*
	(311)	26.4 *(31.5)*	40.7 *(35.3)*	N *(P)*	Y *(Y)*
	(31-1)	25.6 *(31.5)*	-51.3 *(-35.3)*	N *(P)*	Y *(Y)*
	(131)	27.3 *(31.5)*	144.3 *(144.7)*	N *(P)*	Y *(Y)*
	(13-1)	28.3 *(31.5)*	-138.7 *(-144.7)*	N *(P)*	Y *(Y)*
(221)	(111)	13.1 *(15.8)*	0.0 *(0.0)*	N *(N)*	N *(N)*
(111)	(111)	1.5 *(0.0)*	0.0 *(0.0)*	N *(N)*	N *(N)*

Table 4.1 *Quantification of the surface morphology for saw-damage etched wafers, in terms of Miller indices, tilt and azimuth angles of the exposed etch facets, and optical properties in terms of the probability of multiple incidence of light. Y = yes, N = no and P = possible correspond respectively with (i) guaranteed multiple incidence (tilt angles $\theta > 45°$ in air or $\theta > 20.9°$ under encapsulation), (ii) possible multiple incidence of light ($30° < \theta < 45°$ in air) and (iii) no multiple incidence ($\theta < 30°$ in air or $\theta < 20.9°$ under encapsulation).*

4.3.1.2 Reflectance measurements of bare saw-damage etch textures

The texturisation varies widely depending upon the orientation of the particular crystal, as seen from the SEM/AFM photographs in Figures 4.6 & 4.7 and discussed above. Consequently in Figure 4.8, it can be seen that there are also differences between the individual reflectances of the 7 representative wafer orientations. The reflectances lie between 0-4% lower than that for the polished silicon, with the (100) and (110) being the highest and lowest reflecting orientations respectively. For the lower reflecting orientations this indicates that a low level of re-entry of light is present, although generally the majority of facet tilt angles are too low for double bounce reflectance in air. The reflectances at wavelengths above 1.2 µm (i.e. where the silicon is fully transmitting so that the rear surface reflectance is visible in the measured total reflectance) also give an initial indication of the variation in facet tilt angles between the textures. These vary by approximately 7% for the monocrystalline wafers suggesting that significant levels of (internal) light scattering occur for some textures. This point will be further discussed in Chapter 5. (The peak in reflectance at $\lambda = 0.36$ µm corresponds with the position of the direct bandgap of silicon at 3.4 eV.)

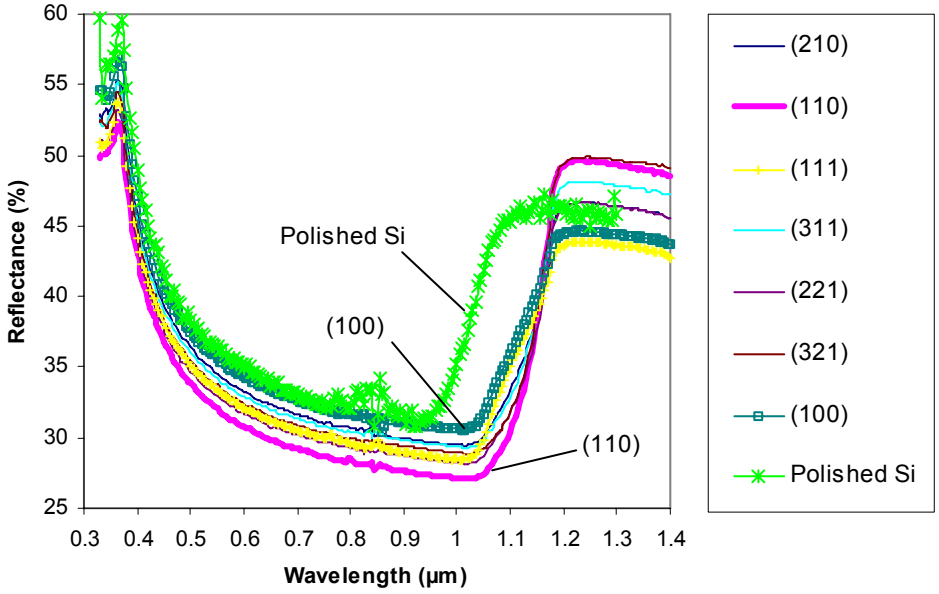

Figure 4.8 *Reflectances for the saw-damage etched monocrystalline wafers (starting thickness ~ 525 µm) and a double polished 100 µm thick silicon wafer. The order of front surface reflectance for the 7 orientations is* $R_{100}>R_{210}>R_{311}>R_{321}>R_{111}>R_{221}>R_{110}$.

As discussed previously, the dominant etch facets exposed for all the crystal orientations (represented in the AFM facet transforms in Figure 4.7 by the "spots" or "facet clusters" with the highest density of surface normals) have tilt angles less than the 30° required for initial double bounce reflectances (see also Table 4.1). This explains the high total reflectances approaching those of polished silicon, as measured for the individual wafer/crystal orientations. Where facets have tilt angles above 30° relative to the wafer surface, there are generally no azimuthally opposing facets with high enough tilt angles onto which the light can be reflected for second incidence (except for near (110) oriented crystals). Thus light is still reflected away from the silicon after its first point of incidence and reflectance remains high.

In summary, the bare saw-damage etched wafers have reflectances in air equivalent to polished silicon. This is because the tilt angles of the dominant etch facets exposed are lower than the 30° required for double bounce reflection.

4.3.1.3 Reflectances of saw-damage etched wafers under encapsulation

In comparison with the case of the bare wafers, where reflectances over the seven orientations lay within 4% of each other, there is a larger spread in reflectances of 7% for these wafers under encapsulation (see Figure 4.9). The reflectances of the different orientations are separated into three groups, with the (100), (210) and (111) having the highest reflectances, the second group including the (311) and (221) having intermediate reflectance, and the third group including (110) and (321) having the lowest reflectances.

Considering the first group, reflectances are almost identical for the (100), (210) and (111) orientation below a wavelength λ = 1 µm, lying approximately 1-2% lower than for the polished silicon under encapsulation. This emphasizes the flatness of these particular textures, with most of the incident light reflected back normally to escape out through the glass encapsulation. Only the (210) has a lower reflectance above λ = 1 µm, indicating the effect of the greater faceting of the etch surface (with two clusters of opposing facets at 16° to the normal, Table 4.1) compared to the particularly flat (100) & (111). Although this facet angle is too low for light confinement at the glass encapsulant by total internal reflectance (minimal facet angle = 20.9°), the difference in reflectance at higher wavelengths suggests that this roughness may have an eventual effect on light trapping. This point will be discussed in Chapter 5.

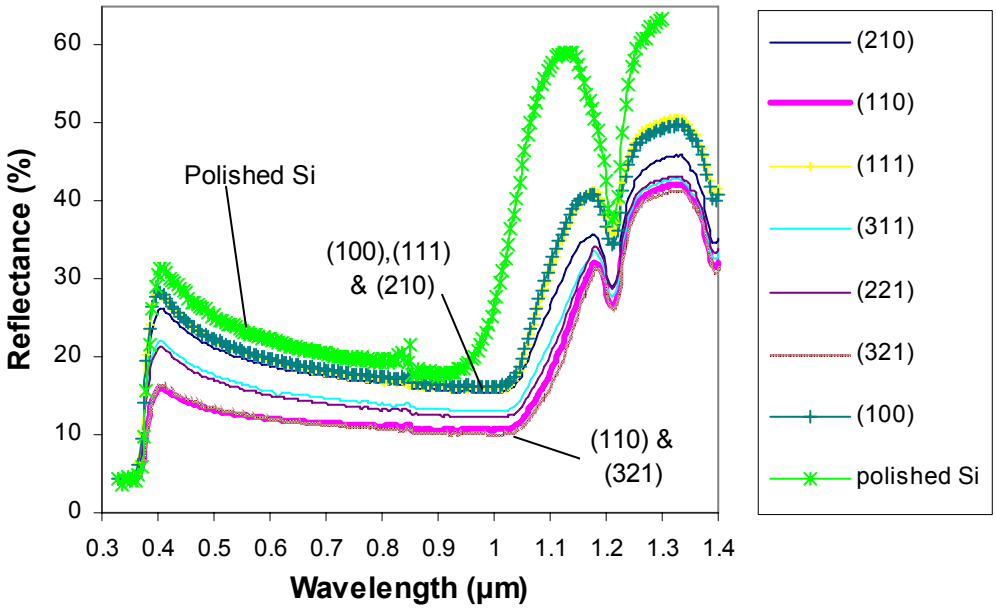

Figure 4.9 *Encapsulated reflectances for saw-damage etched monocrystalline wafers (as-cut starting thickness ~525 µm) and a double polished 100 µm wafer. The drop in reflectances around λ = 1 µm and also for λ < 0.4 µm results from absorption in the EVA encapsulation.*

For the (311) and (221) wafer orientations, reflectance is approximately 6% lower than the polished silicon case. This is caused by the higher facet angles of the texture, whereby in both cases facets exist with tilt angles greater than the 20.9° required for total internal reflectance at the glass-air interface. In the case of the (311), three of the four exposed etch facets have facet angles high enough to allow the confinement of light within the glass. However, the most prominent facet present, the (211), at only 10° to the surface normal, will

reflect equivalently to polished silicon, so that the reflectance is not reduced further than shown. For the (221) wafer orientation, the exposed facets have surface normals spread around the (111) oriented etch facet. Since some facets are thereby angled above 20.9°, some light is confined at the glass-air interface leading to limited reflectance reduction.

The (110) and (321) wafer orientations have such a high level of faceting that a large proportion of the incident light is confined at the glass surface, resulting in the lowest reflectances for the 7 orientations. For the (110) wafer orientation, six of the seven etch facets exposed have tilt angles permitting total internal reflectance as well as double bounce reflectances, but unfortunately, reflectance reduction is restricted by the large proportion of facets angled normally to the base orientation. Similarly for the (321) orientation, the facets all have theoretical orientations large enough to give total internal reflection at the glass-air interface. However, since facet normals around the exposed (111) facet are spread by approximately ± 10° around the measured angle of 23.4° for this latter wafer orientation (see Figure 4.7), a proportion of the etch surface is tilted below the critical angle for light confinement.

In summary, the number of crystals experiencing multiple entry of light is significantly increased for the saw-damaged etched wafers on encapsulation, compared to the bare silicon. This is because many exposed etch facets have tilt angles high enough for light confinement by total internal reflectance at the glass-air interface (i.e. > 20.9°), but too low for even minimum multiple bounce incidence in air (i.e. < 30°).

4.3.2 Texture etching

4.3.2.1 Surface morphology

Figures 4.10 and 4.11 show the texture etched surfaces for the seven representative orientations from SEM and AFM microscopy. Whilst for the saw-damage etch, all wafer orientations commonly exhibited relatively flat surface textures, large variations in roughness exist between the roughest and flattest texture etch surfaces for the different wafer orientations. AFM facet transforms (Figure 4.11) of the various wafers show that for crystal/wafer orientations oriented closest to the (100) (for example (311), (210) etc), one or more of the (dominant) exposed etch facets have tilt angles large enough for double bounce interactions with light, as summarised in Table 4.2. The remaining orientations yield far flatter textures with tilt angles too low for double bounce reflectance in air. In addition, etch texture features are non-uniform in size and distribution over the wafer surface, and are sometimes separated by non-textured (flat) regions.

Laue-scatter investigations of the wafer surface morphologies show that the set of {111} crystallographic planes is particularly stable to the low concentration alkaline texture etch (see also [7] by the author for further detail). Laser scatter patterns for the majority of texture etched crystal orientations exhibit direct reflectance spots in the direction of one or more exposed {111} etch facets. In the case of the (100) wafer/crystal orientation, four orthogonal laser light spots are observed due to the double bounce reflectances originating from each facet on the pyramidal texture (see also [16]). AFM facet transforms in addition to Laue-scatter investigations confirm the corresponding etch facets to be of {111} orientation, with tilt angles of approximately ± 55°.

Figure 4.10 *SEM micrographs of surface morphologies for texture etched wafers as viewed (a) from above and (b) in cross-section (2000x magnification, scaling line = 13 µm).*

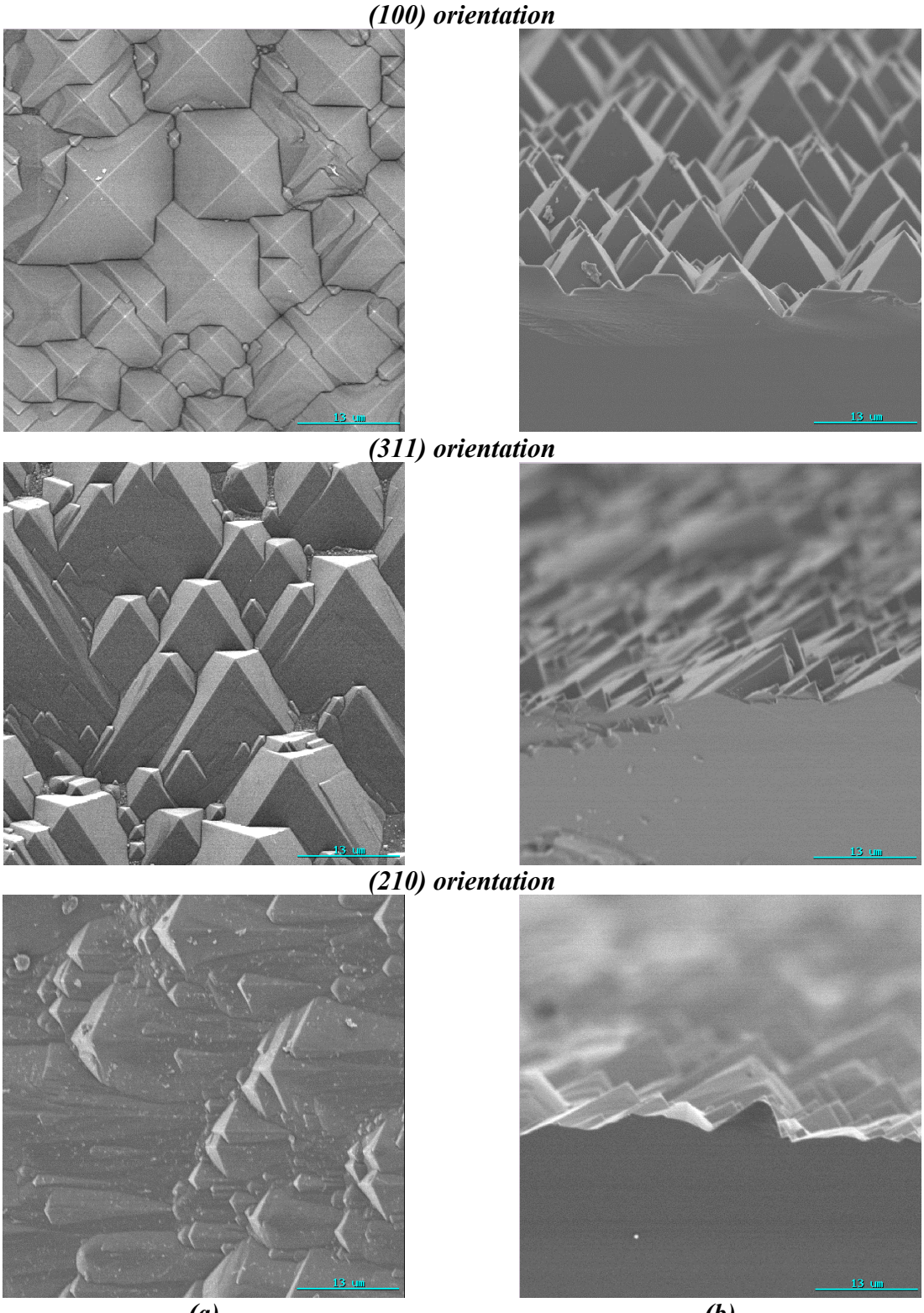

Figure 4.10 (cont.) *SEM micrographs of surface morphologies for texture etched wafers as viewed (a) from above and (b) in cross-section (2000x magnification, scaling line = 13 μm).*

(321) orientation

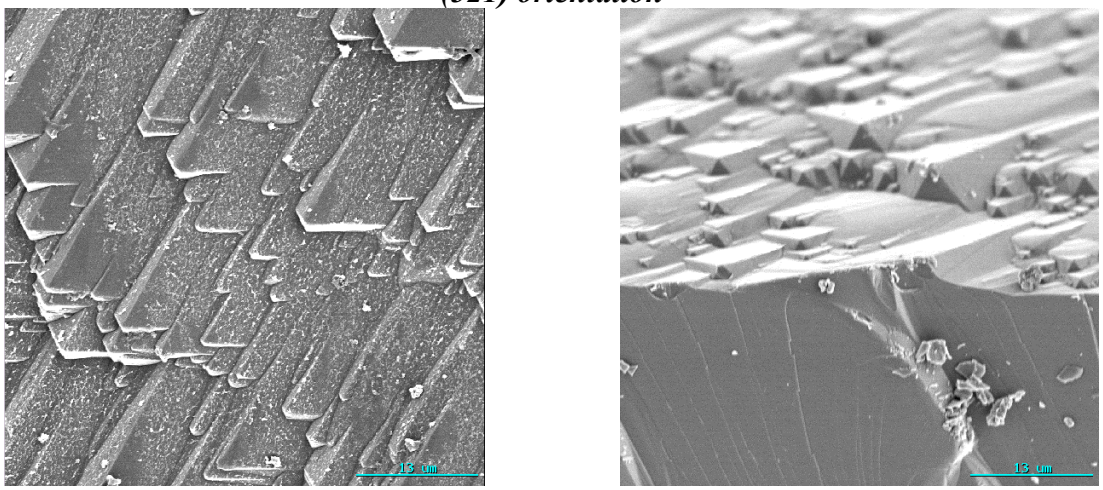

(110) orientation

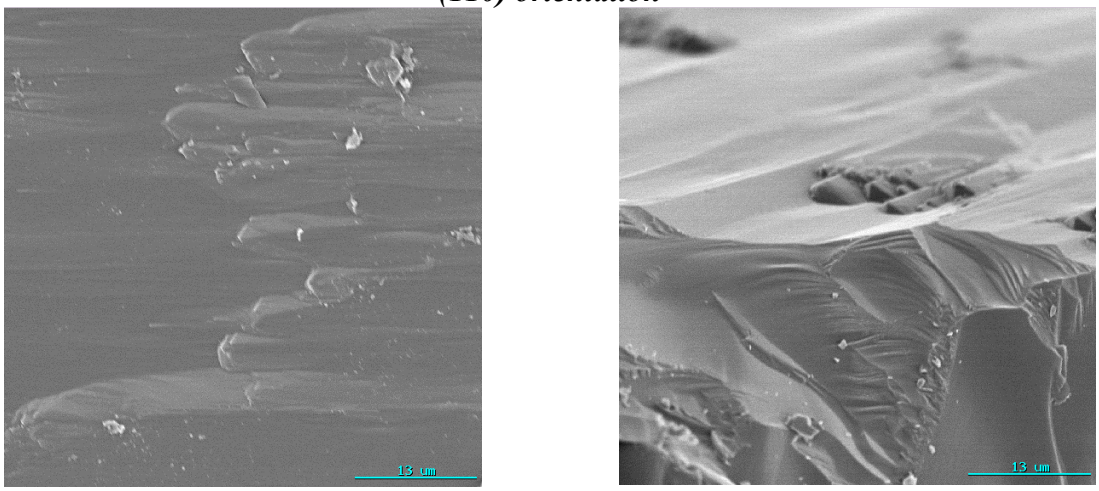

(221) orientation

(a) ***(b)***

Figure 4.10 (cont.) *SEM micrographs of surface morphologies of texture etched wafers as viewed (a) from above and (b) in cross-section (2000x magnification, scaling line = 13 µm).*

(111) orientation

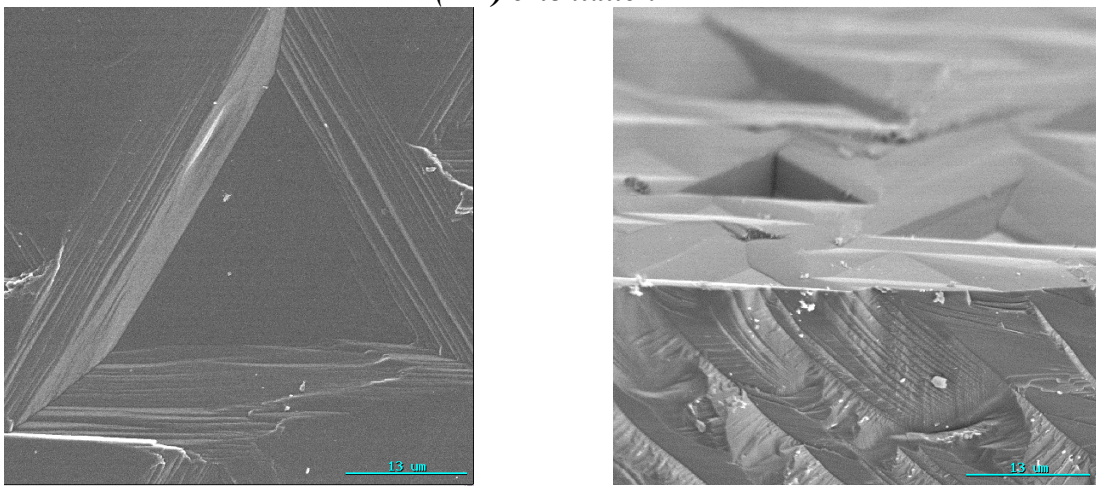

(a) ***(b)***

Figure 4.11 *(a) AFM height mappings of texture etch surface morphologies as viewed from above. The adjacent height scale applies for all the AFM scans shown. (b) Resulting AFM facet transforms of texture etched wafers.*
● = position of etch facet as calculated from theory[2].

(100) orientation

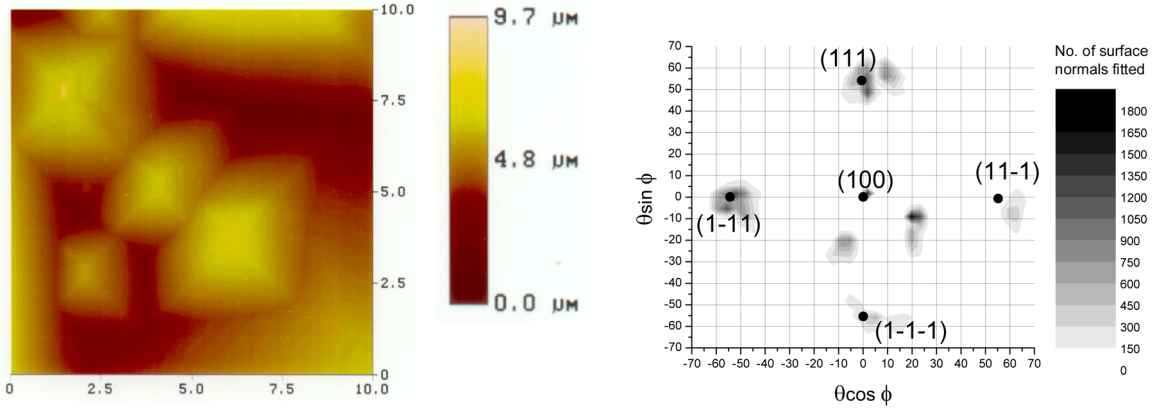

(a) ***(b)***

[2] *Facet angles are calculated from the x,y co-ordinates of the axes of the facet transforms by solving the simultaneous equations $x = \theta\cos\phi$, $y = \theta\sin\phi$. Where an arbitrary {XXY} orientation is exposed, the theoretical position of the closest {111} or other {XXY} orientations is also shown.*

Figure 4.11 (cont.) *(a) AFM height mappings of texture etch surface morphologies as viewed from above and (b) resulting AFM facet transforms of texture etched wafers. ● = position of etch facet as calculated from theory[2].*

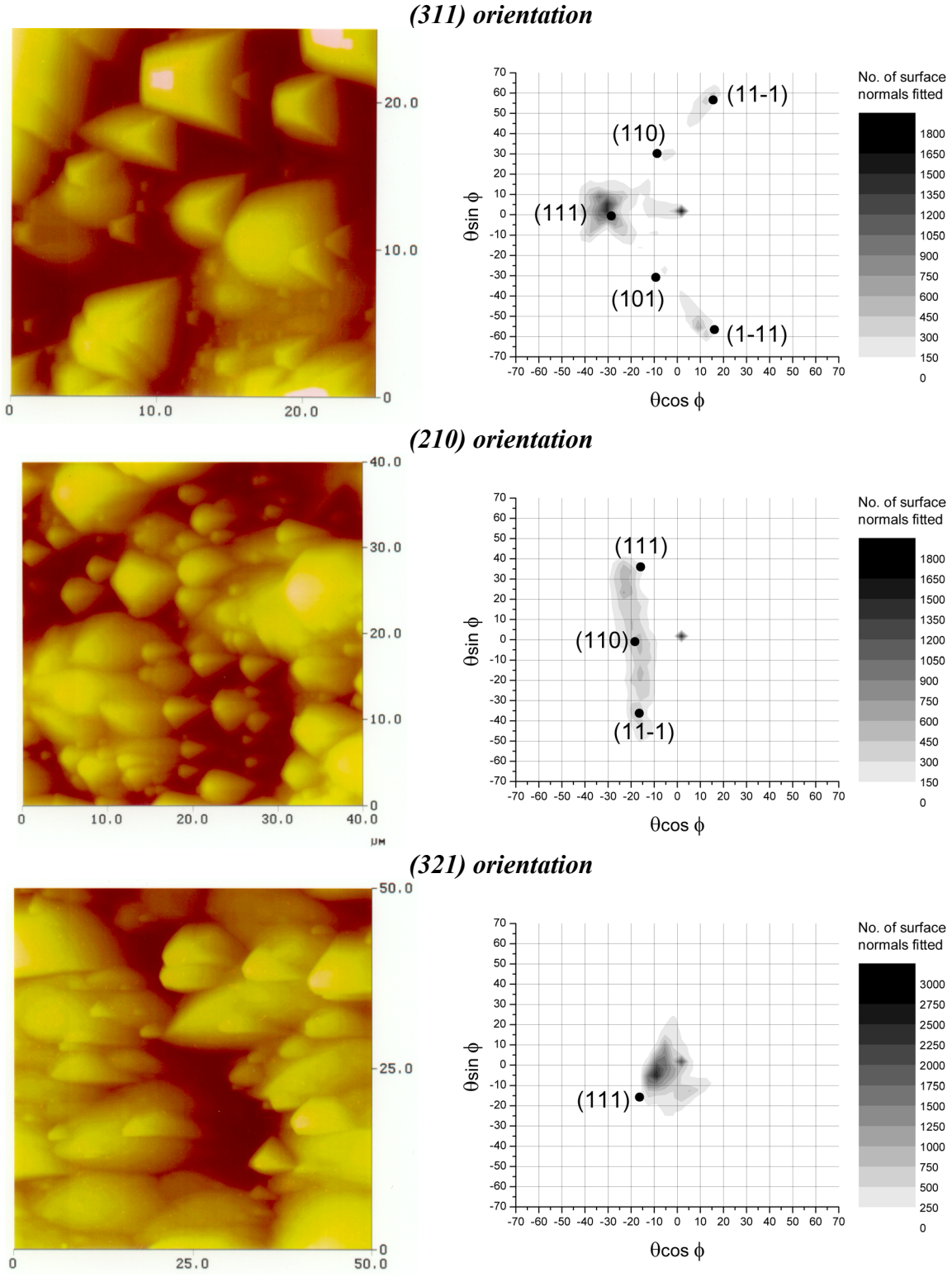

[2] *Facet angles are calculated from the x,y co-ordinates of the axes of the facet transforms by solving the simultaneous equations $x = \theta\cos\phi$, $y = \theta\sin\phi$. Where an arbitrary {XXY} orientation is exposed, the theoretical position of the closest {111} or other {XXY} orientations is also shown.*

Figure 4.11 (cont.) *(a) AFM height mapping of texture etch surface morphologies as viewed from above and (b) resulting AFM facet transforms of texture etch wafers. ● = position of etch facet as calculated from theory[2].*

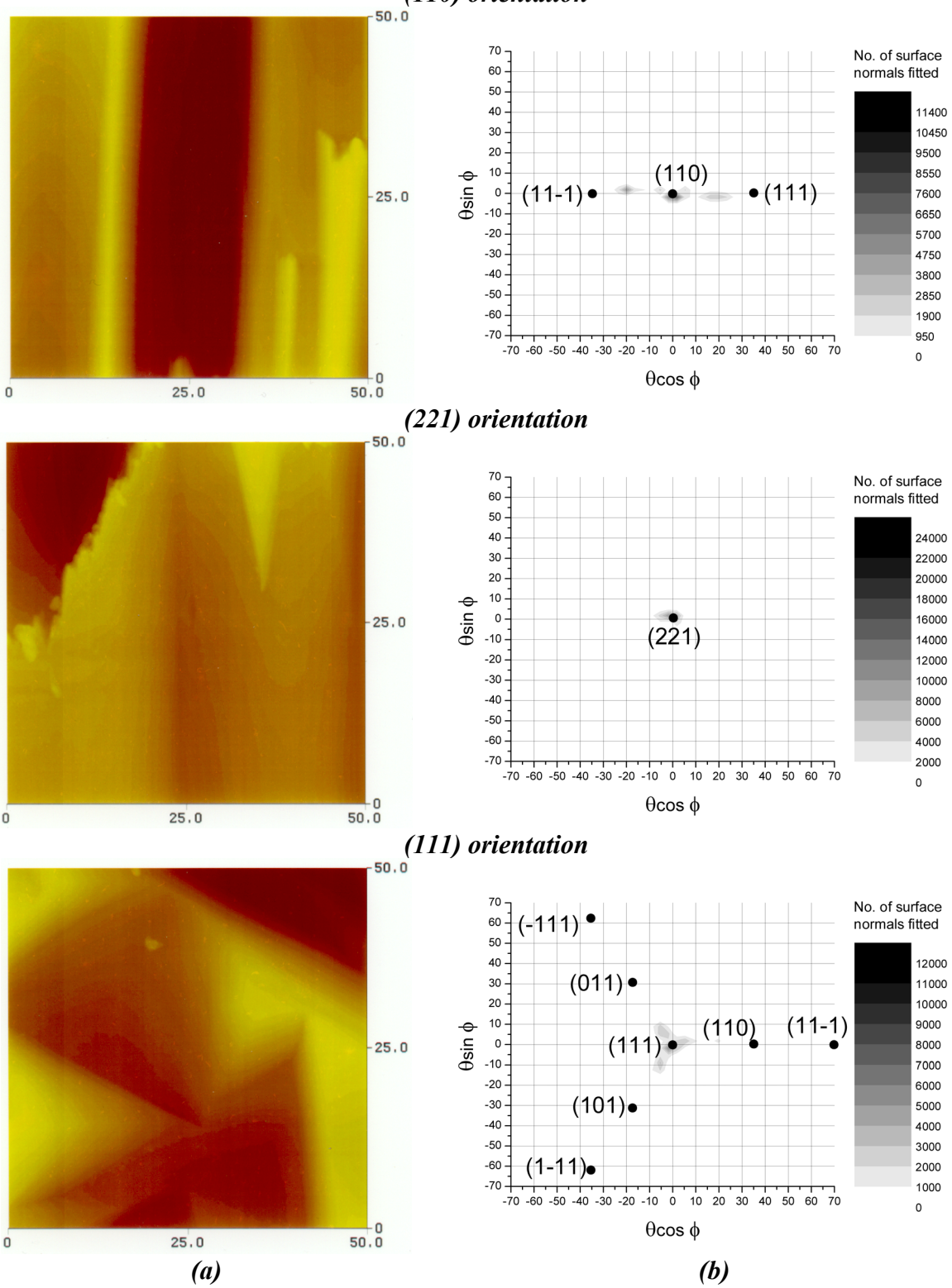

[2] *Facet angles are calculated from the x,y co-ordinates of the axes of the facet transforms by solving the simultaneous equations $x = \theta\cos\phi$, $y = \theta\sin\phi$. Where an arbitrary {XXY} orientation is exposed, the theoretical position of the closest {111} or other {XXY} orientations is also shown.*

Orientations in terms of Miller indices		Facet angles (°) as measured *(calculated)*		Multiple incidence (Y/N/P) due to facet tilt angle θ as measured *(calculated)*	
Wafer	Etch facet[3]	Tilt θ	Azimuth ϕ	In air	Encapsulated
(100)	(111)	57.5 *(54.7)*	95.5 *(90.0)*	Y *(Y)*	Y *(Y)*
	(11-1)	57.5 *(54.7)*	1.9 *(0.0)*	Y *(Y)*	Y *(Y)*
	(1-1-1)	55.5 *(54.7)*	-91.5 *(-90.0)*	Y *(Y)*	Y *(Y)*
	(1-11)	57.4 *(54.7)*	178.5 *(180.0)*	Y *(Y)*	Y *(Y)*
	(100)	5.0 *(0.0)*	0.0 *(0.0)*	N *(N)*	N *(N)*
(311)	(111)	30.6 *(29.5)*	172.5 *(180.0)*	P *(P)*	Y *(Y)*
	(11-1)	58.4 *(58.5)*	77.7 *(73.2)*	Y *(Y)*	Y *(Y)*
	(1-11)	55.8 *(58.5)*	-80.2 *(-73.2)*	Y *(Y)*	Y *(Y)*
	(110)	30.3 *(31.5)*	98.5 *(106.8)*	P *(P)*	Y *(Y)*
	(101)	28.0 *(31.5)*	-101.3 *(-106.8)*	N *(P)*	Y *(Y)*
(210)	From (111)	39.5 *(39.2)*	124.7 *(114.1)*	P *(P)*	Y *(Y)*
	Via (110)	16.7 *(18.4)*	-171.4 *(-180.0)*	N *(N)*	N *(N)*
	To (11-1)	39.1 *(39.2)*	-116.6 *(-114.1)*	P *(P)*	Y *(Y)*
(321)	(111)	11.2 *(22.2)*	-137.0 *(136.9)*	N *(N)*	N *(Y)*
(110)	(110)	0.0 *(0.0)*	0.0 *(0.0)*	N *(N)*	N *(N)*
	(XXY),*(111)*	19.5 *(35.3)*	-5.1 *(0.0)*	N *(N)*	N *(N)*
	(XX-Y),*(11-1)*	20.1 *(35.3)*	176.2 *(180.0)*	N *(N)*	N *(N)*
(221)	(221)	0.0 *(0.0)*	0.0 *(0.0)*	N *(N)*	N *(N)*
(111)	From (111)	0.0 *(0.0)*	0.0 *(0.0)*	N *(N)*	N *(N)*
	To:				
	a) (XXY),*(110), (11-1)*	19.8 *(35.3) (70.5)*	3.8 *(0.0) (0.0)*	N *(N) (Y)*	N *(Y) (Y)*
	b) (XYX),*(101), (1-11)*	16.1 *(35.3) (70.5)*	-120.0 *(-120.0) (-120.0)*	N *(N) (Y)*	N *(Y) (Y)*
	c) (YXX),*(011), (-111)*	11.4 *(35.3) (70.5)*	127.9 *(120.0) (120.0)*	N *(N) (Y)*	N *(Y) (Y)*

Table 4.2 *Quantification of the surface morphology for texture etched wafers, in terms of Miller indices, tilt and azimuth angles of the exposed etch facets, and optical properties in terms of the probability of multiple incidence of light. Y = yes, N = no and P = possible correspond respectively with (i) guaranteed multiple incidence (tilt angles $\theta > 45°$ in air or $\theta > 20.9°$ under encapsulation), (ii) possible multiple incidence of light ($30° < \theta < 45°$ in air) and (iii) no multiple incidence ($\theta < 30°$ in air or $\theta < 20.9°$ under encapsulation).*

[3] *Where facet normals are exposed over a range of orientations as opposed to a distinct crystal plane, the range is described by the most extreme facets exposed (from…to) and/or the most central orientation through which the range passes (…via…). Where an arbitrary {XXY} orientation is exposed, the theoretical position of the closest {111} or other {XXY} orientations is also shown.*

The stability of the {111} planes to the etch is in agreement with the generally accepted texture etch theory. Indeed the shape of the textures on the different wafer orientations, as viewed by SEM microscopy, varies visually from upright pyramids on (100) wafers, to tilted pyramids on "near (100)" wafer orientations (e.g. (311) and (210), angled at 25.2° and 26.6° to the (100) plane), to flat triangular plateaus on the (111) as predicted by Sopori [8] and the matrix transformations described by Campbell [15]. It should however be noted that the exposed {111} facets are not perfect crystallographically. Closer inspection of the (tilted) pyramid morphology reveals that the exposed {111} texture facets may be slightly rounded or even "split", consisting apparently of two facets slightly tilted with respect to one another, in agreement with the observations of [9]. This can be seen for example in the AFM facet transform for the pyramidally textured (100) orientation in Figure 4.11, where the clusters of exposed facets around the individual <111> directions are seen to be split into two groups angled within a few degrees of each other.

In addition, the further away the wafer is oriented angularly from the (100) orientation toward the (110), the less the tilt angles of the exposed etch facets agree with those calculated for the {111} planes expected from theory (see table 4.2). Indeed, both laser scatter and AFM facet transforms indicate that the (111) facet is not exclusively exposed by the etch. In fact the whole range of {XXY} facets (orientations lying on the line between {111} and {110}, e.g. {221}, {331}, {556}, etc.) are exposed by texture etching. In the laser scatter and AFM facet transforms, lines of reflected light or exposed etch facet normals are found extending between {111} and {110} facets, as opposed to direct spots of light or facet clusters in a distinct direction. In fact, in the case of the (110) wafer orientation, where theory dictates the formation of V-shaped grooves consisting of intersecting {111} planes at 35° to the surfaces, far flatter surfaces are obtained with somewhat rounded grooves with tilt angles of ~15°, these facets being closer in orientation to the {221} than the {111}. Whilst the theoretical structure would allow a low level of double bounce interaction at the base of the grooves in air, this is not possible for the actual texture formed.

In summary, the roughness of the multicrystalline surface for texture etching depends upon the angular proximity of crystals from the (100) orientation. Etch structures close to the (100) and (110) have shapes which correspond with those expected from theory, with pyramidal and flat triangular textures forming respectively. However, none of the wafer orientations yield exclusively perfect {111} facets as expected theoretically. In fact a range of orientations (the {XXY}) are exposed so that, particularly near the {110} orientation, much flatter surfaces may be yielded than expected.

4.3.2.2 Reflectance measurements of bare texture etched wafers

There is a far larger spread in the bare wafer reflectances for the 7 orientations with a texture etch, than for the saw-damage etch (compare Figure 4.12 below with Figure 4.9 previously). Reflectances are related to the angular separation between the particular wafer orientation and that of the (100) plane, in correspondence with the facet tilt angles of the texture as described above. The wafers oriented furthest away from the (100), i.e. the (111), (221) and (110) wafers in this case, have the highest reflectances, equivalent to that of polished silicon (front surface reflectance R ~ 31% at λ = 1 μm). This compares to front surface reflectance values for the (100) wafer as low as 13% (at λ = 1 μm for the 525 μm thick wafers after etching) due to its upright pyramid texture (see also section 4.1.2). The tilt angles of etched facets exposed

for these orientations are too low for multiple reflectance (i.e. < 30°, see table 4.2), so that reflectances approach that of polished silicon. As crystals tend closer in orientation to the {100}, tilted pyramids are exposed with facets angled at increasing tilt angles with respect to the wafer surface. When etch facet tilt angles begin to exceed 30°, double bounce reflectance becomes more likely, so that the reflectance in air decreases for crystals closest to the {100} orientations.

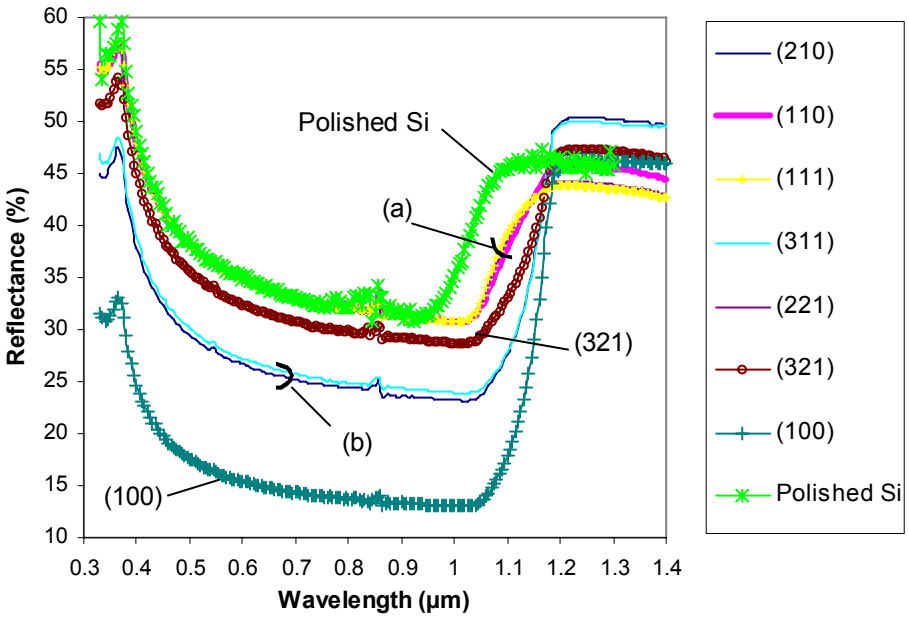

Figure 4.12 *Reflectances in air for the texture etched wafers (initial thickness ~525 µm) compared to polished 100 µm silicon. (a) (111),(221) & (110), (b) (311) & (210) orientations.*

In summary, the reflectances of bare multicrystalline wafers in air are dependent upon the angular proximity of the constituent crystals with respect to the (100). Near (100) orientations have low reflectances in air due to the (tilted) pyramid textures which enable double bounce reflectance. Further away from the (100), the increasing flatness of texture yields still higher reflectances towards (111) and (110) (and other (XXY)) orientations.

4.3.2.3 Reflectances of texture etched wafers under encapsulation

Figure 4.13 shows the effect of encapsulation upon the reflectances of the seven texture etched monocrystalline wafers. The reflectances of the (111), (110) and (221) orientations (i.e. the {XXY} orientations) are highest, as was the case for the bare wafers (Figure 4.12), equivalent to the encapsulated polished wafer due to the flatness of these textures. The tilted pyramid textures on the (210) and (311) wafer orientations have considerably lower reflectances, comparable to those of the encapsulated upright pyramids formed on the (100) orientation. The dramatic reduction in reflectance for these tilted pyramid textures is the result of the internal confinement of light reflected away from the silicon at first incidence at the front glass encapsulant, as was introduced in section 4.1.2. The measured tilt angles of 36° and 27.5° for the predominantly exposed etch facets (see Table 4.2) on the (210) and (311) wafer orientations respectively, are large enough to ensure total internal reflectance of light at the glass-air interface. For the upright pyramid textures on (100) however, encapsulation has minimal effect upon the level of light coupled into the cell, since most light enters the silicon

through the initial double bounce reflectance at the pyramid facets, as is the case in air, prior to approaching the glass-air interface.

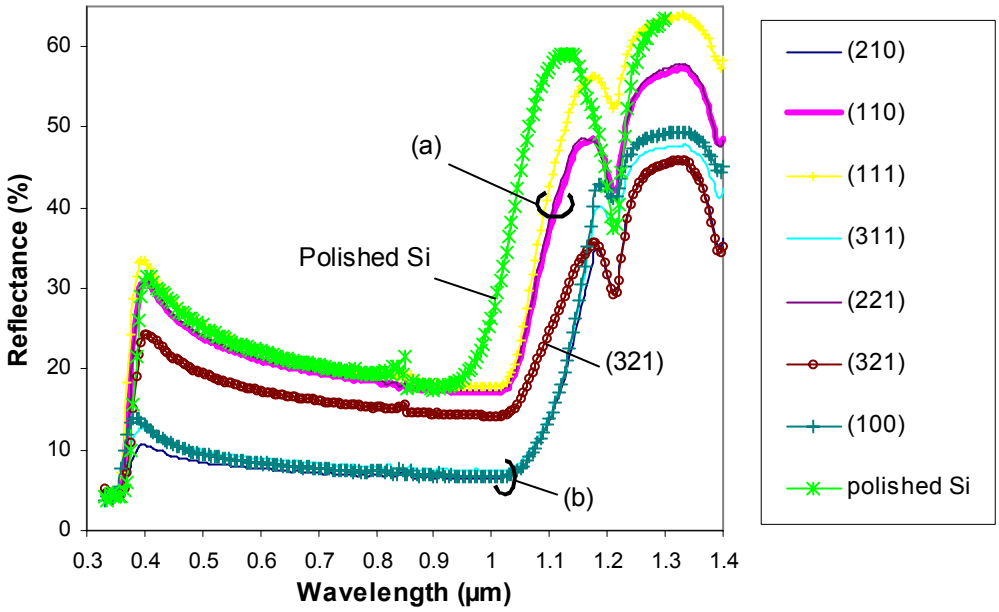

Figure 4.13 *Encapsulated reflectances for the texture etched mono- wafers (starting thickness ~525 µm) and a double polished 100 µm thick wafer. (a) (111),(221) & (110), (b) (311),(210) (100) orientations.*

In summary, reflectance of texture etched multicrystalline wafers under encapsulation depends upon the angular proximity of constituent crystals to the {100} orientations, as is the case for the wafers in air. However, a far larger range of crystals further away from the (100) with tilted pyramid textures now experience multiple bounce incidence of light (and thus low reflectances), since facet tilt angles of only 20.9° satisfy the condition for total internal reflectance at the glass-air interface.

4.3.3 Comparison of measured and theoretical reflectances

4.3.3.1 Wafers in air

Table 4.3 shows the value of R at 630 nm (arbitrary non-transmitting wavelength for silicon, approximately equal to that of the laser light used for (Laue)-scatter recordings as described in Chapter 2) for the different texture etched orientations. Reflectance in air is seen to increase with the increase in angular separation between the particular crystal orientation and that of the (100), in agreement with the trend found for the measured reflectances. However, the theoretical reflectances as calculated by "Sunrays" are approximately 2-5% lower than those measured in practice, with the (110) wafer orientation having the poorest agreement. The exposed etch facets have lower tilt angles than those expected theoretically for the corresponding {111} planes, and non-textured regions will reflect normally to the surface. The actual reflectances are therefore higher than expected theoretically since less multiple incidence of light will occur in practice. The lower facet tilt angles are primarily due to the stability of the {XXY} range of planes leading to a reduction in "sharpness" of texture features with rounding or splitting of etch facets rather than distinct {111} planes as expected.

In summary, the same trends in reflectance are found for the individual bare texture etched wafer orientations for measured and calculated reflectances based on texture etch theory. Both measured and theoretical reflectances increase with the angular separation between the particular crystal orientation and that of the (100). Reflectances are somewhat higher than predicted by theory since etch facets are not perfectly {111} oriented and generally have lower tilt angles than predicted.

Table 4.3 *Measured and calculated reflectances at λ = 630 nm for the seven texture etched wafer orientations.*

Wafer orientation	Reflectances at 630 nm			
	In air		Under encapsulation	
	Measured	Calculated ("Sunrays")	Measured	Calculated ("Sunrays")
(100)	15.0	10.3	8.1	6.5
(311)	26.6	22.4	8.7	5.1
(210)	26.1	21.1	7.5	4.3
(321)	31.8	26.8	16.9	4.7
(110)	34.1	28.8	20.6	8.4
(221)	34.1	31.8	20.8	14.7
(111)[4]	34.1	34.9	21.6	22.1
Polished	34.4	34.9	21.5	22.1

[4] *"Sunrays" crashes during ray-tracing for the (111) orientation; the calculated values shown are for polished silicon, since the triangular structure modelled by the program is seen to be completely flat.*

4.3.3.2 Wafers under encapsulation

Table 4.3 shows measured and predicted reflectances (as calculated by "Sunrays") for the representative orientations on encapsulation. For the majority of orientations, closest to (100) and around the stable (111), any discrepancy between measured facet tilt angles and those predicted by theory has minimal effect on the reflectance reduction expected on encapsulation. The high reflectances measured on the (111) orientation, equivalent to polished silicon, and the low reflectances on upright and tilted pyramids (e.g. on (100), and (210) & (311) orientations) through initial multiple bounce incidence and light confinement at the glass-air interface respectively, are both predicted and measured in practice.

However for wafers oriented closer to the (110), the measured and predicted reflectances on encapsulation differ considerably. For the (very shallow) tilted pyramid texture on the (321) orientation for example, angled closer to the (110) than to the (100), measured and calculated encapsulated reflectances differ by 12.2%. The measured angle for the primary facet exposed is approximately 11°, so that no benefits are gained by light confinement. However, if the (321) tilted pyramid texture was composed of perfect {111} facets, then the theoretical 22.2° tilt angle of the (111) facet would be high enough to ensure total internal reflection at the glass-air interface. The situation for the encapsulated (110) orientation itself is even more extreme. Whilst for the other orientations investigated, predicted reflectances are between 1-5% below those measured, the predicted reflectances for the (110) wafer orientation are approximately 11% lower than is measured. This is because the facet angles of the actual textures are lower than 20.9°, as required for total internal reflectance of light at the glass-air

interface. In contrast according to theory, V-shaped grooves would be formed through intersecting (111) and (-1-11) planes with 35° facet tilt angle with respect to the base (110) orientation. This angle is large enough to allow total light confinement the glass-air interface, whereby double incidence and thus greater reflection reduction would occur as predicted.

In summary, the theoretical model of texture etching predicts that for the majority of wafer/crystal orientations, except those closest to the (111) orientation, etch facet tilt angles will be large enough to achieve reflection reduction under encapsulation. This would result from multiple bounce incidence either primarily at highly facetted textures (for example for upright pyramids) or in any case via total internal reflectance of escaping light at the glass-air interface back towards the silicon. However the stability of all the {XXY} orientations, in particular the (110), limits the proportion of wafer/crystal orientations whose etch facets have tilt angles above 20.9° for light confinement at the glass-air interface. As a result, not only near (111) orientations but also wafers close to the (110) yield highly reflecting etch surfaces.

4.4 Discussion

4.4.1 Comparison of saw-damage and texture etching on monocrystalline wafers

The differences in surface morphology resulting from saw-damage and texture etching result in contrasting reflectances on a per orientation basis. The crystallographic planes exposed by etching are entirely different for the two etches, leading to textures with relatively low facet angles (generally less than 30°) for the majority of saw-damage etched surfaces, compared to surfaces with facet tilt angles up to 55° for texture etching.

Figure 4.14 summarises the resulting reflecting properties for the different orientations, using the principal triangle of orientations described in Figure 4.4 previously. The differences in surface morphology for the two etches mean that completely different regions of the principal triangle of orientations yield high or low reflectances. For example, whilst texture etching of the (100) orientation yields highly facetted pyramids with low reflectance in air, saw-damage etching of the same orientation yields microscopically flat textures with reflectances equivalent to polished silicon.

The effect of the variation in facet tilt angles with orientation is best appreciated for the two etches by observing the change in reflectance in air compared to when encapsulated. This is quantified in Tables 4.4 and 4.5 below, whereby reflectances are related to the proportion of the etch surface yielding facets with tilt angles satisfying the conditions for multiple reflectance in air or under encapsulation. The majority of test orientations for both the etches give reflectances in air approaching or equivalent to polished silicon (see also Figures 4.8 & 4.12). This is because, with the exception of texture etched (tilted) pyramid textures on the (100), (311) & (210) orientations, the test orientations yield textures whereby more than 60% of etch facets have tilt angles below 30° so that no multiple incidence of light is possible. For the saw-damage etch in air for example, near (110) orientations have facets whereby multiple incidence of light may be possible, but its reflectance values are still only 4% lower than for polished silicon due to the large number of facets with angled below 30°. In comparison, for texture etching the upright pyramid textures formed on the (100) orientation have reflectances approximately 20% lower than for polished silicon (see Figure 4.12), through double bounce incidence of all light falling upon pyramid facets. Moving away from the (100), pyramid

structures correspondingly tilt so that dominant etch facets have angles tending below 45°, whereby multiple bounce incidence decreases.

However under encapsulation, many orientations whose etch surface geometries allowed only minimal or even no reflectance reduction in air, have structures whose dominant facets have angles above 20.9° required for light confinement at the glass-air interface (see also Tables 4.1 & 4.2 previously). This is the case for both the texture etch (for the aforementioned tilted pyramid textures) and the saw-damage etch, for the central orientations in between the flat etching (100) and (111). Therefore under encapsulation, the number of optically "useful" orientations is significantly increased as compared to the case when bare.

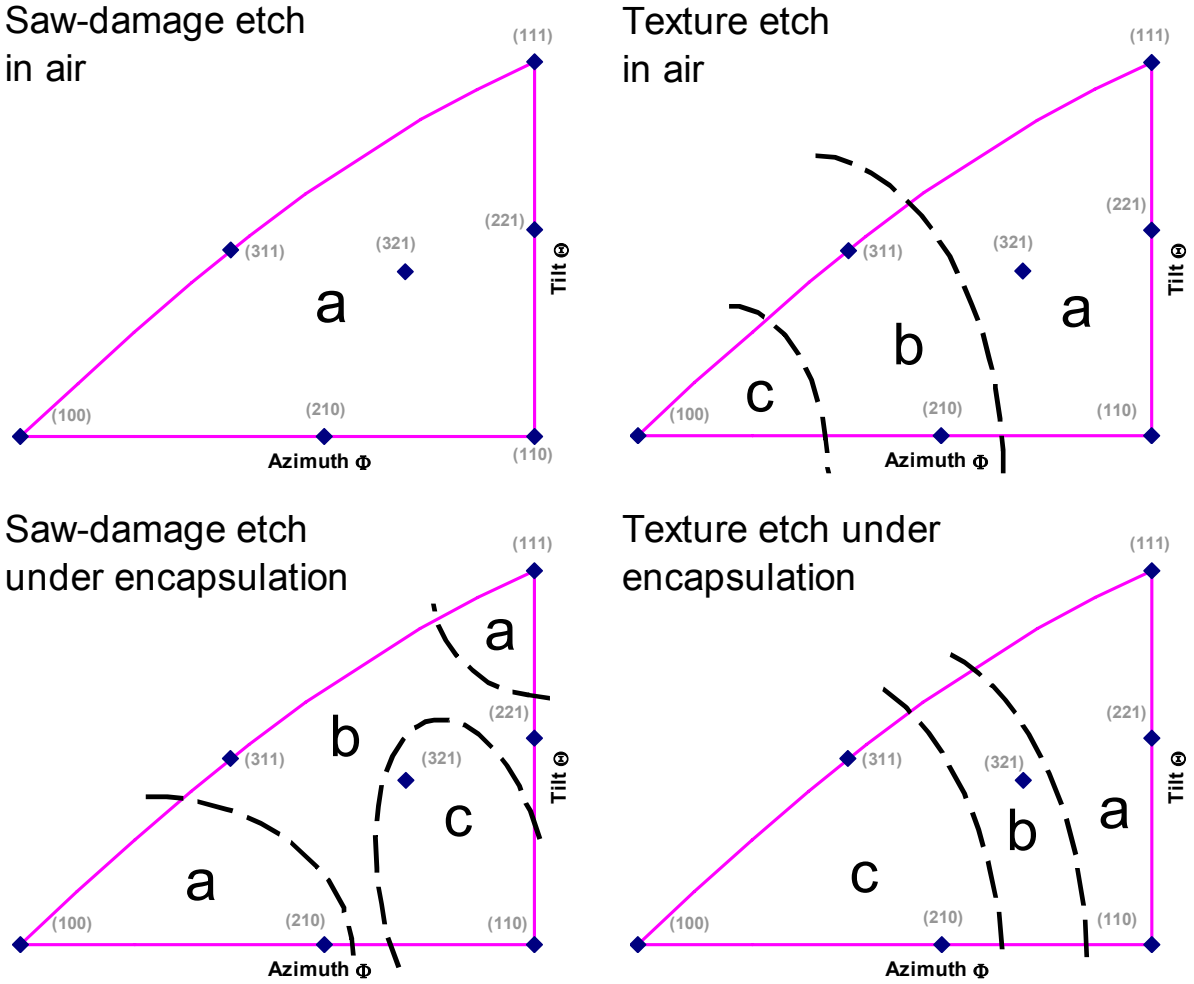

Figure 4.14 *Sketches indicating the reflectances of alkaline etched wafers as a function of orientation, using the principal triangle of orientations as described in Figure 4.4. Reflecting properties are described on the basis of measured reflectance values in the visible by a) reflectances equivalent to polished silicon, b) some multiple incidence of light, c) majority of incident light experiences multiple bounce incidence (reflectances equivalent to upright pyramids on monocrystalline (100) silicon). (For measured reflectance curves see Figures 4.8, 4.9, 4.12, & 4.13 previously).*

Table 4.4 *Relationship between measured reflectances and facet tilt angles for saw-damage etched monocrystalline wafers*[5].

Wafer orientation	Percentage of surface with measured facet tilt angle θ greater than:			Measured Reflectance at λ = 630 nm	
	45° [A]	30° [B]	20.9° [C]	In air	Encapsulated
(100)	0.0	1.0	9.2	33.7	19.3
(311)	1.5	24.8	44.1	32.4	15.4
(210)	1.1	12.4	30.5	32.7	18.4
(321)	1.8	22.1	59.3	31.9	11.9
(110)	0.2	24.6	51.1	30.2	11.9
(221)	1.7	14.8	28.2	31.2	14.7
(111)	4.7	8.9	10.9	31.5	19.0
Polished	*0.0*	*0.0*	*0.0*	*34.4*	*21.5*

Table 4.5 *Relationship between measured reflectances and facet tilt angles for texture etched monocrystalline wafers*[5].

Wafer orientation	Percentage of surface with measured facet tilt angle θ greater than:			Measured Reflectance at λ = 630 nm	
	45° [A]	30° [B]	20.9° [C]	In air	Encapsulated
(100)	59.8	70.3	81.2	15.0	8.1
(311)	21.6	57.3	82.1	26.6	8.7
(210)	14.1	47.8	74.6	26.1	7.5
(321)	2.1	6.8	18.1	31.8	16.9
(110)	0.0	0.1	13.7	34.1	20.6
(221)	0.0	0.0	2.5	34.1	20.8
(111)	0.0	0.0	0.1	34.1	21.6
Polished	*0.0*	*0.0*	*0.0*	*34.4*	*21.5*

[5]*Facet tilt angles are grouped as a function of the probability of multiple incidence of light whereby A = guaranteed multiple incidence for facet tilt angles $\theta > 45°$ both in air and under encapsulation, B = as A with additional facets with angles $30° < \theta < 45°$, for which multiple incidence of light is possible in air but guaranteed under encapsulation, and C = as B with additional facets angled $20.9° < \theta < 30°$, whereby no multiple incidence occurs in air but is guaranteed under encapsulation.*

The results from Table 4.4 and 4.5 are summarised graphically in Figure 4.15 below, which shows the relationship between the measured reflectance and the percentage of the silicon surface having facet angles yielding guaranteed multiple incidence of light, fitted linearly for the wafers in air and under encapsulation. The measured reflectances are seen to decrease as the percentage of the surface yielding guaranteed multiple incidence of light increases.

For the bare wafers, the decrease in reflectance is greatest, from values of 34% as equivalent to polished silicon in air, to values around 2% for surface where 100% of light will experience multiple reflectance (experimental etch textures with optical properties in this latter regime have surface morphologies equivalent to vertical columnar structures, such as those formed by reactive ion etching as was shown in Chapter 3). For the saw-damage etch textures, with

generally less than 5% of the surface yielding guaranteed multiple incidence, reflectances are equivalent to polished silicon, whilst for the texture etched wafers, the differences in facet angles between flat etching {XXY} orientations and (tilted) pyramid textures yields a far greater spread in measured reflectances.

For the encapsulated wafers, the decrease in reflectance is more gradual, from values of ~22% reflectance equivalent to polished silicon under encapsulation, decreasing to values of ~6% where multiple bounce incidence is guaranteed, this value resulting entirely from reflectance from the glass. The reflectance distribution is more evenly spread for the encapsulated saw-damage etched wafers compared to the texture etched wafers. The differences in etch surface geometries now become visible for the saw-damage etch texture, for which the majority of the surface is angled below 45° which lead to multiple reflectances in air. The increase in facet tilt angles with orientation for the saw-damage etched samples, from the flattest etching (100) and (111) orientations to the highest facet tilt angles on the central (110) and (321) orientations, is far more gradual than for the texture etched wafers, where textures contrast over the principal triangle of orientations from polished textures on the {XXY} orientations and to the pyramidal textures.

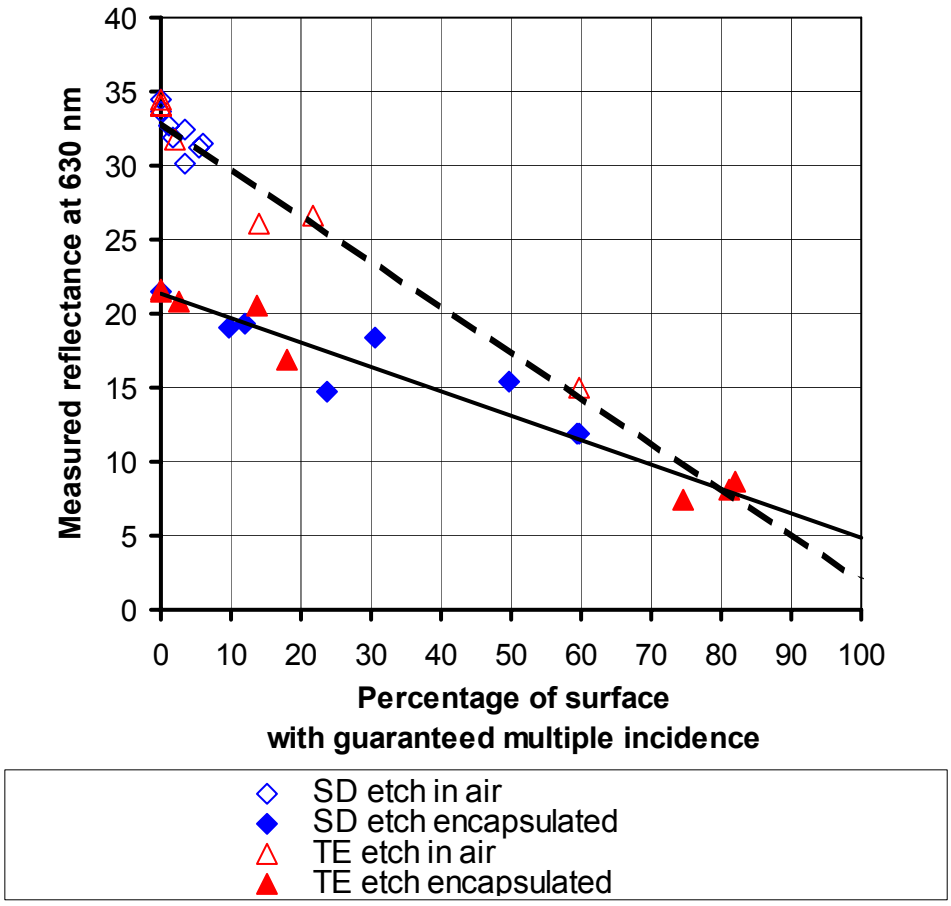

Figure 4.15 *Relationship between reflectance and the proportion of silicon surface yielding multiple incidence, fitted linearly for the bare wafers (full line) and the wafers under encapsulation (broken line).*

4.4.2. Algorithm linking monocrystalline and multicrystalline reflectances

In order to relate the results on monocrystalline wafers to the situation for multicrystalline wafers, an algorithm was developed by Burgers [17] whereby a weighted average is calculated for the quantitative data acquired for the individual wafer orientations. This weighted average accounts for the random orientations of crystals in the wafer, whereby for example the reflectance properties of a multicrystalline wafer may be calculated from the equation:

$$R_t = \frac{\int_{\Phi=0}^{\frac{\pi}{2}} \int_{\Theta=0}^{\tan^{-1}(\sin\Phi)} R(\Phi,\Theta)\cos\Theta \, d\Phi \, d\Theta}{\int_{\Phi=0}^{\frac{\pi}{2}} \int_{\Theta=0}^{\tan^{-1}(\sin\Phi)} \cos\Theta \, d\Phi \, d\Theta} = \frac{\textit{weighted sum of reflectances}}{\textit{area}}$$

where Φ and Θ are defined as in Figure 4.4 previously. This weighting is based upon the projection of the areas of all 48 families of principal {100}:{110}:{111} triangles upon a sphere encompassing all the possible crystal co-ordinates. The accuracy of this method is demonstrated in Figure 4.16, where the weighted average of reflectances for texture etched wafers is compared to the mean of reflectances measured for eighteen multicrystalline wafers. The absolute reflectances derived from weighted averages on the seven monocrystalline wafers average 1 and 1.5 % lower respectively in the visible than measured for the bare and encapsulated multicrystalline wafers. However, the weighted averages lie within the limits of the standard deviation for the eighteen multicrystalline wafers, this being ± 1.9 and ± 1.75 % in absolute reflectance in the visible for the bare and encapsulated wafers respectively.

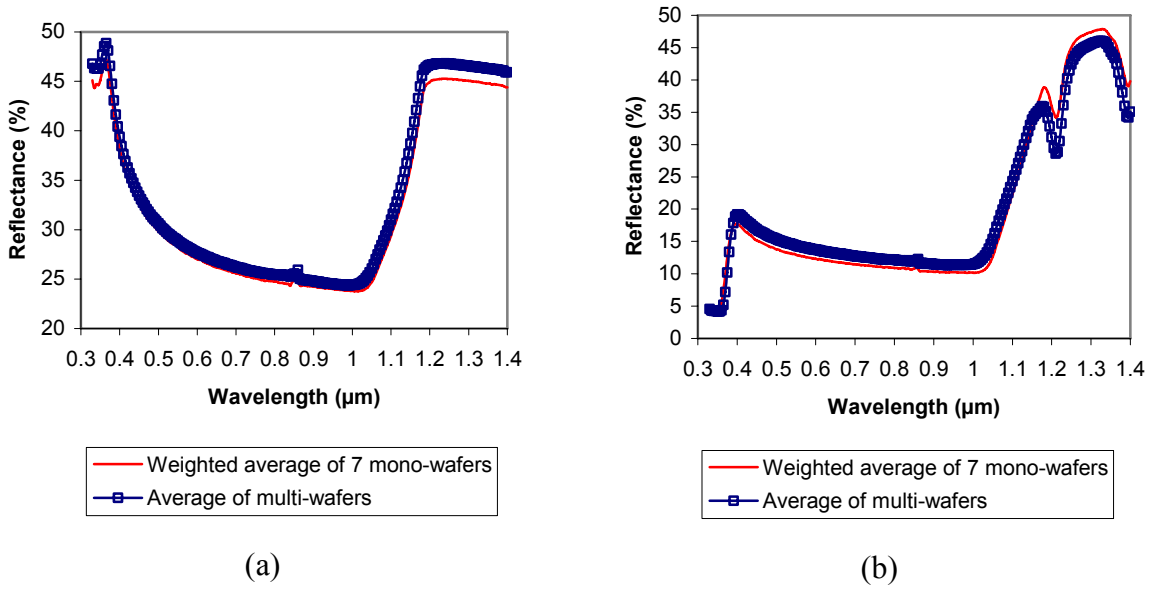

Figure 4.16 *Comparison of the weighted average reflectance for the seven monocrystalline wafer orientations with the actual average reflectance for multicrystalline wafers etched under the same conditions for a) bare and b) encapsulated wafers.*

4.4.3 Application to multicrystalline wafers

The absence of any preferential orientation(s) dominating the crystallographic composition of the multicrystalline wafer renders it essential that reflection reduction be applicable to as many orientations as possible. Since a proportion of crystals invariably yield flat surfaces, it will be impossible to give reflectance reduction by geometrical means on all orientations. However, Tables 4.4 and 4.5 show that both the saw-damage and texture etches yield geometrical surface textures on certain orientations which under encapsulation can give reflectances approaching that of pyramidal texture on the (100) orientation. With so many orientations present in a multicrystalline wafer, will the reflectances of the alkaline etched wafers be significantly improved if observed encapsulated rather than bare?

Figure 4.17 shows the average of measured reflectances on two neighbouring sets of 18 multicrystalline wafers in air and under encapsulation, one set for each of the etches investigated. Additionally, Table 4.6 relates the reflectances of the multicrystalline wafers to their surface morphologies as a function of etch facet tilt angles over the wafer, as calculated using the weighted average algorithm described previously.

Table 4.6 *Relationship between measured reflectances and AFM facet tilt angles for texture etched multicrystalline wafers[6], in comparison to polished silicon and pyramid texture on monocrystalline (100). Facet tilt angles are derived from the weighted average of facet angle data for the seven saw-damage and texture etched monocrystalline wafer orientations as in Tables 4.4 and 4.5 previously.*

Etch type	Percentage of surface with measured facet tilt angle θ greater than:			Measured Reflectance at λ = 630 nm	
	45° *A*	30° *B*	20.9° *C*	In air	Encapsulated
Saw-damage	1.6	17.3	38.3	32.0	15.3
Texture	13.0	28.8	44.2	29.0	13.8
Polished	*0.0*	*0.0*	*0.0*	*34.4*	*21.5*
Mono (100) with texture etch	*59.8*	*70.3*	*81.2*	*15.0*	*8.1*

[6]Facet tilt angles are grouped as a function of the probability of multiple incidence of light whereby A = guaranteed multiple incidence for facet tilt angles $\theta > 45°$ both in air and under encapsulation, B = as A with additional facets with angles $30° < \theta < 45°$, for which multiple incidence of light is possible in air but guaranteed under encapsulation, and C = as B with additional facets angled $20.9° < \theta < 30°$, whereby no multiple incidence occurs in air but is guaranteed under encapsulation.

(a)

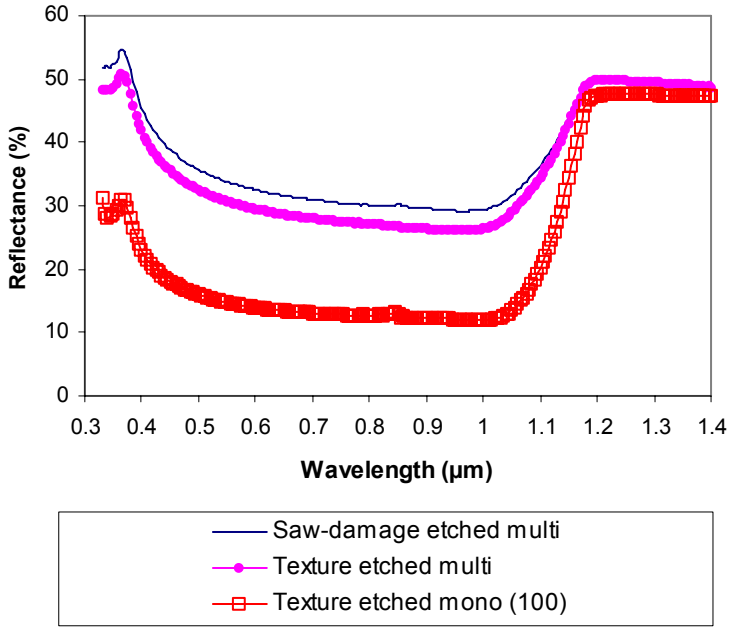

(b)

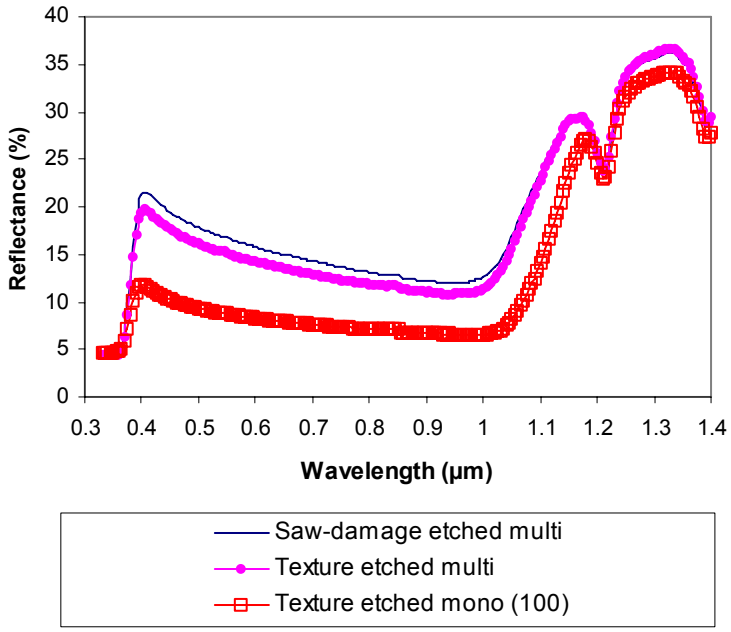

Figure 4.17 *Reflectances for multicrystalline wafers with alkaline saw-damage and texture etches as compared to a pyramidally textured monocrystalline (100) wafer. (a) Reflectances in air (b) Reflectances under encapsulation.*

Unsurprisingly, the absolute reflectances of the multicrystalline wafers in air are far higher than for the pyramidally textured (100) mono- wafer, approximately 14 and 17 % higher for the texture and saw-damage etches respectively in the visible. For the saw-damage etch, this high multicrystalline reflectance highlights the flatness of the etch surface, whereby approximately 75% of the surface has facet tilt angles to low to give double bounce reflectance in air (i.e. tilt angles $\theta < 30°$). For the texture etch, the slightly lower multicrystalline reflectance results from multiple incidence of light on (tilted) pyramids. However the number of near (100) crystals yielding pyramidal textures is too low in

proportion with other orientations in the wafer to bring the overall wafer reflectance in air to the level of the monocrystalline wafer.

For the wafers under encapsulation, the same overall ranking of reflectances is found for the saw-damage and texture etched multi- wafers and the mono-wafer, from highest to lowest reflectances respectively. However, the level of reflectance is dramatically reduced for the multicrystalline wafers, and lies far closer to that of the (100) oriented wafer than was the case when bare. The saw-damage etched wafers have an average reflectance level only 7% higher than for the encapsulated (100) wafer in the visible, compared to the 17% difference between them when in air. This is due to the benefits obtained through light confinement at the glass-air interface, which significantly improves the level of light coupled into the silicon for the alkaline etched wafers.

The improvement under encapsulation is most marked for the saw-damage etched wafers. In this case, 38% of the surface has facet tilt angles above the 20.9° threshold for total internal reflectance at the glass-air interface and thereby the guaranteed multiple incidence of light. This compares to a maximum of 17% of the wafer surface for which multiple incidence is possible in air (angles > 30°). The visible reflectance value for encapsulated saw-damage etched wafers lies only around 1.5% above that of its neighbouring texture etched multicrystalline wafers, compared to a difference of 3% when bare. This is because a large proportion of tilted pyramid structures already facilitate multiple bounce reflectance in air by virtue of facets angled above 30° (amounting to 29% of the wafer surface according to Table 4.6), compared to the far flatter textures for the saw-damage etch. As a result the reflection reduction achieved by light confinement on encapsulation is relatively less.

The fact remains however that both alkaline etch treatments compare much more favourably in terms of their surface reflecting properties with respect to monocrystalline (100) oriented silicon when observed under encapsulation than when bare. This is also a much more practical and realistic comparison, since the finished silicon cells will always be placed under encapsulation in the final module.

4.4.4 Employment of anti-reflection coatings

Although anti-reflection coatings (ARC's) are not investigated explicitly in this work, it is interesting to discuss their effect upon the surface reflecting properties of (textured) silicon solar cells. So-called "quarter wavelength", predominantly single layered ARC's are generally employed industrially, applied directly upon the silicon, which for a coating thickness d_1 and refractive index n_1 satisfy the relationship:

$$d_1 = \frac{\lambda_0}{4n_1}$$

whereby light of incident wavelength λ_0 which is reflected away at the silicon-ARC interface initially, will destructively interfere with light reflected directly away from the ARC-encapsulant (e.g. air or glass) interface with which it will be 180° out of phase, thereby ideally cancelling out reflection (see e.g. [1]). ARC's for silicon solar cells are usually optimised for a maximum current output in the terrestrial solar spectrum (AM1.5G). This is achieved for coatings with a reflectance minimum at wavelengths of around 600 nm, these ARC's giving the finished cells their characteristic blue colour. A reflectance minimum of zero can be

achieved for λ_0 if the refractive index of the ARC corresponds to the geometric mean of the refractive indices of the adjacent media, whereby:

$$n_1 = \sqrt{n_0 n_2}$$

where the suffixes 0, 1 and 2 correspond to the encapsulant layer (e.g. air or glass/pottant), the ARC and the silicon respectively. Taking refractive index values of $n_{air} \approx 1.0$, $n_{glass} \approx 1.5$ and $n_{Si} \approx 3.8$, then optimal refractive index values for the ARC will be 1.9 and 2.3 respectively for the silicon cell in air and under encapsulation. Typical coating materials are SiN_x deposited by (remote) plasma enhanced chemical vapour deposition ((R)PECVD), or TiO_x. These materials have high transparency, can be deposited with a large range of refractive indices and, in the former case can provide electronic passivation of the silicon wafer surfaces.

When used in addition to geometrical texturisation, an anti-reflection coating further reduces front surface reflection losses from the finished solar cell. However, the optimisation of an ARC for alkaline etched multicrystalline wafers presents extra complexities. The optimal thickness of an ARC has been shown to vary with the facet tilt angles of surface texture for the examples of random pyramidal and periodically microgrooved textures [18,19]. The large differences in facet tilt angles between crystals of different orientations found for both the etches investigated here, pose potential problems for the optimisation of the ARC. Coating thicknesses which are appropriate for a particular crystal and surface morphology may thereby be less optimal for other crystals in the wafer. The possibility also exists that, depending upon the deposition techniques used, that the ARC may not coat the textured surfaces uniformly, i.e. for example for a pyramidal texture, that the coating is thicker at the troughs between pyramids than at the peaks.

The geometrical texturisation of the surface also leads to an increase in the front surface area of the wafers. Electronic passivation of the front surface is thereby of particular importance in order to prevent recombination losses, so that the use of a passivating coating such as SiN_x is more important. However SiN_x films become more absorbing as their refractive index is increased [20], which is a problem when coatings are to be optimised for the wafers under glass encapsulation where higher refractive indices are required. In addition, surface recombination velocities have been shown to be orientation dependent on p-type silicon [21]. Although for n-type silicon (and thus the emitter at the top side of the cell) such a relationship was not found, this may potentially cause problems for cells with open rear metallisation where rear-side passivation of the p-type bulk is required. Since particular crystallographic planes are exposed by etching, it may be found that passivation is more effective on some crystal orientations than others, and certainly between the two alkaline etch concentrations examined in this work.

4.4.5 Validity of texture etch theory

4.4.5.1 Comparison of theory and experiment for monocrystalline wafers

The results of texture etching (section 4.3.2) showed that in addition to {111} crystallographic planes the whole range of {XXY} planes lying between (110) and (111) orientations are also exposed by etching. This contrast with what is expected from theory, whereby only {111} planes are predicted to be stable to the etch. For the orientations investigated, the stability of

this range of planes leads to lower facet tilt angles than expected, resulting in higher measured reflectances in practice, particularly under encapsulation.

4.4.5.2 Development of etch texture as a function of etch depth per orientation

It is also observed that, with the exception of the (111) orientation itself, the discrepancy between the measured facet tilt angles and those calculated by theory increases for orientations angled further away from the (100). From Figure 4.18, we see that a similar relationship holds for etch rates on the seven representative orientations. Large variations in etch rate are observed, with the fastest etching orientations having the lowest angular separation from the (100). Since all the orientations were etched for the same duration (as is inherently the case for differently oriented crystals in a texture etched multicrystalline wafer), it may thus be possible that the exposure of non-{111} oriented facets is simply a consequence of a lesser stage of development of the geometrical surface texture for the slow etching orientations. In order to investigate this hypothesis, the 7 wafer orientations were etched to various etch depths to observe the development of the texture etch facets as a function of time.

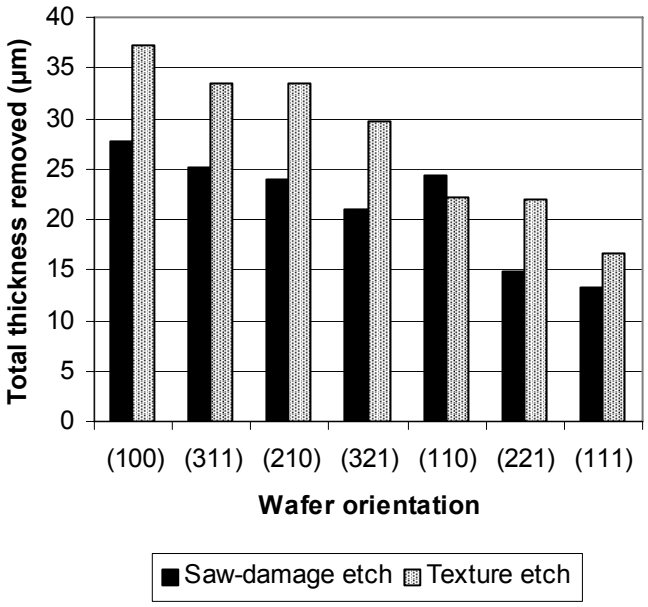

Figure 4.18 *Total etch depths as a function of orientation for saw-damage and texture etches (etch times used give an etch depth of 25 µm on multicrystalline silicon).*

The resulting surface morphologies can be discussed as previously in terms of the distance of the wafer orientation from the (100), whereby tilted pyramids closer to the (100) behave differently to wafers with the {XXY} orientations (110), (221) and (111) used in experimentation. The results are summarised in Figure 4.19 and 4.20 for the examples of the tilted pyramid structure formed on the (321) orientation and the (110) orientation respectively.

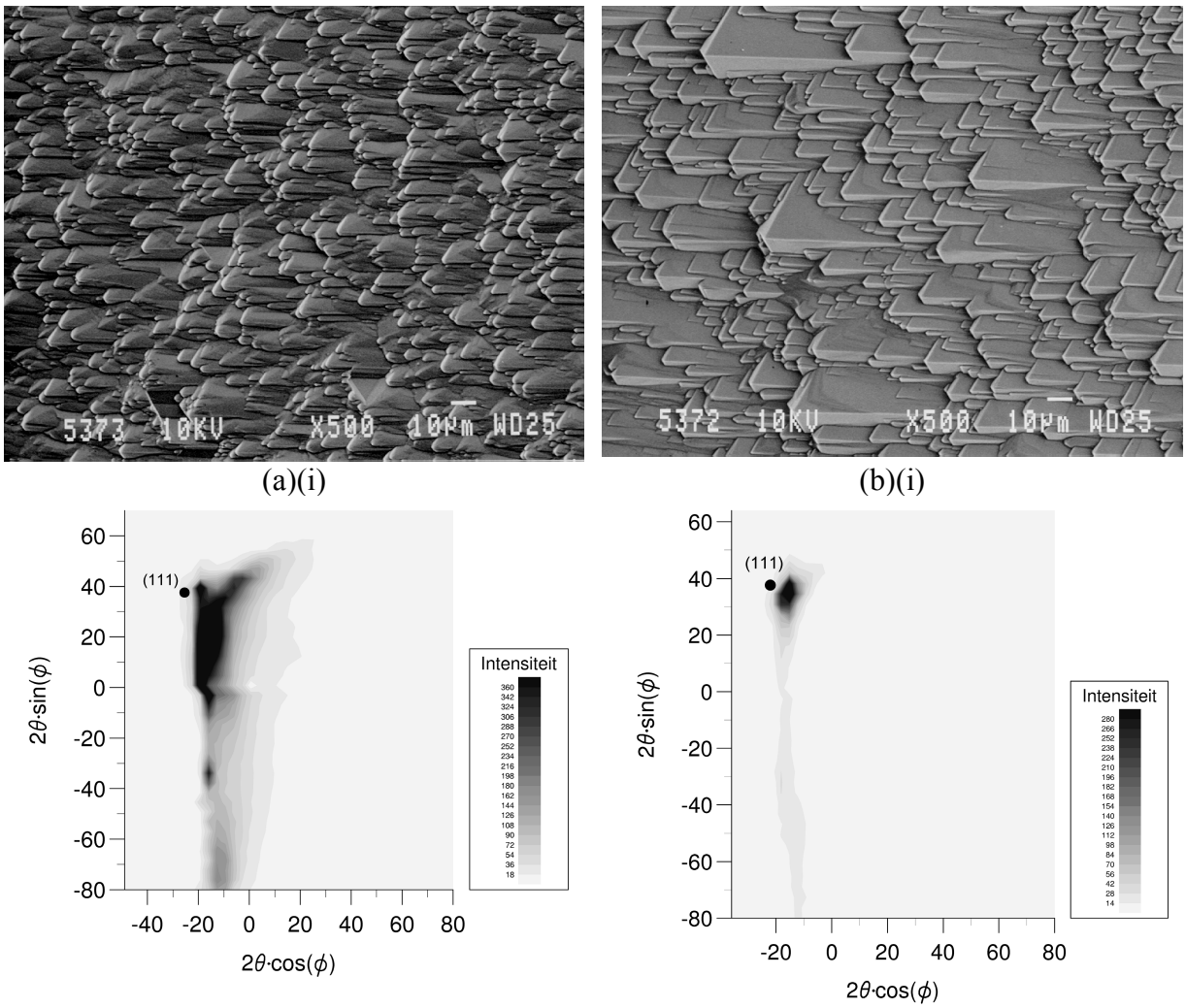

Figure 4.19 *(i) SEM photographs and (ii) laser scatter patterns[7] showing the etch texture development on the (321) orientation, for a) 5 min and b) 25 min etch durations. Tilted pyramid etch facets tend towards the {111} with etch depth.*

- *= theoretical facet position.*

[7] Laser scatter patterns are compared here instead of AFM facet transforms because the 25 minute etch leads to surface roughnesses too great for the AFM (i.e. > 9 µm with the special AFM scanner, see Chapter 2 and Figures 4.7 & 4.11,). For this reason, the axes of the polar plot are multiplied by 2θ rather than θ as for the facet transforms, since the facet positions are now represented by an angle of reflection 2θ as opposed to the tilt angle θ of the surface normal.

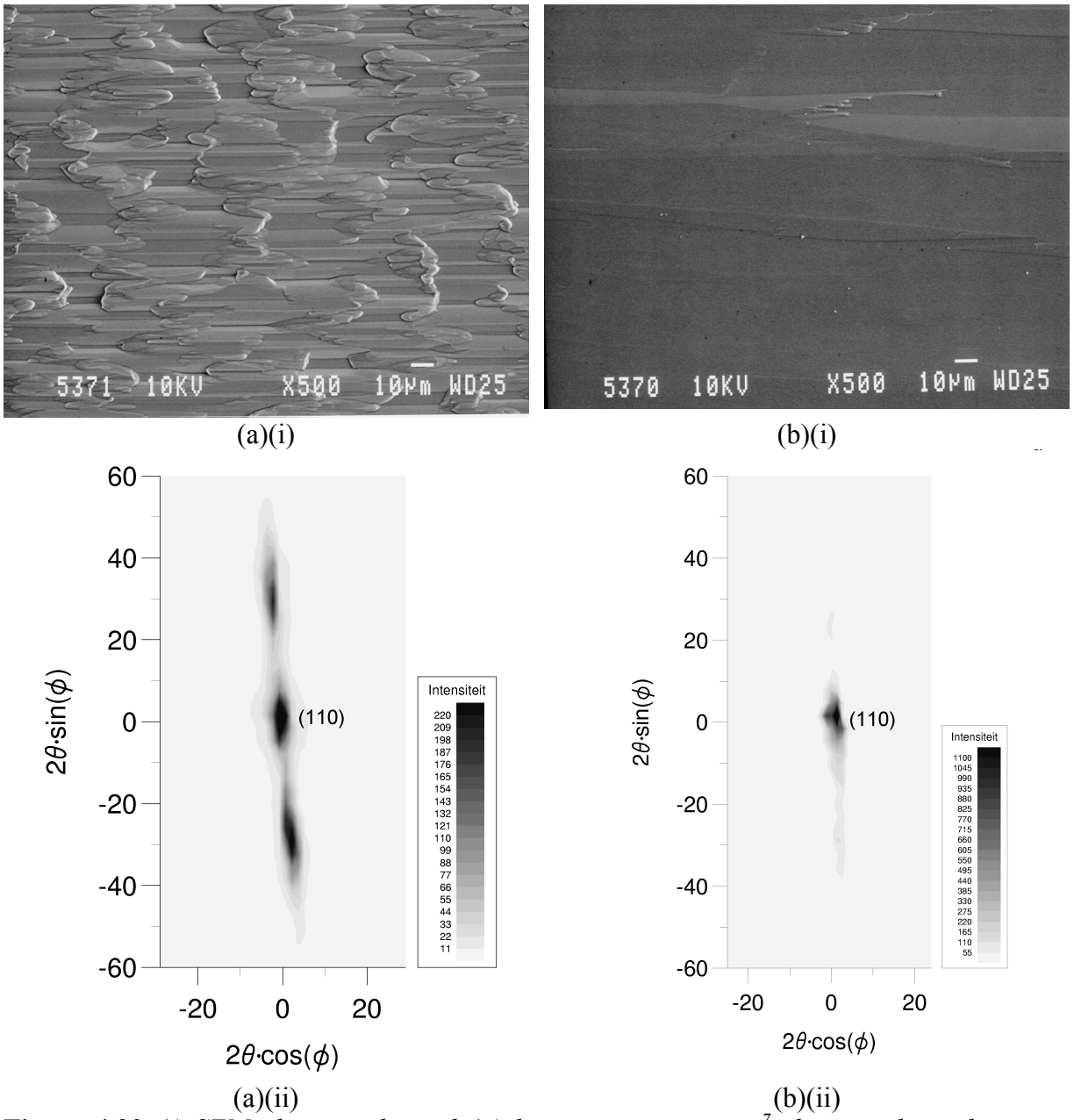

Figure 4.20 *(i) SEM photographs and (ii) laser scatter patterns[7] showing the etch texture development on the (110) orientation, for a) 5 min and b) 25 min etch durations. The (110) orientation is polished by the etch with time showing its stability to the etch.*

- *= theoretical facet position.*

In all cases, the shorter the etch duration, the greater the spread in exposed facet angles, with ranges of {XXY} facets extending up to 10° or more from around the major etch facet orientation. For the (tilted) pyramidal textures, an increase in the etch duration sees a strong tendency of the etch facets towards the {111} orientations predicted by theory. Etch facets become less rounded with time, with increasingly sharp edges bounding the pyramid faces. Fewer flat untextured regions are present between texture features, and the etch structures become larger. Most importantly, as these facets develop with time their tilt angles increase. Consequentially, tilted pyramid structures on those orientations furthest from the (100) now have facet angles which may satisfy the conditions for total internal reflectance (i.e. greater than 20.9°). For the (321) orientation for example, the tendency of the facets towards the

{111} facet with time sees more facets allowing for light confinement at the glass-air interface, whereby its reflectance value under encapsulation decreases from 15.9 to 12.3% at $\lambda = 630$ nm.

However for orientations close to the (110), the etch facets exposed continue to tend towards {XXY} orientations, as opposed to the {111} orientations exclusively. Rather than etch facets becoming steeper, the surface morphology becomes flatter with etch depth. For the wafers investigated, it is observed that whilst {111} facets are indeed exposed on the (111) orientation, the (221) and the (110) both also etch down to their base orientation yielding flat surfaces. This is of particular importance for the measured reflectances, which as a consequence are equivalent to polished silicon, both bare and under encapsulation. It also demonstrates a paradox in the etching process: whilst increasing the etch depth leads to higher facet angles and lower reflectances for (tilted) pyramid textures, it also results in the increased flatness and higher reflectances of textures on orientations furthest removed from the (100).

4.4.5.3 Stability of the (110) orientation

The stability of the {XXY} orientations is particularly significant for the reflectance levels achieved for the (110) orientation. Theoretically, this orientation would yield 2-dimensional V-shaped grooves consisting of intersecting {111} facets angled at 35° to the base orientation. Although in air, only a minimum of multiple incidence would be achievable for this theoretical etch structure at the base of the grooves, the reflection levels achievable under encapsulation would be almost equal to that of an upright pyramid texture. Although a grooved texture is achieved for the shorter etch time shown in Figure 4.20, its 15° facet tilt angles are too low for multiple bounce reflectance, either in air or under encapsulation. Shorter etch durations barely remove the initial sawing damage, and prolonged etching causes the surface to polish down flat to the stable (110) base orientation rather than tending towards the expected {111} facets, so that the majority of light is reflected normally to the surface.

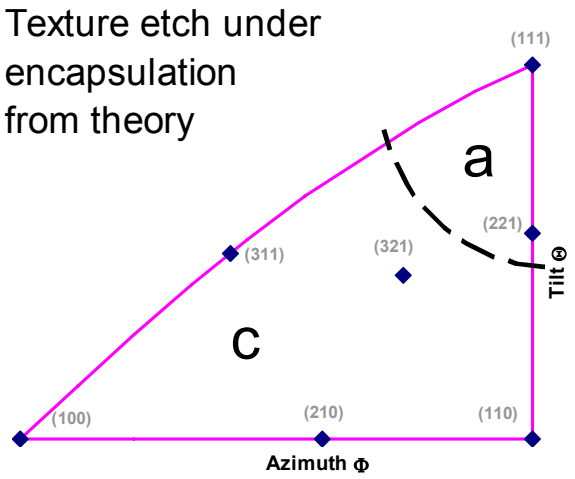

Figure 4.21 *Sketch indicating the encapsulated reflectances of texture etched wafers according to theoretical calculations with "Sunrays". Reflectances are given as a function of orientation, using the principal triangle of orientations. In region c), the majority of light experiences multiple incidence, whilst in region a) reflectances are equivalent to polished silicon since facet tilt angles are less than 20.9°.*

Figure 4.21 translates this to the situation for orientations in the principal triangle of orientations. According to theory, a perfect texture etch, yielding etch surfaces bounded exclusively by {111} facets, would give encapsulated reflectances equivalent to upright pyramids on the majority of test orientations except those closest to the (111) itself. However in practice, the stability of the (110) orientation means that the conditions under which (tilted) pyramids develop (i.e. at longer etch duration) lead to the polishing of the (110) orientation. This leads to the particularly large discrepancies between the measured and theoretical values for the (110) orientation that were shown in Table 4.3. As a result the actual reflectance of the encapsulated multicrystalline wafer will be less than predicted.

4.4.5.4 Comparison of experiment and theory for multicrystalline wafers

The theoretical and experimentally measured reflectances of texture etched multicrystalline wafers are compared in Figures 4.22 and 4.23 respectively for wafers in air and under encapsulation. The experimental values are the average for eighteen wafers, etched for the longest duration whereby facets on tilted pyramid structures tend most strongly to the {111}. The theoretical reflectances are calculated using the weighted average of the reflectances determined by "Sunrays", for the seven orientations used in experimentation.

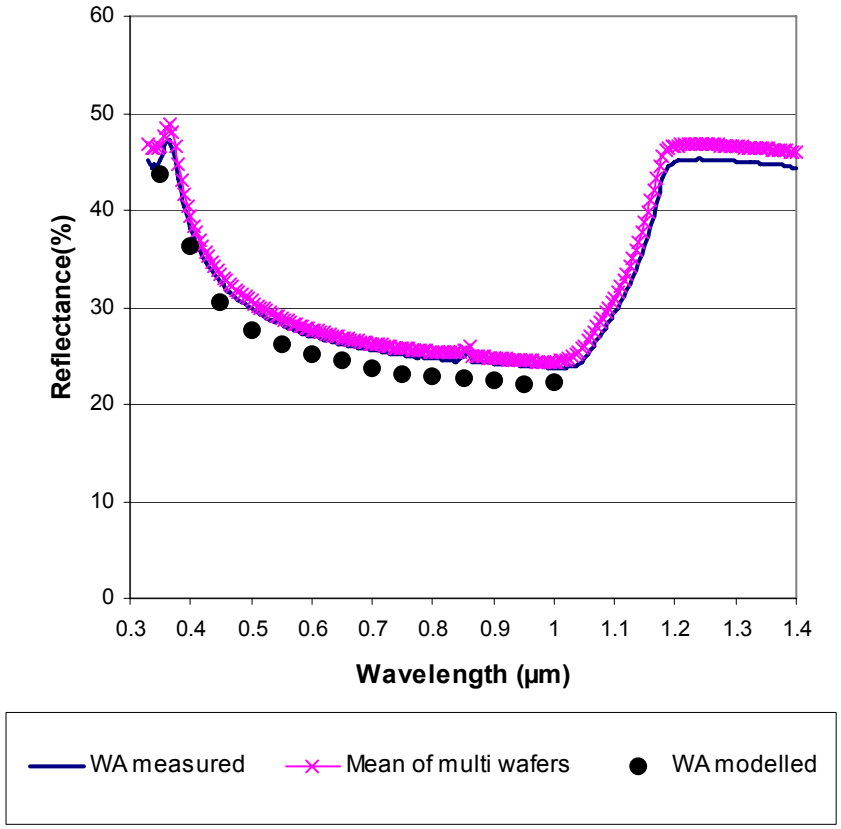

Figure 4.22 *Measured reflectances of texture etched multicrystalline wafers in air, compared to weighted averages (WA) based on the 7 orientations as measured experimentally and as modelled theoretically using the "Sunrays" ray-tracing program.*

For the wafers in air, the difference between theoretical and measured reflectances is relatively small, despite the differences in surface morphology on {XXY} oriented crystals, since only upright pyramids, which are present both in theory and practice on wafers closest

to the (100), allow multiple incidence of light. Theoretical reflectance values in air are indeed lower, (24.7% at λ = 630 nm) due to the imperfections of the textures formed practically (for example polished regions between texture, etc.). However under encapsulation, the measured reflectances for the multicrystalline wafer are 5.4% higher than expected theoretically, as a result of the high reflectance of the stable, flat etching crystals near the (110) orientation.

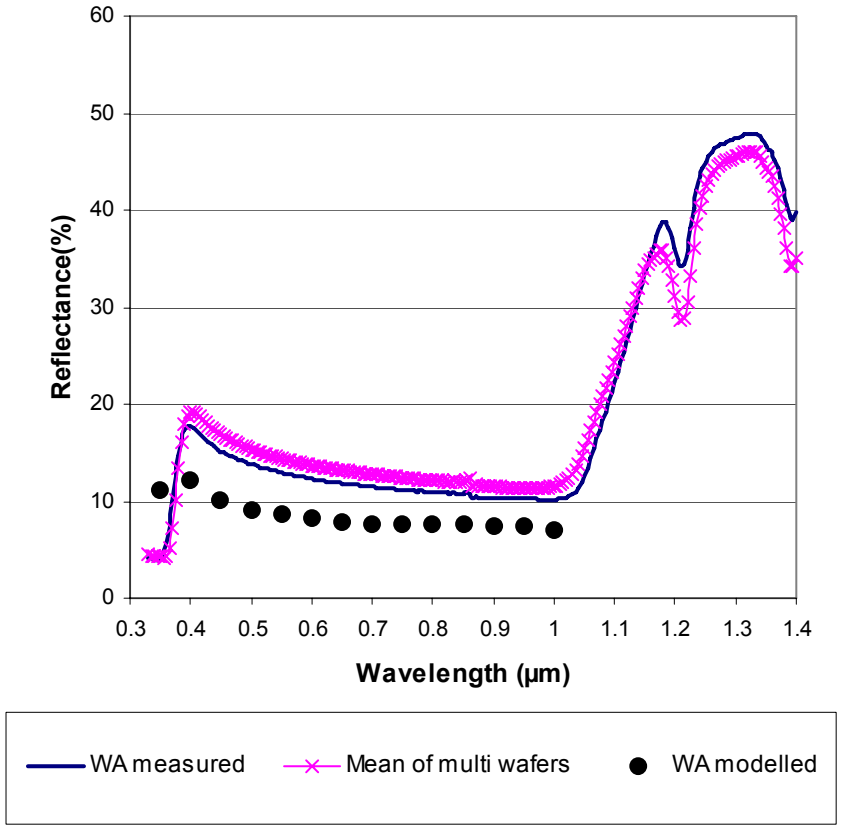

Figure 4.23 *Measured reflectances of texture etched multicrystalline wafers under encapsulation, compared to weighted averages (WA) based on the 7 orientations as measured experimentally and as modelled theoretically using the "Sunrays" ray-tracing program.*

4.5 Conclusions

The surface morphologies of multicrystalline alkaline texture and saw-damage etch textures have been quantified using a series of analysis techniques. Hereby it was possible to relate reflectance properties to the etch geometries on a per orientation basis. By using uncoated wafers the reflectance reduction observed is purely due to the geometry of the wafer surface morphology formed by the etch and the resulting multiple bounce incidence of light, as is responsible for the excellent optical properties of pyramidally textured (100) monocrystalline silicon.

The level of reflection reduction is strongly dependent upon the etch composition and conditions, combined with the orientations of the crystals in the wafer. The surface morphologies of the saw-damage etched wafers are generally relatively flat, in terms of their optical reflective properties in air. The majority of exposed etch facets have surface normals with tilt angles of less than 30°, i.e. lower than is required for even minimal double bounce

incidence of light. This results in reflectances comparable to polished silicon in air. This flatness arises due to the large number of crystallographic planes which are stable to the etch, these being predominantly the {100}, {111}, {110}, {311} & {211} sets of planes.

For the low concentration texture etch, a larger variation in surface roughness arises, depending upon the angular proximity of the constituent crystal orientations to that of the (100). Near (100) orientations have low reflectances in air due to the (tilted) pyramid textures with facet tilt angles up to 55° which enable double bounce reflectance. Further away from the (100) towards (XXY) orientations such as (111) and (110) (where X and Y are integers), the increasing flatness of the texture yields still higher reflectances comparable to polished silicon. As a result, reflectances of individual crystals differ by up to 20% within a given texture etched multicrystalline wafer in air.

The reflectances of neighbouring saw-damage and texture etched multicrystalline wafers, etched to the same etch depth of 25 μm in total by weight, are respectively 17 & 14% higher than for pyramidally textured (100) monocrystalline wafers in air. In the case of the saw-damage etched wafers, this is because the majority of facets on all orientations are too low to allow more than minimal multiple bounce incidence of light. For the texture etched wafers, the random distribution of crystal orientations in multicrystalline silicon means that the weighting of (tilted) pyramid structures on near (100) is too low compared to flat etching orientations to reduce the level of reflection more significantly. In the light of such a comparison in air one may be inclined to reject geometrical texturisation by these two methods as being ineffective for multicrystalline silicon.

However, the situation improves dramatically under encapsulation, with saw-damage and texture etched multicrystalline wafers having reflectances only 7 & 5.5% higher than for the encapsulated upright pyramids on monocrystalline (100). This due to the effect of light confinement at the glass-air interface, whereby light reflected away initially at facets can be totally internally reflected and thus re-directed towards the silicon for a second chance of coupling into the silicon. All etch facets with angles above 20.9° satisfy the condition for total internal reflection, so that this method of multiple bounce incidence is far more effective for the alkaline etched multicrystalline silicon than that required between silicon facets in air. Thus whilst for the saw-damage etch for example, the etch surface is practically devoid of facets with tilt angles allowing for multiple bounce incidence, many of these facets have angles above 20.9° whereby reflection reduction is achievable on the majority of crystal orientations. Similarly, for the texture etch, a far larger range of crystals further away from the (100) with tilted pyramid textures now experience multiple bounce incidence of light and thus low reflectances. However the random orientation of the crystals in the multicrystalline wafers mean that overall reflectances for both saw-damage and texture etches remain higher than for pyramidally textured monocrystalline (100) silicon, since the total reflectance is overweighted particularly flat etching and high reflecting orientations, these being the (100) and (111) for the saw-damage etch, and the {XXY} orientations between the (110) and (111) for the texture etch.

Despite the reflection reduction achieved due to light confinement on encapsulation, the level of reflectance measured for the texture etched wafers was far higher than expected by theory. This theory dictates that alkaline texture etching exposes exclusively {111} facets, whereby (tilted) pyramids form on (near) {100} orientations, with textures tending to two-dimensional V-shaped grooves on {110}, with (near) {111} orientations etching flat to their base orientation. Experimentation showed that the {111} facets were indeed particularly stable to

etching, so that (tilted) pyramidal textures formed on (near) {100} oriented crystals. However it was determined that in addition to the {111} crystallographic planes, the whole range of {XXY} planes is also exposed for the etch duration used. This results in lower facet tilt angles than expected from theory, in particular for the orientations close to the {110}.

However, the speed of development of the texture was in itself orientation dependent. Thus whilst a particular etch duration may lead to microscopically flat {111} etch facets on the (100) orientation for example, a longer etch duration may be required for the full development of tilted pyramid structures for example. This would imply that rounded or "split" facets, or an untextured background as observed by microscopy of the etch surfaces are simply a sign of an earlier stage of stage of development of the etch structure on a slower etching orientation. A longer etch duration allows a more complete development of the {111} facets on tilted pyramid textures. However, etching for a longer period paradoxically leads to increasingly flat, polished surfaces for the (XXY) orientations, which are detrimental to reflection reduction. This is particularly important for the {110} orientations, which according to texture etch theory should yield low encapsulated reflectances comparable to pyramids on (100) silicon by virtue of V-grooves at 35° to the base, but instead etches flat with prolonged etching. As a result, a far larger proportion of crystals in the encapsulated multicrystalline reflect light away at near normal angles to the wafer surface, whereby light confinement is less effective than predicted theoretically. The theory of {111} exclusivity in texture etching is thus proven to be invalid in this case.

References

[1] E. Hecht, "Optics", Addison-Wesley Publishing Company Inc. 2nd Edition (1987)

[2] P. Basore, "Defining Terms for Crystalline Silicon Solar Cells", Prog. Photovolt: Res. Appl. **2** (1994) 177-179

[3] A.R. Burgers, R. Kinderman, J.D. Hylton, W.C. Sinke, "Comparison of alkaline etches on multi-crystalline wafers", in Proc. 13th EPVSEC, Nice (1995) 129-132

[4] A. Eyer, I. Reis, "Defects in crystalline silicon for solar cells (dixsi): A co-operative German research project.", in Proc. 1st WCPEC, Hawaii (1994) 1587-1590

[5] A. Voigt, E. Wolf, H.P. Strunk, "Grain Orientation and Grain Boundaries in Cast Multicrystalline Silicon", in Proc. 14th EPVSEC, Barcelona (1997) 774-777

[6] D. Franke, M. Apel, C. Häβler and W. Koch, "Effect of multicrystalline structure on dislocation multiplication in cast silicon", in Proc. 16th EPVSEC, Glasgow (2000), 1317-1320

[7] J.D. Hylton, A.R. Burgers, R. Kinderman, W.C. Sinke, "Determination of facet orientations on alkaline etched multicrystalline wafers", in Proc. 25th IEEE PVSC, Washington (1996) 1339-1342

[8] B.L. Sopori, "Reflection characteristics of textured polycrystalline silicon substrates for solar cells", Solar cells **25** (1988) 15-26

[9] S. Tan, M.L. Reed, H. Han, R. Boudreau, "Mechanisms of Etch Hillock Formation", J. Microelectromechanical Systems **5** no. 1 (1996) 66-72

[10] J.F. Nijs, J. Szlufcik, J. Poortmans, S. Sivoththaman, R.P. Mertens, "Crystalline Silicon Solar Cell Technology for Today and Tomorrow", in Proc. 16th EPVSEC, Glasgow (2000) 1064-1069

[11] M. Spiegel, C. Gerhards, F. Huster, W. Jooss, P. Fath, E. Bucher, "Industrially attractive front contact formation methods for mechanically V-textured multicrystalline silicon solar cells", Solar Energy Materials & Solar Cells **74** (2002) 175-182

[12] S. de Wolf, P. Choulat, E. Vazsonyi, R. Einhaus, E. v. Kerschaver, K.de Clercq, J. Szlufcik, "Towards Industrial Application of Isotropic Texturing for Multi-Crystalline Silicon Solar Cells", in Proc. 16th EPVSEC, Glasgow (2000) 1521-1523

[13] R. Brendel, "SUNRAYS: A versatile ray tracing program for the photovoltaic community", in Proc. 12th EPVSEC, Amsterdam (1994) 1339-1342

[14] R. Brendel, "SUNRAYS 1.0 Manual", Sunrays program and user manual, distributed by Garching Innovation GmbH

[15] P. Campbell, S.R. Wenham, M.A. Green, "Light trapping and reflection control in solar cells using tilted crystallographic surface textures", Solar Energy Materials and Solar Cells **31** (1993) 133-153

[16] E. Schoonderwaldt, "Hoekafhankelijke reflectiemetingen aan getextureerde silicium zonnecellen", MSc. Dissertation University of Amsterdam (1998), ECN memo number ECN-DE Memo-98-010

[17] Algorithm from A.R. Burgers, ECN, private communication

[18] B.L. Sopori, R.A. Pryor, "Design of Antireflection Coatings for Textured Silicon Solar Cells", Solar Cells **8** (1983) 249-261

[19] P.K. Pal, S.K. Datta, K. Mukhopadhyay, H. Saha, "Role of antireflection coating in microgrooved silicon solar cells", Solar Energy Materials and Solar Cells **43** (1996) 1-14

[20] H, Nagel, A.G. Aberle, R. Hezel, "Optimised antireflection coatings for planar silicon solar cells using remote PECVD silicon nitride and porous silicon dioxide", Prog. Photovolt: Res. Appl. **7** (1999) 245-160

[21] F.M. Schuurmans, A. Schönecker, J.A. Eikelboom, W.C. Sinke, "Crystal-orientation dependence of surface recombination velocity for silicon nitride passivated silicon wafers", in Proc. 25th IEEE PVSC, Washington (1996) 485-488

5: Light trapping in thin alkaline etched multicrystalline silicon wafers

Light trapping as reflection reduction is found to be dependent upon the facet angles of the geometrical surface texture. Considering the principal triangle of (100):(110):(111) orientations, for high concentration alkaline saw-damage etching, central orientations around the (321) with the highest facet tilt angles, provide high levels of light trapping which with a back surface reflector can approach Lambertian levels. In contrast, the flat surfaces yielded on saw-damage etched (100) and (111) orientations have poor light trapping properties.

For low concentration alkaline texture etching, light trapping is greatest for the highly facetted pyramidal textures on near (100) orientations, decreasing to the levels of polished silicon for the flat etching {XXY} orientations between (111) and (110).

The particularly poor light trapping for the {XXY} texture etched orientations means that overall, saw-damage etched multicrystalline wafers have higher levels of light trapping (in terms of the absorption efficiency of light after its initial coupling into the silicon) than texture etched multicrystalline wafers etched to the same depth. However, front surface reflection, particularly under encapsulation, has a far greater influence upon the electrical output achievable than light trapping for the 200 μm thick multicrystalline wafers investigated. Thus texture etched multicrystalline wafers, with lower reflectance by virtue of the particularly high facet angles (up to 55°) present upon (tilted) pyramid textures, have slightly higher maximum short circuit current values than saw-damage etched wafers.

5.1 Introduction

5.1.1 Thin silicon wafers

One way of reducing the costs of silicon solar cell production is to reduce the quantity of the expensive silicon base material used. Improved wafering techniques allow the production of thinner silicon slices from ingots, from typical thicknesses currently of 300 μm down to thicknesses of under 150 μm. The reduction in the silicon volume also has a physical advantage, in that bulk recombination is correspondingly reduced. This will be seen in a

higher open-circuit voltage for the cell, provided that the front and rear of the cell are well passivated to ensure minimum surface recombination [1,2].

5.1.2 Absorption in silicon

However, the poor absorption of the silicon at longer near infra-red wavelengths (see Chapter 1) is a problem on reducing the cell thickness. As the silicon thickness decreases, more light will be partially transmitted out of the cell without the formation of an electron-hole pair, thereby reducing the electrical output of the cell. Figure 5.1 shows the absorption of different wavelengths of light as a function of distance travelled in the silicon, showing the fraction of light which would be absorbed for cells of different thicknesses.

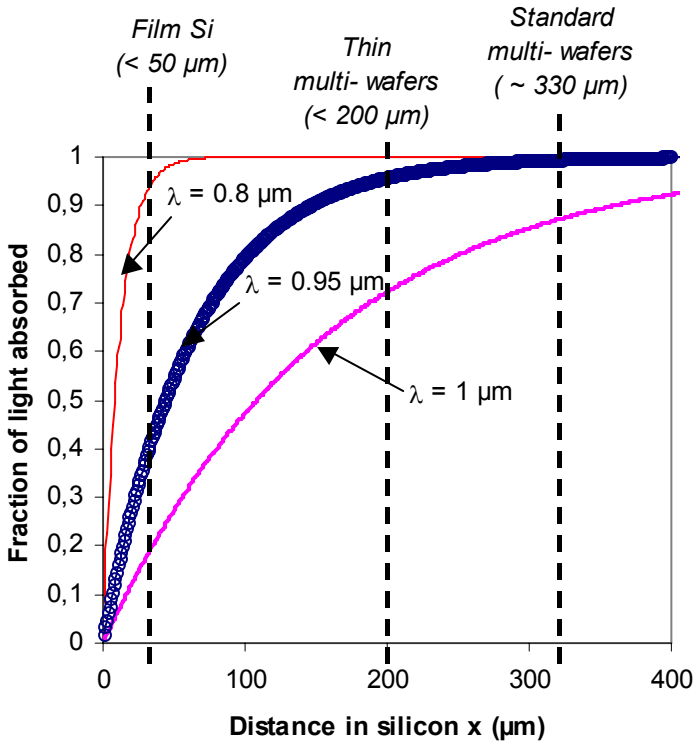

Figure 5.1 *Fraction of light absorbed for a distance x travelled within the silicon, as a function of the wavelength.*

Light trapping schemes (see Chapter 1), incorporating for example highly reflective rears, geometric or randomising textures, are essential. Such schemes ensure that light at partially transmitted wavelengths attain pathlengths within the silicon which are long enough to maximise absorption.

5.1.3 Randomisation schemes

The theoretical light trapping scheme proposed by Goetzberger [3] incorporates both high back-surface reflectance and trapping by TIR. The planar silicon wafer in this system has a 100% reflecting back surface, which additionally is completely diffuse or "Lambertian", giving complete randomisation of all light incident at the rear, as is shown in Figure 5.2. Light falling incident upon the rear of the wafer will be reflected in a completely random hemispherical direction, regardless of its initial (normal) angle of incidence, as shown by rays 1 and 2 in the figure. Light which is reflected from the rear at an angle θ less than the critical

angle θ_c for the silicon-air interface will be transmitted through the front surface, as is shown for ray 1. Light reflected from the rear at angles $\theta > \theta_c$, as for ray 2 in Figure 5.2, will be totally internally reflected at the front surface and thereby trapped for at least two more passes through the silicon wafer, thereby increasing the pathlength of the light in the cell and the possibility of absorption.

Goetzberger calculated that on each passage of the light from the randomizing rear to the front of the cell, a fraction $1/n^2$ of the light will lie within a low enough angle to escape the front surface (where n is the refractive index of the silicon), assuming the front surface is 100% transmitting. The rest of the light receives TIR at the front surface; assuming $n = 3.42$ as [3], the critical angle is 17° for the silicon-air interface, and the percentage of light escaping is only 8.55% for each second pass through the wafer. The maximum pathlength enhancement achievable for light in this system is equal to $4n^2$ [4].

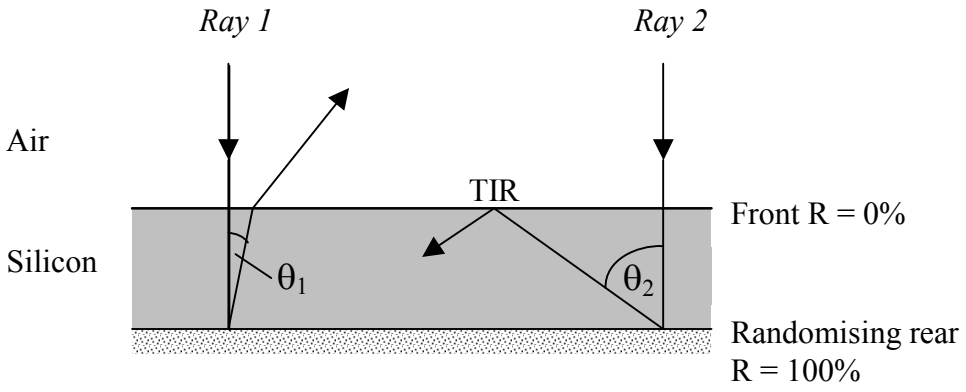

Figure 5.2 *Lambertian light trapping scheme proposed in [3].*
R = reflectance, TIR = total internal reflectance.

5.1.4 Light trapping with geometrical surface texture

Geometrical surface textures provide light trapping by TIR of light approaching the texture facets at angles $\theta > \theta_c$ for the silicon-encapsulant interface. For the rear surface geometrical texture shown in Figure 5.3, the texture facets have tilt angles satisfying this condition for light incident normally to the wafer front surface. Thus for this case, all light reaching the rear of the wafer will be trapped both for a second and at least a third pass in the silicon, in the latter case due to light experiencing TIR at the front surface as shown.

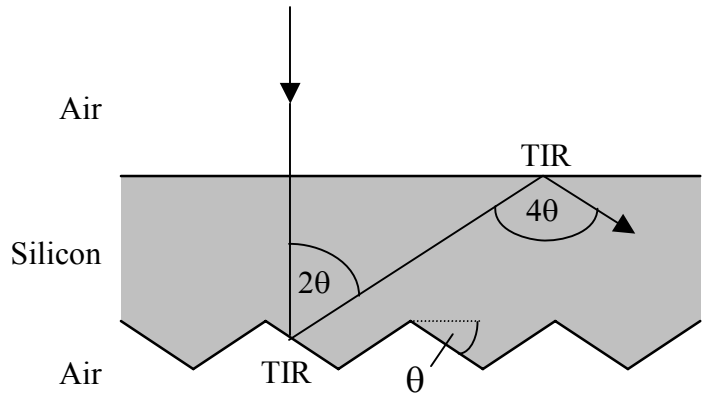

Figure 5.3 *Light trapping due to a rear geometrical texture with facet tilt angle $\theta > \theta_c$ where θ_c is the critical angle for the silicon-air interface (front surface R = 0%).*

5.1.5 Alkaline etched multicrystalline silicon wafers

As was discussed in Chapter 4, the etch surface geometries in multicrystalline alkaline etched wafers are particularly complex. The resulting surface morphology is dependent upon the composition, temperature and duration of the etch, as well as being orientation dependent so that, since crystal orientations are random for the multicrystalline silicon, any number of different geometries may be present over the wafer.

Figure 5.4 shows the measured reflectance curves as in Figure 4.3 from the previous chapter, for the saw-damage and the texture etched multicrystalline wafers in air, except now detailing only the reflectance at longer wavelengths where the wafers become transmitting. For wavelengths between 0.8 and 1 μm, we see the differences in front surface reflectances for the two etches resulting from the differences in texture, the lower reflectance for the texture etch resulting from the higher angles of the facets (see Chapter 4). Thereafter we see the rise in reflectance due to the back surface reflectance component, with both wafers rising to similar final reflectance values of around 46%. This latter part of the curve comprises not only the components of front and back surface reflectance, but importantly also depends upon the effectiveness with which light is absorbed in the bulk. This latter point in particular is intrinsically linked with the length of the paths travelled by the light before either absorption within or coupling out of the silicon, this being dependent again upon the effectiveness of light trapping as a result of the geometry of the etch surfaces.

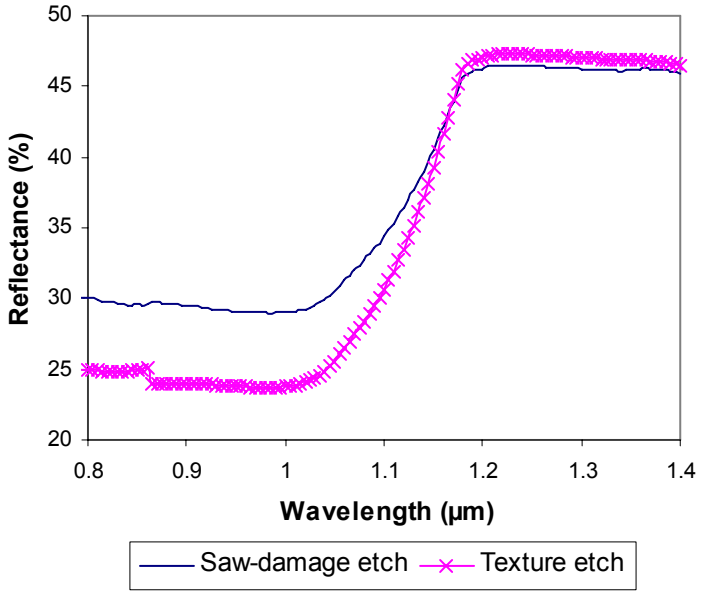

Figure 5.4 *Measured reflectances of saw-damage and texture etched multicrystalline silicon wafers in air (as-cut thickness 330 µm).*

5.1.6 This chapter

In this chapter, it is aimed to establish the quality of light trapping for alkaline etched multicrystalline wafers with a double sided etch texture, in comparison to an ideal theoretical randomisation scheme, and to show how the levels of light trapping can be improved through using a back surface reflector. Important to this work is the use of actual experimental data, using height mappings of the textured surfaces from atomic force microscopy (AFM) as input for the ray-tracing programs used for analysis. Calculations can thereby be directly related to the particular textured wafers investigated through comparison of the measured and calculated reflectances. By optical and ray tracing analysis of samples made experimentally, the light trapping properties can be described quantitatively for the multicrystalline wafers.

5.2 Modelling of optical properties

5.2.1 Introduction

As has been highlighted throughout this thesis, the quantification of the (alkaline) etch texture geometries on the individual crystal orientations is essential to the understanding of the reflection reducing and light trapping properties of the (multicrystalline) silicon. For relatively lightly facetted textures, such as those obtained with a concentrated alkaline saw-damage etch [5,6], optical properties can be well approximated for the entire multicrystalline wafer by assigning a roughness factor to the scattering surfaces [7]. However, this assumes the same level of scattering for all crystal orientations, implying all orientations yield similar levels of faceting, which as has been shown in Chapter 4 is not the case, neither for saw-damage or texture etch structures. Also, in particular for the case of geometrical structures resulting from low concentration alkaline texture etching, the highly faceted texture geometries lead to highly directional and angular dependent (multiple) reflections, as described in Chapter 4, which are poorly modelled by such approximations to a scattering surface.

Solar cell ray-tracing programs such as "Sunrays" (see section 4.2.5 and ref. [8]) allow a restricted range of texture geometries to be defined in terms of a unit cell with fixed dimensions, facet angles and cell thickness, with periodic structures based generally on 2D grooves, three or four-sided pyramids or hexagonal structures. Real structures formed from unmasked chemical (alkaline) etching are thereby difficult to model. For example the only orientation dependent textures which can be modelled by Sunrays are based on low concentration texture etching theory, assuming the exposure of {111} etch facets exclusively (see Chapter 4). It is not possible to accommodate for other stable facets as present for high concentration saw-damage etching or indeed for {XXY} orientations during the texture etching, which is been shown not to conform to the general texture etching theory (see chapter 4). The development of the etch texture is also not accounted for, nor is it possible to model variations in texture size or untextured regions between texture features. Also, modelling is restricted to single front surface textures.

5.2.2 Ray-tracing with program "Birandy"

"Birandy" [9] is a ray-tracing program where the defined texture geometry is no longer confined to restricted unit cell structures. Here, detailed height scans obtained using atomic force microscopy provide the quantitative description of the textured surface. When the incident light ray reaches the textured interface at a point (x,y) of the AFM scan with height z, the surface normal is determined locally from the vector product of the lines linking 4 adjacent data points in the scan (left and right, above and below) and the angle between the ray and surface normal determined. The decision for reflection or refraction is made according to the reflection coefficients, which are pre-calculated as a function of wavelength and incident angle using the matrix method [10,11] for any number of thin films. The reflectance probability for the unpolarised light is calculated from the average of those calculated for the s and p polarisations (electric and magnetic fields in the plane of the incident surface), this approximation having been shown [12] to have negligible effect. It is hereby possible to quantify the true surface geometry for areas large enough to encompass several texture features, so that the texture input is representative of the texture present over the entire crystal. The use of the actual etch surface morphology is preferable for example to

the re-constructed surface morphology proposed in [13] for random pyramid textures. In this case, although experimental data (based on stereographic scans made with scanning electron microscopy SEM) is used, reconstruction of the surface topography uses algorithms which assume the presence of specific crystallographic etch facets (namely {111} facets from texture etch theory, see Chapter 4). This assumption limits the accuracy and at worst (should it be applied to texture etched {XXY} orientations for example) the correctness of the reconstructed model.

5.2.3 Adaptations to Birandy for this work

The original program allows the calculation of several parameters, including the pathlength distribution of the light (in terms of the fraction of rays remaining in the silicon as a function of the pathlength in the silicon), surface reflectance values and maximum short-circuit current densities J_{sc}(max). J_{sc}(max) was calculated using the pathlength distribution at a single (non-absorbing) wavelength. Absorption A in the media was calculated in the silicon only, as the light is incremented spatially along its path (in steps of 0.1 μm) from $A(\lambda)=1-e^{-\alpha(\lambda)x}$, where $\alpha(\lambda)$ is the absorption coefficient of the Si and x is the pathlength travelled within the Si. Tracing is stopped if light is completely absorbed or if the light escapes the cell system, for example into the surrounding air or being lost by absorption in the back surface reflector. Only the angles of incidence and refraction were calculated at the interfaces between absorbing layers, for example at the glass-air interface, before the light continued upon its path. This method thereby neglected possible absorption in the media surrounding the silicon.

The program was adapted so that for the case where the silicon is encapsulated in (partially absorbing) media such as glass, the pathlength of light in these media is recorded and absorption calculated prior to transmission into the silicon, after which the intensity of the light is reduced accordingly. This gives correct values for the wavelength dependent total reflectance, absorption and ultimately for the maximum obtainable J_{sc} in the silicon, whereby the absorbing properties of the other layers surrounding the silicon are accounted for. The total reflectance, absorption and J_{sc}(max) values calculated for typical light trapping structures (e.g. geometrical grooves and pyramids) are compared to values obtained with the ray-tracing program Sunrays in Appendix A of this thesis.

The program was also adapted in this work to allow modelling where the front surface texture had a different (input AFM) texture to the rear. Another change was the treatment of light on reaching the edge of the defined surface (i.e. the edge of the AFM scan area). In the original program, light was simply reflected back again with only the z direction remaining unchanged, as shown in Figure 5.5. This was done due to the non-continuity between the opposite edges of the surface, whereby for example light exiting the one edge from below the silicon-glass boundary could be translated to a position above this boundary on the opposite edge, despite having the same height. This method however gives an unrealistic passage of the light through the silicon for the geometric textures being investigated, as Figure 5.5 shows. The program was thus adapted to use periodic boundary conditions, whereby the directional properties of the light passage are maintained in x, y and z directions, by translating the light to the opposite side of the cell. The position of the ray was controlled with respect to the front/rear surface height at the transfer position as compared to its initial position; if the ray now was positioned on the wrong side of the surface boundary, it was set to a position just above/below the surface on the correct side of the surface.

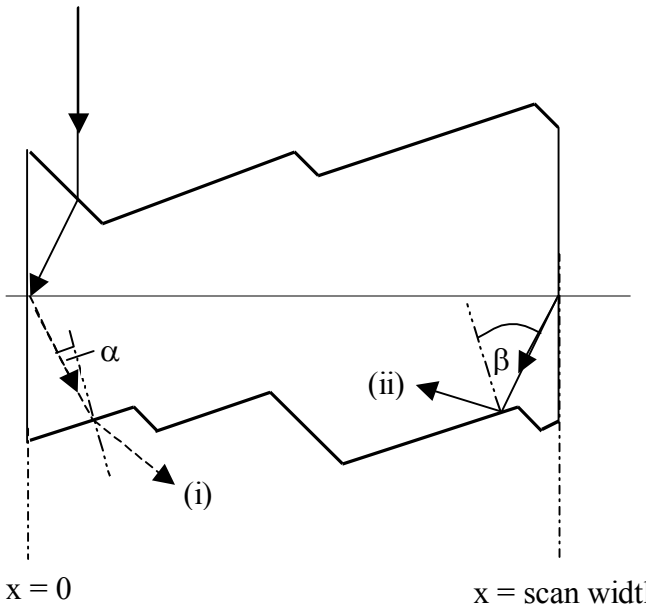

Figure 5.5 *Transfer of ray positions on encountering the edge of the AFM scan area. (i) In the original program, light is reflected in the z direction to approach the rear at an incorrect angle α. (ii) In the adapted program, light is transferred to the opposing edge of the wafer and continues in the same directional path to approach the rear at the correct angle β.*

5.2.4 Limitations to AFM input data

The AFM height data consists of 256 x 256 data points (see Chapter 2.4.3). However, the program Birandy is a DOS-based program (Pascal program language), whereby memory restrictions limit the maximum number of input data points to 170 x 170 data points for each side (front and back) of the wafer. A program was made [14] whereby the AFM height data scan could be reduced either by a) dividing the scan into four quadrants of up to 170 x 170 data points per quadrant using adjacent data points in the original height scan, or b) using every second data point of the starting scan to give a single scan of 128 x 128 data points. The advantage of the former case is the higher resolution of the input data, twice that of in the latter case, whilst the second option allows a larger scan area to be used for ray tracing. In general, the second option was used, especially in the case of very small (10 x 10 and 20 x 20 μm) scan areas. However, 170 x 170 (or smaller) scan quadrants were also used, particularly where the original AFM scan clearly had poorly measured regions where peaks and troughs lay beyond the z range of the scanner.

5.3 Experimentation

5.3.1 Wafers used in experimentation

The same seven monocrystalline wafer orientations used in Chapter 4 form the basis of experimentation and modelling in this chapter, in addition to thin, neighbouring, multicrystalline wafers (approximately 200 μm thick, compared with the current standard of 330 μm as-cut). The orientations of the monocrystalline wafers are distributed evenly over the triangle joining the (normals to the) principal (100), (110) and (111) crystallographic

planes, as was described in section 4.2.1 and Figure 4.4, so as to represent the extent of variation in surface morphology over alkaline etched multicrystalline wafers.

The initially polished/as-lapped monocrystalline wafers, with starting thickness of 525 μm, were first sandblasted with Al_2O_3 powder followed by thorough rinsing and cleaning step to give a starting surface equivalent to as-cut wafers. Both mono- and multicrystalline wafers then received either a high concentration saw-damage etch or low concentration texture etch, for etch durations yielding a total etch depth of 25 μm by weight on the as-cut multicrystalline silicon.

5.3.2 AFM height mapping of monocrystalline wafers

The alkaline etched monocrystalline wafers were scanned using atomic force microscopy (AFM), as described in Chapter 2. This yielded the height mappings shown previously in Figures 4.7 and 4.11 for the 7 orientations with saw-damage and texture etches respectively. These height mappings (with adjustments to data format as discussed in section 5.2.4 previously) were used as the basis of ray-tracing in the program Birandy for the structures investigated.

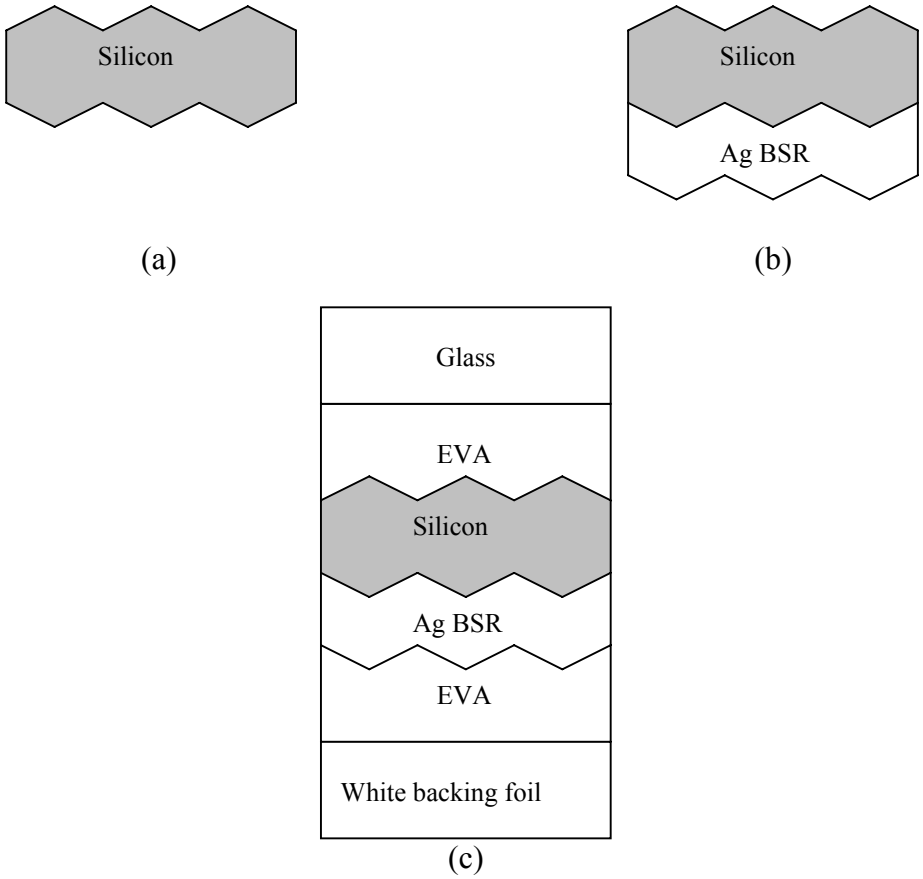

Figure 5.6 *The different systems investigated in experimentation. a) bare silicon in air, b) bare silicon with an intimate Ag BSR, c) encapsulated silicon with an intimate Ag BSR. In case c, the rear EVA and backing foil play no role since light incident at the silicon-Ag interface is either reflected into the silicon or absorbed in the 250 nm thick Ag layer.*

5.3.3 Wafer structures investigated

Three systems were investigated, for the geometrically textured wafers with and without a back surface reflector (BSR) or encapsulation, namely: (a) the bare wafer in air, (b) the wafer in air with an intimate silver BSR, (c) the wafer with an Ag BSR encapsulated under glass and ethyl vinyl acetate (EVA) at the front with EVA followed by a typical module white backing foil at the rear. These systems are shown schematically in Figure 5.6 below.

These systems were made experimentally on the neighbouring alkaline etched multicrystalline wafers. The total reflectances of the different multicrystalline wafer schemes were measured using the integrating sphere/spectroradiometer set-up described in chapter 2, so that the results of ray-tracing could be compared to the situation in practice. The Ag BSR was applied using vacuum deposition with a thickness of approximately 250 nm. Cell laminates were made using window glass with an average thickness of 2.85 mm, corresponding to the 3 mm module glass thickness used typically for finished photovoltaic silicon solar cell modules. The front EVA layer thickness was approximately 0.33 mm. The white backing foil used is from ICOSOLAR, nr. 2116, comprising of a primer layer on top of a film of PETP (polyethylene terephtalate), followed by Al and PVF (polyvinylfluoride, trade name "Tedlar") as base.

5.3.4 Determining the optical characteristics of glass and EVA

In order to correctly model the optical characteristics of the encapsulated wafers, it was necessary to find the wavelength dependent *n* and *k* components of the refractive index (see Chapter 1) for the glass and for the EVA, as shown in Figure 5.7a. These components were derived for glass and EVA from calculations based on reflectance and transmission measurements on the glass and on the glass-EVA-glass sandwich, as described in reference [15]. The corresponding absorption coefficients are compared to those of silicon in Figure 5.7b.

The large absorption peak in the EVA at 1200 nm has minimal influence on silicon absorption since it is beyond the silicon bandgap. The absorption in the window glass, which gradually increases with wavelength is more significant, especially considering the greater thickness of the glass (~3 mm) through which light must travel relative to the silicon (of ~200 μm thickness) as the absorption coefficients for the two media become equivalent. Figure 5.7c compares the absorption in the glass, EVA and silicon as a function of the distance travelled by light of wavelength $\lambda = 1.1$ μm within the respective materials. The absorption coefficients for the glass, EVA and silicon are 0.49 cm^{-1}, 0.01 cm^{-1} and 3.5 cm^{-1} respectively. However, a single (undiverted) pass for example through the ~3 mm thick encapsulation sees the intensity drop to 87% of its initial value, a single pass through the ~300 μm thick EVA sees only a 0.03% drop in intensity (i.e. light travels through almost unattenuated) whilst for the ~200 μm thick silicon, a single pass constitutes a drop to 94% of the initial intensity due to useful optical absorption in the silicon. In other words, percentually more light is lost on a single pass through the encapsulation than is usefully absorbed on a single pass through the silicon. It therefore becomes essential at longer wavelengths that light be trapped within the silicon for as long as possible, particularly within the first passes where the energy content of the light is greatest, with as few passes into the encapsulation as is possible.

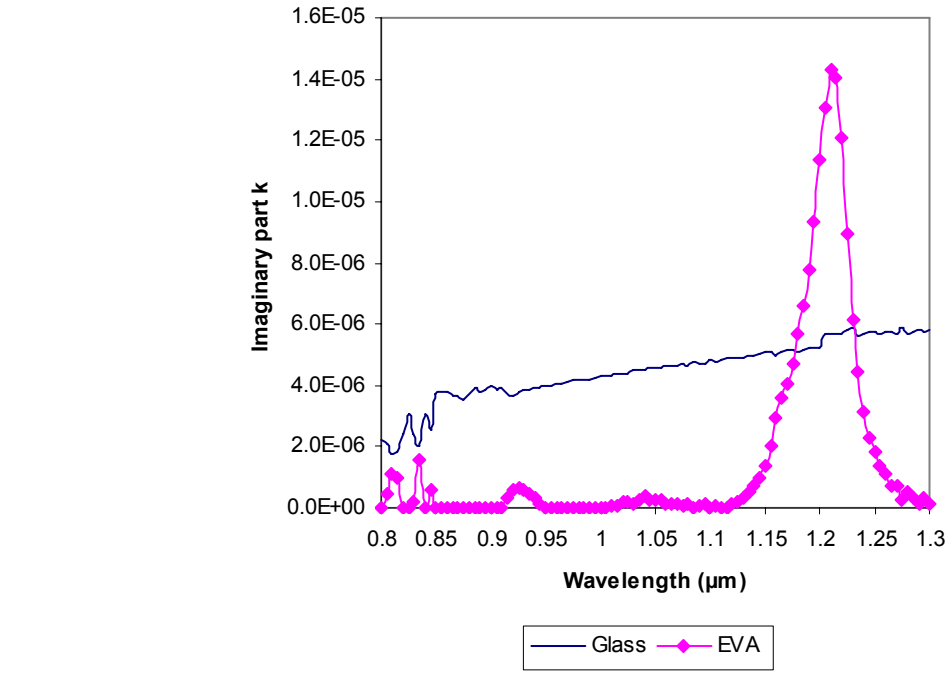

(a)

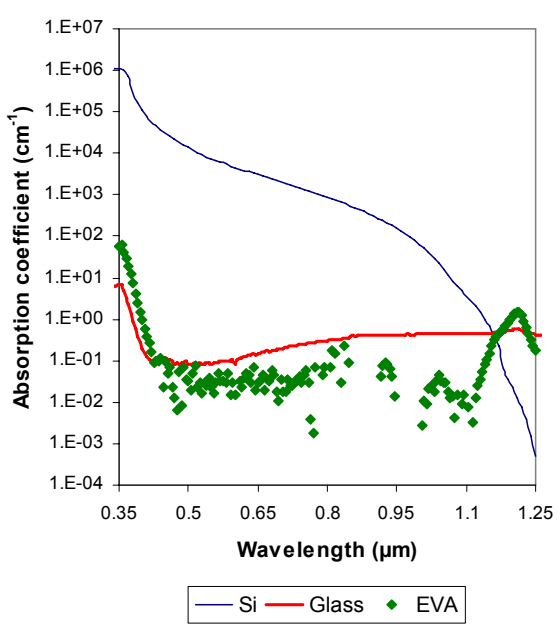

(b)

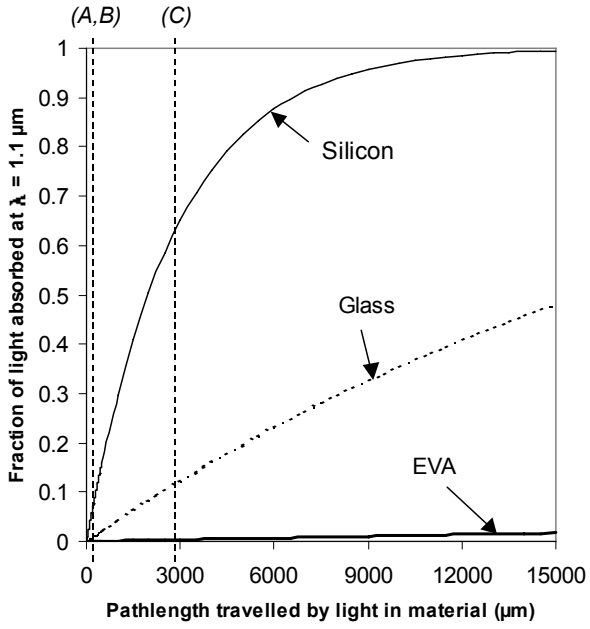

(c)

Figure 5.7 (a) *Experimentally determined optical k values for glass and EVA as used for modelling. The n value for both the glass and EVA used was approximately 1.5 over this wavelength range. (b) Corresponding absorption coefficients for the front encapsulation compared to silicon as calculated from the experimentally determined n & k values. (c) Fraction of light absorbed as a function of distance travelled in the glass, EVA or silicon for light at a wavelength λ = 1.1 µm. (A), (B) and (C) correspond to the thicknesses of the silicon, EVA and glass (approximately 200 µm, 300 µm and 3000 µm respectively).*

5.4 Results

5.4.1 Saw-damage etched monocrystalline silicon wafers

5.4.1.1 Light trapping due to surface texturisation

Figure 5.8 shows the pathlength distributions for the seven representative monocrystalline wafer orientations in air, as compared to polished silicon and an ideal Lambertian light trapping scheme (i.e. 0% reflecting front and 100% reflecting, 100% scattering rear). A logarithmic scale is used for the pathlength distributions in accordance with the exponential nature of light absorption within the silicon in relation to the pathlength travelled within the wafer. The pathlength distributions can be used to calculate the absorption efficiency *a* as also shown in Figure 5.8 (i.e. the percentage of the light coupled into the silicon which is actually absorbed in the wafer) as a function of wavelength, from a summation of the amount of light absorbed per ray entering the silicon. The absorption efficiency is defined as $a = 1-\exp(-\alpha(\lambda)x)$ (where x = the distance travelled by the light in the silicon and $\alpha(\lambda)$ = wavelength dependent absorption coefficient). For light at the non-transmitting lower wavelengths, the absorption efficiencies will be 100%, since the absorption lengths for the light are less than the thickness of the silicon. For longer partially transmitting wavelengths, the fraction of the coupled light which can be absorbed will be dependent upon how effectively light is trapped within the silicon. The same equation forms the basis of calculations for the wafer under encapsulation, except that where light is transmitted temporarily into the (partially absorbing) encapsulant, its pathlength within this medium is recorded and the light intensity reduced accordingly prior to re-entering the silicon, this being accounted for in the calculation. The total wafer thicknesses used for calculations varied from 190 μm for the slow etching (111) as compared to 177 μm for the (100) orientation, based on an average thickness of 186 μm after saw-damage etching of the multicrystalline wafers used; for saw-damage etch rates see chapter 4. For the polished and Lambertian schemes a thickness of 186 μm was used.

For all the textured wafer orientations, it can be seen that a relatively large proportion of light is lost after the first pass due to transmission at the rear. This is typical for double sided etch textures [15], due to the coupling of light out of the silicon through rear facets positioned parallel to the entrance facets on the front of the wafer. This is especially true of the (100) and (111) orientations, for which the majority of the saw-damage etch surface consists of essentially planar crater-like etch pits (see Chapter 4.3.1.1), although height differences between individual etch pits, terracing on the base of the craters for the (111) and the ridges between the pits lead to far rougher surfaces than for planar silicon. Light falling incident upon the craters at the front surface is thereby barely refracted from normal incidence and is easily coupled through craters at the rear, so that light trapping for the first pass is almost as poor as for a polished silicon wafer. For the remaining orientations, the non-periodicity and complexity of the textured surfaces limit the proportion of parallel front and rear faces, so that less light is lost for the first pass. As such, the orientations can be divided into two groups according to this initial level of transmission. The first group comprises the flattest etching (100) and (111) orientations which lose approximately 50 - 55% of light through the rear on the first pass. The second group, containing the remaining five orientations, has a far lower rear surface transmission, with 70 - 80% of light remaining trapped in the silicon after the first pass. In this latter case, (average) texture facet angles are greater than 17°, with the most effective (110) orientation having facet angles up to 40° or more (see Chapter 4.3.1 for detailed texture analysis for all orientations).

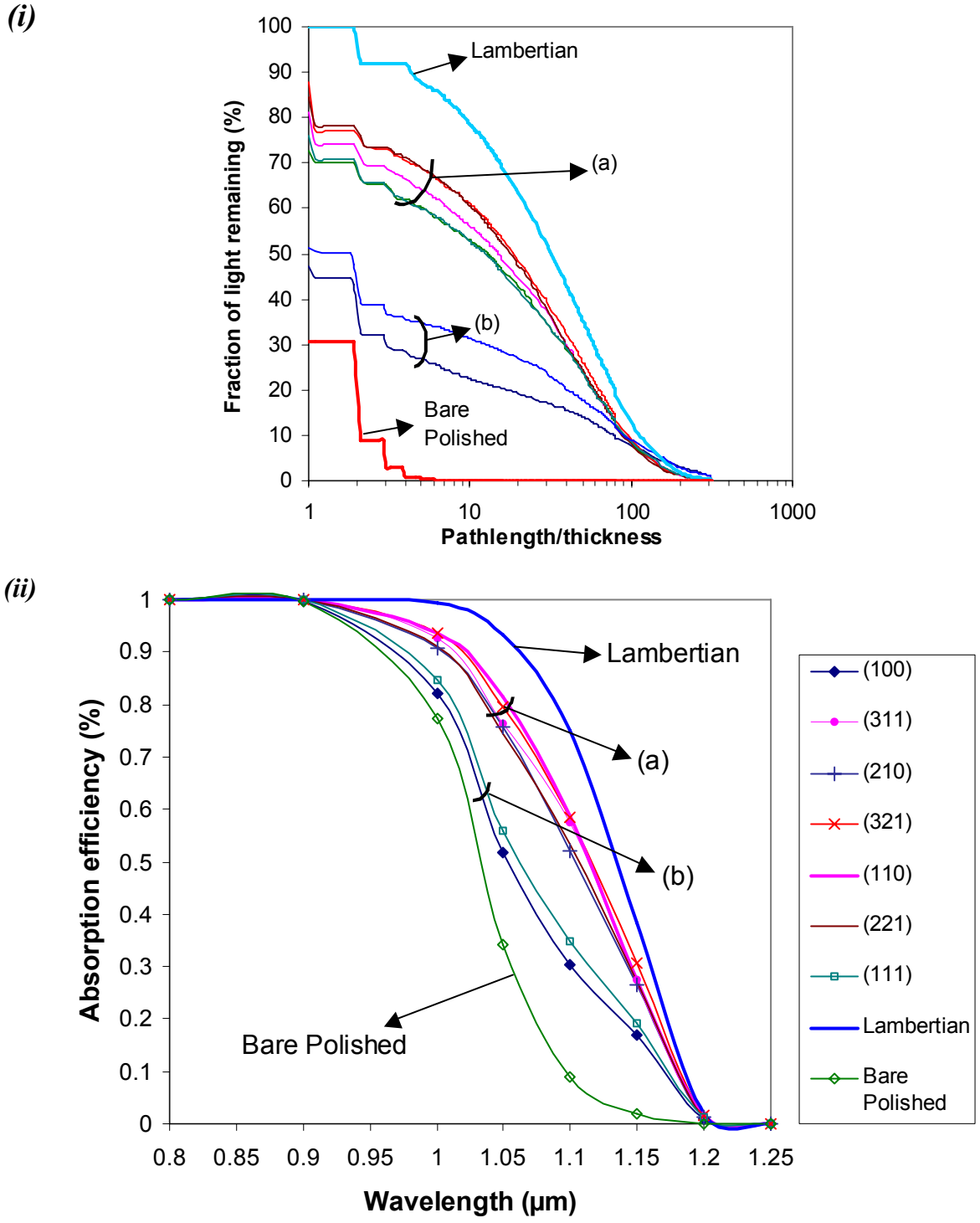

Figure 5.8 *(i) Pathlength distributions and (ii) absorption efficiencies for 7 orientations of monocrystalline silicon with saw-damage etch. (a) corresponds to the group of 5 best performing wafers, in order (110), (321), (311), (210) and (221), and (b) corresponds to the rather flatter etching (111) and (100) orientations.*

Light is trapped more efficiently on subsequent passes. The step-shaped pattern of the pathlength distributions seen for the most extreme case of the planar silicon, becomes steadily shallower for the saw-damage etched wafers within the first 3 passes. This indicates that a

decreasing proportion of the light is able to escape the silicon either without diversion into angles facilitating TIR at the surfaces or else to escape through parallel faces. Thereafter, the pathlength distribution smoothes out so that the step-shape of the distribution is barely visible and the curve tends gently to zero over tens of passes through the wafer. This suggests that the light paths are fairly well randomised within the silicon after 3 or 4 passes, with light scattered into increasingly differing oblique paths and travelling different pathlengths within the silicon, before hitting the textured surfaces at angles allowing either escape into air or trapping within the silicon by TIR.

Figure 5.8 (ii) shows the light trapping behaviour in terms of the absorption efficiency of light as a function of wavelength. For wavelengths up to 0.9 μm, light is absorbed before reaching the rear of the wafers, also for the case of polished silicon. Thereafter, the two groups of wafer orientations become visible (i.e. the more highly facetted central orientations compared to the flatter etching (111) and (100) orientations), as pathlengths exceed the wafer thickness and multiple passes are made within the silicon. At 1.1 μm, absorption efficiencies for the two groups of orientations are approximately 20 and 40% lower (for the central group of orientations and the flatter group of (100) & (111) respectively) than for the ideal Lambertian for which absorption is 75%. However, even the shallow faceting of the flatter (100) & (111) orientations provide higher light trapping levels than for polished silicon, which with an absorption efficiency of only 9% at 1.1 μm is 66% lower than the Lambertian case.

In summary, light trapping for the saw-damage etched textures is orientation dependent in accordance with the different levels of faceting present as a result of the anisotropic etch. For the seven orientations examined, the central orientations of (311), (210), (321), (110) and (221), with facet tilt angles up to 45°, have relatively high levels of light trapping. The surface texture is particularly effective in randomising the paths of the light in the silicon, with levels of randomisation approaching the Lambertian ideal after the initial 3-4 passes, However, light trapping is limited by the high percentage (20-30%) of light by rear transmission during the first few passes, which results from the coupling of light through facets at the rear positioned parallel to the entrance facets on the front of the wafer. The flatter etching (100) and (111) orientations are particularly affected by this escape mechanism, with the majority of the pitted etch surface being essentially planar. Correspondingly these orientations perform relatively poorly, with 50-55% of light lost by transmission at the rear within the first 3-4 passes, although despite this, randomisation and the resulting trapping of obliquely scattered light by virtue of the etch texture is relatively effective for subsequent passes. The employment of a back surface reflector is thereby essential to boost light trapping, in particular for the flatter orientations.

5.4.1.2 Effect of back surface reflectors and encapsulation

The two groups remain visible for the wafers with an Ag BSR as well as under encapsulation, with the order of light trapping performance remaining the same between the orientations. Figures 5.9 and 5.10 show the effect of the employing a BSR and/or encapsulation upon the level of light trapping for the two groups, for the examples of the (321) orientation and the flatter etching (100) orientation respectively.

The application of an Ag BSR leads to a higher trapping level after the first pass compared to the bare wafers, reflecting ~ 94% of light incident upon the rear, this higher level of trapping being continued for the remaining passes. The extra light trapped upon initial incidence at the

rear on the first pass through the silicon, is reflected into oblique paths increasing pathlengths, further increasing the level of randomisation within the silicon. The pathlength distributions for the five best performing wafers lie closer together on addition of the Ag BSR than in the bare wafer case.

Where an intimate Ag BSR is used under encapsulation, the fraction of light trapped is always slightly lower than for the wafers with an Ag BSR in air, particularly for the flatter (100) & (111) wafers. More light is lost on every second pass due to transmission into the front EVA-glass front encapsulation, due to the higher critical angle at the silicon-EVA interface as compared to the silicon-air interface (25° compared to 16.4° respectively at λ = 1.1 μm). Light escaping the silicon between these two critical angles will fall re-incident upon the silicon, since it will still be trapped within the system at the glass-air interface, which it will approach at angles equal to or above its critical angle θ_c = 41.8°. (From Snell's laws of refraction in e.g. [16], $n_{Si}sin\theta_{Si} = n_{glass}sin\theta_{glass} = n_{air}sin\theta_{air} = 1$ for TIR at the silicon-air and/or *glass-air* interface.) However, it will only be partially re-transmitted into the silicon, depending upon the texture facet angles of the silicon at the point of re-incidence and can in principle be partially coupled out of the system at the glass-air interface on subsequent passes. In addition, light escaping into the encapsulation in particular may be partially attenuated during its path through the glass in particular, removing energy which could otherwise be absorbed in the silicon and contribute to current generation. This is seen in the absorption curves in Figures 5.10 and 5.11 for wavelengths above 1.15 μm, in that absorption for the encapsulated wafers decreases below that of the bare wafers in air, as absorption pathlengths increase beyond several hundreds of passes through the cell and inevitably through the encapsulation.

In summary, the employment of an intimate Ag BSR significantly reduces initial transmission losses after the first pass at the rear of the silicon for light, in particular for light approaching the rear at near normal incidence at facets parallel to the front entrance facets. Although light incident at higher angles can now be partially absorbed in the silver rear as opposed to receiving TIR at the silicon-air interface, the high level of reflectance at the silicon-silver interface (~94%) ensures that the majority of all light entering the silicon will travel at least two passes within the silicon, these initial passes being most important for absorption. On the addition of encapsulation, light trapping remains higher than for the bare wafer in air on the whole. However it is somewhat less than for the wafer with an Ag BSR in air due to coupling of light out of the silicon into the slightly absorbing encapsulant during its passage through the system.

(a)

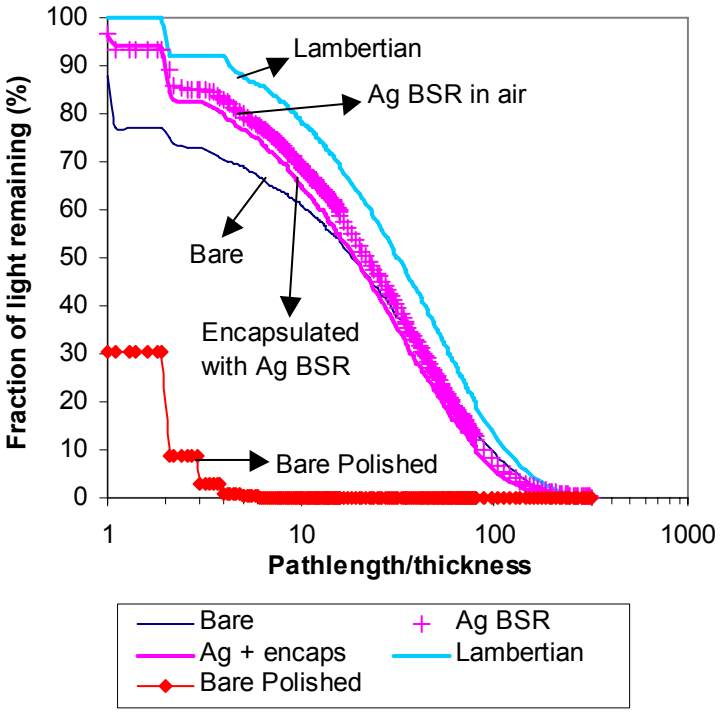

(b)

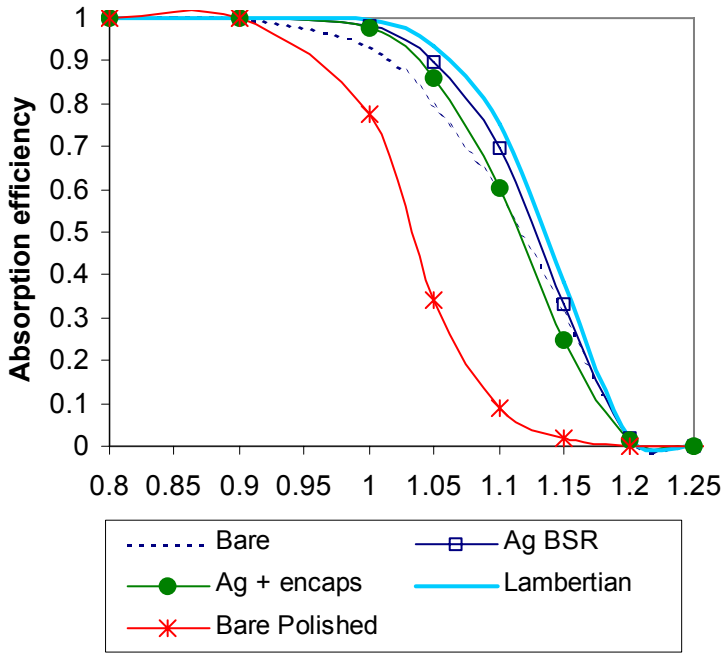

Figure 5.9 Effect of different back surface reflectors for saw-damage etched (321) monocrystalline silicon, with texture geometries yielding light trapping properties approaching Lambertian levels in air.
(a) Pathlength distributions and (b) absorption efficiencies.

(a)

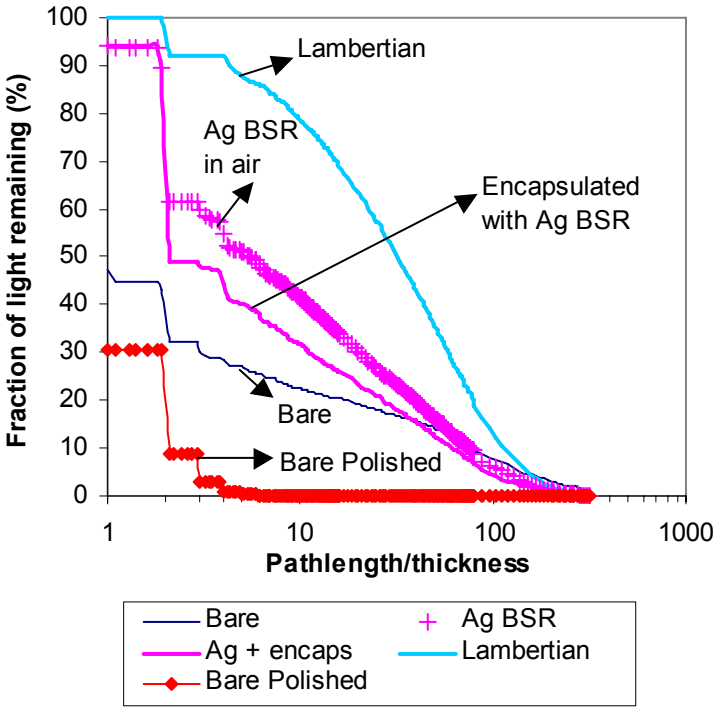

(b)

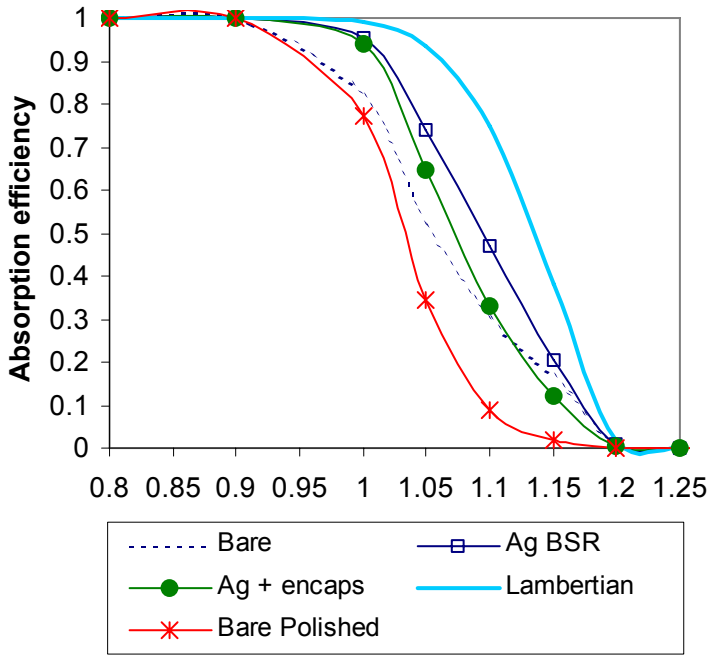

Figure 5.10 Effect of different back surface reflectors for saw-damage etched (100) monocrystalline silicon, with texture geometries giving poor light trapping in air. (a) Pathlength distributions and (b) absorption efficiencies.

5.4.1.3 Average pathlengths

Table 5.1 shows the average pathlengths calculated for the seven saw-damage etched wafer orientations with the systems investigated, as compared to the Lambertian ideal and to polished silicon. The average pathlengths fairly accurately indicate the relative levels of light trapping between the seven orientations and the light trapping scheme employed, in

accordance with the observations above, with the pathlengths tending to a maximum around the central (321) orientation in all cases.

	Lambertian	(100)	(311)	(210)	(321)	(110)	(221)	(111)	Polished
Bare	49.8	23.4	34.4	33.4	37.0	34.9	33.6	28.4	1.5
Ag BSR		25.3	35.9	35.5	37.6	36.7	33.4	29.3	2.9
Encaps + Ag BSR		19.9	32.8	30.5	34.7	32.7	30.9	22.7	2.4

Table 5.1 *Average pathlength enhancement for light at λ = 1.25 μm in the seven saw-damage etched monocrystalline wafer orientations for the three schemes investigated.*

However, as was demonstrated in [17], these values can give somewhat misleading information concerning the level of light trapping for the geometrical textures. Since very effective trapping is sometimes present through randomisation after the initial 3 or 4 passes, then after a large numbers of passes, the mean pathlength can be overweighted by relatively few waves trapped for many tens of passes. Thus the rays escaping in the first few passes may be inadequately accounted for, whilst it is these rays which contribute most to the absorption in the silicon.

5.4.1.4 Maximum short circuit current densities

The more light that is coupled into and absorbed within the silicon, the higher will be the short circuit current density J_{sc}. Assuming that each photon absorbed will contribute to the formation of one electron-hole pair, and that the collection efficiency of the electrons formed is 100% (i.e. every electron formed will also reach the p-n junction), then it is possible to determine the maximum short circuit current density J_{sc}(max) achievable for the cell. Table 5.2 presents the modelled and measured front surface reflectances for the saw-damage etched wafers at wavelength λ = 0.8 μm (at this wavelength light is absorbed within its first pass through the ~200 μm thick silicon and no rear reflectance component is visible in total reflectance measurements), as well as the calculated absorption efficiencies of the wafers at λ = 1.1 μm where the silicon is partially transmitting. These two pieces of data enable a fuller interpretation of the calculated maximum short circuit current densities shown graphically in Figure 5.11. The front surface reflectance indicates the amount of light coupled into the silicon, as determined by the facet tilt angles of the geometrical texturisation and the probability of multiple bounce incidence for the (un)encapsulated wafer, as was investigated in chapter 4. The absorption efficiencies are dependent upon the quality of light trapping provided by the texture in combination with chosen back surface reflector in the (un)encapsulated wafer, and the pathlengths travelled by the silicon before absorption or coupling out of the wafer/laminate.

Orientation	Bare		Ag BSR		Encapsulation with Ag BSR	
	R at λ = 0.8 μm	*a* at λ= 1.1 μm	R at λ = 0.8 μm	*a* at λ = 1.1 μm	R at λ = 0.8 μm	*a* at λ = 1.1 μm
(100)	33.3 *(32.1)*	0.30	32.5 *(32.1)*	0.47	16.8 *(15.1)*	0.33
(311)	32.4 *(30.4)*	0.57	31.6	0.67	12.5 *(11.5)*	0.55
(210)	32.4 *(30.7)*	0.52	32.0	0.64	13.6 *(14.7)*	0.55
(321)	31.6 *(29.9)*	0.59	31.2	0.70	9.6 *(9.5)*	0.60
(110)	30.9 *(28.5)*	0.59	33.3	0.67	10.9 *(10.9)*	0.59
(221)	31.0 *(29.3)*	0.53	31.1	0.67	11.8 *(12.6)*	0.55
(111)	31.2 *(29.5)*	0.35	31.0	0.49	15.0 *(16.0)*	0.39
Polished Si	33.0 *(32.1)*	0.09	33.5	0.15	16.5	0.14
Lambertian	0.0	0.75	---	---	---	---

Table 5.2 *Modelled and (measured) reflectances R at wavelength λ = 0.8 μm and calculated absorption efficiencies a at λ = 1.1 μm for the seven saw-damage etched silicon wafer orientations, indicating the level of light coupling and light trapping respectively.*

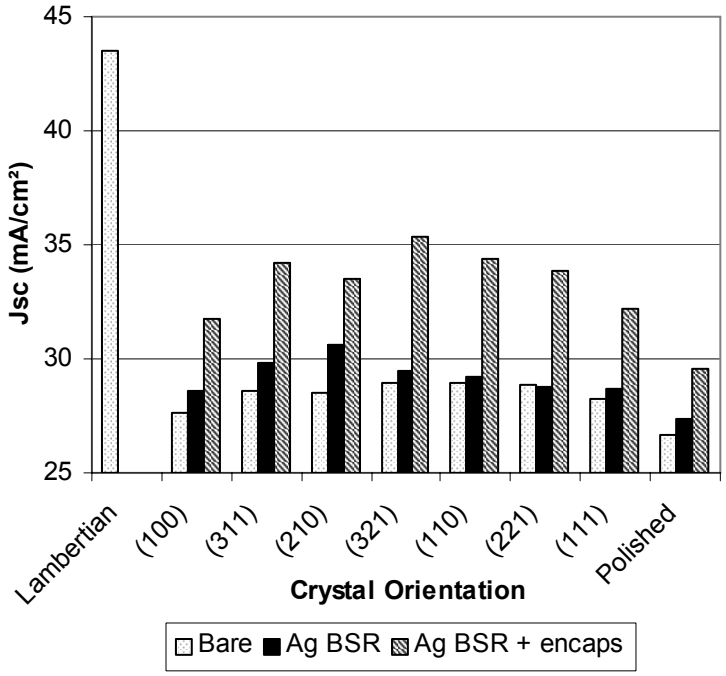

Figure 5.11 *Maximum short circuit current densities for the 7 saw-damage etched silicon wafer orientations.*

A general trend is that encapsulated wafers with Ag BSR have the highest J_{sc}(max) values, followed by the wafers in air with an Ag BSR, with the bare wafers in air having the lowest J_{sc}(max). This is despite the better light trapping in the wafers with intimate Ag BSR in air compared to the other systems investigated.

For the unencapsulated wafers, the low facet tilt angles of the saw-damage etch textures mean that reflectances on all seven orientations lie within 3.5% of polished silicon (at maximum only 6% of facets have tilt angles > 45° whereby multiple reflectance in air is guaranteed; see Chapter 4, Table 4.4). The increases in J_{sc} on application of the Ag BSR are due only to the increased level of light trapping provided, as quantified by the absorption efficiencies in Table 5.2.

The large increase in J_{sc} for the encapsulated wafers can thus be attributed largely to front surface reflectance reduction, this increase being greatest for textures with facet tilt angles large enough for light confinement at the glass-air interface (i.e. greater than 20.9°, see Chapter 4) whereby more light is coupled into the silicon for absorption. For the encapsulated saw-damage etched wafers, the central (321) orientation performs particularly well, with 77% of facets satisfying this condition, compared to only 12% for the flat etching (100) orientation. The significance of the effect of reflectance reduction under encapsulation for the final J_{sc} values is highlighted for example on comparing the values of *a* and R in Table 5.2 for the cases of the wafers with Ag BSR in air compared to under encapsulation. Whilst the change in *a* on encapsulating the wafers is slightly detrimental to cell output through light lost into the encapsulation, the reduction in reflectance, in particular for the central more facetted orientations around (321) is large enough to increase J_{sc} values by up to 6%.

In summary, for wafers of ~200 μm thickness, although light trapping can be significantly improved on application of an Ag BSR, improved light coupling through reflectance reduction is still the predominant method by which optical absorption can be improved. As such, the levels of surface texturisation provided by the central crystal orientations around the (321) provide the highest maximum current densities achievable. These orientations have facet angles sufficient for both significant reflection reduction under encapsulation and light trapping levels approaching that of the Lambertian ideal.

5.4.2 Texture etched monocrystalline silicon wafers

5.4.2.1 Light trapping due to surface texturisation

Although the same etch depth was used for saw-damage and texture etching (i.e. whereby 25 μm total or 12.5 μm per side by weight is removed for a multicrystalline wafer), there was a slightly greater variation in total thickness for the different orientations with texture etching compared to saw-damage etching for the various orientations. Following etching, total thicknesses varied from 192 μm for the slow etching (111) orientation, to 172μm for the (100) orientation. These thicknesses were used in calculations.

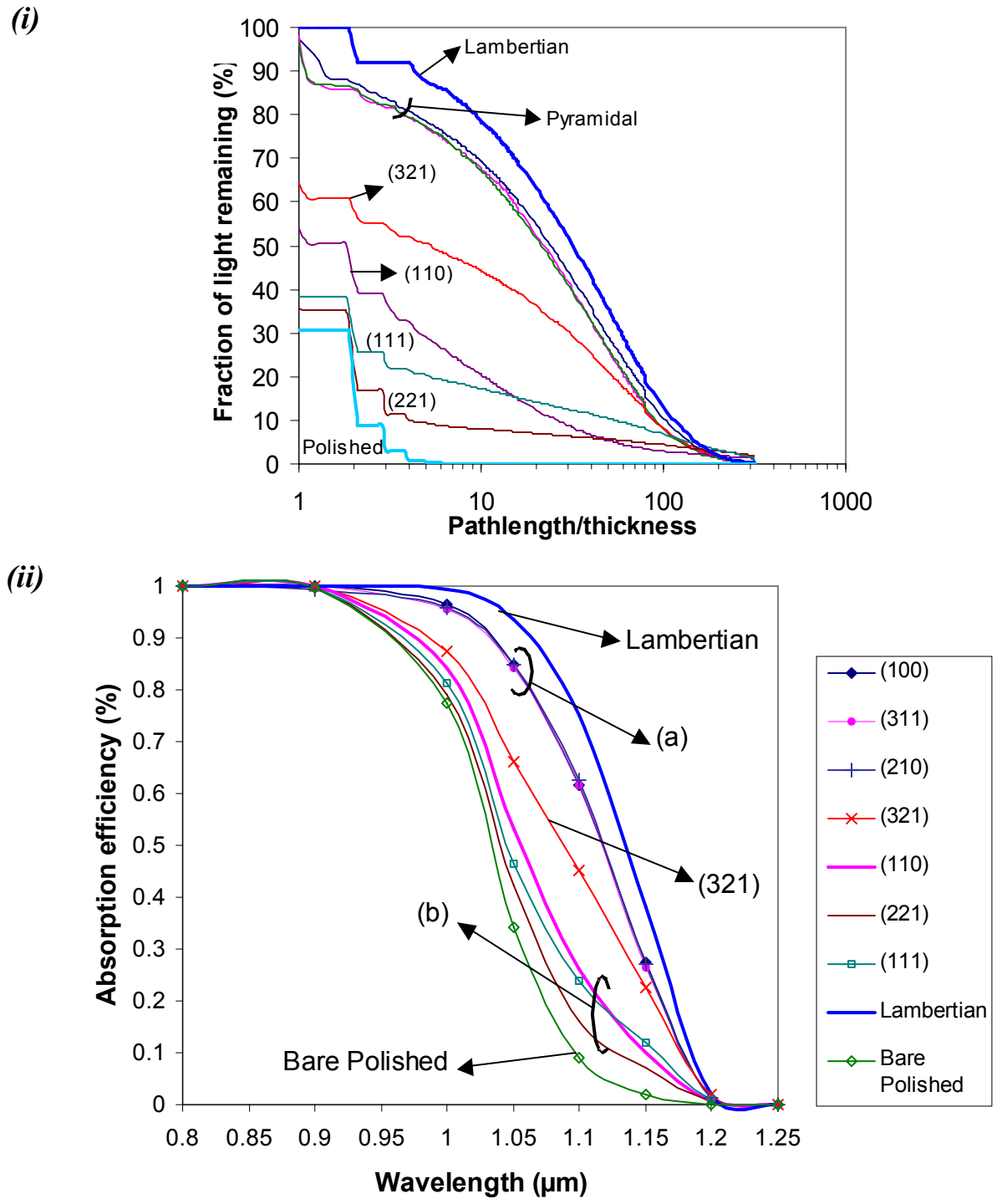

Figure 5.12 *(i) Pathlength distributions and (ii) absorption efficiencies for the 7 texture etched monocrystalline silicon wafer orientations. (a) The (tilted) pyramidal textures on the (100), (210) and (311) lie close to the Lambertian even when bare, whilst (b) the {XXY} orientations of (111), (221) and (110) have light trapping barely above the polished wafer for the first passes.*

Figure 5.12 shows the pathlength distributions and absorption efficiencies for the bare texture etched monocrystalline wafers in air. The quality of light trapping varies for the seven orientations according to their etch facet angles, in a similar way as for the front surface

reflectance as shown in Chapter 4. Considering the case of the bare silicon, the upright and tilted pyramid textures of the (100), (210) and (311) orientations have similarly high levels of light trapping, with a high level of randomisation after the first or second pass, approaching that of the Lambertian ideal. This corresponds with the faceting of these structures, with facet tilt angles up to 54.7° (for the upright pyramids on the (100)), yielding multiple reflectances on normal incidence of light in air and in particular under encapsulation. Light is very effectively trapped at the rear in the first important passes, with only ~10-15% of light escaping through rear facets parallel to the front entrance facets (see section 5.4.1.1 previously), due to the complexity of these 4-sided pyramidal structures combined with the non-uniformity and non-periodicity of the alkaline texturisation.

Thereafter, the (321) orientation has a considerably lower level of light trapping. The tilted pyramid structures formed on this orientation are so far tilted compared to the upright pyramids on the (100), that the surface is dominated by (a tendency of the surface towards) a single {111} facet. This unfortunately means a larger proportion of the front and rear surface facets are positioned parallel to each other, allowing 40% of light to be lost through the rear on the first pass.

The particularly flat etching (110), (111) and (221) orientations perform least well, losing 50% or more of light on the first pass. Randomisation is not achieved until after the second or third pass. Therefore for these {XXY} orientations, the high transmission of light at the silicon-air boundaries and the lack of internal scattering for the first important passes in particular, mean the absorption efficiencies in air barely exceed those of the polished silicon for wavelengths up to ~ λ = 1 μm. However, the particularly low gradient of the pathlength distribution on these orientations after the initial 2-3 passes suggest that the light remaining within the silicon thereafter is very effectively trapped, yielding particularly long pathlengths in the silicon. Thus at still longer wavelengths, the more efficient scattering and light trapping after these initial passes (see the pathlength distributions in Figure 5.12) lead to longer pathlengths within the silicon and an improvement in absorption efficiencies compared to the polished silicon. Unfortunately, this trapped light will contribute relatively little to current generation in its remaining passage through the cell, having lost much of its intensity in the first few passes. This can be seen for example for the (110) orientation in Figure 5.12; from pathlength distribution it is seen that the fraction of light trapped within the silicon decreases rapidly. After ~15 passes the amount of trapped light becomes lower than for the (111) and later (after 50 passes) the (221) orientation. Nevertheless, this is only seen for the absorption efficiencies at wavelengths longer than the indirect bandgap of 1.1 μm, with *a* for the (110) dropping just a few percent below that of the (111), and not being affected at all for the (221) orientation, as the silicon tends to transparency.

In summary, the effectiveness of light trapping varies with orientation for texture etching, as was the case for front surface reflectance (see Chapter 4). Light trapping is best for the (tilted) pyramid structures with high facet tilt angles on near {100} orientations and worst for the polished surfaces resulting on {XXY} orientations. The tilted pyramid structures lose about 10% of light by initial transmission, but thereafter exhibit particularly effective internal scattering at levels approaching the Lambertian ideal. The {XXY} orientations however are so flat that more than 60% of light is lost in the first two passes, so that absorption levels lie barely above polished silicon.

5.4.2.2 Effect of back surface reflectors and encapsulation

Figures 5.13 and 5.14 show the effect of the different back surface reflectors on the pathlength distributions and absorption efficiencies for the (311) and (221) orientations, demonstrating light trapping for the texture etch extremes of a typical (tilted) pyramidal structure and a flat etching {XXY} orientation respectively.

(a)

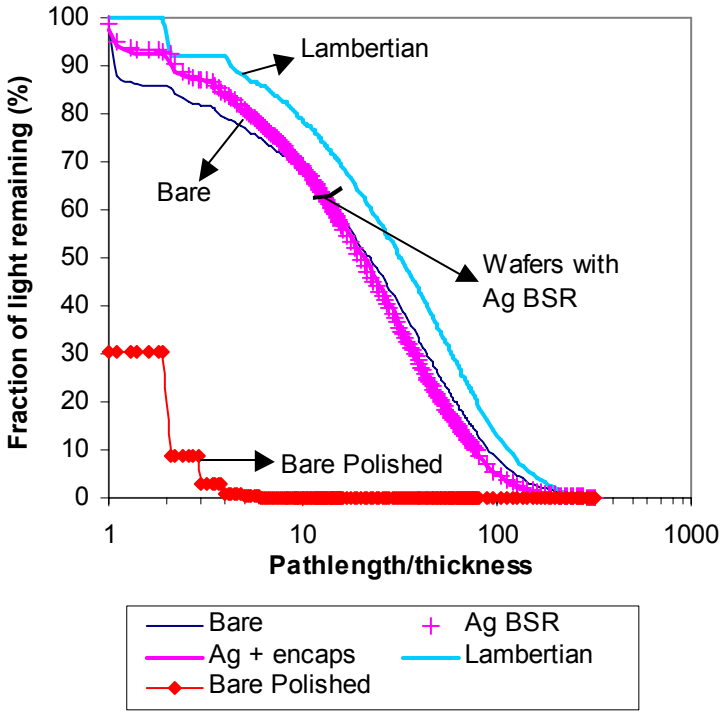

(b)

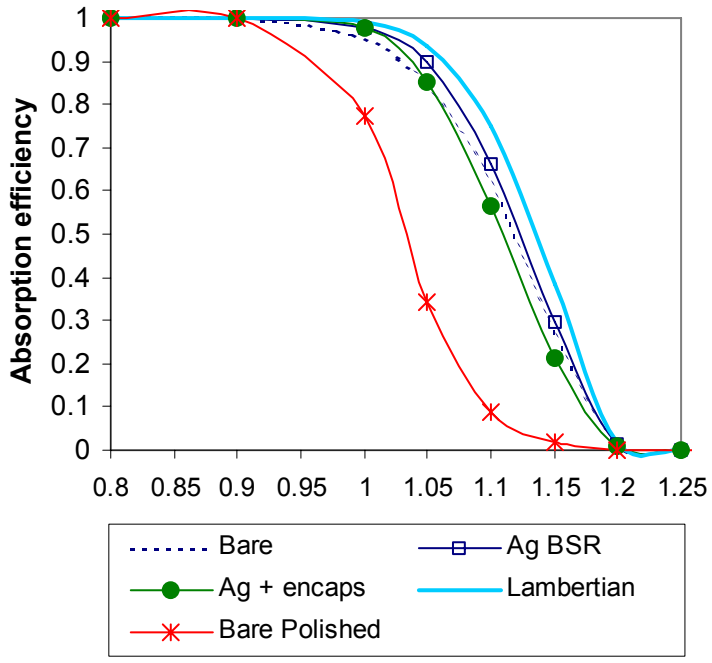

Figure 5.13 Effect of different back surface reflectors for texture etched (311) monocrystalline silicon, with tilted pyramid texture geometries.
(a) Pathlength distributions and (b) absorption efficiencies.

(a)

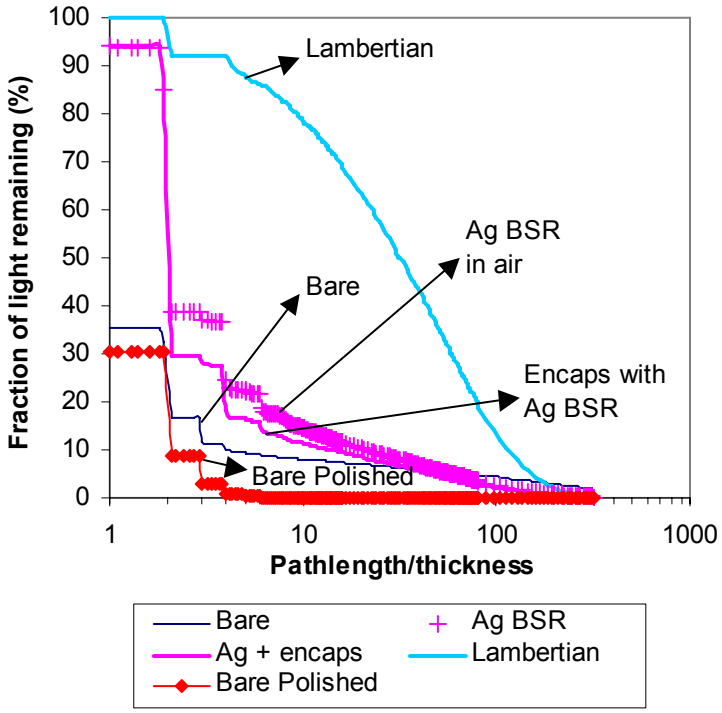

(b)

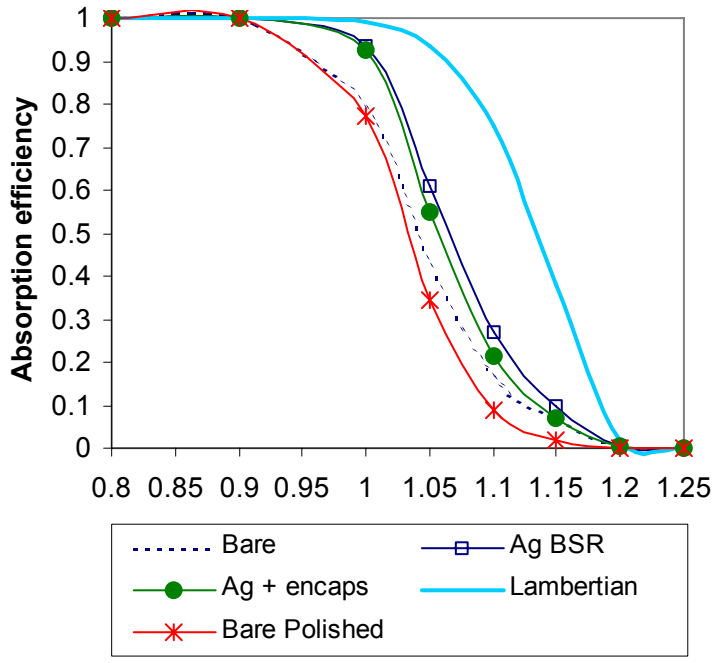

Figure 5.14 Effect of different back surface reflectors for texture etched (221) monocrystalline silicon , with texture geometries giving poor light trapping in air. (a) Pathlength distributions and (b) absorption efficiencies.

The use of a back surface reflector improves light trapping overall, being particularly important for the trapping of light on the first and third passes through the wafer, where the light contains the most energy and relatively little light has been lost through successive interactions with front and rear surfaces.

For the case of the (tilted) pyramid textures, an Ag BSR improves the level of light trapping compared to the bare silicon in air, with more light trapped for the first ten passes leading to

higher levels of absorption for all wavelengths (Figure 5.13). The level of internal scattering is such as to ensure that absorption efficiencies are relatively close to the Lambertian ideal at all wavelengths even for the bare wafers in air, becoming almost equivalent to it if an intimate Ag BSR is employed. However, if the wafers with Ag BSR are then encapsulated, absorption efficiencies can drop even below that of the bare wafer in air for the tilted pyramid textures, whose light trapping qualities are already very high by virtue of the surface morphologies of the textures themselves, due to loss of light scattered into the (partially absorbing) front encapsulation. This is visible at wavelengths of as little as 1.05 μm, where the silicon absorption length (5.65 cm for a = 99.99% ~100%) is equivalent to ~30 passes of light through planar silicon of 186 μm.

For the flat etching {XXY} oriented (111), (110) and (221) wafers, a back surface reflector is essential to raise light trapping levels above those of a polished wafer. The pathlength distribution in Figure 5.14 shows how the Ag reflector reduces rear transmission in the essential initial passes, so that after the first pass more than 94% of light is trapped within the silicon, compared to only 35% when bare. The flatness of the etch surfaces means that light is scattered very little for the initial 10 passes, with the pathlength distributions remaining step shaped initially indicating where large numbers of rays of equivalent pathlength are coupled out of the wafer. Encapsulating the wafer with Ag BSR reduces the level of trapping and resulting absorption somewhat, but contrary to the tilted pyramid textures, absorption efficiencies for these orientations remain higher than when bare in air for all wavelengths. This is because light trapping is improved so substantially in the important first passes compared to the bare {XXY} wafers in air, and because the majority of light travels no more than 4-6 passes before either absorption or coupling out of the wafer, thereby making relatively few passes through the encapsulation.

In summary, the use of an Ag BSR improves light trapping for all orientations in air, particularly due to the reduction of rear transmission on the first and third passes. For tilted pyramid structures however, whilst absorption efficiencies with an Ag BSR are raised even closer to that of the Lambertian ideal, light trapping levels under encapsulation for wavelengths above 1.05 μm fall below that of the wafers in air. This is due to light making tens or hundreds of passes through the partially absorbing encapsulation during its passage through the cell structure.

5.4.2.3 Average pathlengths

Table 5.3 shows the average pathlengths calculated for the texture etched wafers. Pathlengths are greatest for the (tilted) pyramid textures, decreasing with distance of the base orientation from the (100) so that lowest pathlengths are obtained for the flat etching {XXY} orientations (the (110), (221) and (111)). However, as was discussed in section 5.4.1.3 previously, caution should be taken in interpretation of these results, due to the overweighting of rays with very long pathlengths but contributing little to absorption in the silicon compared to rays absorbed within the first few passes within the silicon.

	Lambertian	(100)	(311)	(210)	(321)	(110)	(221)	(111)	Polished
Bare	49.8	42.8	37.7	38.0	30.3	14.0	13.8	20.1	1.5
Ag BSR		33.2	32.8	33.7	31.6	15.0	11.5	21.1	2.9
Encaps + Ag BSR		32.2	32.4	32.1	29.0	12.3	9.3	18.0	2.4

Table 5.3 *Average pathlength enhancement for light at λ = 1.25 μm in the seven texture etched monocrystalline wafer orientations for the three schemes investigated.*

5.4.2.4 Maximum short circuit current densities

Table 5.4 shows the measured and modelled reflectances for the texture etched wafers at wavelength λ = 800 nm, and the calculated absorption efficiencies at λ = 1.1 μm, as used to explain the calculated short circuit current densities shown graphically in Figure 5.17. The trend in maximum J_{sc} values corresponds with that seen for the front surface reflectance and absorption efficiency, in that J_{sc}(max) is greatest for the pyramidal textures, and decreases with distance of the base orientation from the (100) until the {XXY} orientations, where the lowest J_{sc}(max) values occur. This corresponds with the variation in facet tilt angles resulting from texture etching of the different orientations, varying from ~55° for upright pyramids on the (100), to flat triangular etch pits for example on the (111), as was shown in Chapter 4 (see Table 4.2).

In general, the J_{sc}(max) values are seen to improve according to the chosen light trapping scheme as was determined from the corresponding absorption efficiencies. The encapsulated wafers perform best due predominantly to the improved light coupling into the silicon, despite slightly lower light trapping effectiveness due to coupling of light into the encapsulation. Thereafter, J_{sc}(max) values are lower for the wafers in air, with wafers having an intimate Ag BSR having higher J_{sc}(max) values than for where no reflector is used at all.

The level to which J_{sc} is raised for the different schemes under encapsulation differs for the seven orientations. For the tilted pyramid structures, reflection reduction is the most important mechanism by which J_{sc}(max) is improved on encapsulation. From Table 5.4 it is seen that absorption coefficients for (tilted) pyramid textures in air barely differ from those where a BSR and/or encapsulation are used, since light trapping levels are already high by virtue of the level of faceting constituting their etch surface geometries. This is in contrast with the large reduction in reflectance achieved for particularly the (210) and (311) orientations through the resulting multiple bounce incidence of light achieved through light confinement at the glass-air interface on encapsulation (see Chapter 4). For the flatter etching {XXY} orientations however, absorption coefficients improve significantly compared to polished silicon for example on introducing a back surface reflector, although light trapping levels remain very low compared to the Lambertian ideal. Light confinement under encapsulation plays a minor role (i.e. the majority of surface has facet tilt angles < 20.9°), so that the maximum J_{sc} for these orientations remains low.

Orientation	Bare		Ag BSR		Encapsulation with Ag BSR	
	R at λ = 0.8 μm	*a* at λ= 1.1 μm	R at λ = 0.8 μm	*a* at λ = 1.1 μm	R at λ = 0.8 μm	*a* at λ = 1.1 μm
(100)	13.6 *(13.8)*	0.62	13.8	0.66	7.1 *(7.6)*	0.56
(311)	25.6 *(24.8)*	0.62	24.7	0.66	6.4 *(6.8)*	0.57
(210)	25.7 *(24.4)*	0.63	25.4	0.68	7.3 *(7.2)*	0.57
(321)	31.7 *(29.6)*	0.45	33.1	0.61	14.8 *(14.3)*	0.49
(110)	33.2 *(32.1)*	0.26	32.6	0.41	14.6 *(17.0)*	0.31
(221)	32.7 *(32.0)*	0.16	32.9	0.27	17.2 *(17.2)*	0.21
(111)	33.2 *(32.1)*	0.24	32.8	0.42	17.4 *(18.1)*	0.29
Polished Si	33.0 *(32.1)*	0.09	33.5	0.15	16.5	0.14
Lambertian	0.0	0.75	---	---	---	---

Table 5.4 *Modelled and (measured) reflectances R at wavelength λ = 0.8 μm and calculated absorption efficiencies a at λ = 1.1 μm for the seven texture etched silicon wafer orientations, indicating the level of light coupling and light trapping respectively.*

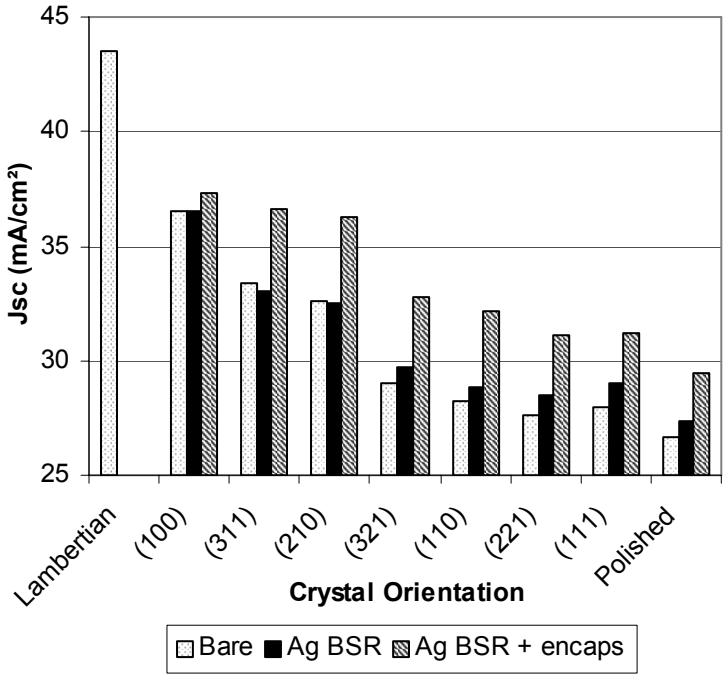

Figure 5.17 *Maximum short circuit current densities for the 7 texture etched silicon wafer orientations.*

In summary for the texture etched ~200 μm thick wafers investigated, the predominant mechanism for maximising optical absorption and J_{sc} is by reducing front surface reflection, particularly under encapsulation, rather than by improved light trapping for example on the application of an Ag BSR.

5.5 Discussion

5.5.1 Comparison of light trapping for saw-damage and texture etching

5.5.1.1 Light trapping resulting from the etch surface morphologies

The quality of light trapping resulting from the two etch types is strongly orientation dependent, in line with the different levels of faceting resulting from the anisotropic action of the etches.

For the saw-damage etch, light trapping levels are particularly high for the central orientations around the (321). Etch structures formed on these central orientations have the highest facet tilt angles, and are beneficial to both trapping of light within the silicon by TIR at the silicon-encapsulant interfaces and, for the wafers under encapsulation, to reflection reduction on initial incidence due to the high proportion of etch facets with angles > 20.9° giving TIR at the glass-air interface. The saw-damage etch thus gives very good levels of light trapping on the majority of orientations, with absorption efficiencies approaching those of the Lambertian case when a reflector is employed. This is in agreement with the observations of Burgers [6] for bare silicon, who stated that due to the small critical cone for escaping light in the silicon with its high refractive index, even the small facet angles of this texture should allow very high levels of light trapping in combination with a back surface reflector. This is a notable result, considering that even the most highly facetted saw-damage etch textures investigated on the (110) and (321) orientations actually yield very high front surface reflectances in air approaching those of polished silicon, with only a minimal level of multiple bounce incidence being possible through a small proportion of facets with angles > 30° (see Chapter 4). However, this is not true of all orientations, with the flat etching {100} and {111} orientations performing considerably less well. These orientations yield saw-damage etch surface geometries consisting of flat etch pits with facet angles which are still too low for light trapping by TIR at the silicon-air or silicon-EVA interface, and certainly provide no benefits to front surface reflectance reduction. Nevertheless, these latter orientations still have higher absorption efficiencies compared to polished silicon, in particular upon the application of a back surface reflector to reduce initial transmission losses, due to the effectiveness with which the textured surface scatters light internally after 3-4 passes of light through the silicon.

The relationship between facet tilt angle and light trapping properties is seen most strongly for the texture etch, where far greater extremes in facet angle exist over the orientations between the pyramidal orientations close to (100) and the extremely flat, almost polished surfaces formed on the {XXY} orientations investigated, in particular the (110) and (221). The (tilted) pyramid textures on the (100), (311) and (210) orientations, yield light trapping properties equivalent to the Lambertian ideal when an Ag BSR is employed. Absorption efficiencies for the pyramidal textures are approximately equivalent to the best performing central orientations for saw-damage etching, although the front surface reflection reduction for the pyramidal textures under encapsulation is still several percent lower than for the

encapsulated saw-damage etched (321) and (110) orientations. Maximum J_{sc} values are thereby higher for the texture etched (tilted) pyramids under encapsulation than for the best performing saw-damage etched wafers around the (321). As the base orientations become further removed from the (100), the light trapping properties decrease significantly until for the {XXY} orientations, light trapping is barely increased above that of the polished wafer. Light trapping for the (221) and (111) orientations in particular is poor, with randomisation of light occurring only after around 5-6 passes on the wafer, whereby at each passage of light, the high levels of transmission at the rear in particular means that very little light is available for absorption once randomisation does occur. Both light trapping and the level of reflection reduction in air or through light confinement on encapsulation are essentially equivalent to polished silicon, so that J_{sc}(max) values for texture etched {XXY} orientations are less than for the poorest performing saw-damage etched (100) and (111) wafer orientations.

5.5.1.2 Effect of the back surface reflector

The use of a back surface reflector is essential for the double sided textures investigated, due to rear transmission losses through exit facets at the rear positioned parallel to the entrance facets at the front surface for the incoming light. These rear transmission losses occur even for the most highly facetted pyramidal textures on near (100) orientations through texture etching or saw-damage etched orientations around (321), with transmission losses on the first pass varying between 10% for the best performing etch textures, to much as 65% for the flattest texture etched {XXY} orientations. The improvement in light trapping resulting from the application of a BSR is greatest for the flattest etching orientations, particularly due to the more effective trapping of this otherwise transmitted light in the initial passes, which is most important due to the exponential nature of absorption in the silicon. The use of an Ag BSR for the wafers in air thereby significantly improves absorption efficiencies compared to the bare wafers in air.

5.5.1.3 Effect of encapsulation

A notable result is that wafers with an Ag BSR have higher absorption efficiencies at partially transmitting wavelengths when in air than if encapsulated under glass. This is due in particular to absorption in the front glass encapsulation of light coupled out at the front silicon-EVA interface on traversing the encapsulant before re-entering the silicon.

Ways of reducing the absorption losses in the front encapsulation are to use a less absorbing glass type or else to use as thin an encapsulating layer as possible. The window glass used in this thesis was not especially optimised for transmission and absorption in the wavelength range of interest. As to the benefits which can be gained by reducing the thickness of the glass used, Figure 5.18 shows that as the thickness of the glass is reduced from 3 to 1 mm, the amount of light absorbed after coupling into the silicon increases. This is because light trapped in the cell structure makes shorter paths in the encapsulation relative to the paths travelled within the silicon, whereby less light is lost by absorption in the glass layer.

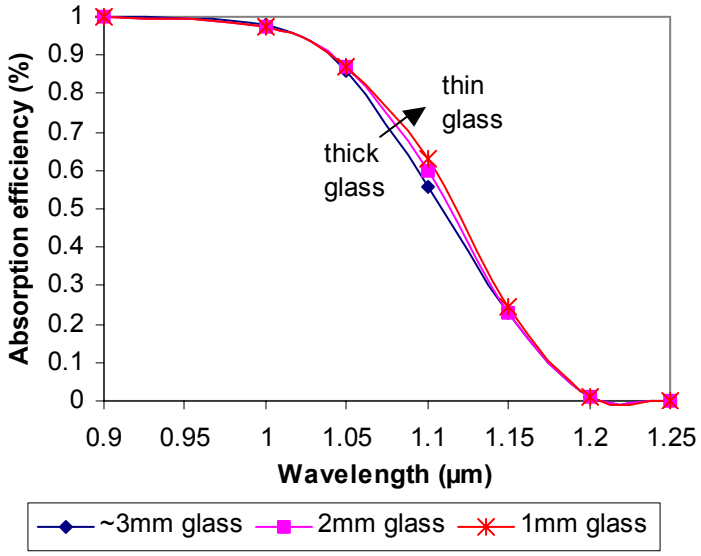

Figure 5.18 *The effect of the thickness of the glass front encapsulation upon absorption efficiencies for (100) oriented texture etched silicon, for glass thicknesses from ~3 mm to 1 mm.*

5.5.2 Application to multicrystalline wafers

5.5.2.1 Absorption efficiencies

In order to relate the above results for single crystal orientations to the overall light trapping performance of the thin (~200 µm) multicrystalline wafers investigated experimentally, the weighted average absorption efficiencies were calculated for the seven orientations in each of the etch systems used. The averaging procedure used was introduced in Chapter 4.4.2.

Figure 5.19 compares the weighted average of absorption efficiencies calculated for saw-damage and texture etching for the four schemes investigated. Absorption levels are improved in order of the bare wafers, wafers with an Ag BSR under encapsulation, and the wafers in air with an Ag BSR, as is the case for the individual orientations.

Light trapping for the multicrystalline wafers is in all cases significantly improved upon the bare polished wafer in air. In the best case (saw-damage etched wafers with an Ag BSR in air), light trapping is equivalent to that of the Lambertian for wavelengths above 1.1 µm. This is due to the high reflecting properties of the Ag BSR combined with the high level of scattering inherent to the saw-damage etch textures themselves, this latter effect becoming particularly visible after the initial passes of the light through the cell. However, these wavelengths have a minimal contribution to absorption in the wafers, with energies lower than the silicon band-gap. At shorter wavelengths that are more important for absorption as the thin wafers become transmitting, absorption efficiencies in multicrystalline wafers are weighed down by the poorer level of light trapping present particularly for the flatter etching orientations, i.e. the (100) and (111) orientations for the saw-damage etch, and similarly the {XXY} orientations for the texture etch.

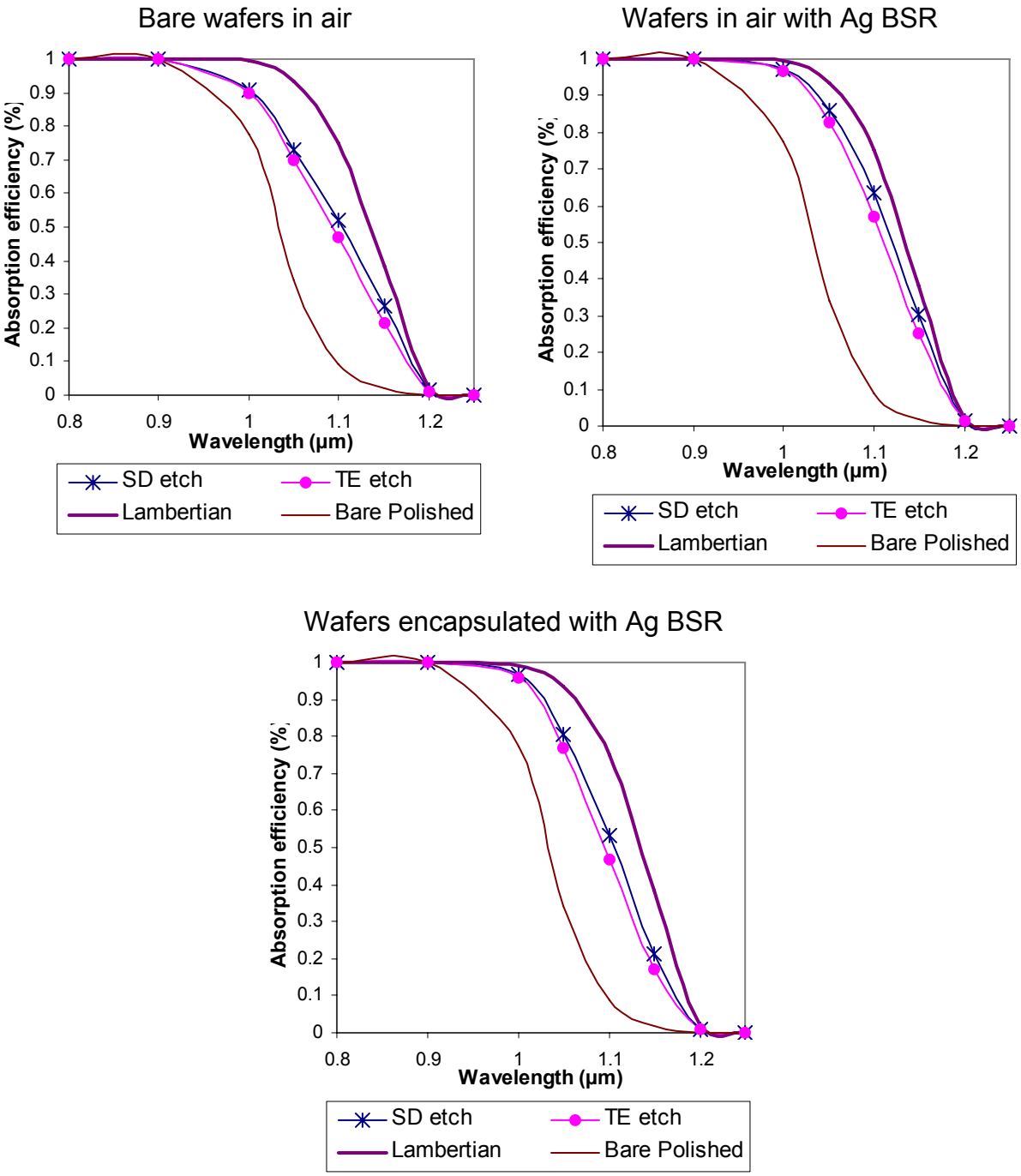

Figure 5.19 *Absorption efficiencies in saw-damage (SD) and texture etched (TE) multicrystalline silicon wafers etched to a total depth of 25 µm (12.5 µm per side), as calculated from the weighted averages for 7 orientations.*

A general trend for all the schemes investigated is that the weighted average absorption efficiencies for the saw-damage etched wafers are consistently higher than for the texture etched wafers. This implies that despite the excellent light trapping present for the tilted pyramid structures formed by the texture etching of near (100) orientations, the particularly flat etch surfaces correspondingly formed on the {XXY} structures weigh down heavily upon the overall level of light trapping for the ~200 µm multicrystalline wafer.

5.5.2.2 Comparison of measured and modelled reflectances

Figure 5.20 shows the average total reflectances measured for the ~200 µm thick multicrystalline wafers experimentally after saw-damage and texture etching, showing several characteristic details of both light trapping and reflection reduction.

(a)

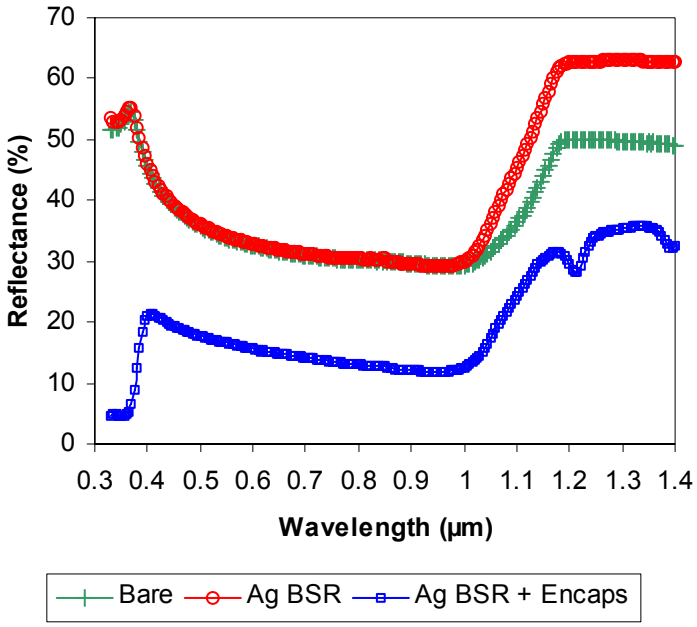

(b)

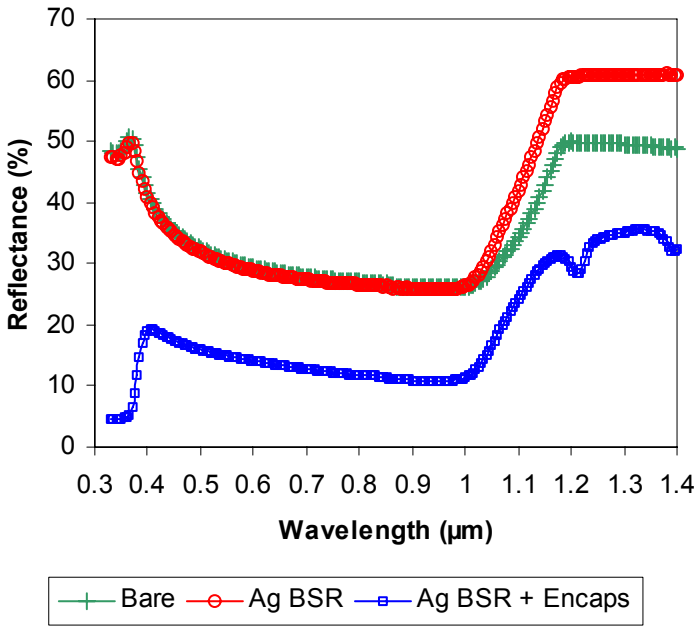

Figure 5.20 *Measured reflectances for 200 µm multicrystalline silicon wafers with (a) saw-damage etch (b) texture etch.*

The application of an Ag BSR upon the unencapsulated wafers leads to an increase of approximately 10% in total reflectance for longer wavelengths above 1.1 µm, indicating the increased reflectance of the rear. A significant drop in reflectance is viewed over the whole

wavelength range on encapsulation, partially due to improved reflection reduction through light confinement at the glass-air interface for central orientations around the (321) for the saw-damage etch, and for pyramids formed by texture etching of near (100) orientations. As mentioned previously, the EVA absorption peak at wavelength $\lambda = 1.2$ µm lies at wavelengths beyond the silicon band gap, thus having negligible effect upon the absorption in the silicon.

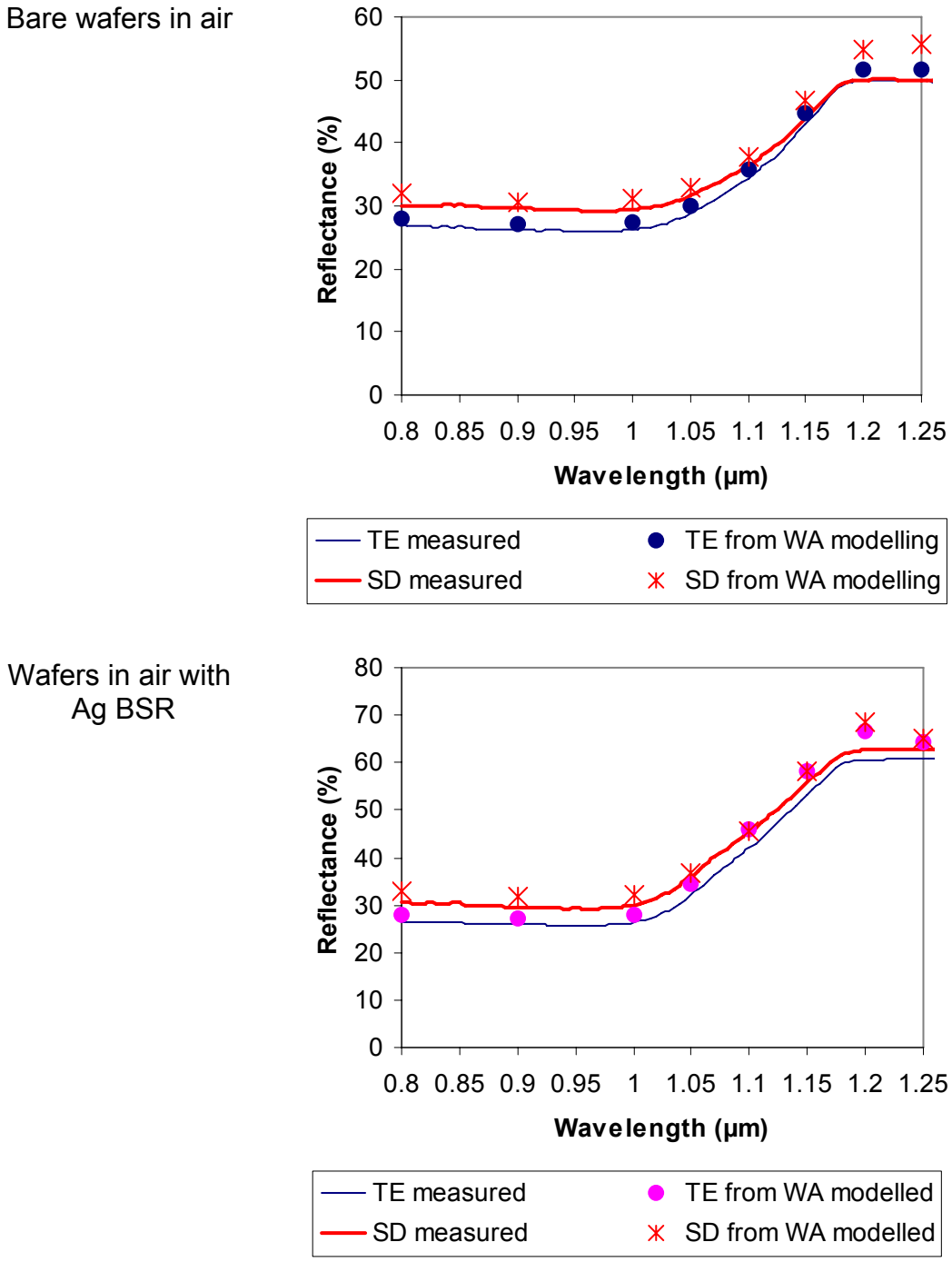

Figure 5.21 *Average of measured reflectances for ~200 µm thick saw-damage (SD) and texture (TE) etched multicrystalline silicon wafers compared to the weighted average (WA) results of modelling for seven orientations.*

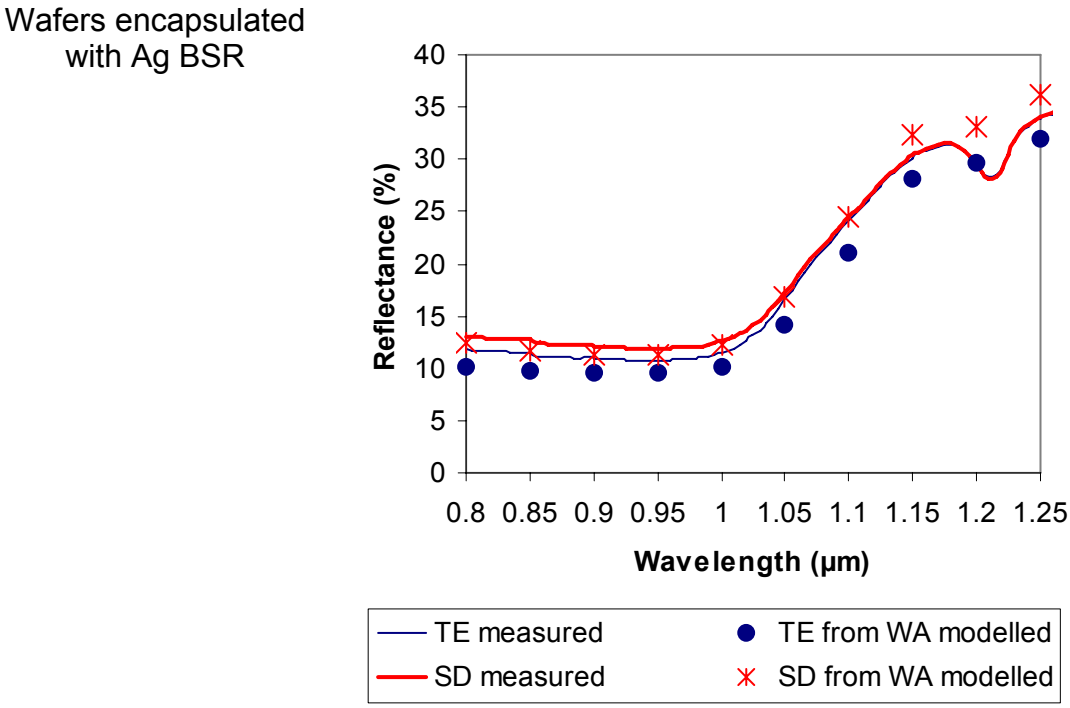

Figure 5.21(cont) *Average of measured reflectances for ~200 µm thick saw-damage (SD) and texture (TE) etched multicrystalline silicon wafers compared to the weighted average (WA) results of modelling for seven orientations.*

The multicrystalline reflectances for the two etches are compared for partially transmitting wavelengths in Figure 5.21. This figure shows the measured reflectances in air and under encapsulation respectively for the saw-damage and texture etched multicrystalline wafers, as compared with the weighted averages of the reflectances modelled for the seven individual monocrystalline orientations. The measured front surface reflectances of the texture etched wafers are always a few percent lower than for the saw-damage etched wafers, due to the high facet tilt angles of the tilted pyramid textures in particular, allowing multiple reflectances both in air and under encapsulation, as was discussed in Chapter 4.

5.5.2.3 Maximum current densities

Table 5.5 shows the maximum achievable current densities J_{sc}(max) calculated for the 200 µm thick multicrystalline wafers, as determined from the weighted average of calculated J_{sc}(max) values for the individual orientations as were shown in Figures 5.11 and 5.17 previously. For all of the light trapping schemes investigated (i.e. uncoated wafer or wafer with Ag BSR, either in air or under encapsulation), J_{sc}(max) values were greater for texture etched wafers compared to saw-damage etched wafers. Despite the fact that light trapping in the saw-damage etched systems is superior to that in texture etched wafers for the partially absorbing wavelengths, it would appear that for this thickness of silicon (i.e. ± 200 µm), the greater level of reflection reduction on coupling light into the texture etched silicon initially plays a more important role in maximising the current output.

	Bare	Ag BSR	Encapsulation with Ag BSR
Saw-damage etch	28.6	29.5	33.9
Texture etch	31.0	31.3	34.3

Table 5.5 *Maximum short-circuit current densities (J_{sc}(max)) in mA/cm² for multicrystalline silicon calculated using weighted averages of values for 7 individual wafer orientations.*

5.5.3 Application to thinner silicon wafers

Decreasing the silicon thickness leads to a corresponding decrease in the maximum attainable J_{sc}, as an increasing proportion of the light entering the silicon is transmitted through the front or rear before absorption (see Chapter 1). Whilst the front surface reflectance largely determines the overall level of J_{sc} particularly for thicker wafers, it is the level of light trapping which is of greatest influence as the wafer thickness decreases. J_{sc}(max) decreases particularly rapidly for thicknesses below ~100 μm as still more useful wavelengths with energies greater than the band gap have absorption pathlengths greater than silicon thickness.

5.5.3.1 Improving light trapping qualities for texture etched multicrystalline silicon

Although texture etching provides the lowest front surface reflectances by virtue of multiple reflectances on the pyramidal textures formed, its light trapping properties as well as the level of reflectance are restricted due to the particularly flat etching {XXY} orientations. This could potentially mean that whilst texture etching of the ~200 μm wafers yields higher maximum current outputs compared to saw-damage etching, the superior light trapping achieved for multicrystalline wafers with saw-damage etching to the same etch depth may make this more appropriate as silicon thicknesses are reduced (see section 5.5.2.3 previously). However, as was detailed in Chapter 4, the levels of faceting for texture etched wafers are dependent upon the depth of etching. A shorter etch yields higher facet tilt structures on these same {XXY} orientations, whilst still yielding pyramidal textures upon the near (100) orientations (although these textures are somewhat underdeveloped, exhibiting rounded and split facets, flat polished areas between texture features, etc.). It may therefore be possible to improve the coupling and trapping of light upon these orientations by reducing the etch duration, whilst still allowing for multiple bounce incidence of incident light for the tilted pyramid textures, thereby increasing the maximum current outputs achievable for the texture etched multicrystalline wafers.

To examine this hypothesis, light trapping was investigated by modelling and experiment for multicrystalline wafers etched to a total etch depth of ~15 μm (7.5 μm per side), as opposed to the 25 μm used for saw-damage and texture etching examples above.

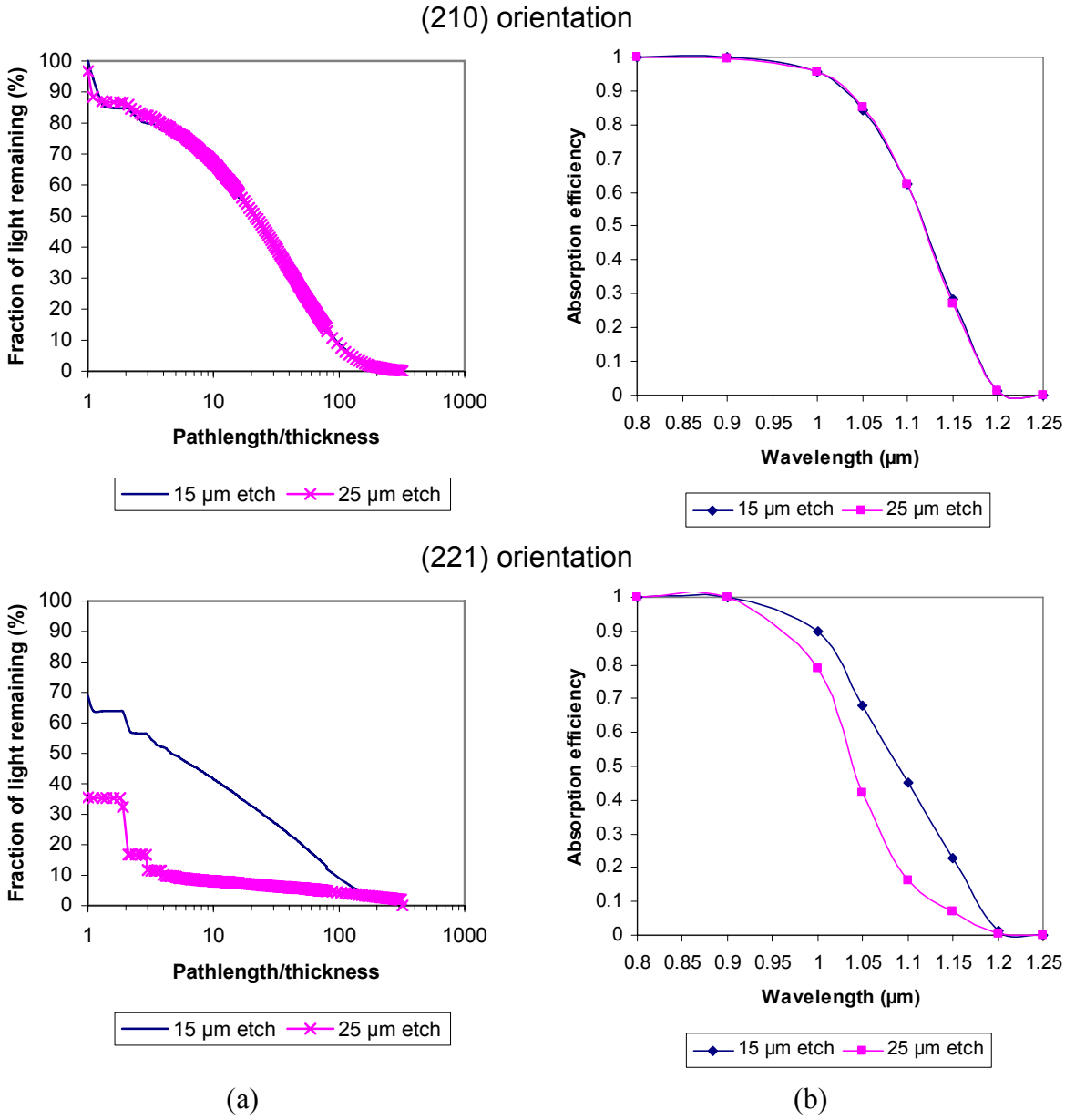

Figure 5.22 *(a) Pathlength distributions and (b) absorption efficiencies showing the effect of reducing texture etching time for (210) and (221) orientations in air with tilted pyramid and flatter etching surfaces respectively.*

Figure 5.22 shows the effect of reducing the etch depth to light trapping for a tilted pyramid structure on the (210) orientation, as compared to that on the far flatter etching (221) orientation. Comparing the two texture etch depths for the bare wafers, it can be seen that the level of light trapping for the (tilted) pyramid structures is minimally influenced by the underdeveloped etch surface when bare, being slightly (a few percent) less for the shorter etch. The facet angles remain substantially higher than is required for TIR at the Si-air (or Si-EVA) interface. However for the remaining orientations, the faceting of the etch surface leads to a significant improvement in light trapping. In particular for the (221) orientation, decreasing the etch depth leads to an increase in the average surface facet angles from 3.5° for the 25 µm etch to 14.5° for the 15 µm etch, with facet angles up to 18.4° in the latter case

allowing TIR for the silicon in air. As a result, rear transmission on the first pass is reduced from 65% (almost equal to polished silicon) to 35% on reducing the etch depth. Thus on using a back surface reflector, light trapping in the {XXY} orientations is significantly improved compared to the longer etch, whilst the almost Lambertian scattering characteristics of the (tilted) pyramid structures are also maintained. Concerning the level of front surface reflectance for the shorter etch duration, reflectances for the tilted pyramid textures are somewhat higher, particularly for the wafers under encapsulation (for the (210), reflectance increases from 7.2 to 10.4% at $\lambda = 0.8$ μm), whilst they actually decrease slightly for the flatter (221) texture (by about 0.7% under encapsulation).

However, the overall reflectance of the multicrystalline wafers remains higher for the shallower texture etch (at $\lambda = 0.8$ μm, reflectances of 11.7 and 12.4% are obtained for the 25 μm and 15 μm etch respectively), although reflectances are still lower than for the saw-damage etched wafers. A shallower etch will therefore be most useful for still thinner wafers, as the quality of light trapping becomes increasingly more important to the output of the finished cells relative to the amount of light coupled into the silicon.

5.5.3.2 Enlargement of the total surface area

Since the reduced volume of the silicon will lead to a reduction in Shockley Read Hall recombination in the bulk (Chapter 1.3), the final efficiency of the thin (film) cell will largely be determined by the effectiveness of light trapping, and also upon the level of surface passivation as a result of the increased surface area due to texturing. It should be noted that surface recombination velocities would appear to be orientation dependent [18], at least on p-type silicon; this may have extra consequences for (rear) surface passivation and the choice of alkaline etch texture used, considering the different crystallographic etch facets exposed (Chapter 4).

Orientation	(210)	(110)	(111)	(311)	(221)	(321)	(100)
SD etch	1.08	1.12	1.07	1.12	1.11	1.15	1.02
25 μm TE	1.29	1.02	1.01	1.35	1.01	1.07	1.50
15 μm TE	1.22	1.07	1.03	1.23	1.06	1.14	1.52

Table 5.6 *Front surface enlargement factors (compared to a polished surface with a surface area of 1) for saw-damage etch (SD) and texture etch (TE) textures as a function of crystal orientation.*

The enlargement of the total surface area as a result of etching differs per orientation per etch as shown in Table 5.6. For the saw-damage etch textures, the increase in surface area over the different crystal orientations in the multicrystalline silicon is fairly modest for the 25 μm etch, with a maximum of 1.15 for the (321) orientation. For the texture etched wafers etched to the same etch depth, the pyramidal structures have the largest surface areas, up to 1.5 for upright pyramids on (100). However, the texture etched wafers also exhibit the very lowest surface areas on the {XXY} orientations, down to 1.03 for the (111) orientation with a 25 μm etch. Using a shorter texture etch reduces the area on the near (100) orientations whose pyramidal structures are then less fully developed, but slightly increases the surface area exposed upon the {XXY} orientations. The increased surface area of the crystals in the wafer increases the need for adequate surface passivation; for the thinner wafers or films, surface

recombination will steadily become more detrimental to cell output relative to recombination in the bulk.

5.5.4 Limitations to etch depth for thin film silicon

Much attention has been paid to the development of thin film silicon technologies in recent years, for silicon base thicknesses from less than 50 μm, to as low as a few microns in thickness. Chemical vapour deposition (CVD) techniques as well as epitaxial growth processes such as liquid phase epitaxy are promising candidates for future film silicon growth methods. Such technologies require cheap, supporting substrates upon which the film can be deposited. In particular for epitaxial growth, the substrate must have a great enough silicon content for nucleation.

Whilst chemical texturing is a relatively straightforward procedure for (thick) silicon wafers, the employment of chemical texturing etches becomes impractical if not impossible for thin films of around 50 μm or less, with the dimensions of the texture being comparable with the total thickness of the film. For example, the pyramids discussed in Chapters 3 & 4 as formed on the (100) orientation, have heights of up to 10 μm. For a 30 μm film, such a texture may be possible in theory, although the etch rate and depth would have to be rigorously controlled. For this film thickness, a single sided texture would allow for light trapping with the removal of less material.

In addition for a multicrystalline film, the variations in thickness occurring between crystals as a result of the orientation dependence of the etch rates, will be in the order of magnitude of the actual film thickness. Considering the differing etch rates of the seven representative monocrystalline orientations, (see Figure 4.18), a potential variation in thickness between crystals in the saw-damage etched multicrystalline silicon wafer or film of up to 13 μm in total may exist between the fast etching (100) and slow etching (111) orientation. Similarly, thickness variations of up to 20 μm in total exist for texture etching to the same etch depth. These etch depths pertain to 6.5 μm and 10 μm per side of the silicon for the saw-damage and texture etches respectively, thereby being somewhat more acceptable etch depths if a single sided etch were employed, as may be essential on a substrate supported film. In fact a double sided texture could probably only be effectively formed by growing conformally to a textured substrate. It is then questionable whether the texture would be transferred to the top surface of the grown layer, and indeed whether chemical etching would be possible (for example on a silicon based ceramic) or appropriate.

For even thinner films, for example 5 μm, texturisation of the silicon layer itself would be nonsensical. In such cases texturisation of the substrate upon which the planar film is grown becomes essential. It is then important that the dimensions, period and facet tilt angles of the substrate texture be chosen carefully to ensure multiple passes of light through the silicon so that absorption is maximised. Thorp [20] for example, suggests the conformal deposition of films onto substrates textured with periodic macroscopic features, so that the film retains the anti-reflection properties of the texture. A small texture period was also found to be advantageous, trapping more of the rays entering at the groove ridges.

5.5.5 Employment of an anti-reflection coating

In this thesis, the reflection reduction and light trapping of the textured silicon has been investigated for the wafers without the use of an anti-reflection coating (ARC). It is however useful to indicate the physical implications of employing such a coating upon the passage of light in the cell.

As this work has shown, for the ~200 μm wafer thickness used, the effectiveness of front surface reflectance reduction plays a more important role in maximising current output than light trapping. Despite the excellent reflection reducing properties of the texture geometries achievable on a number of texture and saw-damage etched crystal orientations under encapsulation (namely tilted pyramids and (321) orientations for the two etches respectively), the poorer performance of the remaining, less highly facetted crystal orientations means that an effective ARC remains essential for maximising the light coupled into the cell. However surface recombination, which becomes increasingly important relative to that in the bulk as the wafer thickness is reduced, and the enlarged surface area due to etching mean that surface passivation is required.

In industry, typical TiO_2 quarter-wavelength anti-reflection coatings have generally been replaced in recent years by hydrogen-containing silicon-nitride (SiN_x:H) layers, which have the added advantage of providing surface and bulk passivation as well as acting as an ARC. The refractive index n of the SiN_x:H, which is deposited by CVD techniques, can be tuned between 1.8 and 2.3 [21,22]. However, it is generally set to approximately 2.0 even for encapsulated wafers (for which ideally n = 2.3, see Chapter 4), as a trade-off between maximising light coupling into the silicon whilst minimising absorption in the SiN_x:H layer (since the extinction co-efficient k and thereby absorption in the layer increases with n [21]). Absorption in the layer could potentially have a minor contribution to light trapping losses at longer wavelengths particularly where multiple passes through the silicon are made, in the same way as for the glass encapsulation. Considering the passivating properties of the nitride, both surface and bulk passivation have been shown to be achieved under thermal processing by virtue of the diffusion of hydrogen out of the layer onto the surface and into the bulk of the cell, where it binds to dangling bonds in the material, thereby eliminating recombination sites for generated minority carriers.

The quality of bulk passivation is found in [21] to be dependent upon the simultaneous (as opposed to sequential) thermal processing of the nitride layer together with that of an aluminium back surface field (BSF). In this process, an aluminium layer is alloyed with the silicon at the rear of the cell to form a p/p+ junction, whose strong electric field repels base minority carriers preventing them from reaching the rear and thereby preventing recombination at the back surface. This enhancement of bulk passivation is thought to be because hydrogen diffusing into the silicon combines with vacancies which are formed and available only during the alloying process, these vacancy-hydrogen complexes diffusing more quickly into the bulk of the silicon.

5.5.6 Comparison of evaporated and screen printed back surface reflectors

In this work, a specular Ag BSR applied by vacuum evaporation has been investigated. In industrially produced cells, a metallic layer is more likely to be applied by a screenprinting technique, for example. Such layers may not be intended primarily or solely as a reflective

layer, but for example as a rear contact or for the formation of a BSF as was discussed in the previous section.

In [21], the reflection and scattering properties of screenprinted metal (Al & Ag) and metal/dielectric back surface layers were determined in order to assess the light trapping provided. These layers are all found to scatter light uniformly in all direction as Lambertian reflectors. This is particularly advantageous for planar silicon compared to the specular reflector investigated in this work, due to the random and oblique passage of light which results and the consequential improvement in light trapping in the silicon (see [3]). The diffuse scattering properties of a screenprinted layer would thereby in any case be preferable on the flatter etching crystal orientations where any appreciable randomisation of light by virtue of the little faceting present only occurs after 5 or 6 passes through the silicon, particularly for the very flat texture etched {XXY} orientations. For the more highly facetted textures, e.g. tilted pyramids, the inherent scattering provided the texture geometries, means that the level of randomisation achieved in combination with the specular reflector investigated in this work would be comparable to that with a diffuse screenprinted reflector.

The reflectance levels of the screenprinted layers, are particularly important for the retention of light incident at the rear of the cell; when a dielectric layer is used for trapping of steeply scattered light by TIR, this is important for light incident at near-normal angles to the rear of the silicon. Considering the reflectance values of the screenprinted layers, a processing temperature of approximately 850°C (which is a typical processing temperature for a screen-printed Al BSF [23,24]), yields rear reflectance for silver and silver-dielectric layers of approximately 95 and 98% respectively at $\lambda = 1.2$ μm. For the single silver layer, this value is equivalent to the ~94% achieved for the specular evaporated silicon investigated in this work. A screenprinted aluminium BSR/BSF was found to have a reflectance of around 80% [21,25]: it should be noted that the aluminium layer in these cases is not pure as for evaporation but alloyed with the silicon, as a results of the high temperatures required for their processing (for Al, alloying with silicon begins at temperatures above 600°C [23]).

To summarise, the evaporated silver layers used in this work appear to have equivalent reflectance values to a screenprinted silver layer, although the scattering properties are entirely different (i.e. specular compared to diffuse). One may thereby expect slightly better light trapping on flatter etching orientations, but comparable levels of light trapping upon the more highly facetted etch textures in the multicrystalline silicon wafers.

5.6 Conclusions

The light trapping properties of multicrystalline wafers with alkaline saw-damage and texture etched surfaces, have been investigated using the ray-tracing program “Birandy”. This program uses experimentally measured AFM height data as the input for quantification of the actual etch surface geometries investigated, for scan areas up to 50 x 50 μm². Seven monocrystalline silicon wafer orientations, spread evenly over the principal (111):(110):(100) triangle were used to represent the range of possible orientations in the wafer (see also Chapter 4).

For the saw-damage etched wafers, the facet tilt angles (which are too low for front surface reflectance reduction through double bounce incidence) are high enough for excellent internal scattering within the wafer if an Ag back surface reflector is used. Only the {100} and {111}

orientations perform poorly, due to the these orientations etching down flat (average angles of 9-10°) in the concentrated alkaline solution. However, due to the relatively small proportion of these orientations in the multicrystalline wafer, the overall quality of light trapping remains high.

For a texture etched multicrystalline wafer etched to the same etch depth, overall light trapping is poorer than for the saw-damage etch. This is due to the {XXY} range of orientations from {110} to {111}, which are virtually polished (e.g. average facet angles less than 5°) as etching in the low concentration alkaline solution proceeds. The poorer light trapping overall for the texture etched multicrystalline wafers compared to the saw-damage etched multicrystalline wafers arises despite the excellent light trapping in the (tilted) pyramid textures on e.g. {100} and {210} orientations, whose pathlength distributions can approach the levels of perfect Lambertian scattering surfaces with a silver rear reflector. However, if the etch duration is reduced, significant improvements can be made for the light trapping in the texture etched multicrystalline wafer. Whilst the etch is still developing, the {XXY} wafers will still exhibit faceting allowing for higher levels of light trapping, whilst the tilted pyramid structures maintain facet angles capable of both total internal reflection (TIR) at the silicon-air or silicon-EVA boundary for effective light trapping within the silicon and front surface reflection reduction by multiple incidence of light to be coupled into the silicon initially. In addition to allowing reflection reduction at tilted pyramid textures, the shallower etch has the advantage of the removal of less silicon material for the already thin and brittle wafers, in particular in the case of future ultra-thin wafers or films. However, caution must be taken that etching is deep enough to remove surface sawing damage and/or resulting surface contaminants.

Despite the higher levels of light trapping for saw-damage etched multicrystalline wafers than for texture etched wafers etched to the same depth, texture etched wafers have slightly higher maximum short circuit current values than for saw-damage etched wafers. This is because front surface reflection has a far greater influence upon the electrical output achievable than light trapping for the 200 μm thick multicrystalline wafers investigated. Optical absorption is thereby higher for texture etched multicrystalline wafers, which have lower reflectance by virtue of the particularly high facet angles present upon (tilted) pyramid textures, particularly under encapsulation where light coupling is improved by light confinement through TIR at the glass-air interface.

However, the encapsulation also forms a limitation to light trapping due to absorption losses in the glass, which at the partially transmitting wavelengths has absorption coefficients equivalent to that in the silicon. Absorption losses in the glass can be reduced by using as thin a glass layer as possible or by using a less absorbing glass. For thinner wafers or films absorption losses in encapsulating layers will be increasingly detrimental to maximum cell output.

References

[1] M.A. Green, "Limiting Efficiency of Bulk and Thin-film Silicon Solar Cells in the Presence of Surface Recombination", Prog. Photovolt: Res. Appl. **7** (1999) 327-330

[2] M.A. Green, J. Zhao, A. Wang, S.R. Wenham, "Very High Efficiency Silicon Solar Cells – Science and Technology", IEEE Trans. Elec. Dev. **46** no. 10 (1999) 1940-1947

[3] A. Goetzberger, "Optical confinement in thin Si-solar cells by diffuse back reflectors", in Proc. 15th IEEE PVSC, Kissimmee (1981) 867-870

[4] E. Yablonovitch, G.D. Cody, "Intensity Enhancement in Textured Optical Sheets for Solar Cells", IEEE Trans. Elec. Dev **29** no. 2 (1982) 300-305

[5] J.D. Hylton, A.R. Burgers, R. Kinderman, W.C. Sinke, "Determination of facet orientations on alkaline etched multicrystalline wafers", in Proc. 25th IEEE PVSC, Washington (1996) 729-732

[6] A.R. Burgers, R. Kinderman, J.D. Hylton, W.C. Sinke, "Comparison of alkaline etches on multi-crystalline wafers", in Proc. 13th EPVSEC, Nice (1995) 129-132

[7] A.R. Burgers, R. Kinderman, J.D. Hylton, W.C. Sinke, H.H.C. de Moor, "Light-trapping in saw-damage etched silicon wafers", in Proc. 14th EPVSEC, Barcelona (1997) 143-145

[8] R. Brendel, "SUNRAYS: A versatile ray tracing program for the photovoltaic community", in Proc. 12th EPVSEC, Amsterdam (1994) 1339-1342

[9] D. Thorp, S. R. Wenham, "Ray-tracing of arbitrary surface textures for light-trapping in thin silicon solar cells", Solar Energy Materials and Solar Cells **48** (1997) 295-301

[10] "Handbook of Optics", McGrawHill, New York, edited by Walter G. Driscoll & William Vaughan, Opt. Soc. Of America (1978). The program "Birandy" includes the correction of an error in equation 33, replacing n with effective indices; this is highlighted in reference [12] below.

[11] D. Thorp, P. Campbell, S.R. Wenham, "Conformal Films for Light-trapping in Thin Silicon Solar Cells", Prog. Photovolt: Res. Appl. **4** (1995) 205-224

[12] B. L. Sopori and T. Marshall "Optical confinement in thin silicon films: a comprehensive ray optical theory", in Proc. 23rd IEEE PVSC, Louisville (1993) 127-132

[13] G. Kuchler and R. Brendel, "Reconstruction of the Surface Topography of Randomly Textured Silicon", Prog. Photovolt: Res. Appl. **11** (2003) 89-95

[14] Program "Convafm", programmed by A. van der Heide, Netherlands Energy Research Foundation ECN, Petten, The Netherlands.

[15] A.R. Burgers, "Optical measurement on transparent sheet- and sandwich samples – Determining the optical properties n(λ) and k(λ) from reflection and transmission

measurements", report of the Netherlands Energy Research Foundation ECN, Petten, The Netherlands, report no. ECN-R-01-001 (2001)

[16] J.D. Hylton, A.R. Burgers, W.C. Sinke, "Light trapping in alkaline texture etched crystalline silicon wafers", in Proc. 16th EPVSEC, Glasgow (2000)

[17] E. Hecht, "Optics", Addison-Wesley Publishing Company Inc. 2nd Edition (1987)

[18] P. Campbell, M.A. Green, "Light trapping properties of pyramidally textured surfaces", J. Appl. Phys. **62** no.1 (1987) 243-249

[19] F.M. Schuurmans, A. Schönecker, J.A. Eikelboom, W.C. Sinke, "Crystal-orientation dependence of surface recombination velocity for silicon nitride passivated silicon wafers", in Proc. 25th IEEE PVSC, Washington (1996) 485-488

[20] D. Thorp, P. Campbell, S.R. Wenham, "Conformal Films for Light-trapping in Thin Silicon Solar Cells", Prog. Photovolt: Res. Appl. **4** (1995) 205-224

[21] F. Duerinckx, J.Szlufcik, "Defect passivation of industrial multicrystalline solar cells based on PECVD silicon nitride", Solar Energy Materials & Solar Cells **72** (2002) 231-246

[22] W.A. Nositschka, C. Beneking, O. Voigt, H. Kurz, "Texturisation of multicrystalline silicon wafers for solar cells by reactive ion etching through colloidal masks", Solar Energy Materials & Solar Cells **76** (2003) 155-166

[23] A. Ristow, M. Hilali, A. Ebong, A. Rohatgi, "Screen-printed back surface reflector for light trapping in crystalline silicon solar cells", in Proc. 17th EPVSEC, Munich (2001) 1335-1338

[24] A. Kaminski, B. Vandelle, A. Fave, J.P. Boyeaux, Le Quan Nam, R. Monna, D. Sarti, A. Laugier, "Aluminium BSF in silicon solar cells", Solar Energy Materials & Solar Cells **72** (2002) 373-379

[25] C.J.J. Tool, A.R. Burgers, P. Manshanden, A.W. Weeber, B.H.M. van Straaten, "Influence of Wafer Thickness on the Performance of Multicrystalline Si Solar Cells: an Experimental Study", Prog. Photovolt: Res. Appl. **10** (2002) 279-291

Summary

Light trapping and reflection reduction in a geometrically textured multicrystalline silicon solar cell can only be understood after a complete quantification of the surface morphology. It is then possible to trace the passage of light through the cell as is introduced in Chapter 1. This is by no means trivial for alkaline etched textures, due to the many different crystal orientations present in the silicon wafer and the nature of the etching process. Each crystal orientation in the wafer will exhibit a different surface morphology due to the anisotropic action of the etch, which in turn will be influenced by the etch composition, temperature and duration of etching. The experimental methods introduced in Chapter 2 have been developed and/or adapted whereby the surface morphology could be accurately mapped and quantified for the different orientations and etches used. On the basis of these experimental investigations, the observed optical properties of the alkaline etched multicrystalline silicon wafers could be explained.

Anisotropic etching in alkaline solutions

Alkaline etchants act anisotropically upon silicon, i.e. dependent upon crystallographic orientation. In Chapter 3 the etching process is investigated for the (110), (111) and (100) orientations, for NaOH and KOH concentrations of 0.2-10 M and temperatures of 70 and 90°C. In general, the higher the concentration and temperature of the solution, the faster the etch is found to progress. The (111) is the slowest etching orientation in all cases. The etch rate for the (110) orientation was higher than the (100) at 70°C. However for lower molarities at 90°C, etch rates for the (100) orientation were equivalent or slightly higher than the (110). The temperature used is found to influence etch rate without significantly affecting the surface geometry. However variation of the alkali concentration strongly affects the resulting surface texture. This is well demonstrated in the case of the (100) orientation, whose etch surface varies from four-sided upright pyramids of several microns in height covering the wafer to a practically polished etched surface on increasing the alkali concentration. The concentrated etches are suitable for the relatively fast removal of saw-damage by virtue of their high etch rates; however the etch facet tilt angles are relatively small, so that the wafer reflectance in air approaches that of polished silicon [1,2]. The density and surface coverage of the aforementioned pyramids, whose geometries are beneficial for reflectance reduction, can be improved on the addition of IPA and/or the elimination of (dissolved) oxygen from the solution [3].

Isotropic etching methods

In contrast to alkaline etching, etch rates and textures formed by isotropic etching are orientation independent. In Chapter 3, acidic solutions based upon 49% HF and 70% HNO_3 are investigated using glacial acetic acid as diluent. For the undiluted HF:HNO_3, etch rates were found to peak at a HF:HNO_3 ratio of approximately 65:35. On increasing dilution, the peak broadens and etch rates generally decrease. Textures can be varied depending upon the composition of the solution, from polished to concave tub-shaped pitted structures. The concave textures form in the region of the etch rate peak. These structures have reflectances in air of less than 20% in some cases, depending upon the curvature of the pitted texture, and down to as low as 10% under encapsulation. However, defects and grain boundaries are strongly attacked in the etching regime for tub-shaped textures, which is a problem for multicrystalline silicon wafers. Defect etching can be minimised whilst retaining the favourable etch pit geometries by keeping etch depths to a minimum, since etch pits become flatter and reflectance higher as the etch depth is increased.

For reactive ion etching, performed in a plasma consisting of SF_6, O_2 and CHF_3, needle-like structures are formed varying in height between ~0.1 and 10 μm depending upon the DC-self bias (between the plasma and the powered electrode). Reflectances of less than 5% are achieved for the bare multicrystalline silicon wafers. However, absorption of light in the needles rather than the bulk leads to a high probability of recombination at the needle surface.

Reflection reduction in alkaline etched multicrystalline silicon wafers

In Chapter 4 the surface morphology of multicrystalline silicon is investigated in detail for both alkaline saw-damage etching and alkaline texture etching. It is determined from Laue photography on many crystals that there is no preferential crystal orientation for the multicrystalline silicon (Solsix material, formerly known as Baysix). It was thus possible to use seven monocrystalline wafer orientations (namely (210), (110), (111), (311), (221), (321), (100)), spread over the principal (100):(110):(111) triangle, to represent the range of surface textures and etch rates present in a multicrystalline silicon wafer for a particular etch.

For a high concentration saw-damage etch, it is found that despite the high reflectances measured for the bare multicrystalline silicon wafers, the etch surface morphology is certainly not polished for all the orientations [1,2]. Using a specially developed technique whereby Laue back-reflectance patterns detailing crystallographic planes are combined with localised laser light scatter patterns [2], the Miller indices of the crystallographic etch facets exposed were determined, these being the {111}, {110}, {100}, {311} and {211}. The stability of these facets leads to complex structures on the majority of orientations, with the exception of the highly stable (100) and (111) orientations where the surfaces etch flat. The facet tilt angles of these structures are generally too small for double bounce reflectance reduction at the silicon front surface in air. However, some wafer orientations (notably the (311), (221), (110) and (321)) have one or more etch facets with tilt angles which are large enough for reflectance reduction by total internal reflection (TIR) of light on encapsulation i.e. > 20.9° for light incident at the glass-air interface for EVA-glass encapsulation with refractive index $n \sim 1.5$. Otherwise escaping light is hereby re-directed towards the silicon for a second chance of incidence and coupling into the silicon.

In the case of a low concentration texture etch, {111} oriented etch facets are predominantly exposed being particularly stable to the etch. This yields (tilted) pyramid structures on crystals oriented towards the (100). This would appear to be in agreement with generally accepted principals of texture etching [4], whereby {111} facets should be exposed exclusively on all crystal orientations in the multicrystalline silicon wafer. However, not only the {111} orientations but the whole range of {XXY} orientations are also found to be stable to the etch. As a result, crystals oriented between (110) and (111) will tend to etch flat as the etch proceeds [5]. This has particular consequences for the expected reflectance properties of the (110) orientation. According to theory, this orientation would have an etch surface covered with V-shaped grooves, formed by intersecting {111} facets angled at 35° to the surface. For the bare silicon wafer, this would lead to minimal reflectance reduction, with double bounce incidence of light occurring only at the base of the grooves. On encapsulation under EVA-glass, the facet angles of the theoretical grooves would allow for reflection reduction by TIR of light at the glass-air interface. However in practice, the polishing of the stable (110) base orientation by the etch leads to a flat surface giving no benefits under encapsulation. This leads to a paradox; whilst increasing the etch time allows the full development of the {111} facetted (tilted) pyramid structures, it also leads to the {XXY} orientations being increasingly polished. The etch depth for multicrystalline silicon should therefore be optimised to maximise reflection reduction for crystals oriented towards both {100} and {110}.

Light trapping in alkaline etched multicrystalline silicon wafers

In Chapter 5 the light trapping properties of thin alkaline saw-damage and texture etched multicrystalline silicon wafers of ~200 μm thickness are determined by ray-tracing. Experimentally measured height data from atomic force microscopy (AFM) is used as input for the ray-tracing program whereby the actual surface morphology is described quantitatively over an area up to 50 x 50 μm². Light trapping is strongly related to the facet tilt angles of the texture, as is the case for front surface reflection reduction. In the case of saw-damage etched wafers, a high level of light trapping is achieved for the majority of orientations, particularly in the region of the central orientations around the (321) and (110) which, when employed with a back surface reflector (evaporated silver) have light trapping properties approaching the Lambertian ideal [6]. Although light trapping is far less effective for the relatively flat etching (100) and (111) orientations, it still is considerably better than for a double polished wafer of equivalent thickness. In general, the light trapping quality far exceeds the reflection reducing properties for the saw-damage etch textures [7]. This is because the angle of incidence required for internal trapping of light is lower than for multiple incidence externally giving reflectance reduction, whereby proportionally more facets have tilt angles satisfying conditions for TIR of light at the silicon-encapsulant interface. For example, at a silicon-air interface, a minimum angle of 30° is required for multiple incidence of normally incident light externally, compared to an internal angle of only 16° for trapping of light within the silicon by TIR of light at the silicon-air boundary.

For a ~200 μm multicrystalline silicon wafer etched to the same depth as the saw-damage etch wafer using a low concentration texture etch, there is a far greater variation in light trapping between the different orientations. The (tilted) pyramid textures have excellent light trapping [8]. For the bare wafers, less than 15% of light is lost at the rear after its first pass through the silicon, and light is well randomised internally after ~2-3 passes. However, for wafers oriented towards the {XXY}, the stability of the base orientations and resultant

polishing of the surface leads to particularly poor light trapping. In the worst cases (e.g. for the (221) orientation) the level of light trapping barely exceeds that of polished silicon in the first few passes. As a result, the texture etched multicrystalline silicon wafer has poorer light trapping than if it were to receive a saw-damage etch to the same depth. Despite this, maximum short circuit current densities for texture etched multicrystalline silicon wafers of this thickness are higher than for saw-damage etched wafers, both in air and under encapsulation. This is because front surface reflection has a far greater influence upon the electrical output achievable than light trapping for the 200 μm thick wafers investigated. Optical absorption is thereby higher for texture etched wafers, which have lower reflectance by virtue of the particularly high facet angles for (tilted) pyramid textures, particularly under encapsulation where light coupling is improved by light confinement through TIR of light at the glass-air interface.

If the ~200 μm multicrystalline silicon wafer is etched to a lower depth, light trapping is improved for the {XXY} orientations by virtue of the initial (shallow) faceting of the surface. This is achieved with little reduction in light trapping for the (tilted) pyramid textures on the near {100} orientations, since facet angles remain large enough for double bounce incidence and/or light confinement at silicon-EVA and/or glass-air interfaces. In this way, light trapping can be brought to the same level as that of the saw-damage etched multicrystalline silicon wafer, with the advantage of improved light coupling particularly on crystals of near {100} orientation.

Effective conditions for reflection reduction and light trapping with alkaline etchants

For the Solsix multicrystalline silicon wafers used, with their randomly distributed crystal orientations, alkaline etching is best performed at low concentrations and temperatures for the reduction of front surface reflectance. A high level of light trapping can also be achieved at low concentrations for thinner wafers (± 200 μm) in combination with a highly reflective rear provided the etch depth is low enough to give tilted pyramids on near {100} orientations together with shallow grooving of the stable orientations near {110}. Otherwise, texturing at high concentrations of alkali will give textures whose facet angles allow for excellent light trapping on the majority of orientations, although front surface reflectance is relatively high compared to the low concentration etch.

However, some properties of the anisotropic etch make it less desirable for texturisation of the multicrystalline silicon. Large differences in the etch rates exist between the different orientations, in particular for the lower etch concentrations, whereby height differences of several microns will be present between crystals across the wafer. Such height variations may lead to problems in further processing of the wafer to a cell. For example, on the application of metallisation, the metal lines may not follow the surface, leading to gaps in the metal lines or poor contact with the surface at grain boundaries. In [9], it has also been shown that contact resistances on finished solar cells processed upon alkaline saw-damage etched multicrystalline silicon wafers varies according to crystal orientation. Higher (poorer) contact resistance is found on crystals having near {100} orientations, whilst contact resistance is seen to be homogeneously low over all orientations when for example isotropic acidic etchants are used.

References

[1] A.R. Burgers, R. Kinderman, J.D. Hylton, W.C. Sinke, "Comparison of alkaline etches on multi-crystalline wafers", in Proc 13th EPVSEC, Nice (1995) 129-132

[2] J.D. Hylton, A.R. Burgers, R. Kinderman, W.C. Sinke, "Determination of facet orientations on alkaline etched multicrystalline wafers", in Proc. 25th IEEE PVSC, Washington (1996) 1339-1342

[3] J.D. Hylton, R. Kinderman, A.R. Burgers, W.C. Sinke, P.Bressers, "Uniform pyramid formation on alkaline etched polished monocrystalline (100) silicon wafers", Prog. Photovolt: Res. Appl. **4** no. 6 (1996)

[4] B.L. Sopori, "Reflection characteristics of textured polycrystalline silicon substrates for solar cells", Solar cells (1988) 15-26

[5] J.D. Hylton, A.R. Burgers, W.C. Sinke, "Alkaline etching for reflectance reduction in multicrystalline silicon solar cells", J. Electrochem. Soc. **151** no.6 (2004) 408-427

[6] A. Goetzberger, "Optical confinement in thin Si-solar cells by diffuse back reflectors", in Proc. 15th IEEE PVSC, Kissimmee (1981) 867-870

[7] A.R. Burgers, R. Kinderman, J.D. Hylton, W.C. Sinke, H.H.C. de Moor, "Light-trapping in saw-damage etched silicon wafers", in Proc. 14th EPVSEC, Barcelona (1997) 143-145

[8] J.D. Hylton, A.R. Burgers, W.C. Sinke, "Light trapping in alkaline texture etched crystalline silicon solar cells", in Proc. 16th EPVSEC, Glasgow (2000)

[9] A.S.H. van der Heide, J. Hoornstra, J.H. Bultman, M.J.A.A. Goris, "Influence of grain orientation on contact resistance at higher emitter resistances, investigated for alkaline and acid saw damage removal", in Proc. 3rd WCPEC, Osaka (2003)

Samenvatting

Lichtinkoppeling en lichtopsluiting in geometrisch getextureerde multikristallijn-silicium zonnecellen kunnen pas begrepen worden nadat de oppervlaktemorfologie volledig gekwantificeerd is. In Hoofdstuk 1 wordt behandeld hoe licht kan worden gevolgd tijdens zijn passage door de cel wanneer de morfologie bekend is. Voor alkalisch geëtste oppervlaktetexturen is dit een complex probleem vanwege de aanwezigheid van vele verschillende kristaloriëntaties in de siliciumwafer en de eigenschappen van het etsproces. Elke kristaloriëntatie in de wafer heeft een specifieke oppervlaktemorfologie dankzij de anisotrope werking van de ets, die bovendien beïnvloed wordt door de samenstelling, de temperatuur en de duur van de ets. In Hoofdstuk 2 worden experimentele technieken geïntroduceerd die zijn ontwikkeld en/of aangepast om de oppervlaktemorfologie nauwkeurig in kaart te brengen en te kwantificeren voor de verschillende gebruikte oriëntaties en etscondities. Op basis van deze experimenten konden de optische eigenschappen van de alkalisch geëtste multikristallijn-siliciumwafers worden verklaard.

Anisotroop etsen in alkaline oplossingen

Alkalische etsen gedragen zich anisotroop bij silicium, dat wil zeggen dat het etseffect afhankelijk is van de kristaloriëntatie. In Hoofdstuk 3 wordt het etsproces beschreven voor de (110)-, (111)- and (100)-oriëntaties, met NaOH en KOH concentraties van 0,2 - 10 M en temperaturen van 70 en 90°C. In het algemeen kan gesteld worden dat het etsproces sneller verloopt naarmate de etsconcentratie en -temperatuur van de oplossing toenemen. In alle gevallen etst de (111)-oriëntatie het langzaamst. De etssnelheid van de (110)-oriëntatie is hoger dan die van de (100)-oriëntatie, bij 70°C. Echter voor lage concentraties bij 90°C zijn de snelheden gelijk of iets hoger voor de (100)-oriëntatie. Er is gevonden dat de etstemperatuur de etssnelheid beïnvloed zonder dat dit significant effect heeft op de etsgeometrie. Een variatie van de alkaliconcentratie heeft echter een sterk effect op de resulterende oppervlaktetextuur. Bijvoorbeeld bij de (100)-oriëntatie verandert de textuur van de siliciumwafer, van opstaande piramides met een vierkante basis over de gehele oppervlakte naar een bijna gepolijst geëtst oppervlak naarmate de etsconcentratie toeneemt. Geconcentreerde etsen zijn geschikt voor het relatief snel verwijderen van zaagschade vanwege hun hoge etssnelheden; de resulterende facethoeken zijn echter relatief klein zodat de reflectie van de wafer vergelijkbaar wordt met die van gepolijst silicium [1,2]. De dichtheid en de oppervlaktebedekking van de hiervoor genoemde piramides, die een

geometrie hebben die gunstig is voor reflectievermindering, kan worden verbeterd door IPA toe te voegen aan de etsoplossing en/of door zuurstof uit de oplossing te verwijderen [3].

Isotrope etsmethodes

In tegenstelling tot de alkalische etsmiddelen zijn de etssnelheden en texturen die gevormd worden door het gebruik van isotrope etsmiddelen onafhankelijk van de oriëntatie. In Hoofdstuk 3 worden de resultaten behandeld van onderzoek aan zure etsoplossingen gebaseerd op 49% HF en 70% HNO_3, met gebruikmaking van azijnzuur als een verdunner. Voor het verder onverdunde HF:HNO_3-mengsel is gevonden dat de etssnelheden een piek vertonen bij een HF:HNO_3-verhouding van ongeveer 65:35. Bij een toenemende verdunning verbreedt de piek en nemen de etssnelheden af. De geometrische texturen variëren afhankelijk van de samenstelling van de oplossing, van gepolijst tot een oppervlakte met een concave kuipjesachtige structuur. De concave textuur wordt gevormd in het piekgebied van de etssnelheid. Deze structuren hebben reflecties in lucht van minder dan 20% en afhankelijk van de kromming van de kuipjes na encapsulatie tot zo laag als 10%. Defecten en korrelgrenzen worden echter zwaar aangeëtst in het regime van de kuipjesachtige structuur, wat een probleem is bij multikristallijn-siliciumwafers. Het etsen van defecten kan worden geminimaliseerd met behoud van de gewenste kuipjesachtige structuur door de etsdiepte zo gering mogelijk te houden, aangezien de kuipjesachtige structuur platter wordt en de reflectie toeneemt naarmate de etsdiepte wordt vergroot.

Bij “reactive ion etching”, die wordt uitgevoerd in een plasma van SF_6, O_2 en CHF_3, worden naald-achtige structuren gevormd met hoogtes tussen ~0.1 and 10 μm afhankelijk van de “DC self bias” (tussen het plasma en de elektrode). Daarbij worden voor multikristallijn-siliciumwafers in lucht reflecties onder de 5% bereikt. Echter, lichtabsorptie in de naalden in plaats van in de bulk van het silicium resulteert in een hoge kans op oppervlakterecombinatie van gegenereerde ladingsdragers en daarom een geringe bijdrage aan de stroom vanuit de naalden.

Reflectiereductie in alkalische geëtste multikristallijn-siliciumwafers

In Hoofdstuk 4 worden de resultaten gepresenteerd van onderzoek aan de oppervlaktemorfologie van multikristallijn-siliciumwafers voor zowel een alkalische zaagschade-ets alsmede een alkalische textuurets. Experimenten met Lauefotografie aan vele kristallen hebben uitgewezen dat er geen preferentiële kristaloriëntatie aanwezig is in het gebruikte multikristallijne silicium (“Solsix” materiaal, voorheen bekend als “Baysix”). Het is daarom mogelijk om de kristaloriëntaties in multikristallijn silicium te representeren met behulp van zeven oriëntaties verspreid over de driehoek van (100):(110):(111) hoofdoriëntaties, te weten (210), (110), (111), (311), (221), (321) en (100). Etsstudies aan een reeks van monokristallijn-siliciumwafers met die oriëntaties kunnen daarom dienen als input voor het modelleren van het etseffect op multikristallijn silicium.

Voor een hoge-concentratie zaagschade-ets is geconstateerd dat, ondanks de hoge reflecties gemeten bij de kale multikristallijn-siliciumwafers, de oppervlaktemorfologie niet voor alle oriëntaties vlak is [1,2]. Een speciaal ontwikkelde techniek, waarbij Laue-reflectiepatronen van kristallografische vlakken in het silicium zijn gecombineerd met lokale laserlichtverstrooiingspatronen van het siliciumoppervlak [2], is gebruikt om de Miller-indices van de door de ets blootgelegde kristallografische etsfacetten te bepalen. Deze indices

zijn {111}, {110}, {100}, {311} en {211}. De stabiliteit van deze facetten leidt tot complexe structuren bij de meerderheid van de oriëntaties, met uitzondering van de zeer stabiele (100)- en (111)-oriëntaties die platte oppervlakten verkrijgen door het etsen. De facethoeken van deze structuren zijn in het algemeen te klein om in lucht reflectiereductie van de wafer te verkrijgen door dubbele of meervoudige reflectie aan de facetten. Echter, sommige waferoriëntaties (namelijk de (311), (221), (110) en (321)) hebben één of meerdere facetten met hoeken die groot genoeg zijn voor reflectiereductie door totale interne reflectie (TIR) van licht aan het glas-lucht scheidingsvlak onder encapsulatie, d.w.z. > 20.9° (voor EVA-glas encapsulatie met brekingsindex n ~1.5). Licht dat anders verloren zou gaan na reflectie wordt hierdoor teruggekaatst naar het siliciumoppervlak. Hierdoor krijgt het licht een tweede kans om in te vallen en om ingekoppeld te worden in het silicium.

Bij een laag-geconcentreerde textuurets worden voornamelijk de stabiele {111}-georiënteerde etsfacetten blootgelegd. Dit leidt tot de formatie van (gekantelde) piramidestructuren op kristallen met oriëntaties dichtbij de (100). Dit lijkt in overeenstemming te zijn met de algemeen geaccepteerde basisprincipes van textuuretsen [4], waarin wordt aangenomen dat bij alle kristaloriëntaties van de multikristallijn-siliciumwafer uitsluitend {111}-facetten worden blootgelegd. Echter, niet alleen de {111} oriëntaties, maar de hele reeks van {XXY} oriëntaties zijn stabiel in de ets, met als resultaat dat de kristallen georiënteerd tussen (110) en (111) steeds vlakker worden naarmate de ets vordert [5]. Dit heeft bepaalde consequenties voor de verwachte reflectie-eigenschappen van de (110)-oriëntatie. Volgens de theorie zou deze oriëntatie een geëtst oppervlakte moeten hebben bedekt met V-vormige groeven, bestaande uit {111}-facetten met een hoek van 35° t.o.v. het oppervlak. Voor een kale siliciumwafer in lucht zou dit een geringe reflectiereductie geven, omdat dubbele inval van licht alleen plaatsvindt aan de basis van de groeven. Onder EVA-glas-encapsulatie zouden de theoretische facethoeken van de groeven ervoor zorgen dat reflectiereductie wel plaatsvindt door TIR van licht aan het glas-lucht-scheidingsvlak. In de praktijk leidt het polijsten van de stabiele (110)-oriëntatie door de ets echter tot een glad oppervlak dat geen optische voordelen ondervindt van encapsulatie. Dit geeft een dilemma: terwijl een langere etsduur de volledige ontwikkeling van de {111}-facetten op de (gekantelde) piramidestructuren bevordert, leidt die ook tot het toenemend afvlakken van de {XXY}-oriëntaties. De etsdiepte van multikristallijn-silicium moet daarom geoptimaliseerd worden om reflectiereductie te maximaliseren voor kristallen georiënteerd dichtbij zowel de {100} als de {110}.

Lichtopsluiting in alkalische geëtste multikristallijn-siliciumwafers

De lichtopsluitingseigenschappen van dunne (~200 μm) multikristallijn-siliciumwafers geëtst met een alkalische zaagschade-ets en een textuurets worden beschreven in Hoofdstuk 5. Er is gebruik gemaakt van "ray-tracing" programmatuur. De werkelijke oppervlaktemorfologie is gekwantificeerd voor oppervlakten tot 50 x 50 μm² met behulp van "atomic force microscopy" (AFM) en deze data zijn gebruikt als invoer voor het ray-tracing-programma. Lichtopsluiting is sterk verbonden met de facethoeken van de textuur, zoals ook het geval is voor de reflectiereductie aan het oppervlak. In het geval van zaagschade-geëtste wafers is een hoge mate van lichtopsluiting behaald bij de meerderheid van de oriëntaties. Dit geldt vooral voor de centraal gelegen oriëntaties rondom de (321) en de (110), die lichtopsluitings-eigenschappen kunnen bereiken vergelijkbaar met het Lambertiaanse ideaal [6] wanneer ze gebruikt worden in combinatie met een reflector aan de achterzijde (opgedampt zilver). Hoewel lichtopsluiting minder effectief is bij de (100)- en (111)-oriëntaties, die relatief vlak worden geëtst, is die nog aanzienlijk beter dan bij een tweezijdig gepolijste siliciumwafer van

dezelfde dikte. In het algemeen is de kwaliteit van de lichtopsluiting veel beter dan de reflectiereducerende eigenschappen van de zaagschade etstexturen [7]. Dit komt omdat de invalshoek die nodig is voor de interne opsluiting van licht lager is dan de invalshoek die nodig is voor de externe meervoudige reflectie van licht aan de voorkant van de wafer zoals benodigd voor reflectiereductie. Er zijn naar verhouding meer facetten met hoeken die TIR van licht geven aan het silicium-encapsulatie scheidingsvlak dan facetten die reflectievermindering geven aan de voorkant van de siliciumwafer. Bijvoorbeeld bij een silicium-lucht scheidingsvlak is een facethoek van minimaal 30° nodig voor meervoudige reflectie van extern loodrecht invallend licht. Dit moet worden vergeleken met een interne hoek van slechts 16° die nodig is voor het opsluiten van licht binnen de siliciumwafer door TIR van licht aan het silicium-lucht scheidingsvlak.

Bij een ~200 μm multikristallijn-siliciumwafer, geëtst met een lage-concentratie textuurets tot dezelfde diepte als een zaagschade ets, is er een veel grotere variatie in de lichtopsluiting tussen de verschillende oriëntaties. De (gekantelde) piramides hebben uitstekende licht-opsluitingseigenschappen [8]. Voor de kale siliciumwafers gaat minder dan 15% van het licht verloren aan de waferachterzijde na de eerste doorgang door het silicium en het licht wordt intern goed verstrooid na ~2-3 doorgangen door het silicium. Echter bij wafers georiënteerd dichtbij de {XXY} leidt de stabiliteit van de hoofdoriëntaties en het resulterende gepolijste oppervlak tot een zeer slechte lichtopsluiting. In de ergste gevallen (b.v. voor de (221) oriëntatie) is het niveau van lichtopsluiting bij de eerste lichtdoorgangen nauwelijks beter dan dat van gepolijst silicium. Daardoor heeft een textuurgeëtste multikristallijn-siliciumwafer een slechtere lichtopsluiting dan een zaagschadegeëtste wafer die geëtst is tot dezelfde diepte. Desondanks zijn maximale kortsluitstroomdichtheden van textuurgeëtste multikristallijn-siliciumwafers van deze dikte hoger dan die van zaagschadegeëtste wafers, zowel in lucht als onder encapsulatie. Dit is omdat reflectie aan de voorzijde voor de onderzochte 200 μm dikke multikristallijn-siliciumwafers een veel grotere invloed heeft op de haalbare elektrische output dan lichtopsluiting. Optische absorptie is daardoor hoger voor textuurgeëtste wafers, die een lagere reflectie hebben voornamelijk vanwege de grote facethoeken aanwezig op de (gekantelde) piramide texturen. Dit geldt vooral onder encapsulatie waarbij lichtinkoppeling verbeterd wordt door TIR van licht aan het glas-lucht scheidingsvlak.

Als een 200 μm dikke multikristallijn-siliciumwafer minder diep geëtst wordt, verbetert de lichtopsluiting voor de {XXY} oriëntaties doordat de oppervlaktemorfologie iets grotere facethoeken vertoont in de initiële fases van de ets. Dit wordt bereikt met weinig verlies aan lichtopsluiting voor de (gekantelde) piramidetexturen dichtbij de {100}-oriëntaties omdat facethoeken in dat geval groot genoeg blijven voor dubbele reflectie van licht op het silicium en/of TIR van licht aan de silicium-EVA en/of glas-lucht-scheidingsvlakken. Op deze manier is de kwaliteit van de lichtopsluiting vergelijkbaar met die van zaagschadegeëtste multikristallijn-silicium wafers, met het voordeel van verbeterde lichtinkoppeling vooral bij oriëntaties dichtbij de {100}.

Effectieve condities voor reflectiereductie en lichtopsluiting met alkalische etsmiddelen

Voor de gebruikte “Solsix” multikristallijn-siliciumwafers met hun willekeurige kristal-oriëntaties, kan alkalisch etsen het beste worden uitgevoerd met lage concentraties én lage temperaturen met het oog op de reductie van oppervlaktereflectie. Een hoog niveau van lichtopsluiting kan voor dunnere wafers (± 200 μm) ook worden bereikt met lage

concentraties in combinatie met een hoog-reflecterende achterzijde, mits de etsdiepte gering genoeg is om gekantelde piramides te verkrijgen op oriëntaties dichtbij de {100}, samen met iets gegroefde texturen op de stabiele oriëntaties dichtbij de {110}. Andersom geeft etsen bij een hoge loogconcentratie texturen met facethoeken die leiden tot uitstekende lichtopsluiting bij de meerderheid van de oriëntaties, alhoewel reflectie aan de voorkant van de wafer relatief hoog is in vergelijking tot de laag-geconcentreerde textuurets.

Sommige eigenschappen van anisotrope etsen maken ze echter minder aantrekkelijk voor het textureren van multikristallijn silicium. De grote verschillen in etssnelheden van de verschillende oriëntaties, vooral bij lagere etsconcentraties, leiden tot hoogteverschillen van enkele microns tussen de kristallen in de wafer. Dergelijke hoogteverschillen kunnen wellicht problemen veroorzaken bij verdere celprocessing, bijvoorbeeld bij het aanbrengen van de metallisatie zouden metaallijnen de oppervlaktestappen niet goed kunnen volgen wat kan leiden tot onderbrekingen of slecht contact met het oppervlak bij de kristalgrenzen. Onderzoek [9] heeft laten zien dat contactweerstanden op zonnecellen gemaakt van multikristallijn-siliciumwafers behandeld met een alkalische zaagschade-ets, variëren per kristaloriëntatie. Hogere (slechtere) contactweerstanden worden behaald bij kristallen georiënteerd dichtbij de {100}, terwijl contactweerstanden homogeen laag zijn bij alle oriëntaties indien bijvoorbeeld isotrope zuuretsmiddelen worden gebruikt.

Referenties

[1] A.R. Burgers, R. Kinderman, J.D. Hylton, W.C. Sinke, “Comparison of alkaline etches on multi-crystalline wafers”, in Proc 13th EPVSEC, Nice (1995) 129-132

[2] J.D. Hylton, A.R. Burgers, R. Kinderman, W.C. Sinke, “Determination of facet orientations on alkaline etched multicrystalline wafers”, in Proc. 25th IEEE PVSC, Washington (1996) 1339-1342

[3] J.D. Hylton, R. Kinderman, A.R. Burgers, W.C. Sinke, P.Bressers, “Uniform pyramid formation on alkaline etched polished monocrystalline (100) silicon wafers”, Prog. Photovolt: Res. Appl. **4** no. 6 (1996)

[4] B.L. Sopori, “Reflection characteristics of textured polycrystalline silicon substrates for solar cells”, Solar cells (1988) 15-26

[5] J.D. Hylton, A.R. Burgers, W.C. Sinke, “Alkaline etching for reflectance reduction in multicrystalline silicon solar cells”, J. Electrochem. Soc. **151** no.6 (2004) 408-427

[6] A. Goetzberger, “Optical confinement in thin Si-solar cells by diffuse back reflectors”, in Proc. 15th IEEE PVSC, Kissimmee (1981) 867-870

[7] A.R. Burgers, R. Kinderman, J.D. Hylton, W.C. Sinke, H.H.C. de Moor, “Light-trapping in saw-damage etched silicon wafers”, in Proc. 14th EPVSEC, Barcelona (1997) 143-145

[8] J.D. Hylton, A.R. Burgers, W.C. Sinke, “Light trapping in alkaline texture etched crystalline silicon solar cells”, in Proc. 16th EPVSEC, Glasgow (2000)

[9] A.S.H. van der Heide, J. Hoornstra, J.H. Bultman, M.J.A.A. Goris, "Influence of grain orientation on contact resistance at higher emitter resistances, investigated for alkaline and acid saw damage removal", in Proc. 3rd WCPEC, Osaka (2003)

Appendix A: Comparison of ray-tracing with Birandy and Sunrays programs

Comparison of ray-tracing programs Birandy and Sunrays

In order to check the accuracy of ray-tracing using Birandy[1], the program was tested against "Sunrays" [2,3], a well established ray-tracing program used in the solar cell community, in addition to comparison to experimental data as was shown in Chapter 5. Polished silicon and silicon textured with periodic geometrical structures such as inverted pyramids and two-dimensional V-shaped grooves, were modelled with both programs and the resulting absorption A, reflection R (with surface and total reflection represented by R_s and R_t respectively) curves and J_{sc}(max) values compared. The cell structures used were as for Chapter 5, these being a) bare silicon in air, b) silicon in air with an Ag BSR, and c) silicon with 3mm glass + EVA front encapsulation and an intimate Ag BSR (see Figure 5.6). The results are shown in the following pages and are found to be in good agreement for the two ray-tracing programs.

References

[1] D. Thorp, S. R. Wenham, "Ray-tracing of arbitrary surface textures for light-trapping in thin silicon solar cells", Solar Energy Materials and Solar Cells **48** (1997) 295-301

[2] R. Brendel, "SUNRAYS: A versatile ray tracing program for the photovoltaic community", in Proc. 12th EPVSEC, Amsterdam (1994) 1339-1342

[3] R. Brendel, "SUNRAYS 1.0 Manual", Sunrays program and user manual, distributed by Garching Innovation GmbH

a) Wafers in air

(i) Lambertian ideal: planar silicon with front surface R = 0%, rear surface R = 100%, polished front, fully Lambertian rear. Silicon thickness = 186 µm

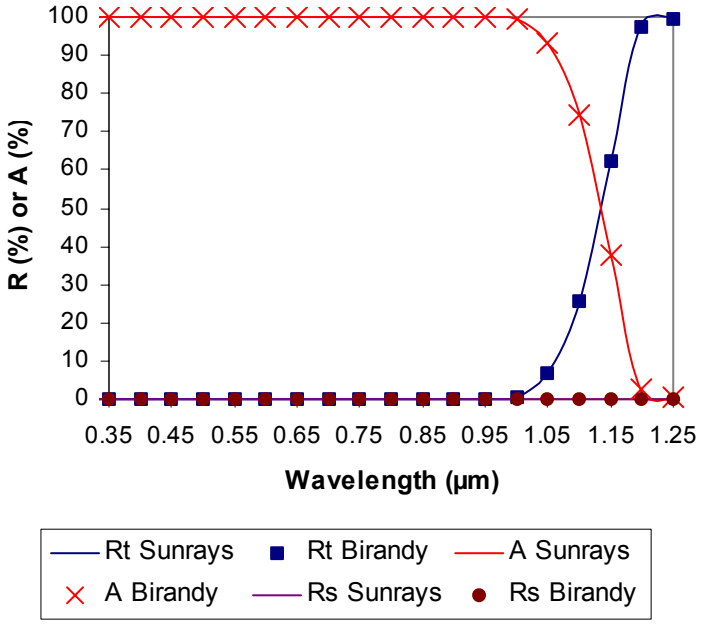

J_{sc}(max) from Birandy = 43.53 mA/cm²
J_{sc}(max) from Sunrays = 43.53 mA/cm²

(ii) Double polished wafer, silicon thickness = 186 µm

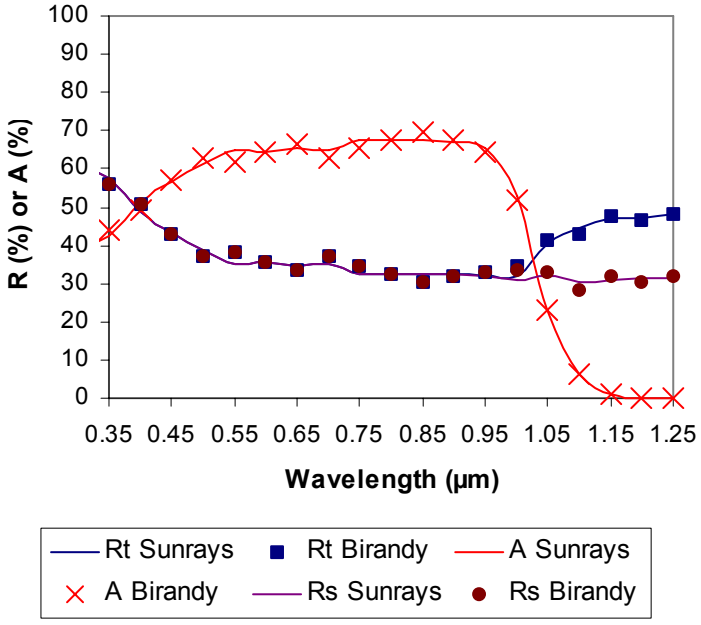

J_{sc}(max) from Birandy = 25.94 mA/cm²
J_{sc}(max) from Sunrays = 26.09 mA/cm²

a) Wafers in air (cont.)

(iii) Perpendicular 2D V-shaped grooves (X-grooves on front surface, Y-grooves on rear), with facet tilt angles θ = 54.7°. Silicon thickness = 30 µm

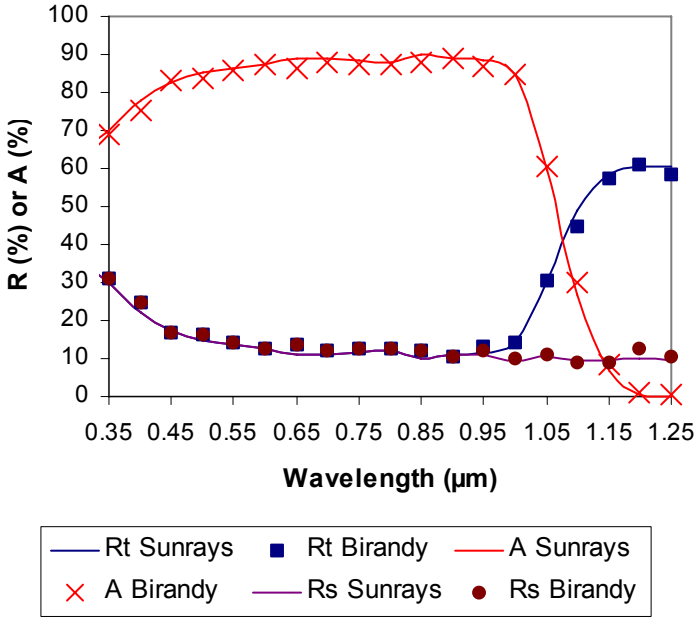

J_{sc}(max) from Birandy = 36.88 mA/cm²
J_{sc}(max) from Sunrays = 36.94 mA/cm²

(iv) Front surface inverted pyramids with facet tilt angles θ = 54.7°, polished rear. Silicon thickness = 30 µm

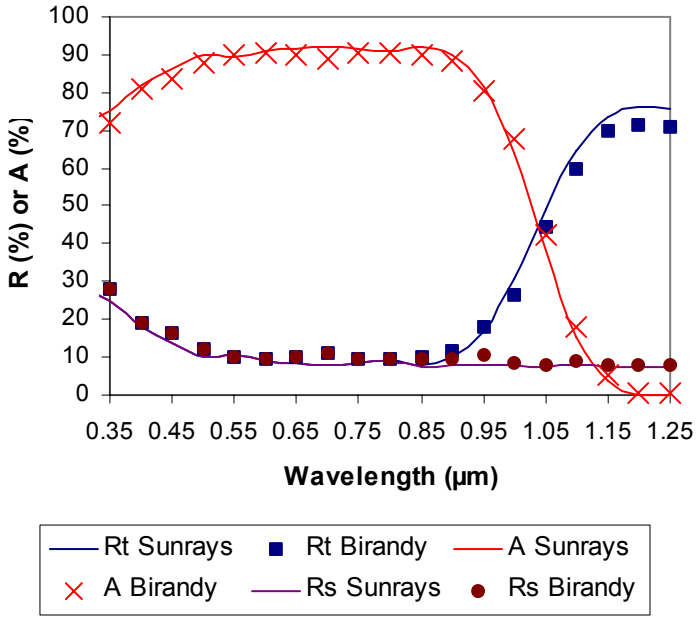

J_{sc}(max) from Birandy = 36.56 mA/cm²
J_{sc}(max) from Sunrays = 36.60 mA/cm²

b) Wafers in air with intimate Ag BSR

(i) Double polished wafer, silicon thickness = 186 µm

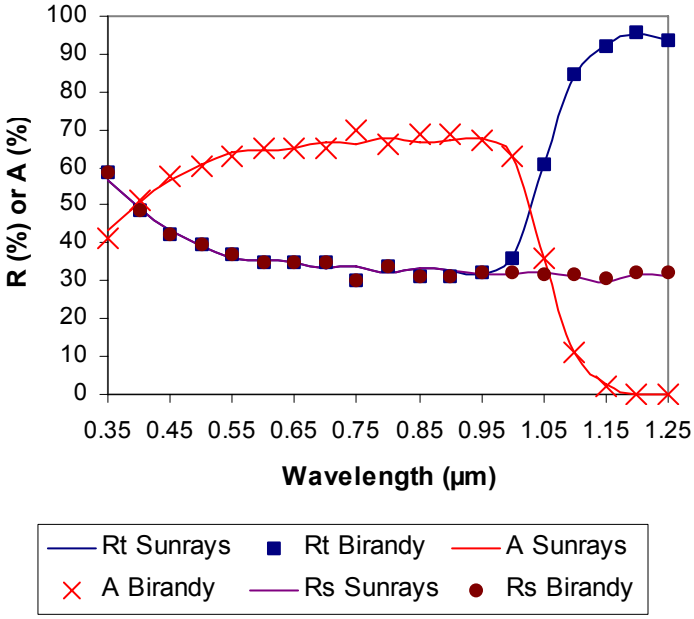

$J_{sc}(max)$ *from Birandy = 26.88 mA/cm²*
$J_{sc}(max)$ *from Sunrays = 26.76 mA/cm²*

(ii) Front surface grooves with facet tilt angle θ = 35°, silicon thickness = 30 µm

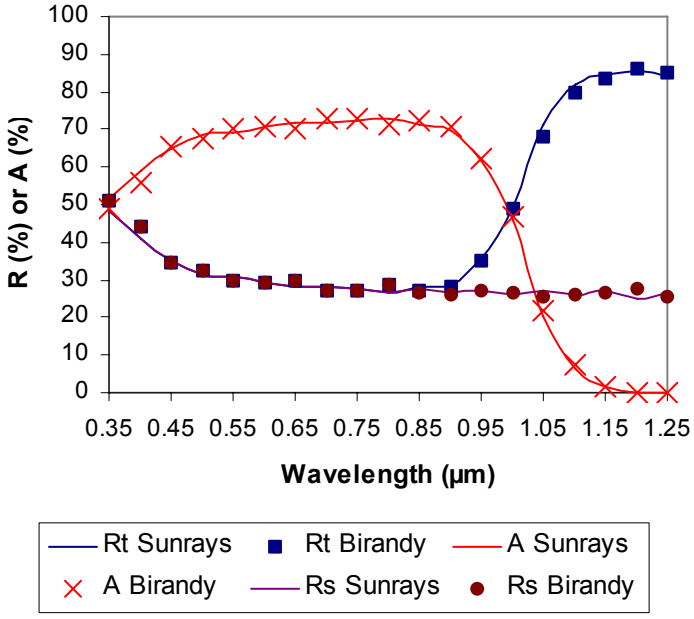

$J_{sc}(max)$ *from Birandy = 27.88 mA/cm²*
$J_{sc}(max)$ *from Sunrays = 27.86 mA/cm²*

c) Wafers encapsulated with an intimate Ag BSR

(i) Double polished wafer, silicon thickness = 186 µm

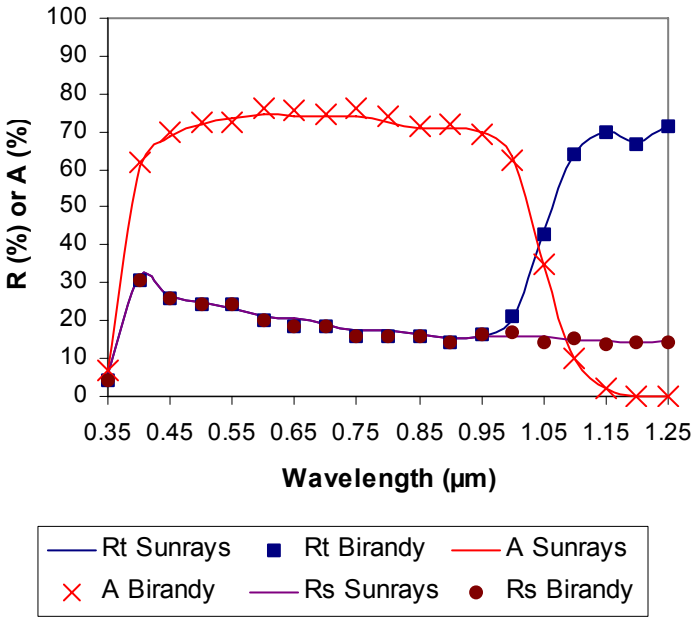

$J_{sc}(max)$ *from Birandy = 29.85 mA/cm²*
$J_{sc}(max)$ *from Sunrays = 29.33 mA/cm²*

(ii) Front surface grooves with facet tilt angle θ = 35°, silicon thickness = 30 µm

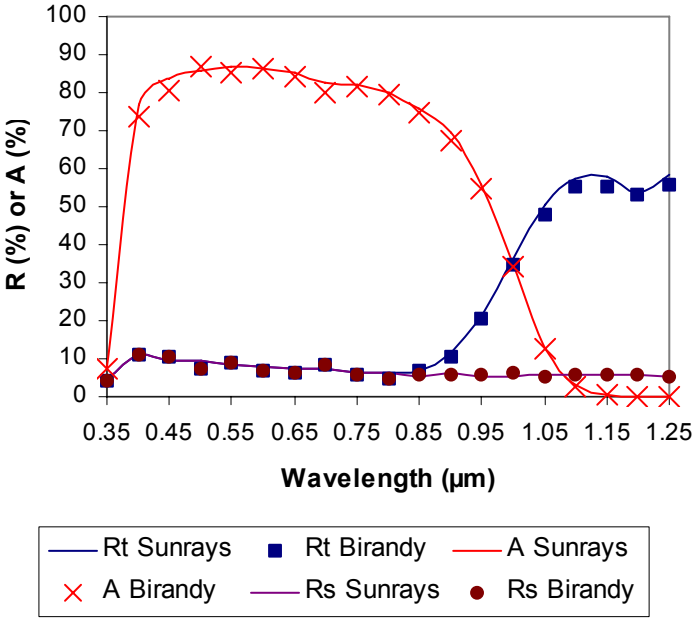

$J_{sc}(max)$ *from Birandy = 30.53 mA/cm²*
$J_{sc}(max)$ *from Sunrays = 30.96 mA/cm²*

c) Wafers encapsulated with an intimate Ag BSR (cont.)

(i) Front surface inverted pyramids, facet tilt angles θ = 54.7°, silicon thickness = 186 µm

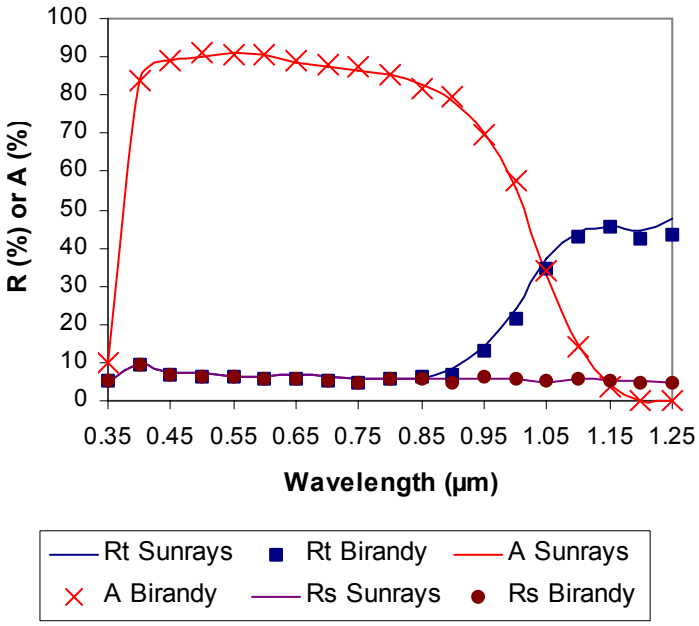

J_{sc}(max) from Birandy = 34.53 mA/cm²
J_{sc}(max) from Sunrays = 34.36 mA/cm²

List of Publications

J.D. Hylton, A.R. Burgers, W.C. Sinke, "Alkaline etching for reflectance reduction in multicrystalline silicon solar cells", J. Electrochem. Soc. **151** no.6 (2004) 408-427

J.D. Hylton, A.R. Burgers, W.C. Sinke, "Light trapping in alkaline texture etched crystalline silicon solar cells", in Proc. 16th EPVSEC, Glasgow (2000)

A.R. Burgers, C.J.J. Tool, J.D. Hylton, A.W. Weeber, A.G.B.J. Verholen, J.G.E. Gardeniers, M.J. de Boer, M.C. Elwenspoek, "Silicon solar cells structured by reactive ion etching and processed with screen printing", in Proc. 2nd WCPEC, Vienna (1998) 1531-1534

J.D. Hylton, A.R. Burgers, W.C. Sinke, "The stability of the (110) orientation in alkaline etched multi-crystalline silicon for solar cells", presented at Workshop on Physical Chemistry of Wet Chemical Etching of Silicon, Holten, The Netherlands (1998)

J.D. Hylton, A.R. Burgers, W.C. Sinke, "Absorption in thin textured silicon wafers", in Proc. 14th EPVSEC, Barcelona (1997) 139-142

A.R. Burgers, R. Kinderman, J.D. Hylton, W.C. Sinke, H.H.C. de Moor, "Light-trapping in saw-damage etched silicon wafers", in Proc. 14th EPVSEC, Barcelona (1997) 143-145

J.D. Hylton, A.R. Burgers, R. Kinderman, W.C. Sinke, "Determination of facet orientations on alkaline etched multicrystalline wafers", in Proc. 25th IEEE PVSC, Washington (1996) 1339-1342

J.D. Hylton, R. Kinderman, A.R. Burgers, W.C. Sinke, P.Bressers, "Uniform pyramid formation on alkaline etched polished monocrystalline (100) silicon wafers", Prog. Photovolt: Res. Appl. **4** no. 6 (1996)

A.R. Burgers, R. Kinderman, J.D. Hylton, W.C. Sinke, "Comparison of alkaline etches on multi-crystalline wafers", in Proc. 13th EPVSEC, Nice (1995) 129-132

Curriculum Vitae

Jessica Hylton was born on 30th April 1971 in Paddington, London (GB). She obtained her "O" levels at Sacred Heart R.C. High School for girls in Wealdstone in 1987 and "A" levels at St. Dominic's VI form College in Harrow-on-the-Hill in 1989. Thereafter she embarked upon a BSc. degree in Physics at Loughborough University of Technology, which she obtained with first class honours in 1993. This study included a one year industrial placement at Van Leer R&D Division in Mijdrecht (NL). Here she performed research concerning the mapping of magnetic fields produced by various current carrying coil configurations, as used for the inductive heat sealing of tamper-evident lids in the packaging industry. Subsequent to her graduation followed a brief placement at the solar energy department at the Energy research Centre of the Netherlands (ECN), Petten (NL) in 1993. Her work concerned the effective planning of experiments by means of main effects studies. Hereby processes containing many variables, in this case the processing of silicon to a completed cell, can be effectively planned and analysed in order to maximise the desired output parameters. Thereafter she obtained her MSc. degree in Non-Destructive Testing of Materials at Brunel University of Technology in 1994. Her final research project, performed in collaboration with industrial partner EEV in Chelmsford, investigated the appropriateness of CCD-scintillator combinations for X-ray detection of defects in industrial applications. In 1995, she emigrated to the Netherlands and embarked upon her PhD research work at ECN in the solar energy group. This research concerned the quality of light trapping and light coupling in chemically etched multicrystalline silicon, the results being described in this thesis.

Acknowledgements

Writing the final acknowledgements section of this thesis gives me a chance to look back at my time at ECN, which started in 1993 with an industrial placement in the solar energy group. Many of my colleagues and friends over the years have had some part to play in the completion of this work. I wish to thank them all, in particular those named below.

Firstly I wish to express my gratitude to my supervisor, or in Dutch *promotor*, Wim Sinke, for giving me the opportunity to do this PhD and for his continued support and enthusiasm throughout this period. I also wish to thank Teun Burgers who, although it was not official, I often saw as a assistant supervisor (*co-promotor)*. Thank you Teun especially for setting up the "PhD club"– it gave me just the motivation I needed to buckle down and start (and keep on) writing in earnest. Doing a PhD in a non-university environment would have been far more stressful were it not for the support of fellow *promovendi* (PhD students) over the years, including Cor Leguijt, Peter Lölgen, Frank Schuurmans, Aissa Azzizi and finally Arvid van der Heide, to whom I am particularly grateful for his companionship throughout most of my years as a PhD student.

Within the solar cell group at ECN, there is hardly anyone who has not contributed in some way to the completion of this thesis, either directly or indirectly and it was a great privilege and pleasure to work with you all. I wish to thank Gertjan Langedijk for the many reflectance measurements which he performed over the years as well as for the great partnership we had as guardians of the spectroradiometer. Since much of my time as a PhD student was spent in the "wet lab", etching, I want to acknowledge those who I worked with or alongside throughout the years, including Ronald Kinderman, Sacha Valster-Schiermeier, Maurice Goris, Peter Bressers, Eric Kossen and Martien Koppes. I also wish to thank Andries Tip for the encapsulation of so many of my samples; the introduction of lamination as an "in-house" technique was a turning point in my research. A special note of appreciation is due to Erwin Schoonderwaldt, who I supervised for his final industrial project (*afstudeeropdracht*) for his MSc. at the UvA. Thank you in particular for the photogoniometry measurements you performed at TNO Delft on the monocrystalline samples used in Chapters 4 and 5. I am also much obliged to those who proof-read and discussed sections of this thesis with me, especially Arvid van der Heide, Mariska de Wild and Bart Geerligs.

Outside of the solar energy group at ECN I wish to thank to Marijke Roos for the AFM scans, and both Gerrit Hamburg and Marijke for the SEM photography. In addition I wish to thank Bert Moleman and Willem Moolhuyzen (University of Amsterdam, UvA) for their help with the Laue photography.

On a more personal note, my time as a PhD student would not have been as fulfilling were it not for the tremendous atmosphere of warmth and friendship which I experienced during my time at ECN. Although I have not mentioned everybody by name in these acknowledgements, I wish to thank you all for the many happy memories I have of working with you.

Finally, I wish to express my most sincere gratitude to my husband Alex, and to both our families for their love and support throughout this period.